Optical and EUV studies of laser triggered Z-pinch discharges

Isaac Tobin

A Thesis presented for the degree of
Doctor of Philosophy

School of Physics
Trinity College Dublin
Ireland

October 2014

Declaration

The work in this thesis is based on research carried out at the University of Dublin, Trinity College, and University College Dublin. No part of this thesis has been submitted elsewhere for any other degree or qualification and it is entirely my own work with exception of assistance recognised in the acknowledgements and the collaborative work noted in the publications. I agree that Trinity College Dublin may lend or copy this thesis on request.

_____

Isaac Tobin

31st October 2014

Summary

This thesis describes the results of experiments with two geometries of laser assisted discharge plasma. Both devices are designed for fast Z-pinch discharge, triggered by laser produced plasma generated by ablation of one or both electrodes. The laser plasma parameters are adjusted to control the plasma load while the discharge parameters are adjusted to yield a rate of rise of current greater than 10^{10} A/s.

The expansion dynamics and emission characteristics of the plasma were analysed, with and without discharge. This was done using ion time-of-flight probes, temporally- and spatially-resolved optical emission spectroscopy, absolutely calibrated extreme ultraviolet (EUV) spectroscopy, in-band EUV energy output, intensified charge coupled device (ICCD) imaging of the EUV emitting region, and thin film deposition. The discharge current was monitored using a Rogowski coil, which gave a clear indication of pinch events.

The experimental results are split into two main sections. In the first experiment a customisable miniature low-inductance discharge device was used to investigate the effect of triggering a discharge with colliding laser produced plasma. This colliding plasma interaction and the subsequent discharge were studied with various triggering conditions. In the second experiment a larger scale laser assisted discharge device was investigated as a source of extreme ultraviolet light with two materials as plasma load. These materials were tin and galinstan, the latter being a eutectic metal alloy of gallium, indium, and tin which is liquid at room temperature. The discharging of this device was triggered by the laser ablation of one of a pair of rotating disc electrodes, coated by liquid metal to avoid the issue of electrode erosion. The device was characterised as a possible short wavelength source for application in metrology.

Acknowledgements

Firstly I would like to thank my supervisor, James Lunney, for the strong support, guidance and understanding. I am very lucky to have had the opportunity to work with him and learn from him.

I would also like to thank all my group members, past and present, Enrique Sterling, Tony Donnelly, and Clelia Pagano for being the knowledge base I could draw from at the start of this work. Along with James Creel, Inam Mirza, Taj Kahn, and all my friends in TCD, especially Gearoid O'Connell for the years of collaboration, banter, and good times. Thanks too to the Spec Group in UCD, where I was always made feel at home and where I am happy to say I gained many good friends. Thanks especially to Larissa Juschkin who was instrumental to UCD experimental work, and a supportive friend. To Emma Sokell, Fergal O'Reilly, Gerry O'Sullivan, and Padraig Dunne I also owe many thanks, for frequent discussions and guidance during my work.

A very big thanks to all of the staff members from the School of Physics, TCD and also UCD. The support from the staff made all of the work possible, without the school office, finance office, mechanical workshop or electronics workshop it would not be possible. My thanks then to: Ken Concannon, Jemer Kavanagh, Alan O'Meara, Nigel Carroll, Chris Smith, Joe McCauley, Dave O'Mahony, Dave Grouse, Pat Murphy, Una Dowling, Colm Stephens, Jeanette Cummins, and all of the staff in School of Physics, TCD.

Finally I would like to thank my family and friends for always being there for me, I count myself very lucky to have such a wonderful group of people to surround myself with. A big thanks to my mother, Karen, and brother, Josh, for proofing several sections and dedicating the time to help me. Most especially to my wife Odette, I do not think I could have ever completed this work without all of the love and support.

Contents

Introduction

The work covered in this thesis was undertaken with the aim of investigating, characterising, and optimising laser plasma triggered discharge devices. Such devices can have a wide range of geometries and applications, in this research the focus was on Z-pinch dynamics and also the spectral emission, both visible and extreme ultraviolet with perspective applications in the development of short wavelength sources.

I. Motivation

Moore's law, formulated by Gordon Moore in 1965[1], stated that the number of components per integrated circuit would roughly double every 18 months. This has been followed by the semiconductor lithography industry, with the number of transistors on the leading Intel processors increasing from 2,300 using the 10 μm processing node in 1971 to 1.4 billion using the 22 nm node in 2012. Increasing the number of transistors means increasing processing power, while smaller transistors means increased switching speed and lower power consumption per transistor. The term processing node is based on half the distance between identical features in a printed array. The 22 nm node is currently the highest resolution process in high volume manufacture, with the 14 nm node due during 2014/2015. To reach the high resolutions required, the current process uses rather complicated, time consuming and expensive lithography techniques in conjunction with 193 nm ArF excimer laser sources. To meet the higher resolutions of the next lithography nodes, a source of shorter wavelength radiation is required to print the semiconductor structures.

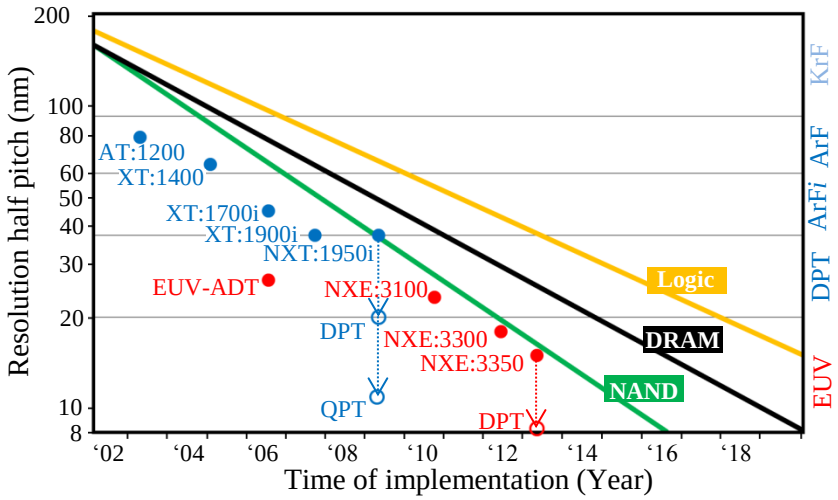

Fig. I.1 – Photolithography tool roadmap proposed by ASML[2] to continue to meet Moore's law, with filled dots indicating source designations.

Fig. I.1 shows the photolithography tool roadmap proposed by ASML[2], the leading manufacturer of industrial lithography tools. The graph shows the tool resolution half pitch for three different silicon chips printed: Logic, DRAM and NAND. The line trends are following Moore's law, with the bullet points indicating the source desgnation or the required source type and time scale of implementation. The labels along the right hand side of the graph show the source used in each of the resolution half pitch ranges. The wavelengths of the KrF and ArF excimer lasers used in photolithography are 248 nm and 193 nm respectively. The labels on the right hand side of Fig. I.1 indicate the technologies required for each range of resolution half pitch, from krypton fluoride (KrF) and argon fluoride (ArF) lasers to the more recent immersion (ArF*i*) and double patterning techniques (DPT). DPT[3] and ArF*i*[4] require expensive tools and add many steps to the lithography process which impacts the number of silicon wafers which can be processed per hour, a key factor in the cost of following Moore's law. The increasing costs associated with DPT and immersion techniques for next generation lithography are a major concern in the semiconductor industry. By utilising a shorter wavelength source to print the features the number of processing steps are decreased. The final tool step shown in Fig. I.1 is extreme ultraviolet lithography (EUVL). Before EUVL can be discussed the wavelength range must be described.

The distinction between vacuum ultraviolet (VUV), EUV, and soft x-ray radiation is not entirely straight forward, but frequently EUV is assigned a wavelength range of 5 nm – 50 nm (250 eV – 25 eV). One characteristic of EUV radiation is that photo-

absorption is high in all matter, due to the presence of a multitude of atomic resonances[5]. This distinction is not entirely unique though, as VUV and soft x-rays are similarly absorbed by many materials. The need for working under vacuum is clear for EUV applications to avoid absorption losses in background gases; refractive optical elements are also not applicable for EUV for this reason. For this wavelength range many materials have high reflectance at grazing-incidence angles[6], and at normal-incidence angles relatively high reflectivity can be achieved through use of complex and expensive multilayer mirrors (MLMs)[7]. Diffractive optics like zone-plates are also useful for these short wavelengths[8].

EUV radiation is suitable for many fields apart from lithography. In surface science specific elemental and chemical signatures can be easily identified due to the characteristic atomic resonances[5]. With the development of EUV optics and detectors in space-born telescopes, the field of EUV astronomy has become possible[9], [10]. EUV is also very useful in high-resolution imaging due to shorter wavelengths which results in limited diffraction. This has led to tools designed for EUV microscopy in application as an enabling technology in lithography for mask defect analysis[11], [12]. Recently sources in the so-called "water-window" between $2.3 - 4.4$ nm have been under investigation too. This band is characterized by a natural contrast between water and carbon, due to the strong absorption contrast between the water and carbon K-absorption edges[13], [14]. This makes the detailed imaging of living cells possible in aqueous samples. The main driver behind research into EUV sources has been the need for high power short wavelength sources for EUVL.

The main factors causing delays in the implementation of EUVL have been source power, dose stability, and reducing downtime. There is also need for development of supporting technologies like EUV resists and reticles, along with debris mitigation techniques to ensure long mirror lifetime. The power required for the implementation of EUVL into high volume manufacture is 250 W[15]. The likely EUVL tool design given by industry has an optical delivery system consisting of 11 Mo/Si MLMs, which have a peak reflectivity of approximately 70%. This system would therefore have a peak EUV throughput of <2% to the wafer, giving roughly 5 W for the initial sources. This is a limiting factor adding to the high power requirements for sources. The main factor behind the source power requirement is a cost effective wafer throughput, the latest

reports of wafer throughput have shown approximately 40 wafers per hour with an EUV fluence of 15 mJ/cm^2 at the wafer[2]. The proposed EUV source must also be scalable to meet the increasing power requirements as feature size decreases further. To make EUVL cost effective, the source must be capable of running with high average power, high dose stability, high duty cycle, and long lifetime. Together these terms equate to a source with an intense EUV source with low variation in output energy per pulse, with high repetition rate, and over a long running time (i.e. robust components that do not cause downtime for repair/replacement). To achieve these requirements there are many challenges facing EUVL tool manufacturers. A key factor in the lifetime is damage caused by the high energy ions or particulate matter associated with plasma based sources. To remove these ions/particulates from the optical delivery path and avoid sputtering or deposition damage of the MLMs, several schemes have been proposed[16]–[19]. The introduction of EUVL is desired for the 10 nm and 7 nm nodes by 2017[15].

The current state-of-the-art EUV source designs fall into three categories; laser produced plasma (LPP), discharge produced plasma (DPP), and laser assisted discharge plasma (LDP). LPP and LDP sources are mostly based around tin as a source material[20]–[25], while DPP sources are typically based on xenon[11], [26]. The choice of material is dictated by the wavelength selected for EUVL, the MLMs mentioned previously have a very narrow-band reflectivity resulting in a 2% bandwidth centred at 13.5 nm after the 11 mirror system proposed[27]. These mirrors consist of hundreds of alternating layers of molybdenum separated by a spacer layer of silicon acting as a Bragg reflector.

The MLMs are based on creating constructive interference between reflected light from each layer to yield high reflectivity of EUV light at a desired wavelength. Each layer pair is designed to have a thickness equal to half the wavelength of light to be reflected. Initially sources using xenon gas under fast high current discharge were investigated, however the EUV emission from xenon peaks at roughly 11 nm. This makes xenon unsuitable due to strong absorption in the silicon layers of the MLM. Lithium was also investigated as a possible source material, with a bright emission line from Li III at 13.5 nm. It was noted that the lithium ions expelled from the plasma penetrate deeply into almost all solid materials due to their small size, causing diffusion

in the MLM coatings. Tin was chosen based on the strong unresolved transition array (UTA) around 13.5 nm[20], although it does have drawbacks compared to xenon and lithium. Tin based sources have issues with particulate debris which are not problematic for xenon. Tin sources also have less spectral purity than lithium due to the relatively wide tin UTA.

A full discussion of all of the proposed geometries of LPP, DPP and LDP EUV sources is beyond the scope of this work, but there are resources available describing each[28], [29]. There are also new source developments reported at the many EUV conferences and workshops held each year. Here, a brief overview of a few of the key source designs will be given, making note of their EUV output and conversion efficiency (Table I.1). The term conversion efficiency (CE) is simply the amount of EUV energy collectable from the source in 2π sr over the amount of laser/electrical energy input. This term is not entirely intuitive when comparing LPP to DPP/LDP sources, as it is common practice to only account for the laser pulse energy rather than the energy supplied to the laser. Discharge based sources have a higher "wall-plug" efficiency as the energy can be coupled electrically to the plasma, rather than electrically to the laser then optically to the plasma. The efficiency of energy coupled from the wall-plug to plasma is approximately 5 times greater for discharge plasma sources than laser plasma sources[29].

Table I.1 – EUV source parameters from various geometries, showing energy input, repetition rate, average EUV power out, conversion efficiency and estimated EUV energy out in 2π sr.

	E_{input} (mJ)	R_{rate} (kHz)	P_{Avg} (W)	CE (%)	E_{EUV} (mJ/2π sr)
Sn LPP with 1064 nm Nd:YAG	650	–	–	2	13
Sn LPP with 10.6 µm CO_2	160	–	–	2.6	4.2
Sn LPP with pre-pulse + CO_2	15 + 95	–	–	2.8	3.1
Cryogenic Xe target LPP	160	–	–	0.9	1.4
Electrode-less Xe DPP	–	2.5	10	–	4.0
Liquid Sn jet LDP	5×10^3	1 – 4	40	1.3	65
Liquid Sn electrode wheel LDP	4×10^3	20	20	~1.5	60

The key advantages of tin based CO_2 LPP sources over Nd:YAG are a higher CE, narrower spectral bandwidth, and approximately 1000 times fewer neutral particles[30]. This has led to the ongoing drive to increase available CO_2 power to meet the required EUV power output for lithography tools. To maximise the coupling of CO_2 laser power into the plasma, the use of a Nd:YAG pre-pulse has been investigated and shown to

yield increases in CE. Theoretical predictions have been given of up to 5% CE from tin based CO_2 sources utilizing a 1064 nm laser pre-pulse[29]. The repetition rate (R_{rate}) of LPP sources is dependent mostly on the laser used and the target management, as the source will need to run for long periods without downtime.

Liquid tin jet electrode based sources under study at the Russian Institute for Spectroscopy (ISAN) have the reported potential to give very high EUV power with minimal debris problems[31], however these sources are quite complex due to the need to pump liquid tin through a pair of nozzles. Electrode wheel LDP sources similarly work treating liquid tin as the electrodes, thus avoiding erosion during operation. Such sources operate by laser ablation of one electrode in a vacuum, with the resultant laser produced plasma acting to trigger the discharge. The laser pulse parameters are key in achieving maximum EUV output as it controls the plasma load in the discharge. A source geometry under study for EUVL applications has been shown to give a stable EUV output of 20 W at 20 kHz with roughly 100% duty cycle[32]. XTREME technologies GmbH reported in 2012 that a 50 W source was under testing. They also reported their latest LDP source designs include the use of multiple laser pulses to control the density distribution in the plasma load[32].

The 250 W average power required for EUVL sources is a challenging goal, especially for lab based sources like those utilised in this work. For this reason the main driver here is instead the investigation of sources for microscopy/metrology applications. In this aim a source would need to be well characterised but require much lower EUV output power. The requirement for metrology sources is high brightness [W cm^{-2} sr^{-1}]. Metrology sources are in high demand due in part to the need for support technologies in EUVL to scan for defects in features which, by design, will be on the same order as the metrology source wavelength.

II. Fast Z-pinch

Z-pinch plasmas have been reported to be intense sources of x-ray and EUV radiation[33], and are under investigation as a viable option for the next generation photolithography sources. Z-pinch plasmas have been studied since the 1930's, although the term only came about in the 1950's to distinguish the self-constriction by an axial (Z directed) current rather than an inductively driven azimuthal (θ) current. In this work only Z-pinch plasma devices were utilised. Much of the early research into Z-pinch plasms was focused on the development of fusion devices driven by magnetic compression. However the presence of strong magnetohydrodynamic instabilities in Z-pinch plasmas pose signification problems for this approach, some complex device designs have been implemented to mitigate such instabilities[34].

In the novel EUV Z-pinch sources of concern in this work the required currents are much smaller than the large scale devices concidered for fusion. These smaller devices generate what are termed fast Z-pinches[35]. Fast Z-pinches are characterised by a relatively short compression time and current pulse duration too short to reach a Bennett-type equilibrium[36], where the magnetic pressure causing compression eqalises with the plasma pressure. These factors typically refer to the small size of the pinched plasma, being on the order of several millimeters to a few centimeters. In this case, provided the rate of rise of the current pulse is sufficient, $>10^{10}$ A s^{-1}, the plasma compression occurs on roughly the same time scale as the current pulse width, hundreds of nanoseconds to a few microseconds. In a pinched plasma the radial implosion leads to accumulation of plasma along the discharge axis, with densities of up to 10^{21} cm^{-3}. The plasma then thermalises and reaches temperatures of 100 – 1000 eV (1.16×10^6 K - 1.16×10^7 K) which is followed by the emission of K-shell radiation, electrons and ions. In the case of fast Z-pinch the plasma will not be sustained at the minimum radius but will instead bounce back after implosion and expand away from the axis. This process will be discussed further in the theory chapter.

These fast Z-pinches are useful sources not only for EUV and x-ray radiation but also as sources of high energy ion beams[37]. This has proven very useful in the study

of high energy density physics[38], for example investigation of high temperature plasmas like those generated in fusion reactors. By using a high current discharge in concert with a laser induced breakdown spectroscopy (LIBS) setup a smaller amount of sample can be used to yield the same results[39].

Many geometries of Z-pinch are possible, with the key variant being the source of the plasma load. Frequently such sources are triggered using annular gas puffs connecting anode and cathode in a coaxial geometry[40], there are also many designs based around solid loads, or targets, composed of wire arrays, foils or foam cylinders[41], [42]. In this work the focus is on Z-pinch sources triggered by laser produced plasma, generated by laser ablation of one or both electrodes. As mentioned previously these laser assisted discharge plasma sources are frequently refered to as LDP or LA-DPP in the literature. There are several geometries of LDP, a representative cross section of them is shown in Fig. I.2. Here we will briefly describe the five LDP sources presented with reference to literature. The design in (a) is a coaxial setup where one electrode is ablated, with a circular opening in the counter electrode for the laser pulse and to view the plasma emission[43]. This source design was augmented by Kieft et al.[44] using a liquid metal bath as the ablated cathode. This did not however remove the issue of errosion of the anode during discharge. In (b) the LDP is triggered using an externally generated LPP, a portion of which is selected as the plasma load using an aperture[45]. The design in (c) is more complex with a pair of liquid metal jets acting as electrodes[31]. A laser plasma is generated by ablation of the cathode jet, expanding in the direction of the anode jet to trigger the discharge. The source designs shown in (d) and (e) are the two types investigated in this thesis; (d) discharge triggered by a pair of colliding laser plasmas and (e) liquid metal coated electrode wheels, triggered by laser plasma generated on the cathode wheel.

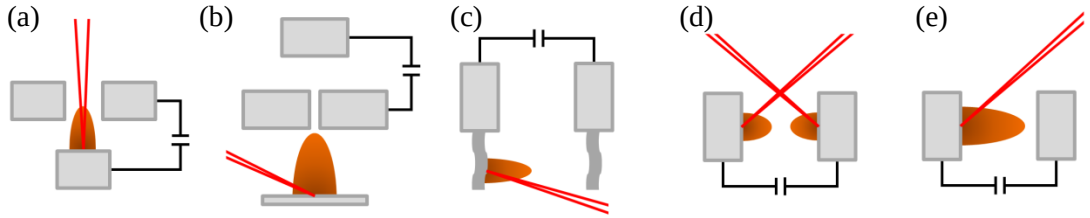

Fig. I.2 – Schematics of various laser assisted discharge plasma geometries. Each is described in the text.

The key differences between these sources are the methods by which the plasma load is introduced and how the issue of source lifetime is approached. The plasma load is crucial in terms of the pinch, controlling the plasma line density enables control of the pinching. Plasma line density is the integrated electron density through a cross sectional area of the plasma column. Source lifetime is a key concern for any source, as frequent replacement of parts due to erosion is undesirable. To avoid this issue in (c) and (e) the electrodes are coated with liquid metal, which is replenished constantly.

III. Thesis breakdown

This thesis is divided into 5 chapters. In Ch. 1 the theoretical background supporting this work is given. Ch. 2 gives the description of the data analysis tools utilised along with a discussion of the equipment and the calibration methods. In both Ch. 3 and Ch. 4 the experimental results from the two source geometries used to investigate laser plasma triggered discharges are presented. In Ch. 3 the colliding laser plasma triggered discharge is described and the results for a range of discharge voltages and a set of laser parameters are presented. This experiment showed the dynamics of aluminium plasmas under various conditions, from the free-ablation case, collision stagnation or interpenetration, and under fast high current discharge. The plasma was characterised using ion time-of-flight measurements, visible emission spectroscopy, and novel visible emission spectral imaging. Plasma temperatures of 8 eV and densities of the order of 10^{18} cm^{-3} were estimated using aluminium spectral line emission from the colliding plasma with a 1 kV discharge. In Ch. 4 the results from the laser assisted vacuum arc lamp are presented, broken down into sections on the laser plasma characteristics, the EUV emission, the ion flux, and finally the optical emission spectroscopy. This experiment was carried out for two different source materials, tin and galinstan. The results for each material are compared and contrasted at the end of Ch. 4. The key point of interest in this experiment was the EUV emission characteristics for the source with each material. In this the general conclusion was that tin provides roughly 2 – 5 times the EUV output in the 2% band desired for lithography while galinstan has a much broader spectrally flat emission in the range 9 – 18 nm. In the final chapter the overall summary and final conclusions are given, along with a discussion on possible topics for future work.

Chapter 1.

Theory and modelling

In this chapter the theoretical background is presented for the physical processes involved in laser ablation, plasma expansion, fast high current discharge, magnetohydrodynamic compression, and emission spectroscopy. This is given to assist in the explanation of the observed phenomena and to outline the physics behind the diagnostics utilised throughout this work. The aim of this chapter is to give the reader a theoretical overview, in order to make the experimental work presented later more accessible. References are given to facilitate further reading on the topics discussed within.

1.1 Laser produced plasma

Laser produced plasmas are created by focusing a high irradiance ($>10^8$ W cm^{-2}) laser pulse onto a solid, liquid, or gas target. Here we will be concerned with solid and liquid targets. The removal of material from the irradiated surface is called laser ablation. This ablation process occurs as the laser pulse locally heats the target material which will begin to melt and vapourise. The vapourised material will be further heated and ionised by the laser, and expands rapidly away from the target surface. This expanding plume will be composed of neutrals, ions and electrons of the target material.

The physics of laser produced plasmas has been researched since the invention of the laser. The research covers a wide range of topics from laser induced breakdown spectroscopy, pulsed laser deposition, micro-structuring, short wavelength sources, and inertial confinement fusion. In this section the main features of laser ablation will be described in detail.

1.1.1 Target heating & plume formation

The main processes involved in the laser ablation of metals have been extensively researched and the characteristics are well understood[46]-[48]. When a laser pulse is incident on the target surface the energy from the pulse is transferred to the electrons through absorption at the surface. The absorption is dependent on the material being ablated and the laser wavelength, and is described by the relation:

$$\alpha = \frac{4\pi k_{ext}}{\lambda} \qquad [\text{cm}^{-1}] \qquad \text{Eqn. 1.1}$$

where α is the optical absorption coefficient of a metal, with extinction coefficient k_{ext}, and λ is the wavelength of the laser pulse [cm]. The absorption depth of the laser pulse into the target surface d_{opt} is the inverse of the absorption coefficient α^{-1}, typically on the order of several nanometers for visible wavelengths. For aluminium with a 1064 nm laser pulse the optical absorption coefficient $\alpha = 1.24 \times 10^6$ cm^{-1}, giving an optical absorption depth ~8 nm.

The energy is absorbed by the electrons in the material; in the case of nanosecond laser ablation the electrons have sufficient time to thermalise (from the electron-phonon coupling time on the order of several picoseconds for metals). This leads to rapid heating of the surface. By looking at a one dimensional heat conduction model for the heat transfer into the target we get:

$$\rho C \frac{\partial T}{\partial t} = \frac{\partial T}{\partial z}\left(k_c \frac{\partial T}{\partial z}\right) + (1 - R)\, \alpha\, I(t)\, \mathrm{e}^{-\alpha z} \qquad \text{Eqn. 1.2}$$

where ρ is the target density, C is the specific heat capacity of the target material, T is the temperature, k_c the thermal conductivity, R the reflectance of the target surface, α absorption coefficient (from Eqn. 1.1), $I(t)$ the incident laser intensity, time t, and position z.

By assuming that the incident laser intensity follows a Gaussian temporal profile, the intensity profile can be written as: $I(t) = I_0 exp[-(t/t_0)^2]$ where I_0 is the peak intensity, t_0 is the half width at half maximum of the temporal profile

Taking the temperature averaged values for parameters ρ, C, and k_c, the surface temperature during the laser pulse can be described by the equation[49]:

$$T(t) = T_i + \frac{2(1-R)I_o}{\rho\, C}\left(\frac{\tau}{\pi k_c}\right)^{1/2} \quad \text{Eqn. 1.3}$$

where τ is the full width at the $1/e^2$ of the Gaussian laser pulse (i.e. the width of the laser beam at 0.135 times the maximum intensity).

The laser pulse heating will cause the formation of a dense vapour layer at the target surface. This vapour will act to shield the target from any further ablation as the vapour layer will absorb the laser energy. The flux of evaporated material from the target $d(Nl)/dt$ can be described by the Hertz-Knudsen equation[47],[50]:

$$\frac{d(Nl)}{dt} = \frac{p_v}{\sqrt{2\pi\, m\, k_B T_S}} \quad \text{Eqn. 1.4}$$

In Eqn. 1.4 (Nl) is the number of atoms and ions per unit area leaving the target surface, T_S is the surface temperature, m is the mass of the atomic/ionic material being removed, k_B is Boltzmann's constant, and p_v the vapour pressure. As this work is only concerned with expansion into vacuum, the pressure difference is taken as the vapour pressure.

The dense vapour layer prevents further mass removal as it absorbs the laser pulse energy. This leads to heating and ionisation of the vapour, which will typically reach thermal equilibrium rapidly as the dense gas is highly collisional. Assuming this ionised vapour is in local thermodynamic equilibrium (LTE) the degree of ionisation can be estimated by the Saha equation[51]:

$$\frac{n_e\, n_b}{n_a} = 2\frac{g_b}{g_a}\left(\frac{2\pi\, m_e\, k_B T}{h^2}\right)^{3/2} exp\left(-\frac{\chi}{k_B T}\right) \quad \text{Eqn. 1.5}$$

where n_e is the electron number density, n_l and n_{l+1} are the number densities of the a and b ion stages, h is Planck constant, and χ is the ionisation potential of the ionisation stage a.

The ionised vapour will have free electrons in the presence of ions, which will absorb photons from the incident laser pulse, and then through collisions with neutral and ionised atoms in the vapour lead to heating in the vapour. This process is called inverse Bremsstrahlung (IB). The IB absorption coefficient of the vapour is given by[52]:

$$\alpha_{IB} = 4.1 \times 10^{-23} \frac{\overline{Z}^2 n_i n_e}{T^{7/2}} \left(\frac{k_B T}{hv}\right)^3 \times \left(1 - exp\left(\frac{hv}{k_B T}\right)\right) \quad [\text{cm}^{-1}] \quad \text{Eqn. 1.6}$$

where $\overline{Z}$ is the mean ionisation, n_i and n_e are the ion and electron densities per cm^3, and hv is the photon energy[eV], T is the temperature [K].

The absorption of the laser pulse in the vapour leads to plasma formation, giving the initial conditions for our laser produced plasma plume. The layer of hot (~1 eV), dense (~$10^{18} - 10^{19}$ atoms/ions cm^{-3}) plasma at the target surface is taken to expand with ion sound velocity c_s~ 3 ×10^3 m/s[47]. Using this assumption a rough estimate for the thickness of the plasma layer at the end of the τ_l= 7 ns laser pulse is found to be $c_s \tau_l$ ~ 20 μm. After the laser pulse, the plasma plume will expand due to the internal pressure gradients. Typically, the dimensions of the laser spot will be greater than the thickness of the plasma layer so we expect the strongest pressure gradient driving the expansion in the direction normal to the target. This leads to a semi-ellipsoidal plasma plume shape in vacuum, shown in Fig. 1.1.

1.1.2 Plume expansion & cooling

A model for laser produced plasma expansion was developed by Anisimov et al.[53]; it considers the expansion of the plume to be adiabatic and isentropic in a vacuum following the termination of the laser pulse energy. It has been shown that the Anisimov model can be used for a plasma at temperatures up to 12 eV[54]. Typically we expect the laser plasmas used here to have an initial temperature of <3 eV. The model is used to describe the three-dimensional adiabatic expansion of a plasma plume in vacuum after the termination of the laser pulse (which is taken as time zero).

The Anisimov model is based on three main assumptions[53]:

- the plasma can be considered as an ideal gas,
- it is an isentropic expansion,
- and the expansion is self-similar.

The first assumption justifies the use of gas dynamics equations in the description of the plasma plume expansion. The second assumption means heat exchanged during the plasma expansion can be neglected, as the thermal diffusion is slow compared with the expansion rate. Lastly the self-similar expansion assumes that the temperature and density of the expanding plasma are self-similar across expanding semi-ellipsoidal surfaces.

The gas dynamic equations which are used to model the plume expansion are[53]:

$$\frac{\partial \rho}{\partial t} + \nabla(\rho v) = 0 \qquad \text{Eqn. 1.7}$$

$$\frac{\partial v}{\partial t} + (v \cdot \nabla)v + \frac{1}{\rho}\nabla p = 0 \qquad \text{Eqn. 1.8}$$

$$\frac{\partial S}{\partial t} + (v \cdot \nabla)S = 0 \qquad \text{Eqn. 1.9}$$

where ρ is the plasma density, v is the velocity, p is the pressure, and S is the entropy.

As the plasma is being taken as an ideal gas we can write the adiabatic constant $\gamma = C_{\mathrm{P}}/C_{\mathrm{V}} = 5/3$, where C_{P} and C_{V} are the specific heat capacities at constant pressure and constant volume respectively.

At the end of the laser pulse (that is, at time zero) the plume is considered to have initial values of mass M_{p}, length Z_0, energy E_{p} and initial radius is taken as the radius of the focused laser spot. From the assumption stated previous the initial length can be approximated as $Z_0 \approx c_s\,\tau_l$ where c_s is the sound velocity and τ_l the laser pulse duration.

Solving the gas dynamic equations for an isentropic expansion to obtain the density, pressure, and entropy profiles of the plume with respect to time:

$$n(x,y,z,t) = \frac{N_0}{I_1 X_t\, Y_t\, Z_t}\left(1 - \left(\frac{x}{X_t}\right)^2 - \left(\frac{y}{Y_t}\right)^2 - \left(\frac{z}{Z_t}\right)^2\right)^{1/\gamma - 1} \quad \text{Eqn. 1.10}$$

$$p(x,y,z,t) = \frac{E_0}{I_2 X_t\, Y_t\, Z_t}\left[\frac{X_0 Y_0 Z_0}{X_t\, Y_t\, Z_t}\right]^{\gamma-1}\left(1 - \left(\frac{x}{X_t}\right)^2 - \left(\frac{y}{Y_t}\right)^2 - \left(\frac{z}{Z_t}\right)^2\right)^{\gamma/\gamma - 1} \quad \text{Eqn. 1.11}$$

$$S(x,y,z,t) = \frac{1}{\gamma - 1}\ln\left\{\frac{E_0}{I_2 X_0\, Y_0\, Z_0}\left[\frac{I_1 X_0\, Y_0\, Z_0}{M_\mathrm{p}}\right]^{\gamma} \times\left(1 - \left(\frac{x}{X_t}\right)^2 - \left(\frac{y}{Y_t}\right)^2 - \left(\frac{z}{Z_t}\right)^2\right)\right\} \quad \text{Eqn. 1.12}$$

where I_1 and I_2 are functions of γ[53], $E_0 = (\gamma - 1)^{-1}\int p(r,t)dV$ and $N_0 = \int n(r,t)dV$. These parameters n, p, and S will be constant over semi-ellipsoidal surfaces.

From the gas dynamic equations Eqn. 1.7 – Eqn. 1.9 using the above solutions Eqn. 1.10 – Eqn. 1.12 three coupled ordinary differential equations can be written to describe the expansion dynamics in X, Y and Z:

$$X_t\frac{d^2X}{dt^2} + Y_t\frac{d^2Y}{dt^2} + Z_t\frac{d^2Z}{dt^2} = A\left(\frac{X_0 Y_0 Z_0}{X_t\, Y_t\, Z_t}\right)^{\gamma-1} = \left(\frac{V_0}{V}\right)^{\gamma-1} \quad \text{Eqn. 1.13}$$

where the term $A = (5\gamma - 3)\,E_\mathrm{p}/M_\mathrm{p}$.

Several expansion characteristics arise from this model[55]:

1. During the initial phase of plasma expansion the strong pressure gradients in the layer drive the expansion in all directions, with the acceleration quickly going to zero making the expansion inertial.

2. Initially the pressure gradients are largest in the Z direction, as typically the layer thickness is substantially smaller than the laser focal spot, giving the modelled expansion a semi-ellipsoidal shape.

3. The pressure gradients in X and Y give rise to a "flip-over" effect, as typically the laser spot is not circular the initial dimensions can be taken as $X_0 < Y_0$. In this case the pressure gradient will be higher in the X direction, which implies the plasma will expand at a higher rate in X, meaning that at a later time $X_1 > Y_1$.

A numerical solution of Eqn. 1.13 yields the temporal variation of the radii of the plume front. An equation for the angular distribution of plasma over a semi-circular trace $F(\theta)$ (number of atoms or ions per cm^{-2}) can be derived from the gas dynamic model discussed above[53]:

$$F(\theta) = F(0)\left(\frac{1 + tan^2(\theta)}{1 + k^2\, tan^2(\theta)}\right)^{3/2} \qquad \text{Eqn. 1.14}$$

where $F(0)$ is the fluence normal to the plasma expansion, θ is the angle off normal along an arc drawn at a set distance from the ablation spot, and k is a parameter describing the expansion aspect ratio in either x or y. This equation can be rewritten to fit the angular distribution across a flat plane to find the expansion aspect ratio:

$$F(\theta) = F(0)\left(\frac{1}{1 + k^2\, tan^2(\theta)}\right)^{3/2} \qquad \text{Eqn. 1.15}$$

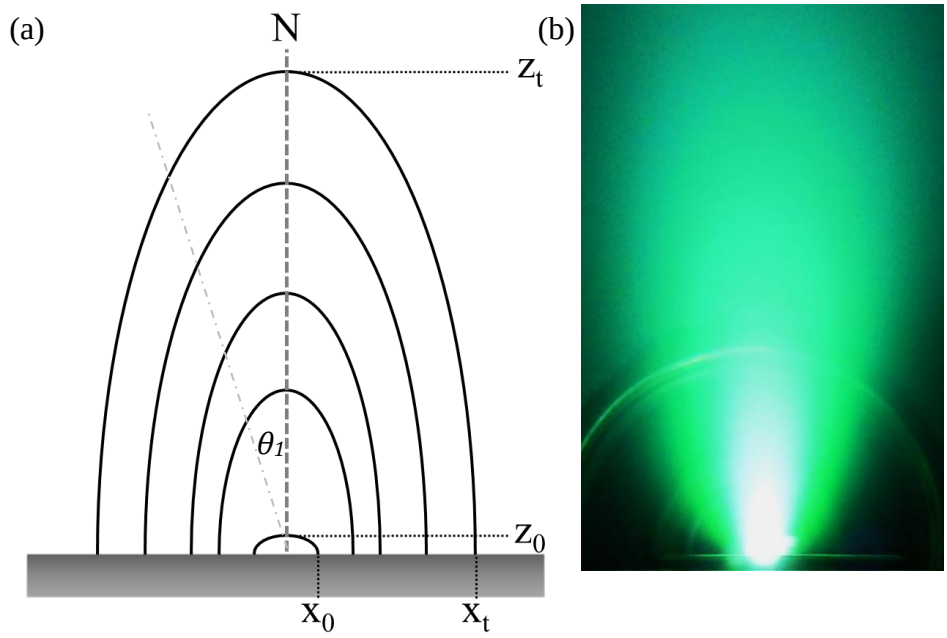

Fig. 1.1 – (a) schematic of a laser produced plasma plume expansion, showing the typical semi-elliptical expansion away from the target surface along the normal N and (b) a time integrated photograph of an aluminium laser plasma plume, ablated by a ~2 J/cm^2, 7 ns, 1064 nm laser pulse.

1.2 Fast current discharges; heating, compression & Z-pinch

1.2.1 Discharge conditions

Typically in the case of discharge produced plasmas (DPP) and laser assisted discharge plasmas (LDP), a pair of electrodes, connected to a charged capacitor bank, are positioned in a vacuum. The stored charge is not able to leave the capacitor bank while the electrodes are in vacuum, but at a sufficient pressure ignition will occur, for example with the introduction of a gas puff. This pressure is dependent on a number of parameters of the electrodes, electric field and medium experiencing breakdown. To look at the case of a fast Z-pinch[35] we will start at t_0 when the voltage is imposed on the medium, in this simplified case a gas puff, we can write:

$$eE\lambda_{ea} > I_{ion} \qquad \text{Eqn. 1.16}$$

where I_{ion} is the ionisation threshold, E is the electric field, and λ_{ea} the mean free path for electron scattering is given by $\lambda_{ea} = 1/n_a\sigma_a$, where n_a is the neutral atom density and σ_a is the electron cross section for scattering on atoms. E is expected to be large in Eqn. 1.16 meaning the inequality will be satisfied for relatively low densities. However there must be a sufficient density to yield considerable charge multiplication along the current path to the anode. This sets a lower limit for the density required to generate a plasma from a discharge breakdown of a neutral gas puff. Let us set a minimum value for the product:

$$L\, n_a\sigma_i > 10 \qquad \text{Eqn. 1.17}$$

where L is the inter-electrode distance. If $L = 4$ mm and $\sigma_i = 3 \times 10^{-16}$ cm^2[35] the minimum neutral atom density $n_a \sim 8 \times 10^{16}$ cm^{-3}. This is not a full description of the ignition process, and it is also different to the case for laser plasma triggered discharge, but it is a helpful guide for initial discussion. Typically the laser plasma will be substantially ionised at the time it reaches the counter electrode, directly before onset of discharge.

A high current pulse travels through the connecting medium in the inter-electrode gap. This current pulse leads to Ohmic heating in the medium which causes further ionisation. A magnetic field is also generated azimuthal to the direction of current flow. With magnetic fields present in the vicinity of the plasma, magnetohydrodynamic (MHD) equations are required to describe plasma flow[56]. In MHD a closed set of formulae, including Maxwell's equations, are used to describe the interaction of the magnetic field with the plasma dynamics. There are many models used for MHD plasma flow, here the ideal and resistive models are outlined to give a description of the Z-pinch dynamics.

1.2.2 Bennett condition for static pinch

In this section a derivation of the Bennett condition undertaken by the author is presented for instructional purposes. The Bennett condition[36] is a MHD balance relation between the plasma pressure and magnetic pressure in a magnetic compression of a column of plasma. This is important as it can easily be used to approximate the conditions necessary for a plasma pinch.

In the case of a static electric field the line integral of the magnetic field B (magnetic flux density) [T] around a closed loop s [m^{-2}] (Fig. 1.2) can be related to the electric current flowing in the loop from the Maxwell-Ampère equation:

$$\oint B.ds = \mu_0 i + \mu_0 \varepsilon_0 \frac{d}{dt} \int E.dA \qquad [Tm^{-2}] \qquad \text{Eqn. 1.18}$$

where μ_0 is the permeability of free space [Hm^{-1}], i is the electric current [A], ε_0 is the permittivity of free space [Fm^{-1}], E the electric field [NC^{-1}] and dA is the area [m^2]

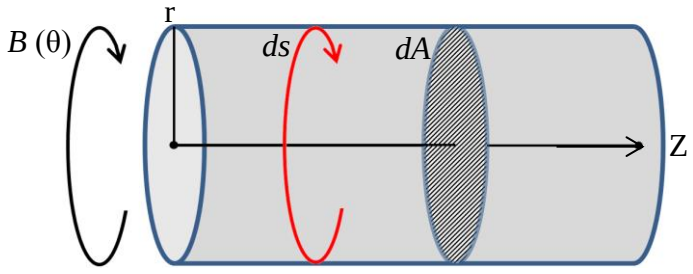

Fig. 1.2 – Illustration of a plasma column, showing loop *ds*, area *dA*, azimuthal magnetic field *B*(θ) and cylindrical coordinates r and Z.

Using Kelvin–Stokes theorem Eqn. 1.18 can be written in differential form as:

$$\nabla \times \boldsymbol{B} = \mu_0 \mathbf{J} + \mu_0 \varepsilon_0 \frac{d\mathbf{E}}{dt} \qquad [\mathrm{Tm}^{-2}] \qquad \text{Eqn. 1.19}$$

where E is the electric field, J is the current density [Am^{-2}] given by: $\mathbf{J} = \sigma \mathbf{E}$ (σ is the electrical conductivity [Sm^{-1}]). The current density can be defined as the flow of charge through a given area $\mathbf{J} = qnv$ where q is the charge [C], n is the number density [m^{-3}] and v is the average velocity [ms^{-1}].

To derive the Bennett condition a resistive model of the plasma MHD behaviour will be used, in this model it is assumed that there are no losses due to heat conduction or viscous flow and that the plasma is not an ideal conductor (i.e. $\sigma \ll \infty$) although plasmas are typically very good electrical conductors due to their inherent ionisation. It is also assumed that the temporal variation is slow enough such that the displacement current in the Maxwell-Ampère equation $\left(\mu_0 \varepsilon_0 (d\mathbf{E}/dt)\right)$ is negligible compared to the current density J and that the plasma is essentially neutral so $\nabla . \mathbf{E} = 0$[56].

In the Bennett condition it is also assumed that the system is in static equilibrium i.e. the velocity $v = 0$ and therefore $\frac{dv}{dt} = 0$. From this, we get the equation for conservation of momentum $[\rho_m (dv/dt) = c^{-1}\mathbf{J} \times \boldsymbol{B} - \nabla P]$ where ρ_m is the mass density [kgm^{-3}] and ∇P is the gradient of the plasma ion pressure $P_i = n_i k_B T$ [Pa]. As $(dv/dt) = 0$ the force balance can be rewritten as:

$$\frac{1}{c}\mathbf{J} \times \boldsymbol{B} = \nabla P \qquad \text{Eqn. 1.20}$$

Eqn. 1.20 is a force balance equation between the $\mathbf{J} \times \boldsymbol{B}$ forces and ∇P. As $\nabla \times \boldsymbol{B} = 4\pi c^{-1}\mathbf{J}$ the force balance equation can be rewritten in the form:

$$\nabla P = \frac{1}{4\pi}(\nabla \times \boldsymbol{B}) \times \boldsymbol{B} \qquad \text{Eqn. 1.21}$$

From the vector identity $(\nabla \times \boldsymbol{A}) \times \boldsymbol{A} = (\mathbf{A}.\nabla)\boldsymbol{A} - \frac{1}{2}\nabla \mathbf{A}^2$ the above can be further rewritten:

$$\nabla P = \frac{1}{4\pi}(\boldsymbol{B}.\nabla)\boldsymbol{B} - \frac{1}{8\pi}\nabla \boldsymbol{B}^2 \qquad \text{Eqn. 1.22}$$

$$\therefore \nabla\left(P + \frac{\boldsymbol{B}^2}{8\pi}\right) = \frac{1}{4\pi}(\boldsymbol{B}.\nabla)\boldsymbol{B}$$

$$\text{or} \qquad \nabla\left(P + \frac{\boldsymbol{B}^2}{2\mu_0}\right) = \frac{1}{\mu_0}(\boldsymbol{B}.\nabla)\boldsymbol{B} \qquad \text{Eqn. 1.23}$$

where $\frac{\boldsymbol{B}^2}{2\mu_0}$ is the magnetic pressure [Pa]

Applying Eqn. 1.23 to the case of a column of a quasi-neutral plasma in local thermodynamic equilibrium (LTE) and using cylindrical coordinates (where $\bar{\boldsymbol{B}} = [0, B_\theta(r), B_z(r)]$) we have the following identities for the convective operator[57] and the gradient:

$$(\boldsymbol{B}.\nabla)\boldsymbol{B} = \left(-\frac{\boldsymbol{B}_\theta^2}{r}, \frac{\boldsymbol{B}_\theta}{r}\frac{d\boldsymbol{B}_\theta}{d\theta} + \boldsymbol{B}_z\frac{d\boldsymbol{B}_\theta}{dz}, \frac{\boldsymbol{B}_\theta}{r}\frac{d\boldsymbol{B}_z}{d\theta} + \boldsymbol{B}_z\frac{d\boldsymbol{B}_z}{dz}\right)$$

$$\nabla f = \left(\frac{df}{dr}, \frac{1}{r}\frac{df}{d\theta}, \frac{df}{dz}\right)$$

Now, we can write the left-hand side of Eqn. 1.23 as:

$$\nabla\left(P + \frac{\boldsymbol{B}^2}{2\mu_0}\right) = \nabla P + \frac{\nabla\left(\boldsymbol{B}^2\right)}{2\mu_0}$$

$$\nabla\left(\boldsymbol{B}^2\right) = \nabla\left(\boldsymbol{B}_\theta^2 + \boldsymbol{B}_z^2\right)$$
$$= \left(\frac{d}{dr}\left(\boldsymbol{B}_\theta^2 + \boldsymbol{B}_z^2\right), \frac{2}{r}\left(\boldsymbol{B}_\theta\frac{d\boldsymbol{B}_\theta}{d\theta} + 2\boldsymbol{B}_z\frac{d\boldsymbol{B}_z}{d\theta}\right), 2\boldsymbol{B}_\theta\frac{d\boldsymbol{B}_\theta}{dz} + 2\boldsymbol{B}_z\frac{d\boldsymbol{B}_z}{dz}\right)$$

Now looking at Eqn. 1.23 in terms of the r components only

$$\frac{d}{dr}\left(P + \frac{\boldsymbol{B}_\theta^2}{2\mu_0} + \frac{\boldsymbol{B}_z^2}{2\mu_0}\right) = -\frac{\boldsymbol{B}_\theta^2}{\mu_0 r} \qquad \text{Eqn. 1.24}$$

In the Z-pinch case which is of interest in this work we can write: $\boldsymbol{B} = \boldsymbol{B}_\theta$ as $\boldsymbol{B}_z = 0$ and similarly $\mathbf{J} = \mathbf{J}_z$ as $\mathbf{J}_\theta = 0$ and so for this case equation Eqn. 1.24 can be rewritten as:

$$r^2\frac{dP}{dr} = \frac{d}{dr}(r\boldsymbol{B}_\theta)^2 \qquad \text{Eqn. 1.25}$$

Manipulating the Biot-Savart law the current flowing in a cylinder of radius r can be written as:

$$I(r) = 2\pi \int_0^r \mathrm{J}_z r\, dr = \frac{2\pi}{\mu_0} r\boldsymbol{B}_\theta \qquad \text{Eqn. 1.26}$$

$$\therefore r\boldsymbol{B}_\theta = \frac{\mu_0}{2\pi} I(r) \qquad \text{Eqn. 1.27}$$

Subbing equation Eqn. 1.27 this into equation Eqn. 1.25:

$$r^2 \frac{dP}{dr} = \frac{d}{dr}\left(\frac{\mu_0}{2\pi} I(r)\right)^2 \qquad \text{Eqn. 1.28}$$

$$\therefore r^2 \frac{dP}{dr} = \frac{\mu_0}{8\pi} \frac{d}{dr} I^2(r) \qquad \text{Eqn. 1.29}$$

Recalling $P = n_i k_B T$ where $T = T_i + T_e \overline{Z}$ ($\overline{Z}$ is the mean ion charge) and expanding Eqn. 1.29:

$$2\pi \int_0^a P\, r\, dr = \frac{\mu_0}{8\pi} I_a^2$$

$$\therefore 2\pi k_B T \int_0^a n_i r\, dr = \frac{\mu_0}{8\pi} I_a^2 \qquad \text{Eqn. 1.30}$$

where a is the radius of the plasma cylinder. Now letting $2\pi \int_0^a n_i r\, dr = N_i^l$ (ion line density) and assuming thermal equilibrium equation Eqn. 1.30 can be rewritten in the form of the Bennett condition[36]:

$$8\pi N_i^l k_B T_e (\overline{Z} + 1) = \mu_0 I_a^2 \qquad \text{Eqn. 1.31}$$

1.2.3 Z-pinch models

The above is based on the assumption of a static equilibrium where the magnetic and plasma pressures are equal. This assumption is obviously not valid in the case of the dynamic Z-pinch plasmas we are concerned with here. There are several models describing the dynamic pinch diameter, compression time, maximum temperature, and maximum density. In this work two such models[58], [59] are of interest: the snowplough model and the slug model. In the snowplough model the plasma is taken as a perfectly conducting infinitely thin cylindrical shell. During implosion the cylinder is treated as a magnetic piston collapsing on axis, "ploughing" the material radially towards the centre axis. The snowplough model is a more simplistic model than the slug model. In the slug model the infinitely conducting shell compresses behind an imploding shock-front. The slug model also includes terms to account for an internal plasma pressure[59], allowing for the prediction of a minimum radius of compression of a plasma column, independent of the voltage and current. It is noted by D. Potter[58] that none of the models describe the entire pinch process well. However they suggest that the snowplough model is useful for describing the time history of the implosion, while the slug model can be used to describe the cylindrical dynamics and estimate a minimum pinch radius.

The time-to-pinch and the minimum pinch radius can be written as[58], [59]:

$$t_{pinch} = 0.377 \frac{4\pi\, r_0^2}{I_{peak}} \left(\frac{\rho_0}{\mu_0}\right) \qquad \text{Eqn. 1.32}$$

$$r_{min} = \left(\frac{\gamma}{\gamma+1}\right)^{\frac{\gamma}{\gamma-1}} r_0 \qquad \text{Eqn. 1.33}$$

where r_0 is the initial shell radius, with a mass density ρ_0, a peak discharge current I_{peak}, and a ratio of specific heats γ typically set equal 5/3. In this case Eqn. 1.33 simplifies to: $r_{min} = 0.309\, r_0$.

1.2.4 Compression instability

Calculations of the magnetic compression typically assume a cylindrical plasma with uniform distribution, which is convenient for modelling. This is not the case in experiment, here a typical laser plasma distribution can be assumed in the inter-electrode gap at the onset of discharge. This distribution is quite complex with respect to the cylindrical uniform assumption. The physical processes involved in compression instability and explosion in the pinch plasma are very complex and can take many forms in the plasma dynamics. Moreover kink and sausage instabilities are common in fast Z-pinch discharges.

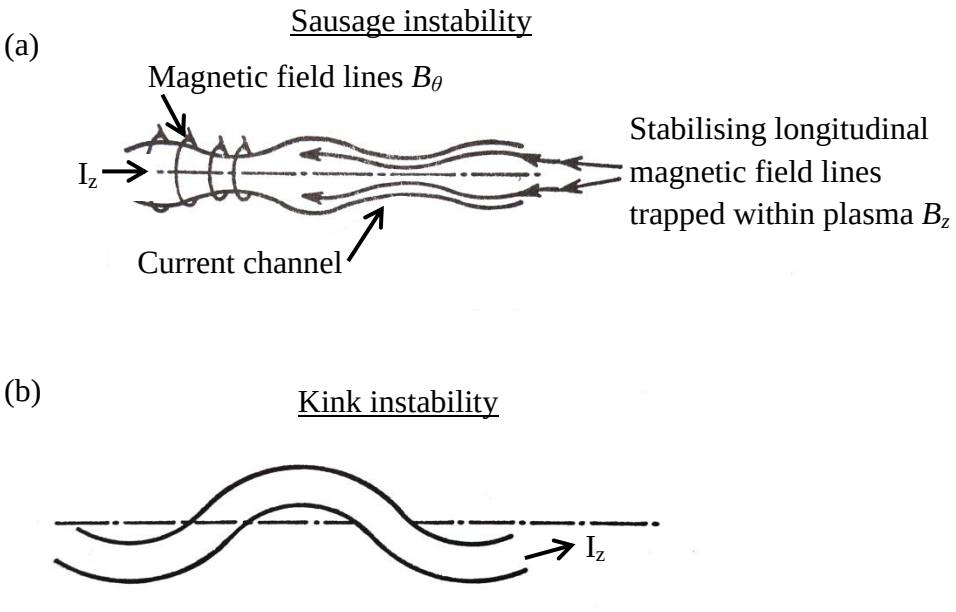

Fig. 1.3 –simplified side profiles of (a) Sausage and (b) kink instabilities in a cylindrical linear pinched plasma. In both cases the current direction is marked, the instabilities shown forming along the length of the plasma column. In (a) the magnetic field lines are shown, both the compression lines B_θ and the field lines trapped in the column B_z which act against the compression.

The complex processes leading to pinch instabilities are outside the scope of this thesis. Many experimental and theoretical publications are available on these Z-pinch instabilities and the steps necessary to mitigate them[60]–[64].

1.3 Emission spectroscopy

1.3.1 Atomic line transitions

Plasma spectroscopy is a useful tool in materials analysis owing to the characteristic emission of atoms/ions. In this section spectroscopy will be discussed as a diagnostic tool for plasma characterisation[48], using it to study the temporal and spatial evolution of plasma temperature and density. During the initial stages of laser ablation the plasma emission is typically a strong continuum observed near the target surface. As the laser produced plasma expands the density decreases and the emission goes to distinct less broad spectral lines. The emission measured from a specific line transition is dependent on several factors: the transition probability, the population of the upper energy level of the transition, the statistical weight of the upper level, and the probability emitted photons will not be absorbed while traveling in the plasma.

1.3.2 Local thermodynamic equilibrium & opacity

For a system in local thermodynamic equilibrium (LTE)[56] the population densities, and levels a and b, follow a Boltzmann distribution:

$$\frac{n_b}{n_a} = \frac{g_b}{g_a} \mathrm{e}^{\frac{-(E_a - E_b)}{kT}} \qquad \text{Eqn. 1.34}$$

where n is the number density, g is the statistical weight, and E is the energy level of the state. A system in LTE must have a common temperature over a microscopic area, but is allowed to vary over the entire plasma. Furthermore, for the system to be considered as being in LTE the transitions must also be dominated by collisional rather than radiative rates, and finally the excited state must have a higher probability of de-excitation by collision than by spontaneous emission. This is essentially a requirement that the electron density $n_e \gg \frac{A_{ba}}{C_{ba}}$ where $n_b C_{ba}$ is the collisional transition rate.

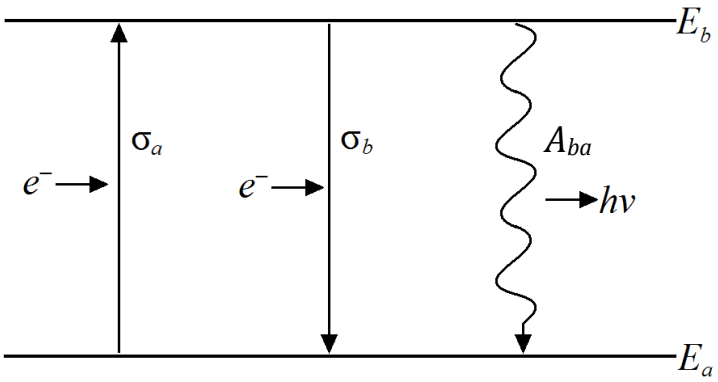

Fig. 1.4 – Transition diagram showing collisional and radiative emission transitions between two bound energy levels E_a and E_b.

The assumption that the ion states in the plasma follow a Boltzmann distribution (Eqn. 1.34) requires that the plasma is in LTE. Ionisation and recombination in a plasma is the result of either collisional or radiative effects[65]. These effects can be described for transitions in equilibrium:

(Collisional excitation or 3-body recombination)

$$A + e^- \Leftrightarrow A^+ + 2e^- + \Delta\epsilon$$

(Photoionisation or radiative recombination)

$$A + h\nu \Leftrightarrow A^+ + e^- + \Delta\epsilon$$

where $\Delta\epsilon$ is the electron kinetic energy balance.

A system in LTE will be in equilibrium only over certain regions for certain times, where Boltzmann distributions are realised for a given temperature. The Saha equation is used in the case of an ionised gas where collisions between electrons and atoms are causing considerable ionisation. To describe the ionisation balance of a gas at temperature T:

$$\frac{n_b n_e}{n_a} = 2\frac{g_b}{g_a} e^{-\left(\frac{\chi}{kT}\right)} \sqrt{\frac{2\pi\, m_e kT}{h^2}} \qquad \text{Eqn. 1.35}$$

where g is the degeneracy associated with the state, or the statistical weight.

The collisional transition rate should exceed the radiative transition by at least a factor of 10 to maintain LTE, therefore $C_{ba} \geq 10\, n_b A_{ba}$ and therefore the inequality shown previously can be rewritten as:

$$n_e \geq 1.6 \times 10^{18} \sqrt{T} (\Delta \mathrm{E})^3 \quad [\mathrm{m}^{-3}] \qquad \text{Eqn. 1.36}$$

This is referred to as the McWhirter criterion[66]. It is worth noting then that the energy difference to any adjacent energy level (ΔE) which the electron could make a transition to scales with the degree of ionisation Z^2 and therefore the McWhirter limit scales with Z^6.

If we consider a two-level system where the electrons are excited to n_b and decay to n_a a collisional interaction can be written as:

$$C_{ba} = n_e n_b X \qquad \text{Eqn. 1.37}$$

where X is the coefficient of decay to n_a. To estimate the electron temperature via emission spectra it is necessary to assume that there is no self-absorption of the lines used for the line ratio i.e. all of the emitted light passes the boundary of the plasma without reabsorption. If this assumption holds true the line is said to be optically thin. The optical depth, τ_λ, can be expressed in terms of the absorption coefficient, α_λ, and the distance, x, from the emitter to the boundary of the plasma for a homogenous medium as:

$$\tau_\lambda = \alpha_\lambda x \qquad \text{Eqn. 1.38}$$

If $\tau_\lambda \ll 1$ the plasma is said to be optically thin for that line and if $\tau_\lambda \gg 1$ it is optically thick. The absorption coefficient for a column of plasma with radius r_0 can be expressed in terms of a specific line transition as[65]:

$$\alpha_\lambda = r_0 \lambda^2 f_{ab} n_a \left(1 - e^{-\frac{hc}{\lambda k t}}\right) P(\lambda) \qquad \text{Eqn. 1.39}$$

where f_{ab} is the absorption oscillator strength and $P(\lambda)$ is the spectral line profile function (i.e. a Lorentzian or a convolution of Lorentzian and Gaussian, termed a Voigt profile[65], [67]). The absorption oscillator strength can be related to the transition rate A_{ba} as:

$$f_{ab} = \frac{\varepsilon_0 m_e c \lambda_2^2}{2\pi e^2} \left(\frac{g_b}{g_a}\right) A_{ba} \qquad [s^{-1}] \qquad \text{Eqn. 1.40}$$

where ε_0 is the permittivity of a vacuum, m_e is the electron mass, c is the speed of light, λ_2 is the emission wavelength of the transition, e is the charge of an electron, and g_b and g_a and the degeneracies of both upper and lower states respectively.

Modelling of the plasma spectral emission was carried out using the collisional-radiative simulation software PrismSPECT® made by Prism Computational Science Incorporated[68]. The software can be used to match and interpret experimental spectra. The program gives the user the option to input one constant and 2 variable selections from ion density, plasma thickness and electron temperature in order to obtain modelled spectra for specific elements along with full transitions, mean plasma ionisation and electron density. A perfect match is not always possible as certain transitions are absent in the software. This can be avoided by changing to a different spectral range or using a different material. PrismSPECT was not successful in modelling the tin or gallium spectral emission in this work, it was noted that several intense emission lines are not present in the modelled spectra in the visible spectral range studied. This is due to relevant transitions not being included in the model database tables. PrismSPECT has been a useful tool in the study of other materials by our research group[69]–[71].

1.3.3 Spectral temperature estimation

Based on the assertion that the plasma is in LTE, the spectral radiance measured from the plasma can be related directly to the line transitions' level population and transition probability. The calibrated spectral emission measured in this work will be presented as spectral radiance [W m^{-2} sr^{-1} nm^{-1}] denoted here by the term $L(\lambda)$.

$$L(\lambda) = \frac{dW}{\lambda\, A \cos\theta\, d\Omega} \qquad \text{Eqn. 1.41}$$

$$L(\lambda) = \frac{1}{4\pi}\delta x A_{ba} n_b h v_{ba} \qquad \text{Eqn. 1.42}$$

where dW is the power emitted from an area A, at an angle θ to the surface normal, contained within a solid angle $d\Omega$. While δx is the thickness of the emitter, $hv_{ba}$is the energy of the radiative emission, and A_{ba} is the transition probability, sometimes referred to as the Einstein coefficient of the probability of a spontaneous radiative transition from E_b to E_a. The number of spontaneous emissions per second in δx and unit cross-section is $A_{ba}\delta x n_b$.

The Boltzmann excitation equation is:

$$\frac{n_j}{N} = \frac{g_j}{Q(T)} e^{\frac{-E_j}{kT}} \qquad \text{Eqn. 1.43}$$

In Eqn. 1.43 $Q(T) = \sum_j g_j e^{\frac{-E_j}{kT}}$ is the partition function or state sum, g_j is the statistical weight of level j, and the total number density: $N = (n_0 + n + \cdots)$ and therefore $N = \frac{n_0}{g_0}(g_0 + g_1 e^{\frac{-E_1}{kT}} + \cdots)$.

A ratio of the two populated states E_a and E_b can be written as:

$$\frac{n_b}{n_a} = \frac{g_b}{g_a} e^{\frac{-(E_b - E_a)}{kT}} \qquad \text{Eqn. 1.44}$$

Substituting for n_b in Eqn. 1.42 the spectral radiance can be written as:

$$L(\lambda) = \frac{1}{4\pi}\delta x A_{ba}\left(n_a g_b e^{\frac{-E_b}{kT}}\right)\frac{hc}{\lambda_{ba}} \qquad \text{Eqn. 1.45}$$

The irradiance I then is:

$$I = 4\pi \int L(\lambda) d\lambda = \delta x \frac{hc}{4\pi} \frac{g_b A_{ba} e^{\frac{-E_b}{kT}}}{\lambda_{ba}} \quad \text{Eqn. 1.46}$$

By letting $\alpha = \delta x \frac{hc}{4\pi}$ this can be rewritten to give the a relation for the irradiance of the line emission I_{ba} [W m^{-2}] as:

$$I_{ba} = \alpha \frac{g_b A_{ba}}{\lambda_{ba}} e^{\frac{-E_b}{kT}} \quad \text{Eqn. 1.47}$$

Therefore Eqn. 1.44 can be rewritten as:

$$\frac{I_i}{I_j} = \frac{g_i A_i \lambda_j}{g_j A_j \lambda_i} e^{\frac{-(E_i - E_j)}{kT}} \quad \text{Eqn. 1.48}$$

Based on Eqn. 1.48 a plot of the natural log of the intensity times wavelength over the degeneracy of the upper state times transition probability versus the energy of the upper state for a series of lines will yield a slope of $1/kT$. This gives an estimate for the plasma temperature based on the ion transitions, which is called a Boltzmann plot.

1.3.4 Line broadening electron density approximation

In the measured spectra the shape of the line emission from a specific transition is dependent on both the emitter and the tool used to record the emission. The spectral broadening inherent to the measurement tool is called instrumental broadening and typically has a Gaussian profile[67], [72]. There are many different schemes to minimise the instrumental broadening of a system, however it is often a trade-off with other factors such as light throughput or spectral range. The line broadening mechanisms inherent to the emitter/source are natural broadening, Doppler broadening and pressure broadening. In this work the plasma temperature will be in the range 1 – 10 eV, in this regime the Doppler broadening is expected to be negligible with respect to the pressure broadening.

Pressure broadening is broken down into three types: resonance, Van der Waals and Stark broadening. The latter of these is caused by the electric field interaction from charged perturbers. The half-width at half-maximum (HWHM) line width ω_{se}, in frequency units, is given by[73]:

$$\omega_{se} \approx 8\left(\frac{\pi}{3}\right)^{\frac{3}{2}} \frac{\hbar a_0}{m} N \left(\frac{E_H}{kT}\right)^{\frac{1}{2}} \times \left[\sum_{i'} |\langle i'|\, r/a_0 \,|i\rangle|^2 \, \overline{g}_{se}\left(\frac{3kT_e}{2|E_{i'} - E_i|}\right) + \sum_{f'} |\langle f'|\, r/a_0 \,|f\rangle|^2 \, \overline{g}_{se}\left(\frac{3kT_e}{2|E_{f'} - E_f|}\right)\right] \quad \text{Eqn. 1.49}$$

where $\overline{g}_{se}$ is the semi-empirical effective Gaunt factor, i and f denote the initial and final states of the transition, and $\overline{E} = \frac{3}{2}kT_e$. The notations i', f' and i, f are used to mark the perturbing level versus the perturbed level respectively. $\langle f|x|i\rangle$ are the matrix elements of the position vector of the radiating electron as measured from the nucleus (or in the case of several electrons it is the sum of these vector components). The atomic dipole matrix element connecting the initial and final atomic states in the inelastic collision is $\langle i'|r^2|i\rangle$[73]. Therefore:

$$\omega_{se} \approx 8\left(\frac{\pi}{3}\right)^{\frac{3}{2}} \frac{\hbar}{m a_0} n_e \left(\frac{E_H}{kT}\right)^{\frac{1}{2}} \times \left[\langle i'|r^2|i\rangle \, \overline{g}_{se}\left(\frac{3kT_e}{2|\Delta E_i|}\right) + \langle f'|r^2|f\rangle \, \overline{g}_{se}\left(\frac{3kT_e}{2|\Delta E_f|}\right)\right] \quad \text{Eqn. 1.50}$$

An estimation of the matrix element r^2 can be written for the case of a hydrogen like ion[73]:

$$\langle i'|r^2|i\rangle = \frac{{n_i}^2}{(2z+1)^2}[5{n_i}^2 + 1 - 3l_i(l_i+1)]{a_0}^2 \quad \text{Eqn. 1.51}$$

where l_i is the orbital quantum number of the bound valence electron, z is the charge of the ion and n_i is the effective quantum number given by: $n_i = (z+1)^2 E_H/(\chi - E_i)$, with ionisation energy χ, and the empirical excitation energy E_i. This is the semi-empirical solution[73] for the line width, other methods are also used like the semi-classical approach[74]–[76]. A detailed account of the models used to calculate Stark parameters is given by M. Gigosos[77].

It is more convenient to work in terms of the full-width at half-maximum (FWHM) in wavelength units, we write:

$$\Delta\lambda = \frac{\omega_{se}\lambda^2}{\pi c} \quad \text{[nm]} \qquad \text{Eqn. 1.52}$$

The line broadening here is related directly to the atom, ion, and electron density of the plasma, typically the atom and ion densities are negligible[78] for the range of plasma parameters expected in this work, and only the contribution from electron density is discussed. The electron density of the emitting plasma can be estimated from the measured line width $\Delta\lambda_s$ by:

$$\Delta\lambda = 2\omega\left(\frac{n_e}{n_x}\right) \quad \text{[nm]} \qquad \text{Eqn. 1.53}$$

The measured line width $\Delta\lambda_s$ is the FWHM [nm], taking into account the instrumental broadening. The Stark width parameter ω is obtained from literature[76], [79]–[81] and here ω is the HWHM [nm] for a quoted density n_x, typically $10^{16} - 10^{17}$ cm^{-3}. The data tables for these parameters will follow in the experimental results section. The profile of the measured line is accurately fit by a convolution of Gaussian (instrumental broadening) and Lorentzian (Stark broadening) line profiles, which is a Voigt profile. The inherent instrumental broadening is accounted for by setting an appropriate minimum Gaussian width based on the tool used. The Lorentzian line width can be de-convolved from the Voigt fit to give $\Delta\lambda_S$.

The instrumental line width was measured experimentally by recording spectral line emission from a low density mercury lamp, shown in Fig. 1.5. The mercury lamp is also used for spectral calibration which will be covered in Section 2.4.2. An example spectra showing broadening line emission from a tin laser assisted discharge plasma, is also included to show the extent of broadening in a dense (upper spectra having an estimated n_e ~1.2 ×10^{18} cm^{-3}) plasma emission spectrum. The instrumental broadening of the spectrometer used in this work was measured as $\Delta\lambda_{Inst}$ = 0.95 nm.

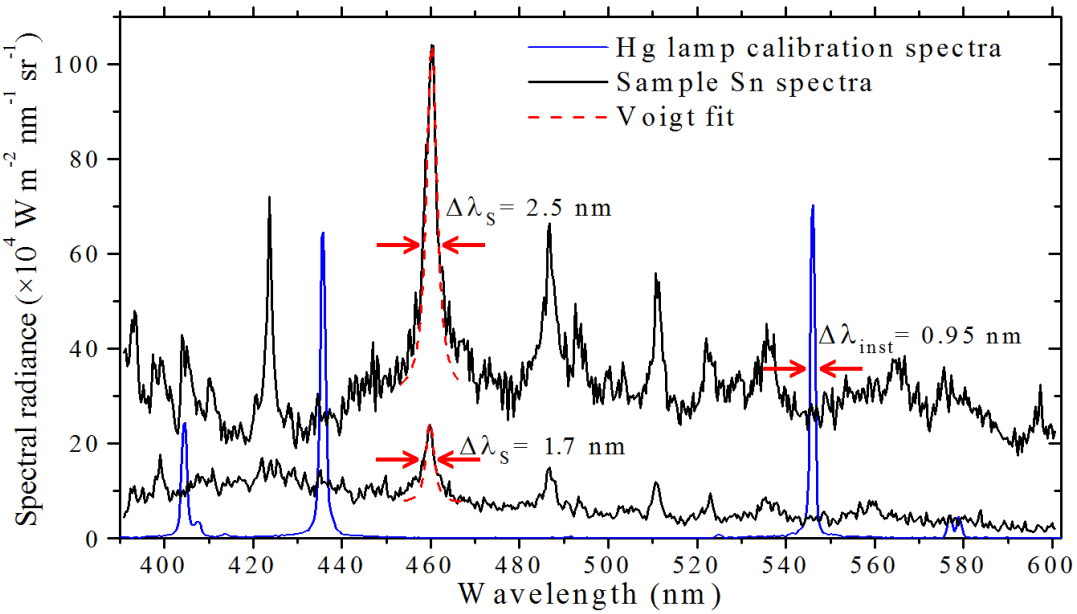

Fig. 1.5 – Mercury lamp spectrum showing the measured instrumental line width ($\Delta\lambda_{Inst}$ = 0.95 nm), with two example broadened line spectra from tin laser assisted discharge plasma, the broadened lines correspond to an estimated electron density of n_e ~1.2 ×10^{18} cm^{-3} and n_e ~8.4 ×10^{17} cm^{-3}.

Chapter 2.

Experimental methods

In this chapter the diagnostic tools and characterisation techniques used during this thesis work are described. Specific experimental setups will be described alongside the corresponding experiments. The topics covered here are the electrical discharge circuit design, ion time-of-flight diagnostics, and the tools used to measure the visible and extreme ultraviolet (EUV) light emitted by the laser assisted discharge plasmas studied.

2.1 The discharge circuit design

There are many different geometries available in the literature for plasma (or vapour) triggered electrical discharges. In this thesis three such geometries will be discussed; a coaxial laser plasma triggered discharge, a colliding laser plasma triggered discharge, and finally a replenishable target discharge triggered by laser ablation. But regardless of geometry the discharge circuit will typically follow the same design.

It is desired in fast, high current discharges that the majority of the discharge energy is efficiently used to heat and compress the plasma load by maximising the current delivered in a given time (e.g. first period of the discharge); for this reason the discharge characteristics must be tuned for the plasma load used.

The experimental factors which can be adjusted are:

- discharge current rise-time; controlled by inductance and capacitance,
- discharge current peak; controlled by capacitance and voltage supplied, and
- plasma load; controlled by the laser ablation parameters.

To achieve a fast discharge the inductance L and capacitance C of the circuit must be minimised (Eqn. 2.1); however for a high current pulse a large capacitance value is required. Therefore the inductance becomes crucial in yielding a fast, high current electrical discharge.

The peak current I_{peak} and resonant frequency of a discharge ω are given by:

$$\omega = \frac{1}{\sqrt{LC}} \qquad \text{Eqn. 2.1}$$

In Fig. 2.1 an electrical circuit is shown, where the closing trigger switch and plasma current path resistor represent the triggering laser plasma. The damping of the discharge current is dependent on the resistance of the discharge circuit. As the plasma is transient this resistance value is expected to vary on the order of the expansion velocity of the plasma with respect to the size of the gap between electrodes.

The total effective inductance of the circuit will be the sum of each electrical component's inherent inductance, the inductance of the plasma load and the inductance of the circuits connecting wires. The latter of these is typically the dominant factor.

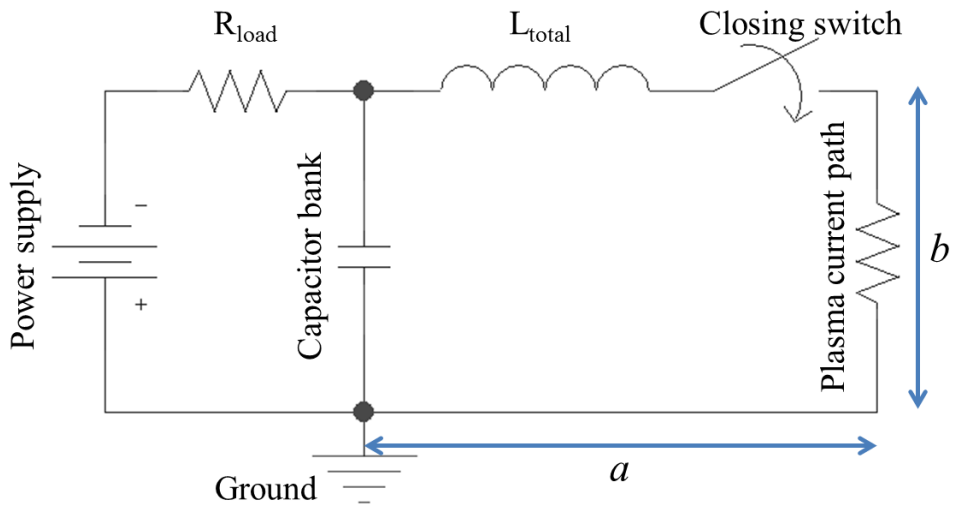

Fig. 2.1 – Electrical circuit showing the components of a typical discharge setup, with the closing switch and plasma current path resistor representing the trigger laser plasma.

The equation describing the inductance L of a rectangular circuit is[82]:

$$L = \frac{\mu_0}{\pi}\left(a \ln\left(\frac{2a}{r}\right) + b \ln\left(\frac{2b}{r}\right) + 2\sqrt{a^2+b^2} - a \operatorname{arcsinh}\left(\frac{a}{r}\right) - b \operatorname{arcsinh}\left(\frac{b}{r}\right)\right) \quad \text{Eqn. 2.2}$$

where a is the circuit length, b circuit width, and r is the wire radius. This equation is only valid if $a \gg r$ and $b \gg r$. From Eqn. 2.2 it is clear that by decreasing the dimensions of a circuit and/or increasing the cross section of any connecting wires, the inductance will be reduced. This is an important consideration when designing a fast high current discharge circuit. For example a circuit with length and width, $a = 3$ cm and $b = 1.2$ cm and wire radius $r = 0.2$ cm will have an inductance of 28 nH.

The discharge current profile $I(t)$ for a simple underdamped LCR circuit is given by:

$$I(t) = C\,\frac{dV(t)}{dt} = -\omega_d C V_0 \sin(\omega_d t) e^{-\alpha t} \quad \text{Eqn. 2.3}$$

for a circuit with a capacitor bank C, a charging voltage of V_0, and where ω_d is the underdamped resonant frequency of the circuit, given by:

$$\omega_d = \sqrt{{\omega_0}^2 - \alpha^2} \quad \text{Eqn. 2.4}$$

With the damping of the resonant frequency found by the damping coefficient α:

$$\alpha = {}^{R}/_{2L} \quad \text{Eqn. 2.5}$$

In Eqn. 2.3 the peak discharge current is at $\sin(\omega_d t) = -1$, therefore $I_{max} = \omega_d C V_0$. For the 28 nH circuit above, with a 0.5 µF capacitor bank charged to 2 kV, and a total current path resistance of 100 mΩ:

$$I_{max} = CV_0\sqrt{\left(\frac{1}{\sqrt{LC}}\right)^2 - \left(\frac{R}{2L}\right)^2} \quad \text{Eqn. 2.6}$$

The plasma load in the discharge can be varied by changing the laser ablation parameters, laser fluence (energy per unit area) or pulse duration. It is also possible to use an aperture to select a portion of plasma plume for discharge[45], [83]. The line density in the plasma plume is a critical parameter in generating an effective Z-pinch.

If the density is too high the plasma pressure will always be far greater than the magnetic pressure generated by the discharge. The laser plasmas' ion density will not be constant along the discharge path due to the distribution of ion velocities in the plume[53].

2.2 Electrical discharge monitor

To measure the timing and amplitude of the electrical discharge current it is not possible to use direct measurement with the high current pulses involved here. Therefore a magnetic field sensing device is used to transduce the passing current pulse into a voltage measured on a fast oscilloscope based on Ampere's Law. This non-intrusive flux-to-voltage transducer device is called a Rogowski coil[84], [95], [96] which consists of a multi-turn solenoid, toroidal or planar, which is made to surround the path of the current pulse or placed in proximity to it (Fig. 2.2).

The advantages of using a toroidal Rogowski coil to measure the current are: the measurement is not dependent on the path of the current through the solenoid opening, thus calibration is not position dependent, the coil can be readily made to fit many geometries due to the small size and simple design, and the measurement is linear within a wide range of current values[84].

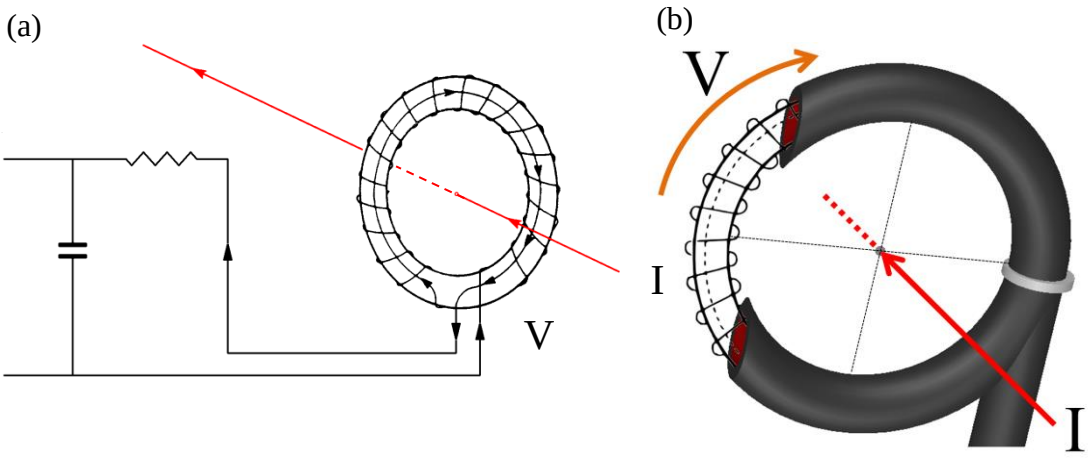

Fig. 2.2 – Geometric representations of toroidal Rogowski coils. The coil is wrapped around a coaxial cable with one end of the coil connected to the core and the other to the shielding. Here the plasma column or current carrying conductor is marked red.

The voltage transduced by a toroidal Rogowski coil is related to the current by:

$$V = -\alpha\left(\frac{dI}{dt}\right) \qquad \text{Eqn. 2.7}$$

In Eqn. 2.7 the constant α is related to the coil characteristics, coil winding area A, the number of turns N, and the coil length l by:

$$\alpha = \frac{AN\mu_0}{l} \qquad \text{Eqn. 2.8}$$

As the coil measures the derivative of the current (Eqn. 2.7), the output must be integrated to yield the current as a function of time, this can be done by means of a passive RC circuit or by mathematical integration. A sample signal is presented below in Fig. 2.3 along with the resultant current profile.

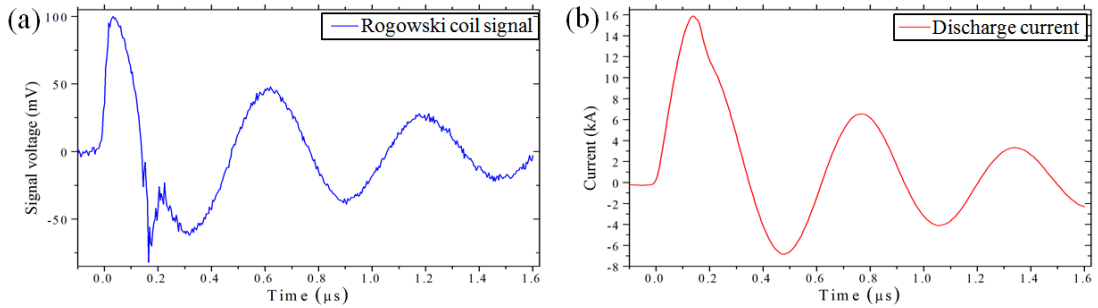

Fig. 2.3 – Sample signals of (a) voltage measured by Rogowski coil and (b) discharge current profile found by integration of the voltage signal in (a).

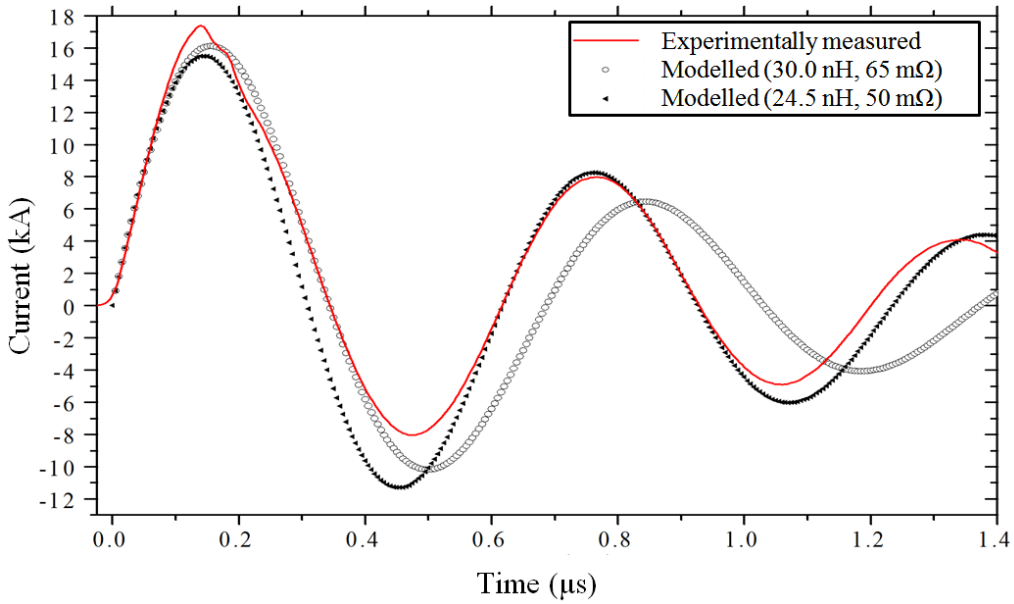

Fig. 2.4 – Typical measured discharge current profile (red line) with overlay of the modelling results used to estimate the equivalent inductance and resistance of the discharge circuit (symbol scatter plots).

By fitting the amplitude and the full-width half-max time of the first current pulse, values for the equivalent inductance and resistance of the discharge circuit were estimated for each setup. A sample graph of the modelled discharge current compared to that measured is shown in Fig. 2.4. The current profile here clearly displays a shift in period between each half cycle with the model estimate of equivalent inductance and resistance shifting from 30 nH and 65 mΩ for the first positive peak to 24.5 nH and 50 mΩ for the second positive peak. The notch present at the first peak in current is an indicator of a pinching event. This notch is caused by the sudden change in resistance and impedance characteristics of the current carrying plasma column as it experiences compression.

The initial experiment presented in this thesis was carried out with a calibrated toroidal Rogowski coil. However the work in Chapter 4 on the Laser Assisted Vacuum Arc-lamp used a planar Rogowski coil. Planar coils are highly position sensitive with respect to the current path, making it impractical to calibrate the coil accurately due to variation in plasma or coil position during experiments. However the peak current can still be estimated by comparing the measured current profile with calculation.

2.3 Time-of-flight ion and debris analysis

2.3.1 Langmuir & Faraday cup ion probes

To study plasma plume expansion dynamics in vacuum ion time-of-flight (ToF) measurements were made, using a planar Langmuir ion probe and a Faraday cup. The Langmuir probe can be used to study plasma parameters including ion and electron density, electron temperature and ion kinetic energy distributions. Ion probe characterisation of laser produced plasmas is understood[85], in this section the general properties and experimental processes will be outlined.

In both the planar probe and Faraday cup a biased metallic electrode is inserted into the plasma flow, measuring the impinging ions/electrons as a change per probe area over time. The probe is biased either positively or negatively to measure electron or ion fluence. In the case of the Faraday cup the addition of a means to limit secondary electron escape is employed. Secondary electrons are a relevant concern for plasmas with high energy ions, above the order of 100 eV, or in the presence of photo-ionising light sources. There are many methods to accomplish the limiting of secondary electron escape. Here a magnetic field transverse to the flux of ions ensured any secondary electrons were recaptured by the walls of the cylindrical cup electrode (Fig. 2.5). Although the effect of secondary electrons was not investigated here it was expected to contribute a reasonable uncertainty to measurements[97], [98], leading to the use of the Faraday cup.

The magnetic field used to limit secondary electron escape was generated by two separate pairs of NdFeB magnets (50 mm diameter, 5.75 mm height) attached externally on a KF-32 vacuum flange. A pair of shimmed soft-iron pole pieces were included with the magnets, to shape the magnetic field at the cup position. The Faraday cup ion ToF diagnostic tool is shown in Fig. 2.5. The device was designed to fit snuggly onto a standard size bayonet Neill-Concelman (BNC) connector. The cylindrical copper cup slots into the live electrode while an aluminium shielding cylinder sits around the grounded BNC connector piece. A 2.7 mm diameter aperture gives the tool an effective

probe area of 0.057 cm^2. The device is mounted on a KF-30 BNC electrical vacuum feedthrough in a ~20 cm long KF-30 vacuum flange.

The magnetic field shaping yielded a uniform measured field of ~65 mT inside the cup. The deflection of any secondary electrons (D), with an initial velocity (v),due to the magnetic field (B) over the length of the cup (l) is given by:

$$D = \frac{l^2 eB}{2m_e v} \qquad \text{Eqn. 2.9}$$

The cup has a radius of 2 mm and a length of 13 mm, assuming any secondary electrons are generated at the back surface of the cup a velocity limit can be calculated for reabsorption in the cup walls. Taking $D = 2$ mm and $l = 13$ mm in Eqn. 2.9 we find electrons with a velocity under 4.8 ×10^{11} cm/s will be reabsorbed. A photoelectron generated by EUV light at 13.5 nm will have a velocity ~5×10^8 cm/s.

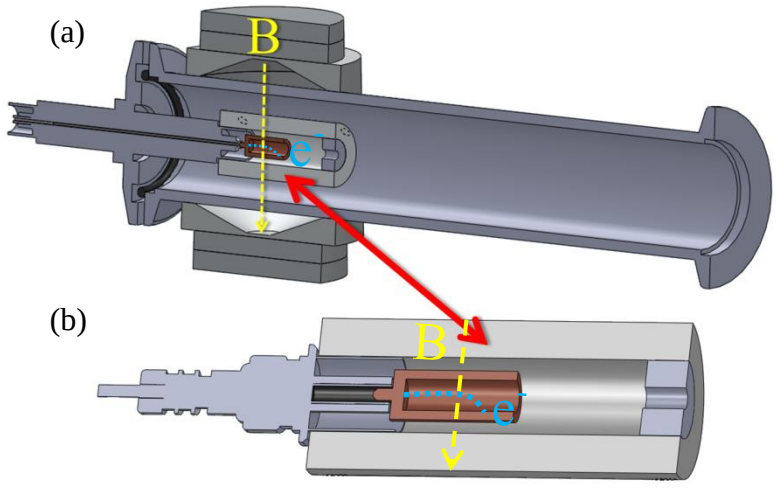

Fig. 2.5 – Cross sectional geometric images of the Faraday cup ion ToF diagnostic tool (a) in vacuum flange and (b) close up view of the central pieces of the device, with simplified electron trajectory and magnetic field indicated on each..

The ion probe is connected via coaxial cable to an oscilloscope, through a Koopman biasing circuit[86]. The biasing circuit is shown in Fig. 2.6 below, where the value of R_L is variable and set depending on the sensitivity required as the voltage signal measured $V_{osc} \propto R_L$. The oscilloscope used throughout this this work was a Tektronix, 300 MHz, 4 channel oscilloscope (model number TDS 3034).

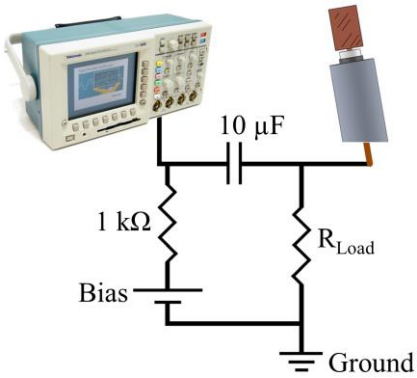

Fig. 2.6 – Biasing circuit used for Langmuir ion probe and Faraday cup experiments where RLoad was varied from 10 Ω to 1 kΩ depending on the sensitivity and signal saturation required.

The charge stored on the capacitor is the limit of the measured ion fluence; in the case of the 10 µF capacitor biased at -25 V the total charge will be $Q = CV = 2.5 \times 10^{-4}$ C, therefore a total ion fluence of ~1.6×10^{15} ions would saturate the biasing capacitor.

2.3.2 Ion flux & energy distribution

The voltage signal recorded by the oscilloscope from the bias circuit is a measure of the ion fluence impinging on the probe area over time. The ion current fluence j_i [mA cm^{-2}] is given by: $j_i(t) = V(t)/A_p R_L$ where $V(t)$ is the voltage signal, A_p the probe area, and R_L the load resistor. Sample ion and electron ToF measurements are shown in Fig. 2.7.

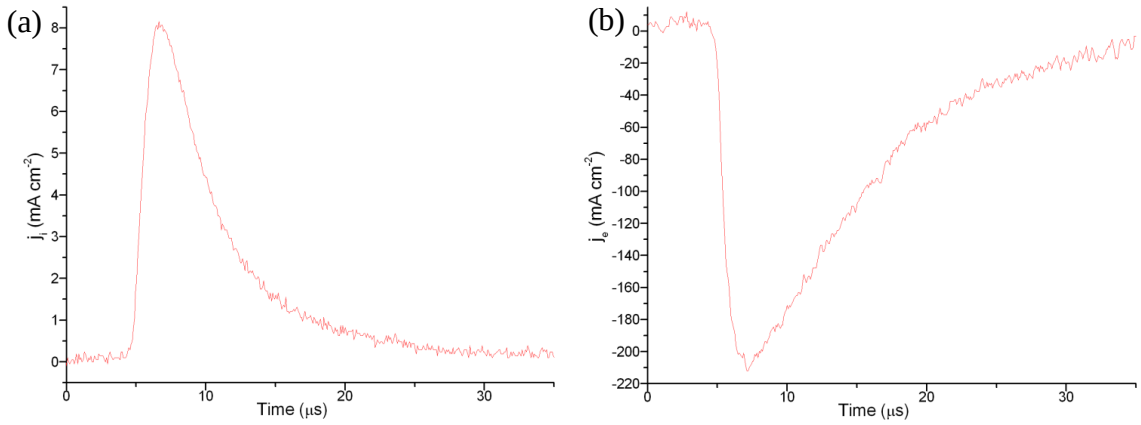

Fig. 2.7 – Sample (a) ion and (b) electron ToF measurements shown in ion/electron fluence (mA cm^{-2}), recorded with a planar probe positioned at 16.5 cm from an Al target surface with ablation by an Nd:YAG laser.

The current measured can be written as:

$$I_i = A_p e v \sum_j n_j Z_j \qquad \text{Eqn. 2.10}$$

where A_p is the probe area, e the electron charge, v the ion velocity and n_j is the ion number density for a given ionisation stage Z_j.

Using this equation, assuming $Z = 1$ for simplicity here, the ion number density can be estimated from the measured time-dependent ion current. A sample ion density plot is shown in Fig. 2.8 assuming the ion flux in Fig. 2.7 is all singly ionised. Looking again at Eqn. 2.10 for a singly ionised plasma we can transform the measured current profile, assuming a self-similar expansion of the plasma plume (see Section. 1.1.2), to plot a number density profile for a given time t' (Eqn. 2.12) or at a given probe position z' (Eqn. 2.13). The velocity v of the plasma is calculated from the distance of the probe z_0 and the time read off the ion current time-of-flight profile t.

$$n_i(z_p, t) = I_i(t)/Aev \qquad \text{Eqn. 2.11}$$

$$n_i(z_0, t') = n_i(z_p, t) \times (z_p/z_0)^3 \qquad \text{Eqn. 2.12}$$

$$t' = t(z_0/z_p)$$

$$n_i(z', t_0) = n_i(z_p, t) \times (t/t_0)^3 \qquad \text{Eqn. 2.13}$$

$$z' = z_p(t_0/t)$$

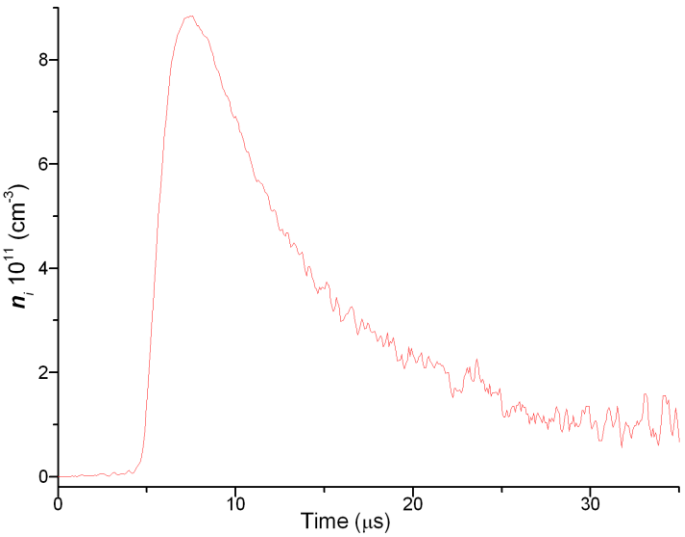

Fig. 2.8 – Sample ion number density plot, calculated from the ion current presented above in Fig. 2.7 for a planar probe at a distance of 16.5 cm from the target with an area of 0.2 cm^2.

The total ion fluence F_i [cm^{-3}] can be determined from the probe signals using the following relation:

$$F_i = \frac{1}{e}\int j_i(t)dt \qquad [\text{cm}^{-3}] \qquad \text{Eqn. 2.14}$$

From the above we can infer both the velocity distribution and the ion energy distribution of the ions in the plume[87]. Rewriting Eqn. 2.14:

$$F_i = \frac{1}{e}\int j_i(t)dt = \int \frac{dN}{dv}dv = \int \frac{dN}{dE}dE \qquad \text{Eqn. 2.15}$$

and taking $E = \frac{1}{2}(mv^2)$, where we found $v = x/t$.

$$\frac{dN}{dv} = \frac{j_i(t)t^2}{ex} \qquad \text{Eqn. 2.16}$$

$$\frac{dN}{dE} = \frac{j_i(t)t^3}{emx^2} \qquad \text{Eqn. 2.17}$$

Using this set of equations we can now approximate the ion fluence, ion energy or velocity distribution and total number of ions at a set time or set spatial position following the laser pulse. This is a useful tool for making estimates of ion density at specific times or positions to help diagnose the pre-ignition phase of the laser trigged discharge devices studied here.

2.3.3 Angular distribution of debris outflow

During this work some angular thin film depositions were made on curved acetate sheet substrates, placed such that the centre of curvature was roughly aligned with the centre of the plasma expansion axis. The thickness profile of the deposited material was found by measuring the optical transmission, around 515 nm, of the film with a Epson Perfection flatbed transmission scanner (model number V700 PHOTO 6400 dpi). The scanner was calibrated by means of scanning a series of known neutral density filters and assigning the known transmissions to the signal values recorded (the blue squares shown in Fig. 2.9), a second order polynomial fit was made and the equation obtained is used as a calibration scaling factor. The polynomial calibration curve presented has the following line equation:

$$Y = -0.34473 + 0.09395X + 0.00111X^2 \qquad \text{Eqn. 2.18}$$

Once the scanner signal is calibrated to a spatial map of transmission of the thin film it can be further analysed by calculating the thin film transmission for the material deposited. The theoretical transmission can be calculated from X-ray Oriented Programs' IMD[88], assuming bulk values for the complex refractive index. This program can calculate the optical properties (reflectance, transmittance, and absorptance) of multilayer structures of varying thickness and material. It includes a range of optical constants for the x-ray to far infrared region.

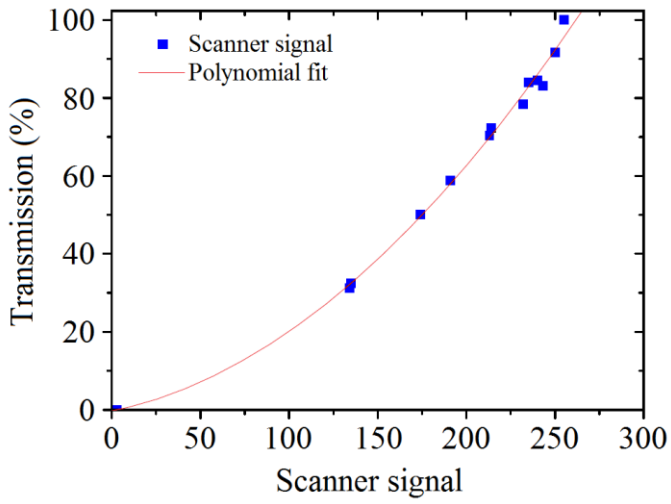

Fig. 2.9 – Calibration curve for the digital optical transmission scanner to convert scanner signal into percentage transmission.

2.4 Optical emission spectroscopy

2.4.1 Spectrometer spatial imaging

Optical emission spectroscopy (OES) was carried out using an Oriel Cornerstone MS260i, 1/4 meter Czerny-Turner imaging spectrometer, with an Andor DH520 intensified charge couple device (ICCD) camera. The ICCD has a 1024 x 256 pixel array and a minimum gate time of the micro channel plate (MCP) was 7 ns. A horizontal slice of the plasma object is imaged onto the 3 mm × 50 µm spectrometer slit as illustrated in Fig. 2.10 below. The camera has an inherent delay of ~40 ns to allow for the CCD to be fully open before initiating recording; this additional time must be taken into account when judging the precise timings of events.

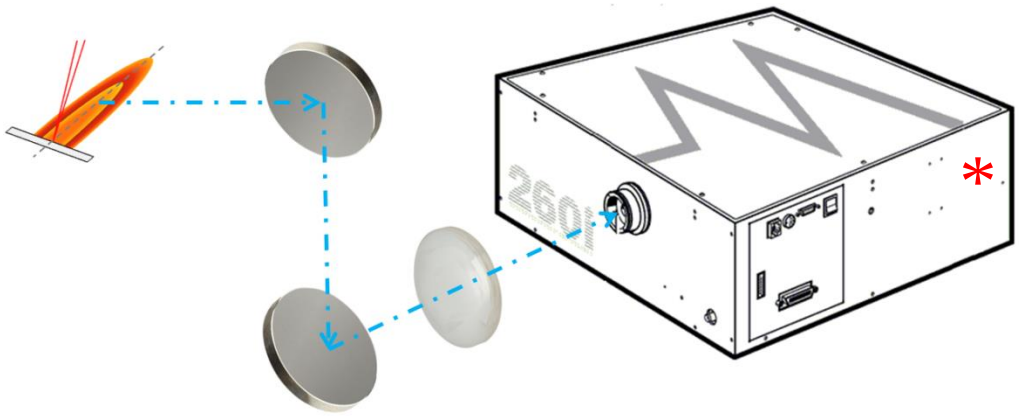

Fig. 2.10 – Optical emission spectroscopy beam path imaging a horizontal slice of a laser produced plasma plume via periscope and imaging lens onto spectrometer slit. The red asterisk on the spectrometer indicates the position of the ICCD.

To image a horizontal object plane onto the 3 mm vertical spectrometer slit a periscope (composed of two 2.5 cm diameter aluminium mirrors with protective coating) is employed to rotate the imaging axis 90º, typically a single UV rated achromatic plano-convex lens is used to magnify this object plane. The main concerns in setting the optical imaging system are that enough light is collected for high signal-to-noise ratio and the region being imaged is the desired area and angle. To ensure high signal to noise a background count is subtracted and each optical element is fine adjusted while running the system to track the measured signal.

2.4.2 Spectrometer calibration

The MS260i spectrometer was calibrated spectrally for each range selected by the rotatable diffraction gratings using well known line emission from a mercury lamp, and a built-in polynomial regression suite in the ICCD software to calibrate the wavelength scale.

The theoretical spectral resolution of the OES spectrometer can be determined by calculating the reciprocal linear dispersion R_d [nm mm^{-1}] of the spectrometer, defined as:

$$R_D = \frac{d\lambda}{dx} = \frac{D\cos\beta}{mf} \qquad \text{Eqn. 2.19}$$

where D is the diffraction grating ruling separation, β the diffraction angle, m the diffraction order, and f the focal length of the spectrometer (0.25 m). Only first-order diffraction lines are considered (m = 1), and these occur at small angles ($10^o - 20^o$), Eqn. 2.19 is approximated by: $R_D = D/f$. Therefore, given the 300 lines/mm grating used, the reciprocal dispersion R_D = 13.3 nm mm^{-1}. To find the spectrometer resolution then the relation: $\delta\lambda_T = WR_D$, where W is the spectrometer slit width, in our case 50 µm. Therefore the theoretical maximum spectral resolution of the spectrometer $\delta\lambda_T$, using the 300 lines/mm grating, is 0.665 nm.

As mentioned before, the ICCD camera has a 1024 × 256 pixel array, where each pixel is 26 × 26 µm so the total detector area is 26.6 mm × 6.65 mm (6.8×10^3 mm^2). However the full ICCD range is not used, to determine the active area of the array a spectrally calibrated image can be used. In this case a spectral range of 226 nm spanned a length of 690 pixels on the ICCD. Rewriting Eqn. 2.19 in terms of spectral range $\Delta\lambda$ and the length of active pixels l_{px} a reciprocal linear dispersion $R_D = \Delta\lambda/n_{px}$ = 12.6 nm mm^{-1} is found. Thus the maximum spectral resolution per pixel $\delta\lambda_E$, for a 300 lines/mm grating and an ICCD with 1024 pixels is found to be $\delta\lambda_E$ = 0.63 nm. Both of these values for the spectral resolution are in good agreement. The spectral range was calibrated using known line transitions from a low density mercury lamp, positioned in front of the spectrometer slit. An example mercury lamp

spectra recorded for the same experimental setup as described in the theoretical spectral resolution calculation is shown in Fig. 2.11. The experimentally measured minimum spectral line full-width at half-maximum was 0.95 nm. Typically each strong emission line profile was noted to have approximately 10 to 15 data points.

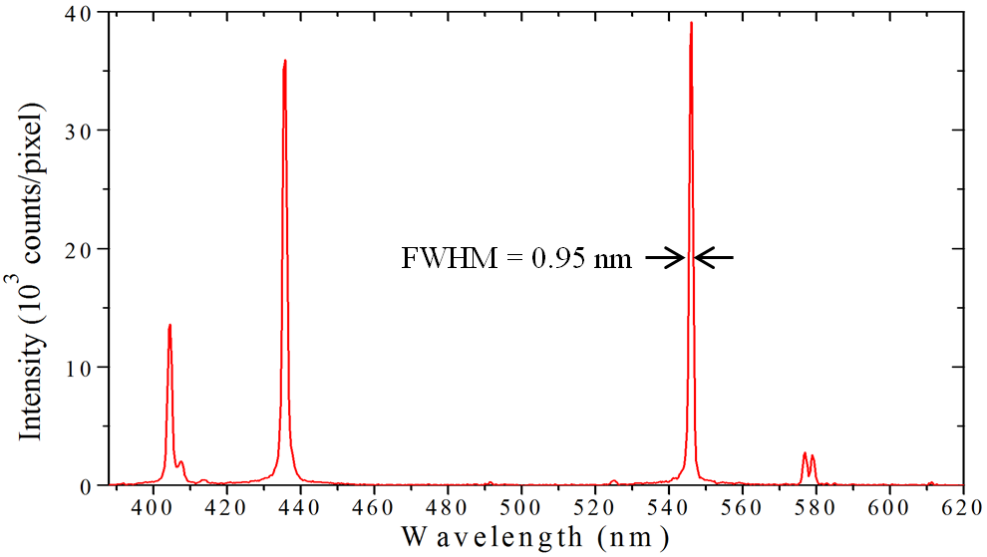

Fig. 2.11 – Optical emission spectra of low density mercury lamp lines, used for spectral calibration, showing the minimum spectral line full-width at half-maximum as 0.95 nm.

The recorded spectra are related to the plasma emission by the throughput and spectral sensitivity of the optical system and spectrometer. By projecting a source with known spectral irradiance [$Wm^{-2}nm^{-1}$] through the full optical system and recording with the ICCD we can find this relation and calibrate the spectra. Quartz tungsten halogen (QTH) calibration lamps (1000 W Oriel 6315 and 100 W Oriel 6333) were used to record a blackbody curve with a known spectral irradiance on the spectrometer. Both lamps produce a uniform flux density over a 2.5 cm^2 area in the visible emission range when placed at a distance of 50 cm from the OES imaging plane.

The counts recorded for the QTH calibration lamp $C_L(\lambda) = F(\lambda)I_L(\lambda)n_L^{Aq}\, n_L^{Px}\, \Delta t_L$, where $F(\lambda)$ is a calibration function found to account for the variables in the optical system, $I_L(\lambda)$ is the known spectral irradiance of the lamp, n_L^{Aq} and n_L^{Px} are the number of acquisitions and number of pixels binned (summed over) respectively, and Δt_L is the gate time used to record the lamp intensity. It is important to ensure that any additional

electronic settings are maintained between measurement and calibration, for example any digital gain set on the ICCD during experiment.

The Oriel 6315 1000 W QTH calibration lamp spectral irradiance $I(\lambda)_{\text{lamp}}$ was taken as quoted from the manufacturer specification sheet and fit using a polynomial function. The spectral irradiance of the lamp, in [$\text{mW m}^{-2}\,\text{nm}^{-1}$], is given by the following fifth order polynomial:

$$I(\lambda)_{\text{lamp}} = \lambda^{-5} exp^{\left(44.47-\frac{4.55\times10^3}{\lambda}\right)} + \left(\frac{-5.87\times10^3}{\lambda^2} + \frac{-1.24\times10^7}{\lambda^3} + \frac{1.57\times10^9}{\lambda^4} + \frac{0}{\lambda^5}\right) \quad \text{Eqn. 2.20}$$

For the calibration of the laser assisted vacuum arc lamp an additional mirror had to be placed before the imaging plane of the spectrometer. The spectral reflectivity factor $R(\lambda)$ (Fig.4) had to be included to account for this. The reflectivity of the mirror was supplied by the manufacturer and verified using an ellipsometer. The spectral reflectivity$R(\lambda)$ was fit with a polynomial over the range of interest (380 nm – 620 nm):

$$R(\lambda) = \left(0.9 + 0.024\,(Z) - 0.031\,(Z^2) + 9.2\times10^{-3}\,(Z^3) + 0.011\,(Z^4) - 3.2\times10^{-3}\,(Z^5) - 8.8\times10^{-4}\,(Z^6)\right) \quad \text{Eqn. 2.21}$$

where Z is the wavelength λ [nm] with a scaling factor applied to allow for fitting:

$$Z = \frac{(\lambda - 490)}{65}$$

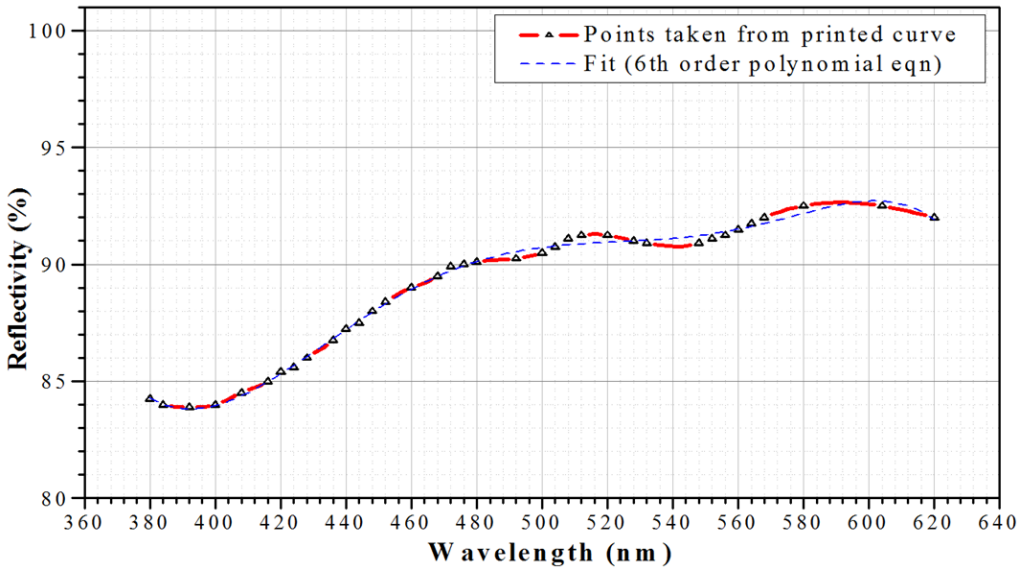

Fig. 2.12 – Mirror reflectivity function fit based on factory calibration data from Eksma Optics. A region of this reflectivity curve was verified using an ellipsometer.

This function $R(\lambda)$ yields a spectral reflectance for the mirror. By applying the additional term $R(\lambda)$ to $I(\lambda)_{\text{lamp}}$ in the process to find $F(\lambda)$ outlined above we can now find the plasma spectral radiance $L(\lambda)$ [W m^{-2} nm^{-1} sr^{-1}] as:

$$L(\lambda)_{\text{plasma}} = \frac{C_{\text{plasma}}}{F(\lambda)R(\lambda)\left(n^{pixel}_{\text{plasma}} * n^{acq}_{\text{plasma}} * \Delta t_{\text{plasma}}\right)}\Omega_{\text{sys}} \qquad \text{Eqn. 2.22}$$

where Ω_{sys} is the solid angle of the cone viewed by the spectrometer given by: $\Omega_{\text{sys}} = \frac{(\pi r^2)}{x^2}$ [sr], where r is the radius of the limiting aperture and x the distance from aperture to light source.. A convenient number quoted for spectrometer solid angle is the acceptance half-angle, given by $\theta = \tan^{-1}\left(\frac{r}{x}\right)$. The MS260i spectrometer has a manufacturer quoted acceptance half-angle of $\theta_{spect} = 7.4^{o}$. When aligning the spectrometer imaging system it should be aimed to match this acceptance angle in order to collect the greatest amount of light from the source with the maximum spectral range.

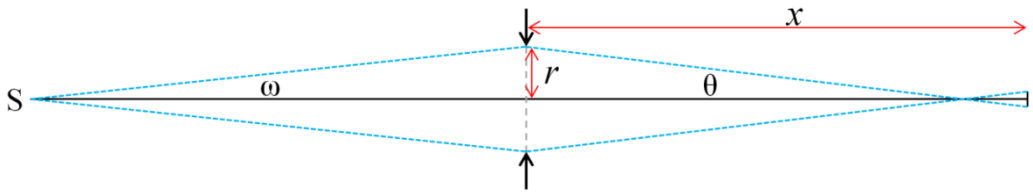

Fig. 2.13 – Solid angle through an optical system from source S to spectrometer slit, with a lens of radius *r* being the limiting aperture, at a distance *x* from the slit.

In the case of the optical setup used for the discussion on spectral resolution $\theta_{sys} \sim 1.5^{o}$. This means the spectrometer was under-filled, which could account for the larger experimentally measured spectral resolution as the entire grating was not illuminated. It is important to ensure the optical delivery system is matched to the slit such that grating is appropriately illuminated to avoid loss of light through the system, introducing stray light into the spectrometer, and also to maximise spectral resolution.

2.5 Extreme ultraviolet emission diagnostic tools

2.5.1 EUV sensitive photodiodes

The PhysTeX EUV detector tool[89] was previously studied[90] in UCD alongside the absolutely calibrated Jenoptik EUV spectrometer using a combination of National Institute of Standards and Technology (NIST) standard radiation sources. These studies showed that the in-band sensitivities are consistent to within 7% between the PhysTex and Jenoptik measurements.

To measure the radiation in the 2% bandwidth at 13.5 nm, the PhysTeX is equipped with a 250 nm thick zirconium filter is used to select the ~6 – 18 nm range (Fig. 2.14), a pair of Mo/Si multilayer mirrors (MLMs), and an International Radiation Detectors (IRD) SXUV-100 silicon photodiode. The photodiode has a manufacturer calibrated sensitivity $S_d = 0.19$ C/J. The pair of MLMs used were manufactured to mimic the band-pass of an 11 MLM system, the resulting reflectance is shown in Fig. 2.15. The choice of an 11 MLM system is due to the industry expectation for a working source-to-wafer optical delivery system for 13.5 nm lithography[15]. An entrance aperture is also installed on the device to minimise the amount of particulate debris contaminating the tool along with a magnet trap to minimise electron flux.

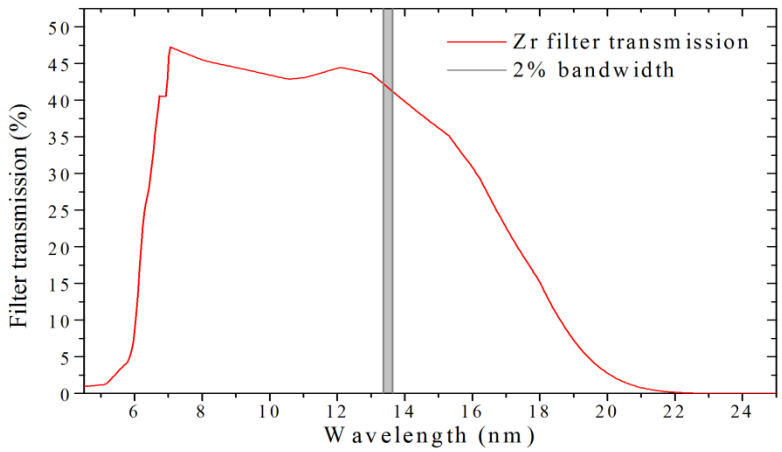

Fig. 2.14 – Transmission calculated using CXRO[99] for the 250 nm thick zirconium filter used. This curve does not account for the fine mesh used to support the thin zirconium film, the mesh was calculated to have approximately 70% transmission.

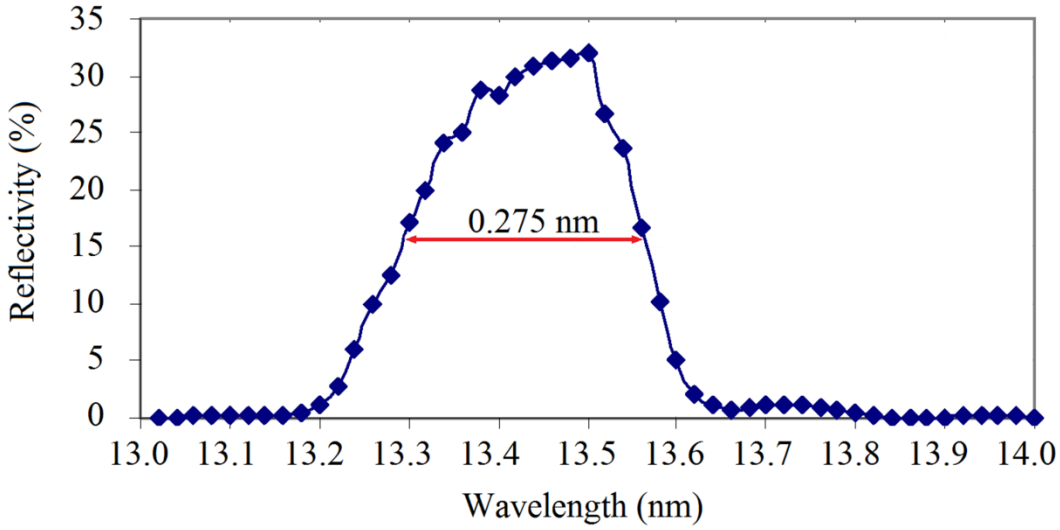

Fig. 2.15 – Reflectivity of the of the MLM assembly in the PhysTeX EUV detector.

The EUV detector tool is mounted inside a vacuum flange with an edge welded bellows and tilt screws to allow for fine angular adjustment once attached to a chamber port. The front aperture can house multiple filters to allow for the measurement of several wavelength ranges out-of-band, as the Mo/Si mirrors are highly reflective in the visible wavelength range[91]. The detector was biased at -12 V by the BT-250 supplied with the tool. Applying a reverse bias to the detector can raise the threshold of saturation as well as reduce the rise-time. *IRD BT-250 (Fig. 2.16) is capacitively coupled*, using a bias tee designed specifically for use with SXUV photodiodes for low noise applications with a DC blocking capacitor. It should be noted that there is an approximate 5% loss of signal in the bias tee that must be accounted for when making absolute measurements.

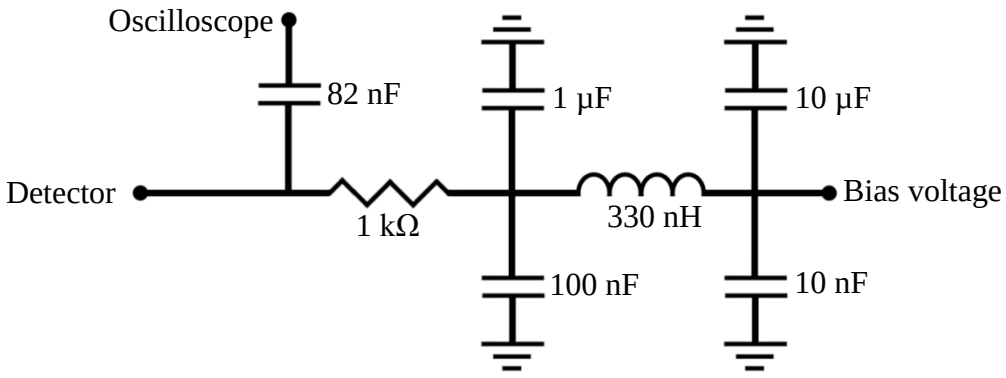

Fig. 2.16 – BT-250 bias circuit used with the PhysTeX EUV detector tool, allowing for bias voltages up to 250 V to increase detector sensitivity.

2.5.2 Jenoptik EUV grazing incidence spectrometer

The time-integrated EUV emission spectrum was measured in the 10 - 18 nm range using the absolutely calibrated grazing incidence Jenoptik spectrometer equipped with a back illuminated silicon charge coupled device (CCD) detector[92], [93] viewing the plasma in the horizontal plane at 60º from the discharge axis and facing the anode. The spectral resolution of the spectrometer is approximately 0.03 nm. The Jenoptik spectrometer spectral sensitivity was absolutely calibrated at the PTB radiometry beamline at the BESSY II electron storage ring in Berlin[100].

A schematic of the Jenoptik spectrograph is given in Fig. 2.17 below. The spectrograph itself consists of a horizontal piezo-driven entrance slit, an Hitachi spherical variable line spaced diffraction grating (with radius 0.25 m), a zero order stop multilayer mirror, a number of apertures to block stray light, and a Princeton Instruments PI-MAX: 1K SX 1024EB/TE CCD camera for recording the spectra.

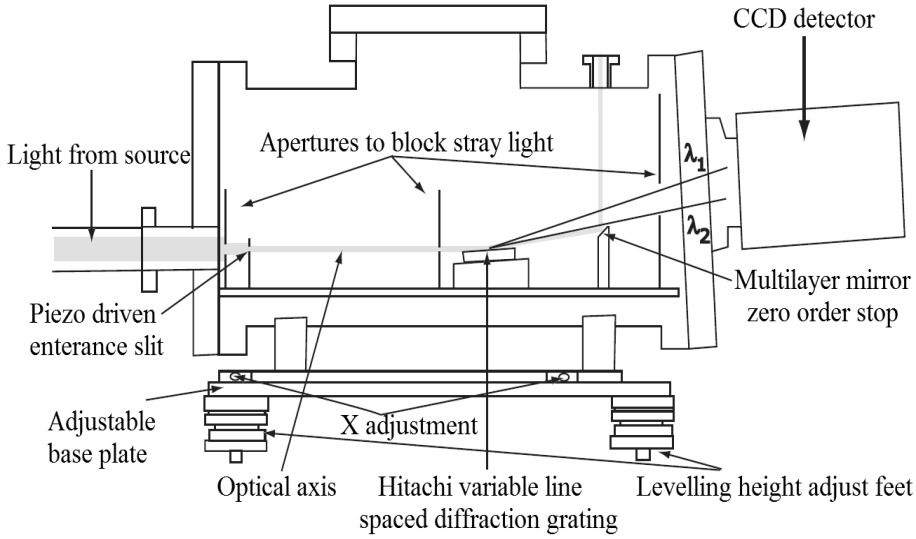

Fig. 2.17 – Side-on schematic diagram of the Jenoptik spectrometer used to record EUV spectra, illustrating the light path from the optical axis to the grazing incidence grating, and the CCD detector with the shorter wavelength at the top of the detector.

The CCD array has 2048 × 2048 pixels, with a pixel size of 13 µm × 13 µm. It is a thinned silicon back-illuminated CCD, which allows for high sensitivity but also means the readout time of the array is relatively long (~1 s). Due to this inherently long readout

time a piezoelectrically driven slit is included to gate the light pulse incident on the CCD. The piezo-driven slit is controlled by an external Princeton Instruments ST-133A camera controller. The slit itself consists of a pair of knife edges mounted in a frame which are spread apart by a piezoelectrical actuator to open the slit. When fully opened the slit has a maximum height of 36 µm, and fixed horizontal length of 4 mm. The ST-133A camera controller sends a transistor transistor logic (TTL) low signal to the piezo controller, which in turn sends a -10 V signal to the slit when it is in the closed position, to ensure that it is entirely shut. When the slit is to be opened during an exposure the controller sends a TTL high signal to the piezo controller which then supplies a driving voltage of between 0 V and 150 V (with 150 V corresponding to the maximum width of 36 µm). The slit requires ~2.5 ms to fully open and the same length of time to fully close, which gives a minimum exposure time of ~5 ms for the spectra. This long integration time necessitates that we limit the repetition rate of the source, typically maintained at one or two shots per capture. The ST-133A could be triggered from the same software package, WinSpec32, which was used to run the CCD triggering and cooling.

The zero order stop multilayer mirror is in place to reflect the zeroth order diffraction to a window flange at the top of the spectrometer. The mirror is tuned for the 2% bandwidth around 13.5 nm (although Mo/Si mirrors are also highly reflective in the visible range). This stop also casts a shadow on bottom 34 pixels of the CCD which gives a measure of the stray light and/or thermal noise to subtract.

The spectrometer grating was protected by an aperture to avoid contamination. It has an independent turbomolecular pump and a gated flange so it could be closed off from the rest of the chamber while not in use. It should be noted that unlike most grazing incidence spectrographs, the Hitachi spherical (radius 0.25 m) variable line spaced diffraction grating gives a flat field image on the CCD rather than a curved plane[94].

2.5.3 EUV imaging

The spatial distribution of the EUV source was recorded using a 125 mm radius spherical Mo/Si multilayer mirror at near normal incidence to form a 13× magnified image on an Andor DX436-BN back illuminated CCD, as shown in Fig. 2.19. The CCD array has 2048 × 2048 pixels, with a pixel size of 13.5 × 13.5 µm. Since air is strongly absorbing in the EUV, the CCD has to be vacuum compatible to measure the radiation from inside the chamber. The quantum efficiency of the CCD is rated around 40% at 13.5 nm.

The imaging system had a resolution of ~5 µm with an imaged region 1.3 mm in diameter which could be scanned spatially using tilt screws. The imaging system included a set of apertures to block stray light and a 1 µm zirconium filter to provide spectral filtering in the 10 – 18 nm region.

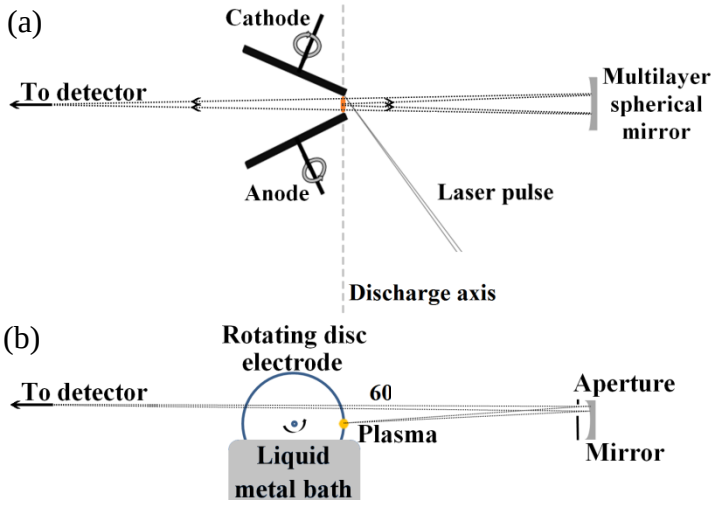

Fig. 2.18 – EUV imaging system viewed from (a) above and (b) the side, illustrating the position of the rotating disc electrodes and the off-axis imaging achieved with an aperture positioned in front of the Mo/Si mirror.

The location of the ablation spot in the image was determined by removing the zirconium filter, allowing the visible emission of the laser produced plasma (LPP) without discharge to be observed. By observing the LPP, a starting point could be selected for each spatial scan. This process was required to locate the EUV emission

region of the plasma in the inter-electrode gap. This alignment process was quite challenging owing to the coarse adjustment on the mirror tilt along with the inherent shot-to-shot variation in position of the EUV emitting region. This issue, along with time constraints, meant that only Galinstan was studied using this diagnostic and not tin. Previously Kieft[23], [44] reported on the time-resolved pinhole imaging of the EUV emitting region for a similar laser assisted vacuum-arc source with tin as the source material. They used a pinhole camera and observed the bright region of the plasma moving away from the cathode laser target after the pinch. One point of interest to take from their work was the observation that the ionisation appears to take place before and during compression, not after. So we can expect our EUV region to be emitting over a shorter time scale.

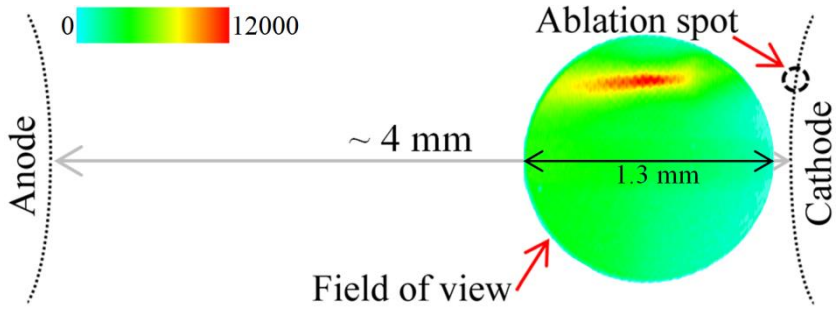

Fig. 2.19 – Time-integrated EUV emission of a typical 4.05 J discharge in galinstan triggered by a 5 mJ, 30 ns laser pulse. The schematic shows that the 1.3 mm diameter field of view is located in the 4 mm inter-electrode gap, close to the cathode.

Chapter 3.

Colliding Laser Plasma Triggered Discharge

In this chapter the results from the Colliding Laser Plasma Triggered Discharge (CLP-TD) are presented. The results are broken down into three sections; first the laser plasma is characterised, then the collisional interaction of the laser plasmas, followed by the discharge studies initiated with a single laser plasma and with colliding laser plasmas. In each of the three results sections the plasma will be discussed in terms of the ion fluence measured by a planar Langmuir ion probe and the visible emission spectroscopy. Results from a novel spectral imaging technique are also presented.

Various materials can be investigated with this geometry as the targets are easily replaced. This is useful for studying the interpenetration of colliding laser plasmas. In the experiments presented here colliding aluminium laser plasmas, and a colliding laser plasma triggered discharge were characterised. The device is very small, making it easy to install in a vacuum chamber. It is also easily customised, such as replacing capacitors to give different discharge characteristics. Aluminium was chosen as a target material due to readily available spectral information.

The laser plasmas used here typically have a velocity on the order of 10 km/s, while inter-electrode gap is 1 cm long in this geometry. The period of the discharge is on the order of microseconds, this leads to accumulation of plasma at one electrode before the discharge current has ceased ringing (observed by this author with E. Sterling et al.[83]). Here, a colliding pair of laser produced plasmas was investigated as the triggering mechanism. The aim was to generate a stagnating plasma plume in the inter-electrode gap, and thus maximise the coupling of the discharge energy to the plasma load. This geometry also presents novel opportunities in shaping the plasma load in the discharge by adjusting the laser pulse parameters of both beams.

3.1 Experimental apparatus

Minimising the inductance is a key concern in designing a fast Z-pinch discharge setup, to maximise the rate of rise of current to yield $>10^{10}$ A s^{-1} in the initial current pulse. The damped oscillation following the initial current pulse will only have a small portion of the plasma load remaining to interact with, as the plume rapidly accumulates at one electrode or is removed during the explosive post-pinch phase. To minimise the inductance in the design of the CLP-TD the capacitor bank was mounted directly onto two 1 cm^3 aluminium cubes acting as electrodes and ablation target mounts. The capacitor bank could be changed, but here was comprised of four 0.47 µF capacitors in parallel. The total capacitance was $C_T = 1.88$ µF and could be charged to a maximum voltage $V_{Max} = 2$ kV. The inductance of the circuit is mostly from the capacitors with an inherent inductance of 35 nH, by combining them in parallel the circuit inductance was approximately 8.75 nH. The discharge characteristics were different for triggering by the colliding laser plasmas or by a single laser plasma. A top down schematic view of the CLP-TD setup, in vacuum chamber, is shown in Fig. 3.1 (a). The capacitor bank was held in place on insulator mounting posts connected to the electrode cubes (Fig. 3.1 (b)).

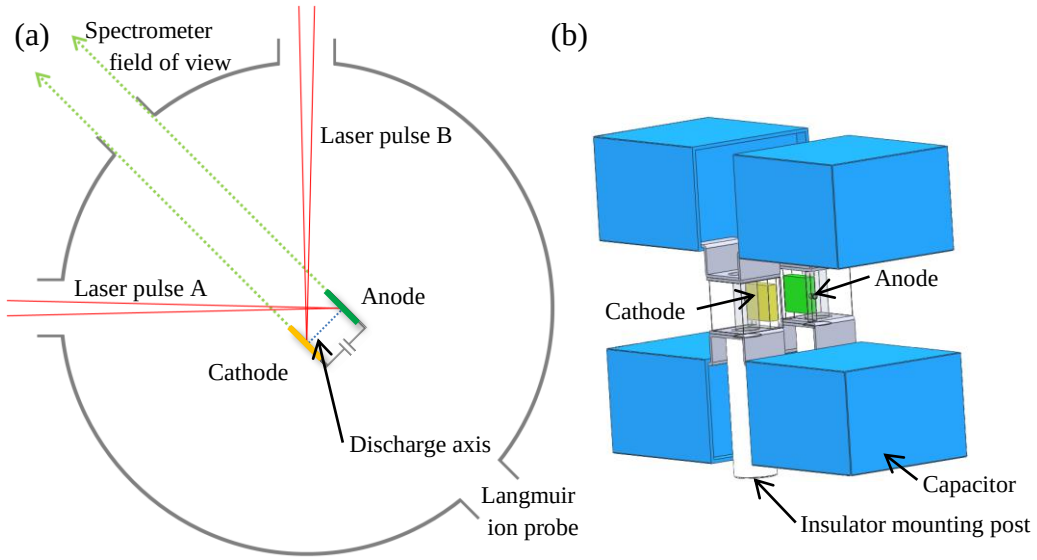

Fig. 3.1 – Schematic showing a) top down view of Colliding Laser Plasma Triggered Discharge in vacuum chamber and the positioning of diagnostic tools and b) capacitor bank & electrodes on insulator mounting posts.

Each of the electrode cubes was machined to have a groove facing toward the counter electrode to allow for replaceable targets of various materials to be attached. This also allowed for easy replacement of targets to avoid laser drilling. To further minimise laser drilling of the targets the setup was mounted on computer operated translation stage such that the entire setup could be rastered inside the chamber under vacuum in between laser shots, cleaning shots were also taken on each fresh target spot to remove any adsorbed material from the surface.

The laser fluence was varied to control the plasma load delivered to the discharge. This was accomplished through the use of reflective neutral density (ND) filters. Four reflective laser line ND filters, transmission 65%, 45%, 15%, and 8%, were arranged in such a way to allow for combinations of pairs or single filters. In this way the 1064 nm 7 ns Nd:YAG pulse energy was varied from ~5 mJ to 145 mJ. For the colliding laser plasmas a polarising beam-splitter was employed to give two laser pulses of equal energy along an equal path length to the opposing electrodes. The laser beam had an initial diameter of 5.8 mm and was focused to a spot size of ~1.5 mm diameter at each electrode surface. It was possible to block either laser pulse and investigate each laser plasma separately in both discharge and free ablation modes. During the investigation the voltage on the capacitor bank was varied from 500 V up to 2 kV, it was noted that below 500 V no appreciable discharge was detected by the Rogowski coil, while at 2 kV the capacitors would occasionally self-discharge. The vacuum chamber was maintained at a pressure of ~5 $\times 10^{-5}$ mbar for the duration of the experiments.

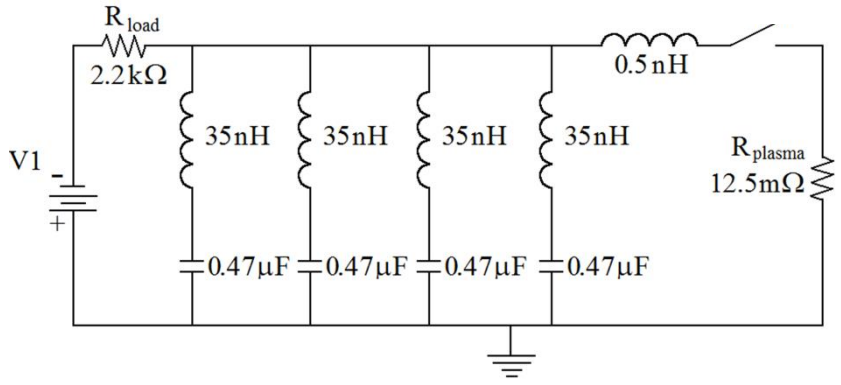

Fig. 3.2 – Circuit diagram for the CLP-TD setup, where the laser plasma trigger is represented by the inductor, open switch, and resistor combination on the right hand side.

3.2 Laser plasma characteristics

Both targets were ablated by approximately equal laser energies over the same ablation spot area. It was intended that both laser plasmas would have equal initial conditions. It was difficult to ensure both laser beam paths were precisely equal to give identical laser plasma conditions from each of the targets. In the following section we investigate a single laser plasma, with the second target removed. The second target was removed to allow us characterise the trigger plasma and diagnose the laser plasma parameters at and before the time of discharge.

The laser pulse width was monitored using a fast photodiode which detected back reflection from the focusing lens of one of the beams. The full-width at half-maximum was measured as 10 ns. As mentioned already the laser energy was controlled by introducing reflective neutral density filters immediately after the laser exit aperture. In these experiments two laser energies were used: 17 mJ and 24 mJ. The spot area was approximately 0.018 cm^2; therefore the fluences used were approximately: 0.96 J/cm^2 and 1.36 J/cm^2.

3.2.1 Translational ion probe with single laser plasma

To make the translational ion probe measurements it was necessary to remove one electrode, to give access to the probe. The probe was positioned at 7 cm from the target and translated in a plane perpendicular to the laser plasma forward direction (Fig. 3.3).

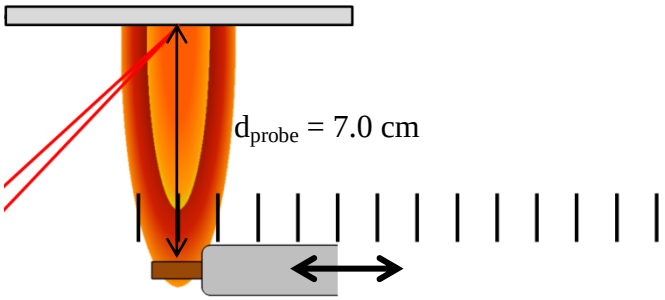

Fig. 3.3 – Schematic of translational ion probe positioned 7 cm from the target surface, translated perpendicular to the plasma forward direction (z axis).

The ion probe translation was measured in one direction away from the normal, assuming the plume is symmetrical about the normal. A selection of measured ion time-of-flight profiles at various angles away from normal is shown in Fig. 3.4. As the probe was moved linearly the larger angles are also further away from the laser ablation spot causing the ion front to appear slower. The ions have a distribution of velocities, but for convenience the quoted numbers will be the front velocity and peak velocity (indicated on Fig. 3.4). In the case of the 0.96 J/cm^2 laser ablation the ion velocity was measured as 4.8 ×10^4 m/s and 3.6 ×10^4 m/s at the ion plume front and peak respectively.

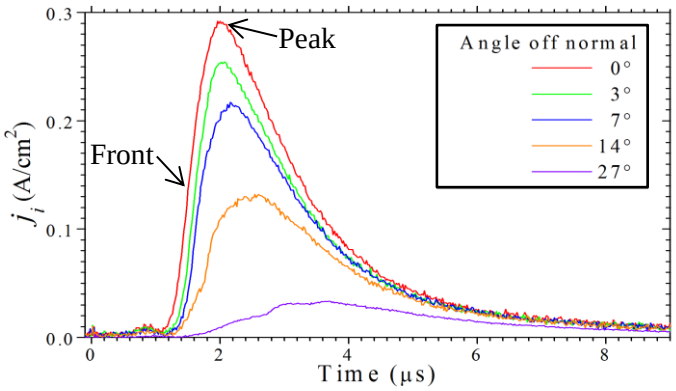

Fig. 3.4 – Sample set of ion time-of-flight profiles from the translation ion probe experiment, measured at various angles from the target normal.

The integrated ion fluence versus angle is plotted in Fig. 3.5 together with a fit of the angular distribution made based on the Anisimov distribution discussed in Section 2.3. The k value obtained for the fit of plasma angular distribution is 2.0.

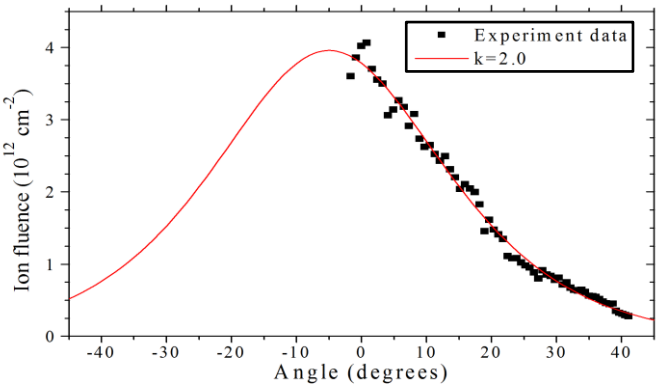

Fig. 3.5 – Angular distribution of the integrated ion fluence fit with k value of 2.0.

From these laser plasma parameters we can infer information about the plasma conditions at the time of discharge, which are very important for modelling the discharge process.

3.3 Discharge experiments

Having investigated the laser plasma characteristics we now move to discuss the discharge experiments undertaken. The discharge was triggered with single laser produced plasma and also by the collision of two laser plasmas. During the remainder of this section we will be discussing both of these triggering schemes.

The discharge current and voltage were measured using a Rogowski coil and a voltage divider circuit. Both of these measurements give indications of changes in the plasma impedance which typically occur due to pinching events. These kinks are clear on the sample discharge current plot given in Fig. 3.6. Here the laser pulse, Rogowski coil, and discharge voltage signal are all included on the plot.

The onset of discharge occurs at between 90 ns and 100 ns after the laser pulse for the colliding laser plasma case, as the plasmas are assumed to collide in the centre of the inter-electrode gap the plasma velocity is estimated as 5×10^4 m/s, this is in good agreement with the ion front velocity measured in the previous section.

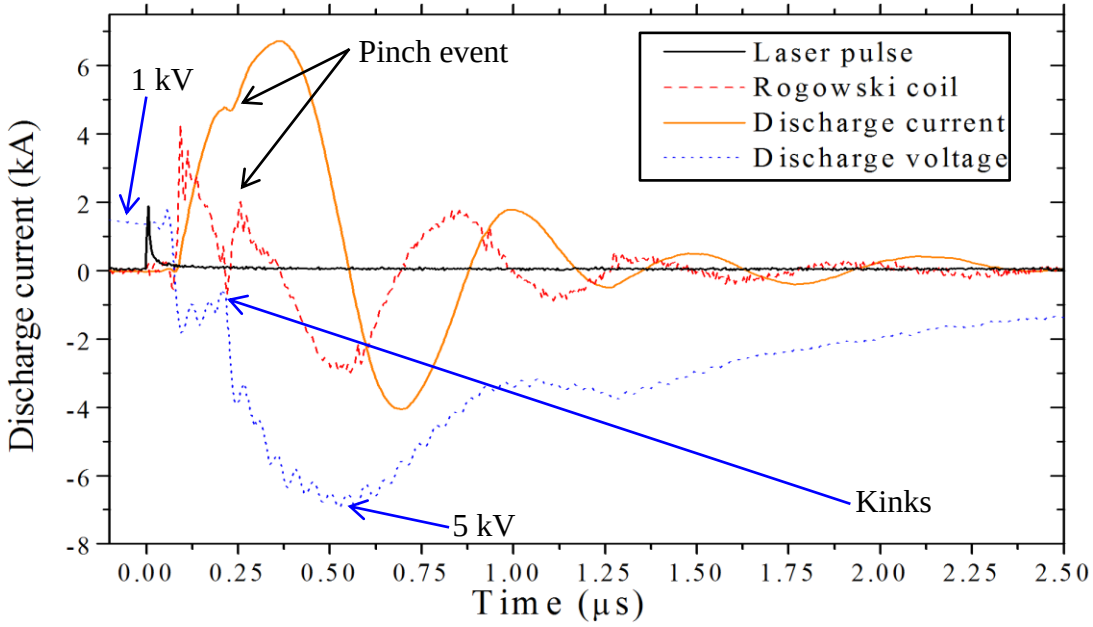

Fig. 3.6 – Sample 1 kV discharge current profile triggered by colliding laser plasmas. The Rogowski coil dI/dt (red dash) and discharge voltage (blue dot) are included. All three have apparent kinks indicating changes in the plasma impedance.

The pinching event is given by the notch in both the dI/dt signal measured by the Rogowski coil and the current profile obtained by integration. It is desirable to have the pinching event synchronised with the time of peak current, this is to ensure the most efficient coupling of discharge energy to the pinch.

In the case of a discharge triggered by a single laser plasma the onset time of discharge is approximately 250 ns after the laser pulse, this gives an estimate for plasma velocity of 4×10^4 m/s. The distribution of ions through the inter-electrode gap will be different in each case, as the typical ion time-of-flight profile shown in Fig. 3.4 will be mirrored, moving from each target towards the centre of the gap. A sample comparison of the single laser plasma versus colliding laser plasma trigger case is shown in Fig. 3.7. The discharge current profile was analysed for charging voltages from 200 – 1000 V under three triggering conditions.

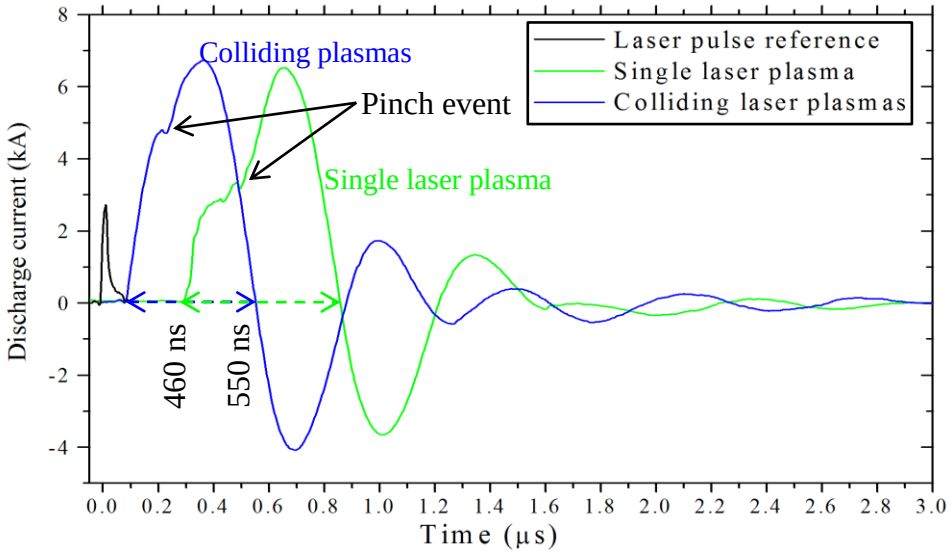

Fig. 3.7 – Comparison of the discharge current profile for a 1 kV discharge triggered by a single laser plasma versus the colliding laser plasma case.

The peak current, half period and rate of rise of current are plotted for these conditions in Table 3.1. This table was made for an average of 8 shots for each voltage and each triggering schemes. These triggering schemes were the colliding laser plasma triggered discharge using both laser beams, or the single laser plasma triggered discharge where either the anode or cathode were ablated to ignite the discharge. Using Fig. 3.1 given at the start of this chapter we will name the anode ablation ‘Plasma A’ and the cathode ablation ‘Plasma B’ for convenience.

Table 3.1. Discharge parameters for various voltages for three trigger conditions.

Voltage (V)	Peak current (kA)	Half period (ns)	Rate of rise (A/s)	Trigger scheme
200	1.6	590	0.6×10^{10}	Colliding plasmas
	1.3	500	0.6×10^{10}	Plasma A
	1.3	440	0.6×10^{10}	Plasma B
400	4.0	530	1.7×10^{10}	Colliding plasmas
	3.0	500	1.5×10^{10}	Plasma A
	3.0	480	1.3×10^{10}	Plasma B
600	4.9	430	2.1×10^{10}	Colliding plasmas
	4.0	430	1.5×10^{10}	Plasma A
	5.6	530	2.5×10^{10}	Plasma B
800	8.3	450	3.6×10^{10}	Colliding plasmas
	5.8	450	2.5×10^{10}	Plasma A
	5.4	510	2.2×10^{10}	Plasma B
1000	8.4	450	3.6×10^{10}	Colliding plasmas
	6.2	480	2.5×10^{10}	Plasma A
	6.4	490	2.7×10^{10}	Plasma B

From this collection of data we can see that the colliding plasma case yields a higher peak current for most discharge voltages, and that with higher discharge voltage the discharge half period decreases for most cases. We can also see the greatest rate of rise of current was for the colliding case with an 800 V and 1000 V discharge.

3.3.1 Ion probe diagnostics

Each of the ion time-of-flight profiles in Fig. 3.8 is an average of 4 consecutive shots; an average was taken to reduce the influence of noise. The noise observed near the zero time is caused by electrical pick-up from the discharge current. The ion probe was placed at 31 cm from the discharge axis, as shown in Fig. 3.1. This distance was large to avoid the electrical noise saturating any ion signal arriving to the probe at early times. The ion probe was utilised at this position for all discharge triggering schemes, as it was in a location which was unobtrusive to the colliding or single laser plasmas.

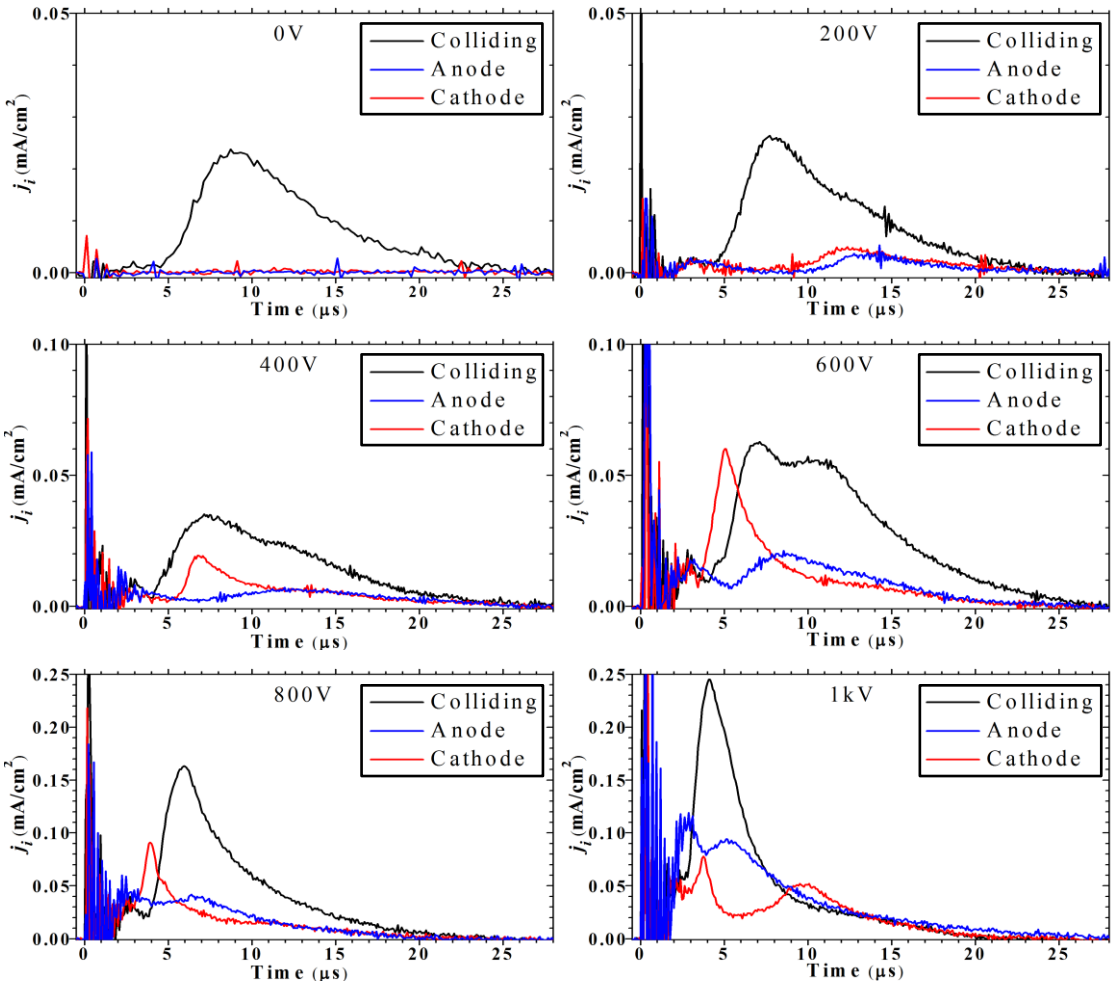

Fig. 3.8 – Ion current fluence for various discharge voltages from 0 V to 1 kV, showing the comparison of triggering by colliding plasma, ground electrode ablation and live electrode ablation. It is clear from these graphs that increased voltage leads to an increased peak ion velocity. It is also apparent that the anode and cathode ablation plumes A and B produce significantly different discharge plasmas, based on their ion time-of-flight profiles.

The probe used in these experiments was a small round pin, 4.5 mm in diameter, attached directly to an electrical vacuum feedthrough on the chamber wall. A grounded fine mesh was also positioned in front of the probe, with a small opening directly facing the probe face, to help limit the discharge effecting the recorded time of flight signals. The trend in the data is clear, with increasing voltage the ion velocity increases.

The ion kinetic energy in the colliding plasma case increased from approximately 800 eV at 0 V to 3.65 keV at 1 kV, while the total ion fluence increased by a factor of 6. The ion kinetic energy measured along the target normal was also approximately 800 eV without a discharge. In the case of either of the single laser plasmas with no discharge no appreciable ion signal is measured, while for the colliding laser plasmas at 0 V an ion fluence of 4.8×10^{11} ions/cm^2 is measured. The difference between ion time-of-flight between anode and cathode ablation is also clear. A faster peak ion velocity is observed for the cathode laser plasma triggered discharge from 200 – 800 V. In the case of the 1 kV discharge the ion front is arriving at the probe during the discharge noise. For this reason voltages above 1 kV were not extensively studied.

3.3.2 Optical emission spectroscopy

3.3.2.1 Spectrometer set up

Visible emission spectra from the plasmas were recorded to diagnose the temperature and density of the plasma, both spatially and temporally. A 1 cm horizontal section of the inter-electrode gap was imaged onto the 3 mm × 50 µm spectrometer slit as illustrated in Fig. 3.9 below.

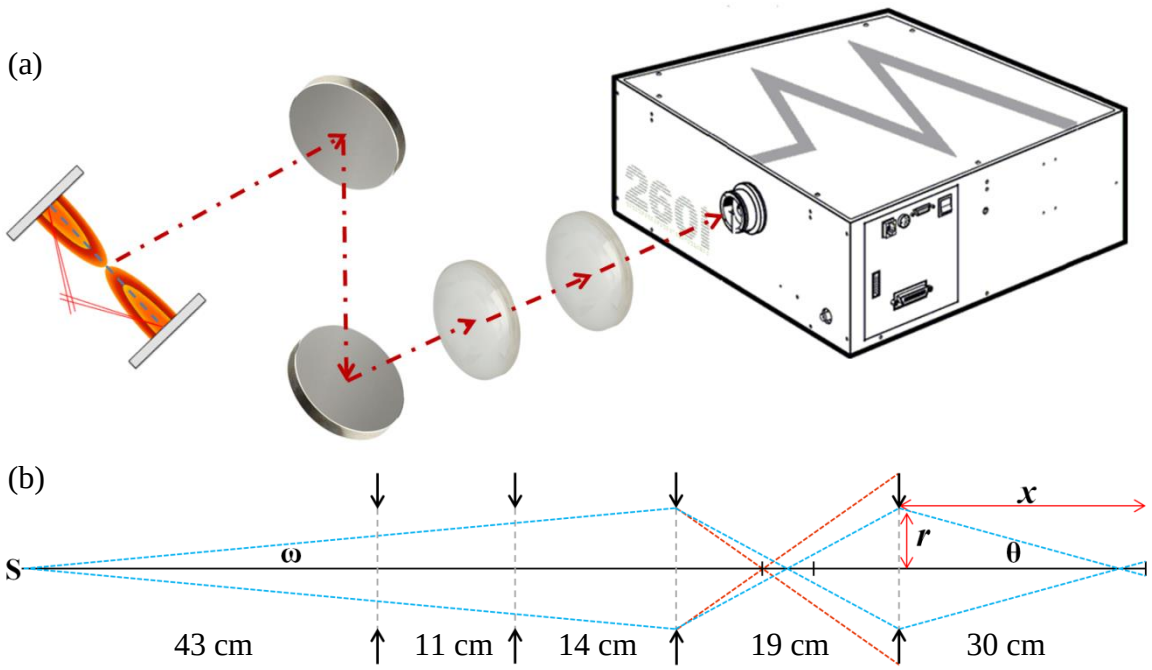

Fig. 3.9 – (a) Isometric plan of optical emission spectroscopy beam path and (b) scale schematic ray diagram of light collection in the two lens system. The limiting aperture is the final lens, giving an acceptance half angle θ = 2.4°.

The information obtained from the literature for Al I – VI visible line emission is presented on the following pages. The tabulated transition probabilities and Stark width parameters are given along with the accompanying Grotrian energy level diagrams. The information presented is for the intense lines observed between 350 nm and 560 nm.

3.3.2.2 Transition line information from the literature

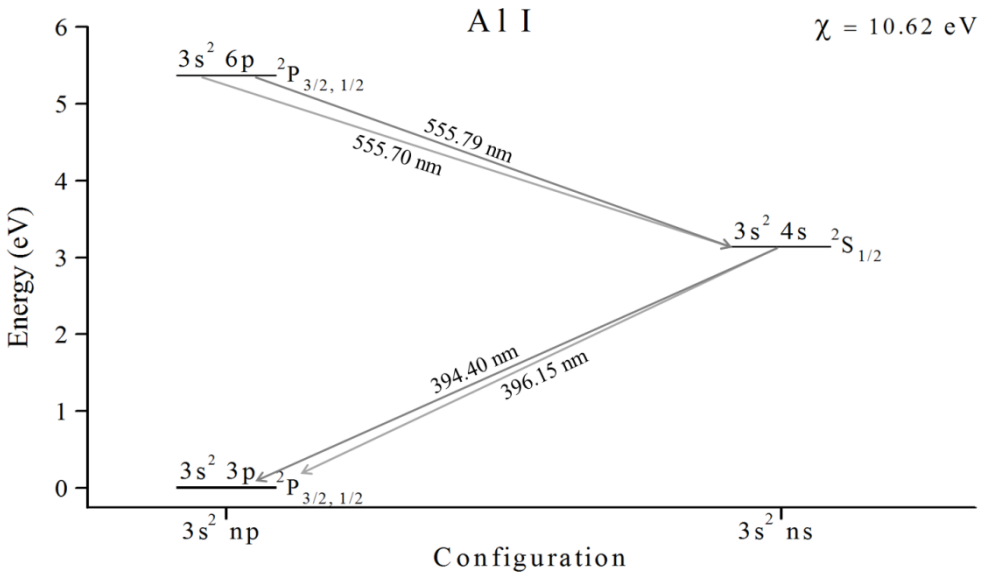

Fig. 3.10 – Grotrian diagram for lines of interest in Al I, line information taken from NIST[101]. With the ionisation potential χ given as 10.62 eV.

Table 3.2. Transition probabilities for Al I spectral lines of interest taken from NIST[101].

Transition	λ (nm)	E_i (eV)	E_k (eV)	g_i	g_k	A_{ki} ($10^8 s^{-1}$)
$3s^2 4s\ ^2S_{1/2} \rightarrow 3s^2 3p\ ^2P_{1/2}$	394.40	0	3.1427211	2	2	0.499
$3s^2 4s\ ^2S_{1/2} \rightarrow 3s^2 3p\ ^2P_{3/2}$	396.15	0.0138938	3.1427211	4	2	0.985
$3s^2 6p\ ^2S_{3/2} \rightarrow 3s^2 4s\ ^2S_{1/2}$	555.70	3.1427211	5.3732132	2	4	0.0023
$3s^2 6p\ ^2S_{1/2} \rightarrow 3s^2 4s\ ^2S_{1/2}$	555.79	3.1427211	5.3728580	2	2	0.00229

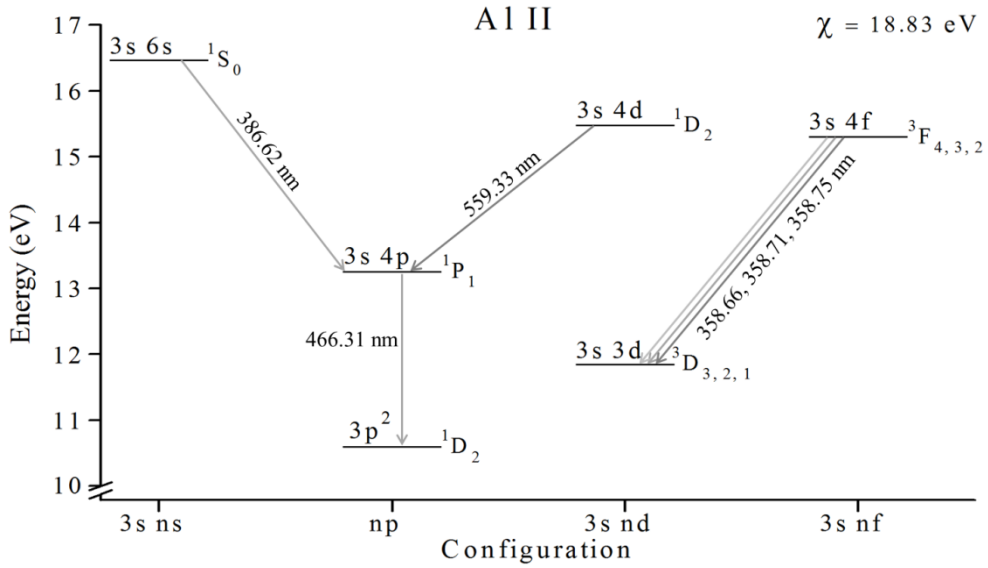

Fig. 3.11 – Grotrian diagram for lines of interest in Al II, line information taken from NIST[101]. With the ionisation potential χ given as 18.83 eV.

Table 3.3. Transition probabilities for Al II spectral lines of interest taken from NIST[101].

Transition	λ (nm)	E_i (eV)	E_k (eV)	g_i	g_k	A_{ki} ($10^8 s^{-1}$)
3s 4f $^3F_4$ → 3s 3d $^3D_3$	358.656	11.846618	15.302546	7	9	2.35
3s 4f $^3F_3$ → 3s 3d $^3D_2$	358.707	11.846753	15.302185	5	7	2.09
3s 4f $^3F_2$ → 3s 3d $^3D_1$	358.745	11.846868	15.301941	3	5	1.97
3s 6s $^1S_0$ → 3s 4p $^1P_1$	386.616	13.256459	16.4624517	3	1	0.426
3s 4p $^1P_1$ → 3p^2 $^1D_2$	466.306	10.598336	13.256459	5	3	0.581
3s 4d $^1D_2$ → 3s 4p $^1P_1$	559.330	13.256459	15.472500	3	5	0.926

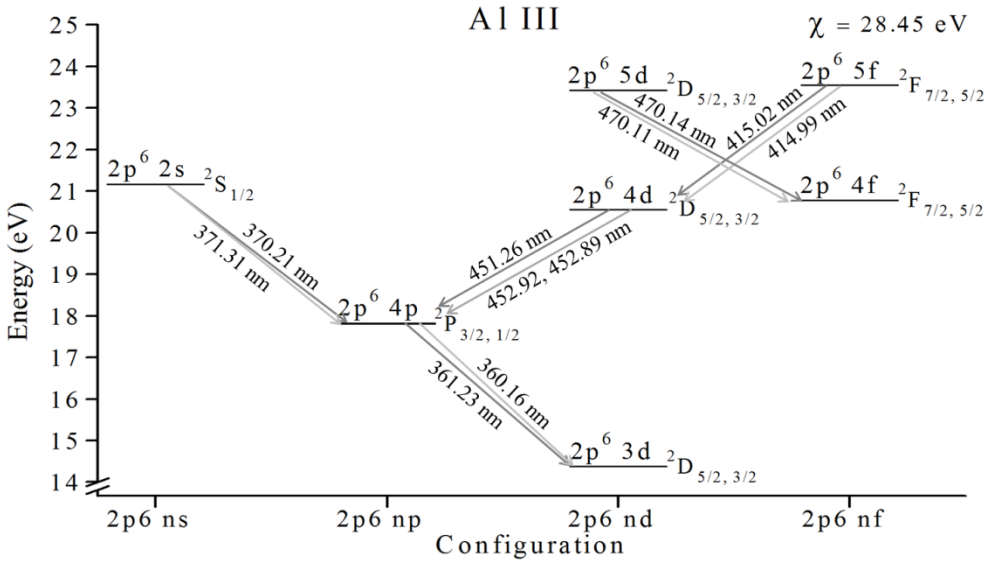

Fig. 3.12 – Grotrian diagram for lines of interest in Al III, line information taken from NIST[101]. With the ionisation potential χ given as 28.45 eV

Table 3.4. Transition probabilities for Al III spectral lines of interest taken from NIST[101].

Transition	λ (nm)	E_i (eV)	E_k (eV)	g_i	g_k	A_{ki} ($10^8 s^{-1}$)
$2p^6 4p\ ^2P_{3/2} \rightarrow 2p^6 3d\ ^2D_{5/2}$	360.163	14.376737	17.818202	6	4	1.31
$2p^6 4p\ ^2P_{1/2} \rightarrow 2p^6 3d\ ^2D_{3/2}$	361.23	14.377021	17.808269	4	2	1.45
$2p^6 2s\ ^2S_{1/2} \rightarrow 2p^6 4p\ ^2P_{1/2}$	370.21	17.808269	21.156334	2	2	1.13
$2p^6 2s\ ^2S_{1/2} \rightarrow 2p^6 4p\ ^2P_{3/2}$	371.31	17.818202	21.156334	4	2	2.27
$2p^6 5f\ ^2S_{7/2} \rightarrow 2p^6 4d\ ^2D_{5/2}$	414.99	20.554883	23.541675	6	8	2.05
$2p^6 5f\ ^2F_{5/2} \rightarrow 2p^6 4d\ ^2D_{3/2}$	415.02	20.555031	23.541635	4	6	1.91
$2p^6 4d\ ^2D_{3/2} \rightarrow 2p^6 4p\ ^2P_{1/2}$	451.26	17.808269	20.555031	2	4	2.09
$2p^6 4d\ ^2D_{3/2} \rightarrow 2p^6 4p\ ^2P_{3/2}$	452.89	17.818202	20.555031	4	4	0.415
$2p^6 4d\ ^2D_{5/2} \rightarrow 2p^6 4p\ ^2P_{3/2}$	452.92	17.818202	20.554883	4	6	2.49
$2p^6 5d\ ^2D_{3/2} \rightarrow 2p^6 4f\ ^2F_{5/2}$	470.11	20.781332	23.417914	6	4	0.0767
$2p^6 5d\ ^2D_{5/2} \rightarrow 2p^6 4f\ ^2F_{7/2}$	470.14	20.781408	23.417833	8	6	0.0731

Stark width information was collected from the literature for observed lines from Al I – Al III. The Al II 466.3 nm line was used throughout this work for estimating the electron density. This line was chosen as it was observed to be the only intense line which we had sufficient information to use and was not obscured by overlapping lines from other transitions.

Table 3.5. Stark broadening full-width at half-max (FWHM) of Al I – Al III spectral lines for stated electron temperatures (T_e) and electron densities (N_e) from cited literature.

Species	λ (nm)	T_e (eV)	N_e (10^{17} cm^{-3})	$\Delta\lambda$ (nm)	Ref.
Al I	396.15	1.0	2.5	0.084 ± 0.02	[80]
Al I	394.40	1.0	2.5	0.084 ± 0.02	[80]
Al II	390.07	0.9	0.1	0.001 ± 0.0002	[81]
	466.3	1.6	1.0	0.09 ± 0.009	[102]
	559.32	0.9	0.1	0.038 ± 0.01	[81]
Al III	360.52	4.3	64	0.85 ± 0.06	[81]
		4.3	119	2.9 ± 0.3	[81]

3.3.2.3 Parameters and control factors in the OES

The spatially resolved spectra presented in this section show the visible emission recorded in the range approximately 335 nm – 559 nm. The spectra are labelled according to delay time t_d, gate time Δt, and maximum counts observed per pixel C_{max}. This can be set in the software during post processing to allow us to investigate the less intense emission features. In this experiment the electrode at the bottom of the images was the grounded anode while the electrode at the top was the live cathode. Both electrodes are ablated with equal laser energy, 17 mJ, over equal spot size, 1.5 mm diameter. The spectral resolution was measured as 0.95 nm using lines emission from a low density mercury lamp. The spatial resolution was approximately 0.7 mm, taken from the shadow edge of the electrodes using a back lighter.

3.3.2.4 Colliding laser plasmas without discharge

The spectra in Fig. 3.13 and Fig. 3.14 show the intense continuum emission at the time of the laser pulse along with a colliding laser plasma spectrum 200 ns after the laser pulse. The ion species in the plume are seen to separate, with the accumulation of Al III in the centre of the inter-electrode gap beginning at 100 ns after the laser pulse. This central emission region is observed until roughly 1.8 µs after the laser pulse, over this time the emission decays from Al III to Al II and finally Al I as the plasma cools and the density decreases. The emission decays faster in the case of a single laser plasma, ceasing at roughly 1 µs after the laser pulse.

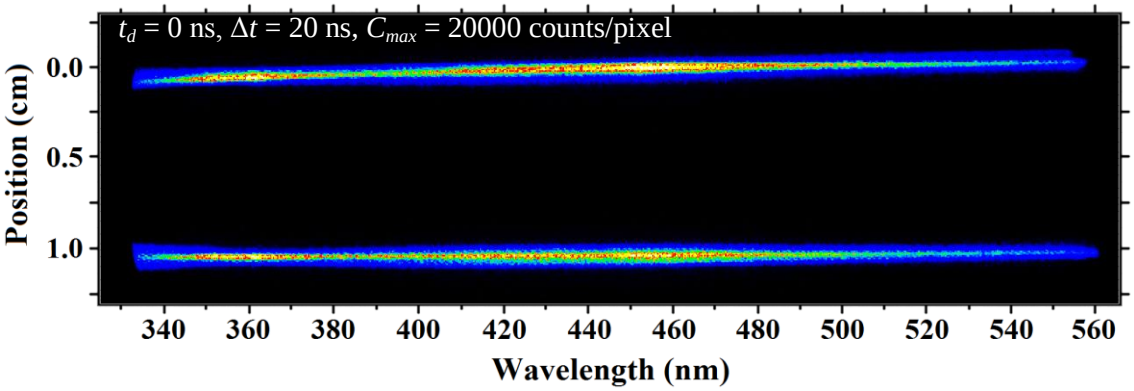

Fig. 3.13 – OES of a pair of laser plasmas recorded during the laser pulse with no discharge.

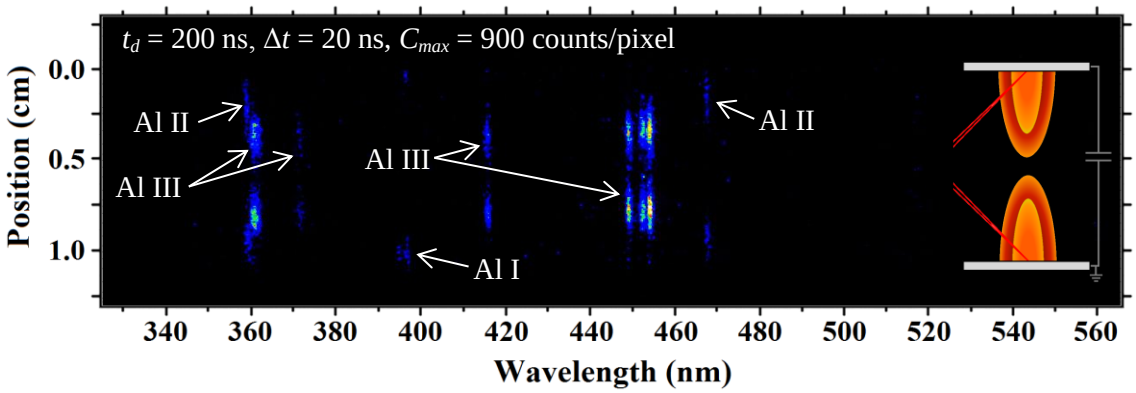

Fig. 3.14 – OES of a colliding laser plasma with no discharge, the lines in the centre of the inter-electrode gap are all Al III while the faint Al I and Al II emission lines are observed closer to the electrodes.

By fitting the Al II and Al III lines in Fig. 3.14, in the centre region and near the electrodes the electron temperature was estimated by making a Boltzmann plot. The Boltzmann plots made for the spectra shown at 200 ns after the laser pulse give an estimated temperature of 1.8 ±0.2 eV in the centre region and 1.0 ±0.3 eV near the electrodes. The spectra near to each electrode are approximately equal, giving confidence to the assumption that both laser plasmas have identical initial conditions. The line width is on the order of the spectrometer resolution, based on the Stark width parameter the electron density must be less than 10^{16} cm^{-3}. We can make this assumption as we should expect a line width above the spectral resolution from the broadening parameters give in Table 3.5 when the electron density is above 10^{16} cm^{-3}.

3.3.2.5 Colliding laser plasmas triggered discharge

These spectra were recorded for a 1 kV (0.96 J) colliding plasma triggered discharge. The onset of discharge occurs roughly 100 ns after the laser pulse. The first two spectra in Fig. 3.15 (a) and (b) show the laser plasma expansion up to the onset of discharge at roughly 100 ns. In (c) and (d) the discharge is indicated by an increase in the max counts per pixel along with the dominant emission shifting to Al III lines. The pinching event occurs around the time of image (g), with the first half-period of the discharge ending by image (j).

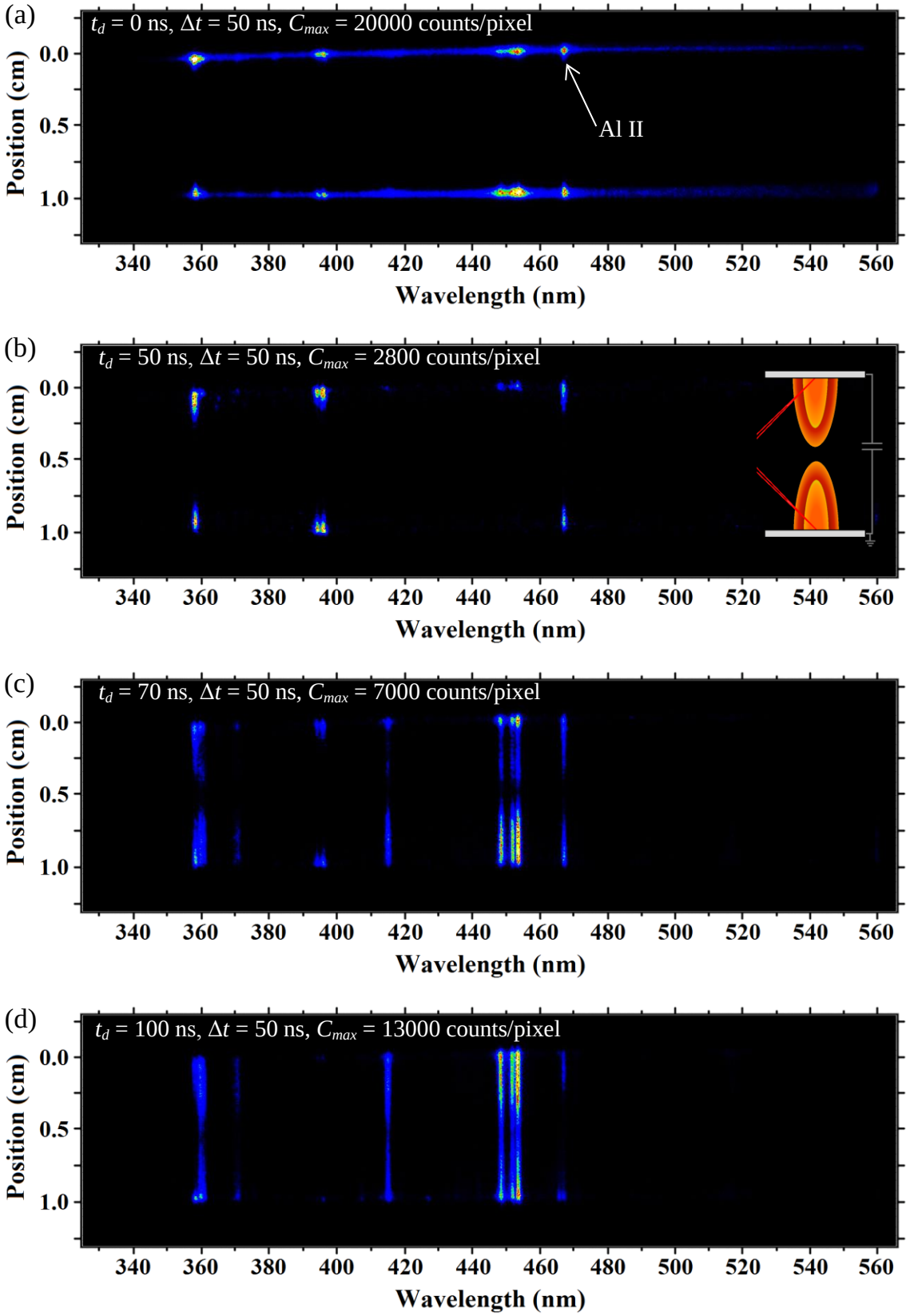
(a)
t_d = 0 ns, Δt = 50 ns, C_{max} = 20000 counts/pixel
Al II
(b)
t_d = 50 ns, Δt = 50 ns, C_{max} = 2800 counts/pixel
(c)
t_d = 70 ns, Δt = 50 ns, C_{max} = 7000 counts/pixel
(d)
t_d = 100 ns, Δt = 50 ns, C_{max} = 13000 counts/pixel
Position (cm)
0.0
0.5
1.0
340 360 380 400 420 440 460 480 500 520 540 560
Wavelength (nm)

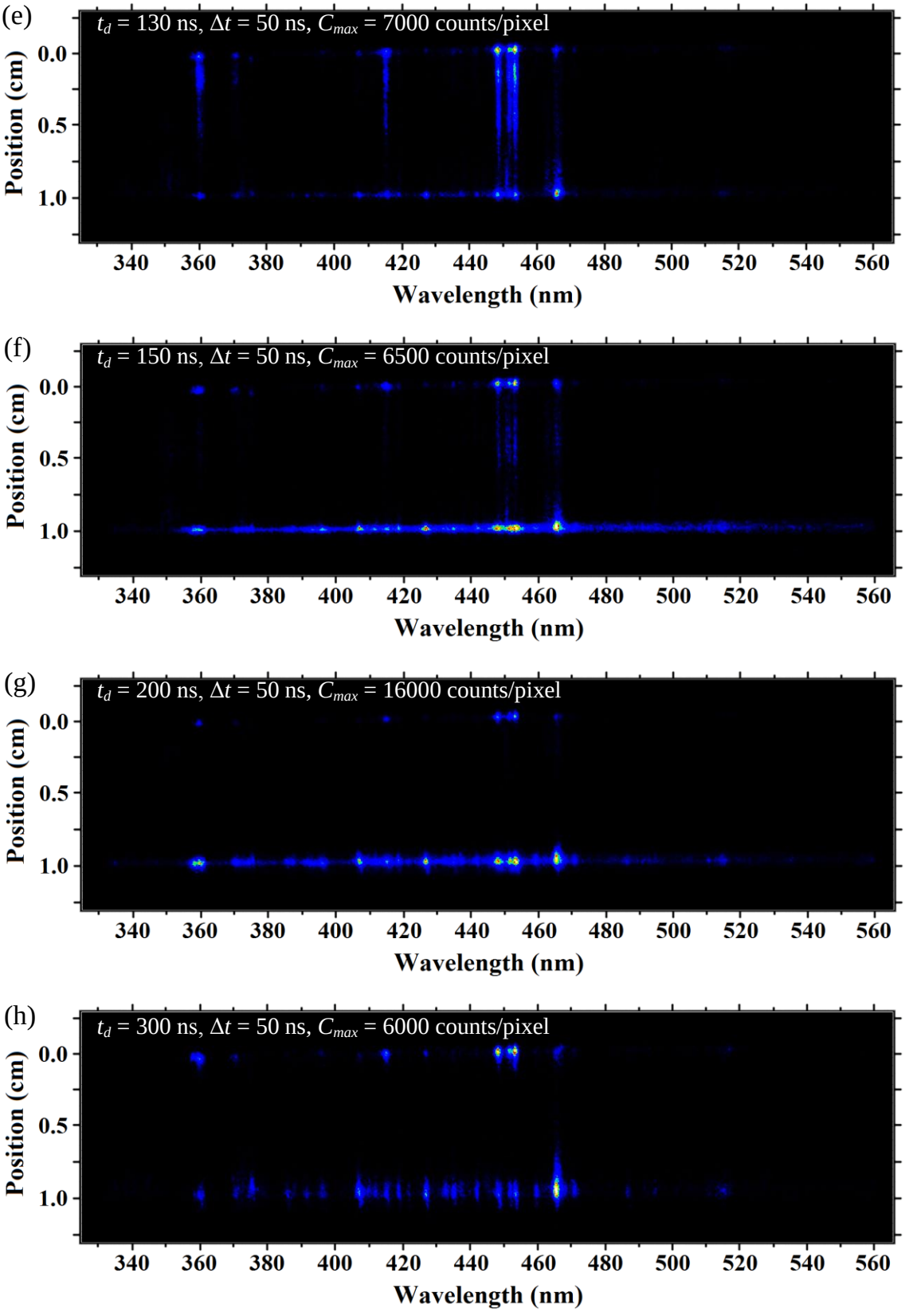
(e)
t_d = 130 ns, Δt = 50 ns, C_{max} = 7000 counts/pixel
(f)
t_d = 150 ns, Δt = 50 ns, C_{max} = 6500 counts/pixel
(g)
t_d = 200 ns, Δt = 50 ns, C_{max} = 16000 counts/pixel
(h)
t_d = 300 ns, Δt = 50 ns, C_{max} = 6000 counts/pixel
Position (cm)
0.0
0.5
1.0
340 360 380 400 420 440 460 480 500 520 540 560
Wavelength (nm)

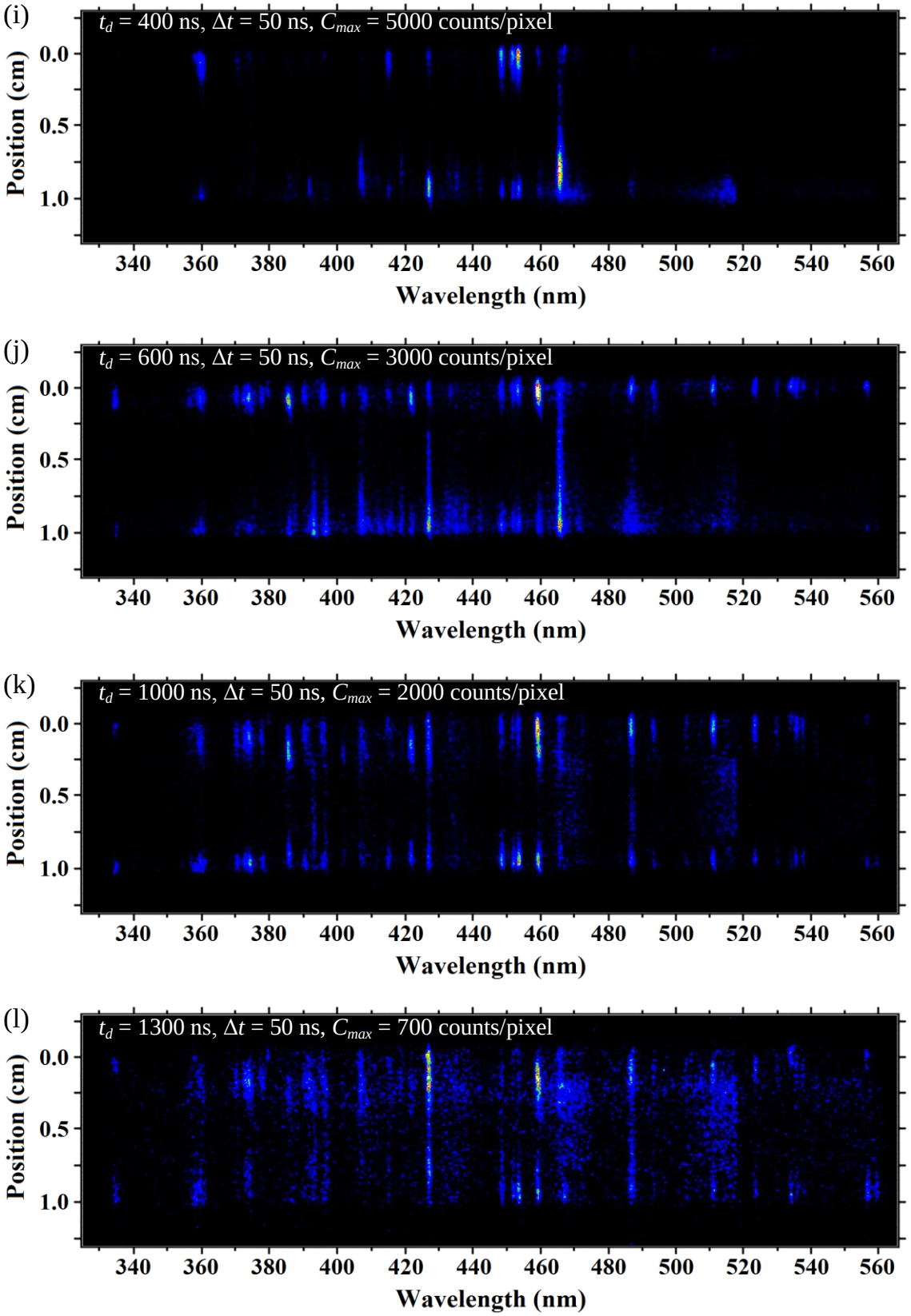

Fig. 3.15 – (a) – (l) Visible emission recorded at given time delays t_d, for a 1 kV (0.96 J) colliding plasma triggered discharge. The delay times here were varied from 0 ns, when the laser pulse hits the target, to 1.3 μs when the maximum counts observed per pixel is getting too low with respect to the background noise. The gate time was constant throughout Δt = 50 ns.

The visible emission recorded after the laser pulse, as the plasma begins to expand, is composed mostly of broadened Al II and Al III lines close to the target surface. The line emission has reached approximately 1.6 mm from the target surfaces during the 50 ns gate time of the first spectral image 3.2×10^4 m/s, which is in good agreement with the velocity from the ion time-of-flight measure. By taking spectral plots at several positions across the spatial scale a temperature and density map (see Fig. 3.21) can be made, for the early times the laser plasma has not expanded far from the target and so there are fewer data points. In the first image in Fig. 3.15 the temperature and density for 4 positions were estimated from Boltzmann plots and Stark widths. A sample Boltzmann plot is given in Fig. 3.17 for the spectral data in Fig. 3.16. Plots of temperature and density are made by analysing the spectra at various spatial positions are made from the laser pulse at 0 ns through the discharge up to 1.2 μs delay.

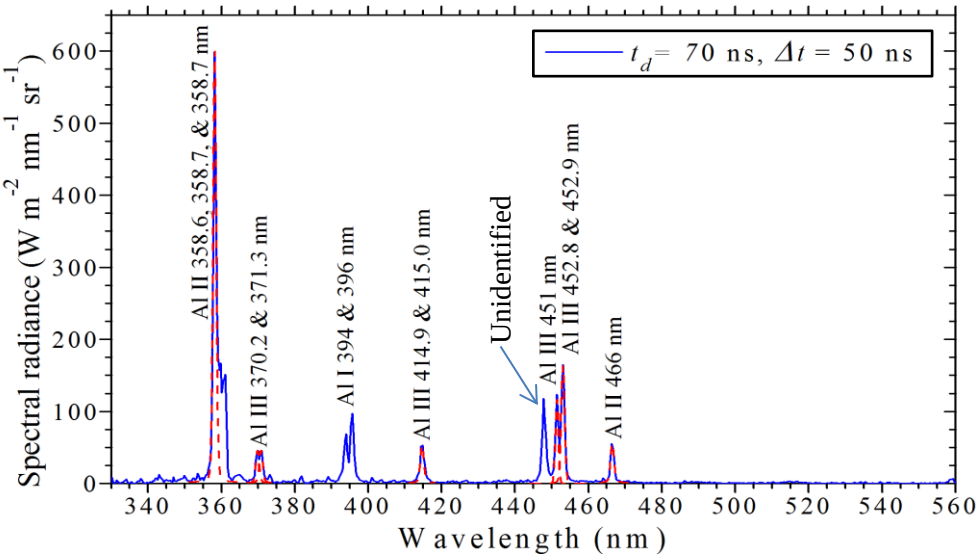

Fig. 3.16 – Plot of spectra radiance taken by averaging over 12 pixels at the ground electrode. The lines identified for Al I, Al II, and Al III are labelled. Voigt profiles were fitted over several Al II and Al III lines to obtain intensity and full-width at half-maximum. This information was used estimate the electron temperature and density in the plasma.

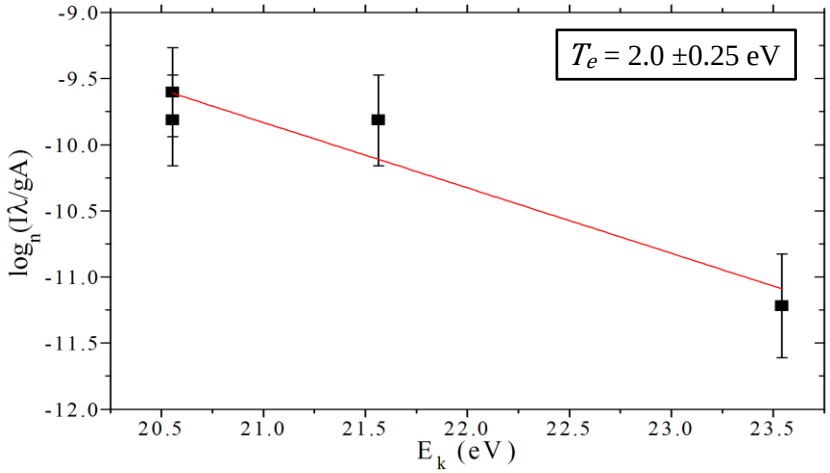

Fig. 3.17 – Boltzmann plot of Al III line emission fit in Fig. 3.16, giving an estimated electron temperature of 2.0 ±0.25 eV.

A Boltzmann plot is not possible for Al I lines in this range, as the observed lines are from the same upper energy level. To make a Boltzmann plot it is necessary that the plasma be in local thermodynamic equilibrium (see Section 1.3) and that there are measurable emission lines from a single ion stage which have a sufficiently large spread in upper energy level. The ionisation fraction (Fig. 3.18) at a set density can be used to estimate plasma temperature using the Saha ionisation equation[65], modified to compare the intensity ratio of lines from consecutive ion stages[103]. This can also be used as a guide for plasma temperature based on observed ion stages, for example at an ion density of 1×10^{17} cm^{-3} a dominantly Al IV spectra can be assumed to have a temperature of at least 3.5 eV from the calculated ion fractions in Fig. 3.18.

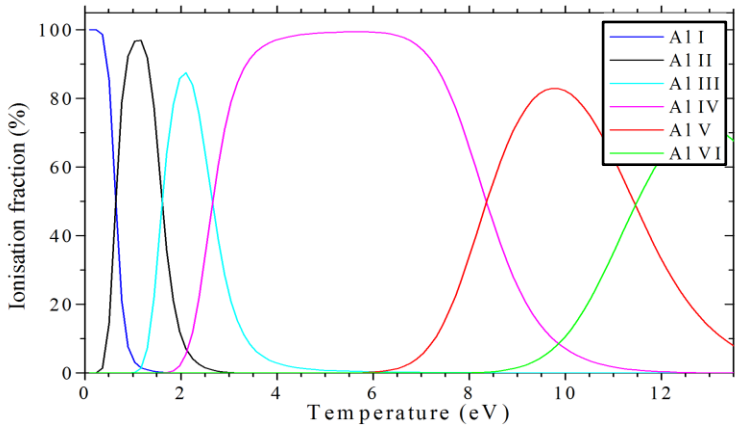

Fig. 3.18 – A calculated ionisation fraction for aluminium at an ion density of 1×10^{17} cm^{-3} for a temperature range of 0 – 13 eV.

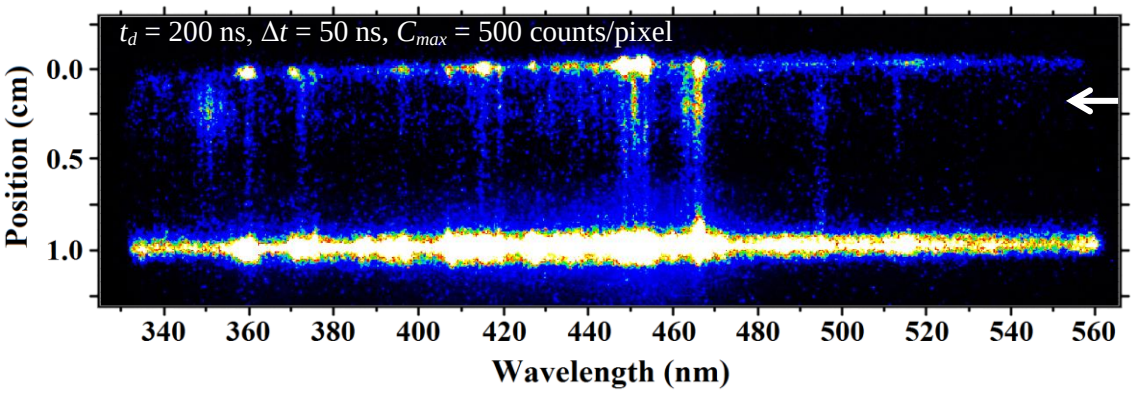

Fig. 3.19 – Saturated visible emission spectra showing the emission in the inter-electrode gap around the time of the pinch event. The interesting feature revealed by saturating the image is the emission close to the cathode, indicated by the white arrow. This feature is of interest as it appears to have line emission from higher ion stages suggesting a substantially higher temperature plasma in this region during pinch.

The emission in the inter-electrode gap can only be examined by saturating the visible spectra in Fig. 3.15 (g), setting the maximum counts per pixel from the peak value of 16000 counts/pixel to 500 counts/pixel. In this image the emission observed near both the anode and cathode (bottom and top of the image respectively) is composed of several unidentified lines. The emission lines observed close to the cathode at ~350 nm are from Al IV and Al V. The line information available for Al IV line emission is limited, with no transition probabilities obtained for the observed lines. Based on the assumption of a plasma in LTE, and assuming a density of the same order of magnitude as that estimated from Al II emission; the plasma temperature can be assumed based on the ion population plot in Fig. 3.17, provided the electron density is approximately 10^{17} cm^{-3}. Based on this a temperature of ~7 eV is expected for the plasma to be composed of mainly Al IV and Al V.

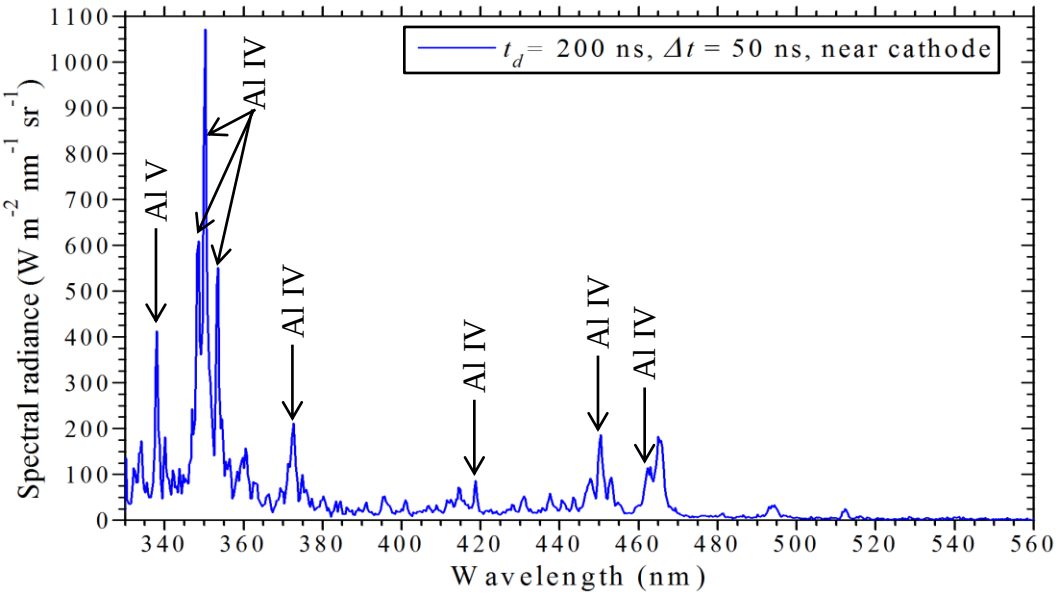

Fig. 3.20 – Plasma spectra taken across the line marked in Fig. 3.19, showing the dominating spectral features are from Al IV and Al V.

The spectra at each electrode also have strong Al IV and Al V emission, which overlap with several of the Al II and Al III lines making it difficult to diagnose the plasma parameters by using Stark line widths or Boltzmann plots.

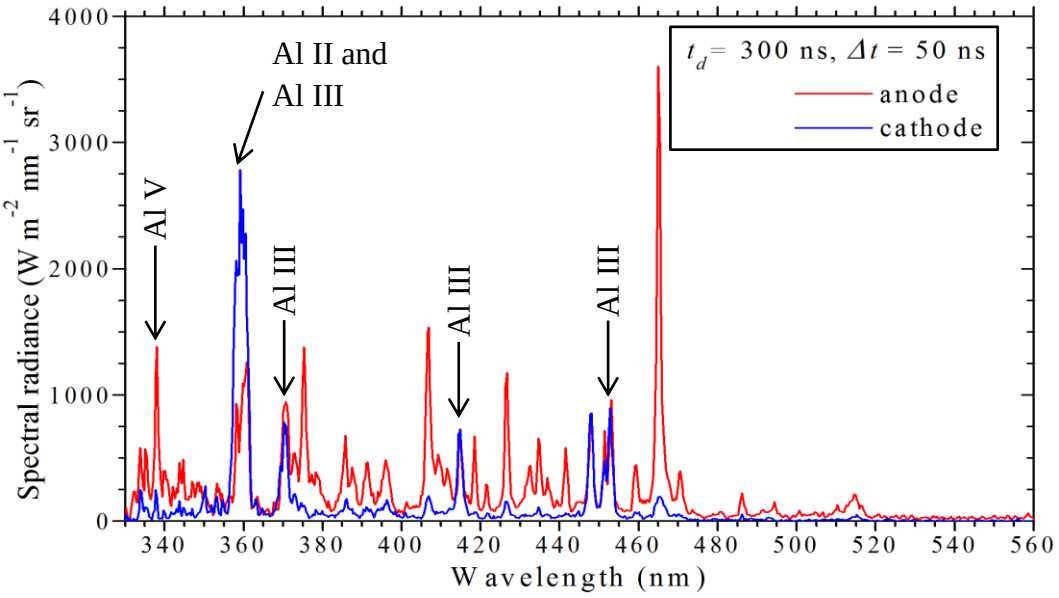

Fig. 3.21 – Visible emission at each target surface, averaged over roughly 150 µm. The emission at the anode shows higher ion stages contributing, with approximately equal Al III emission. This suggests that the anode plasma is not homogenous but instead composed to different emission layers.

In the time directly after the pinch event, 250 ns to 400 ns, the plasma is very hot with Al III – Al V lines observed at both electrodes, the emission in the inter-electrode

gap is very weak for the first half-period of the discharge has ended at approximately 450 ns after the laser pulse. Many of the lines recorded during the first half-period of the discharge, near the anode surface, have not been identified here. These lines are possibly due to contaminants although precautions were taken to avoid and remove any unwanted materials from the high grade alnuminium target surface. The presence of Al V emission lines could suggest that these unidentified lines are from Al V or higher ion stages, for which little information has been found in the visible emission range from the literature. Although the emission during discharge has many strong overlapping lines plots of temperature and density versus time and spatial position have been made, using Al II and Al III emission lines. It is important to note that for some time delays the plasma emission was noted to possibly be non-homogenous with emission from plasma layers with different temperature and density.

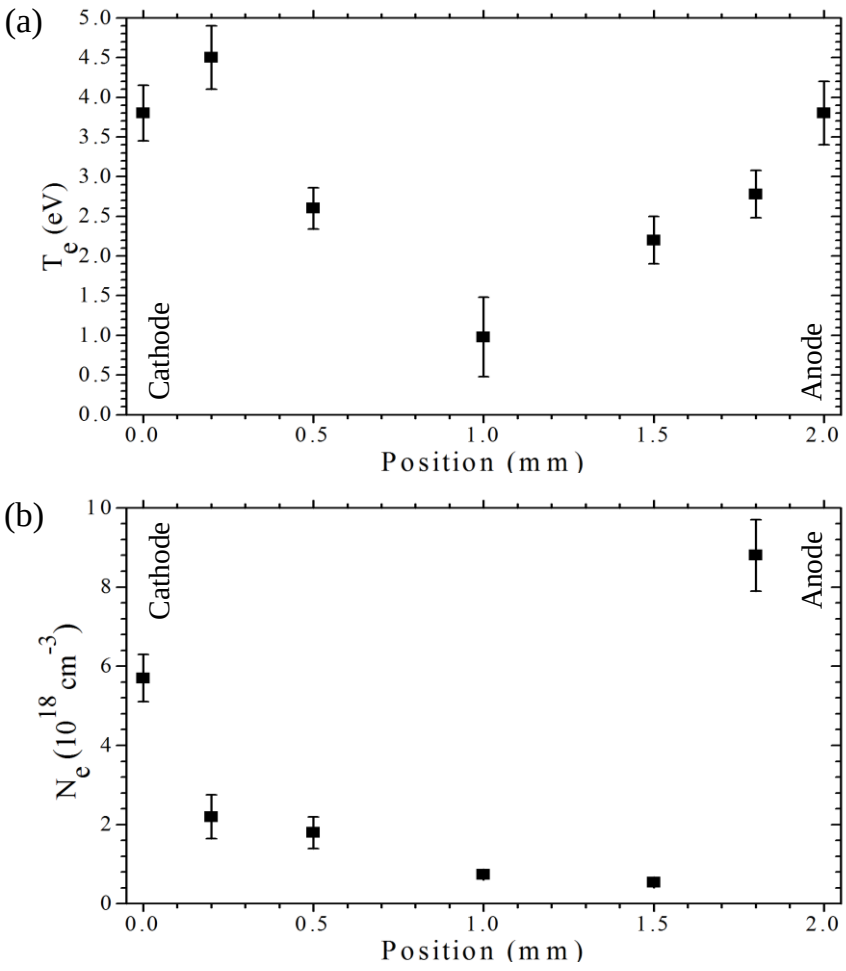

Fig. 3.22 – Spatial distribution of plasma electron (a) temperature and (b) density 200 ns after the laser pulse. Where the position 0 mm is the cathode and 2 mm the anode.

The visible emission at the peak of the discharge current is very intense close to the electrodes, this emission is composed of very broad overlapping lines making the line fitting unreliable. For this reason the temperature and density estimate for some time delays and spatial positions are not presented. One spatial location close to the cathode was chosen for an intensive survey of temperature and density. This region was chosen based on the interesting features noted in Fig. 3.15 at this position. Some of the points included do not fit with the expected temperature profile, perhaps due to the visible emission lagging behind the discharge current or due to the emission from multiple temperature/density layers within the plasma. The temperature is observed to reach approximately 4.5 eV around the peak of current with a density of (8.0 ±1.5) $\times 10^{18}$ cm^{-3}.

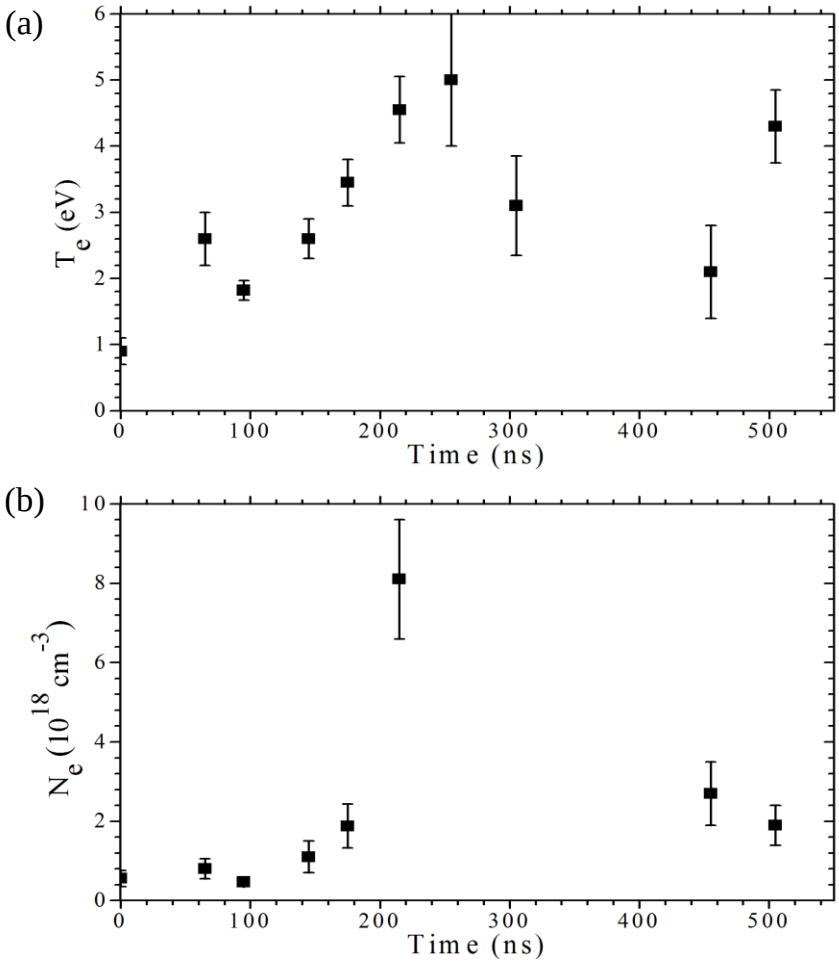

Fig. 3.23 – Temporal plot of plasma electron (a) temperature and (b) density at approximately 200 µm from the cathode surface. The temperatures are estimated from Al III emission lines and densities from the line width of the 466.3 nm Al II line. The error bars are based on the line fitting and accuracy associated with the spectral line information.

3.3.3 Novel spectral imaging

In this section the results from a novel spectral imaging experiment are presented. Here the spectrometer slit was removed with the spectrometer in the same arrangement as in the previous section. This resulted in the imaging of each spectral line with an x and y spatial dimension. Some of the spectral lines overlap strongly, being similar in wavelength. Using an imaging spectrometer to record 2D images of the plasma can also be accomplished by using the diffraction grating as a mirror, imaging the zero order onto the ICCD. The advantage of using the grating to separate the spectral lines is that it gives information on the distribution of different ion species in the imaging plane.

The experimental parameters were the same here as for the main OES results presented; 1 kV discharge, triggered by colliding laser plasmas by laser pulses with fluence = 0.9 J/cm^2. As with the OES the main lines observed are Al I, Al II and Al III, the ion species of each key line is labelled in the first image of the spectral run in Fig. 3.27. The spectra are also oriented in the same way as previously, with the cathode at the top of the image. As with the OES the discharge is noted to heat the plasma changing the most intense line emission in the inter-electrode gap from Al I and Al II to mostly Al III. For comparison a single colliding laser plasma spectral image is presented in Fig. 3.24. In the 0 V case the colliding laser plasmas have a very weakly emitting Al III portion, which gets slightly more intense at the time of collision. It is also apparent that the Al I portions of the plasma remain close to the targets as the more energetic Al II and Al III combine in the middle of the gap.

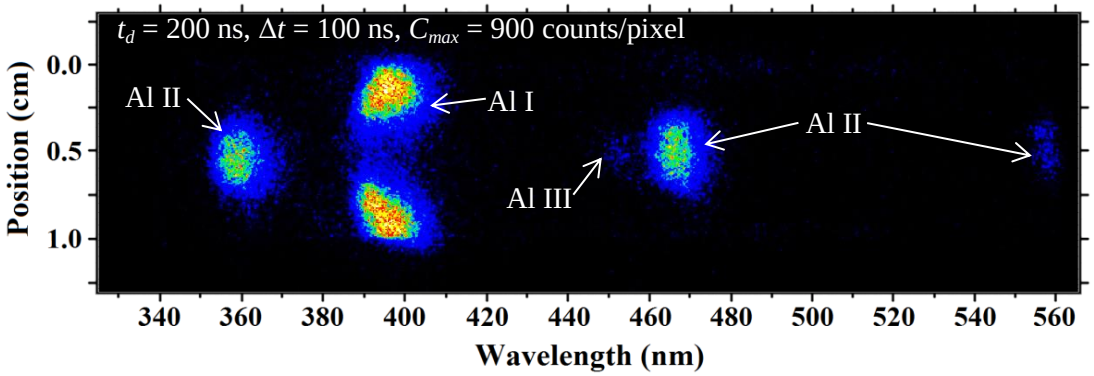

Fig. 3.24 – Spectral imaging of the colliding laser produced plasmas with no charging voltage.

Comparing Fig. 3.24 to Fig. 3.25 the collisional interaction of the two laser plasmas is clear, with a shift in emission from Al I to Al II and a much lower maximum counts per pixel.

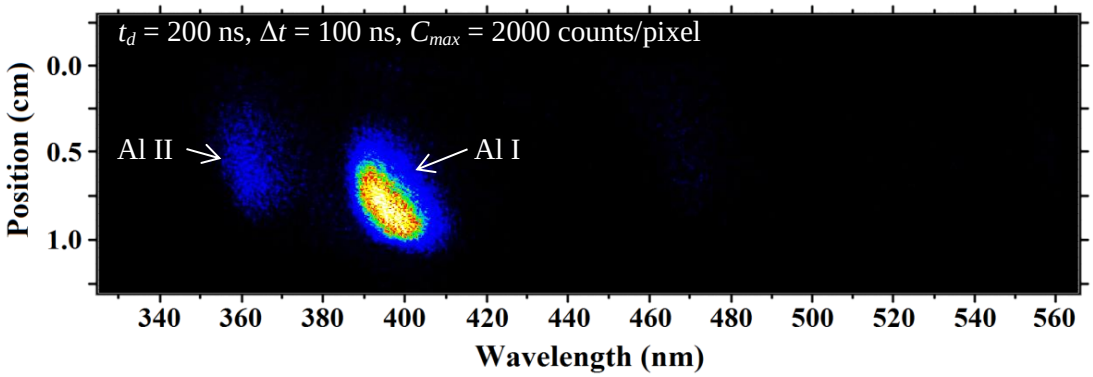

Fig. 3.25 – Spectral imaging of the colliding laser produced plasmas with no charging voltage.

In the single laser plasma triggered discharge the onset time is long enough after the laser pulse (>250 ns) for the plasma line emission to have become almost entirely Al I. After ignition the line emission is Al II and Al III, with emission at the counter electrode increasing in intensity. This was also observed with the OES. The image shown in Fig. 3.26 was for a single laser plasma ablated from the grounded electrode, at the bottom of the image.

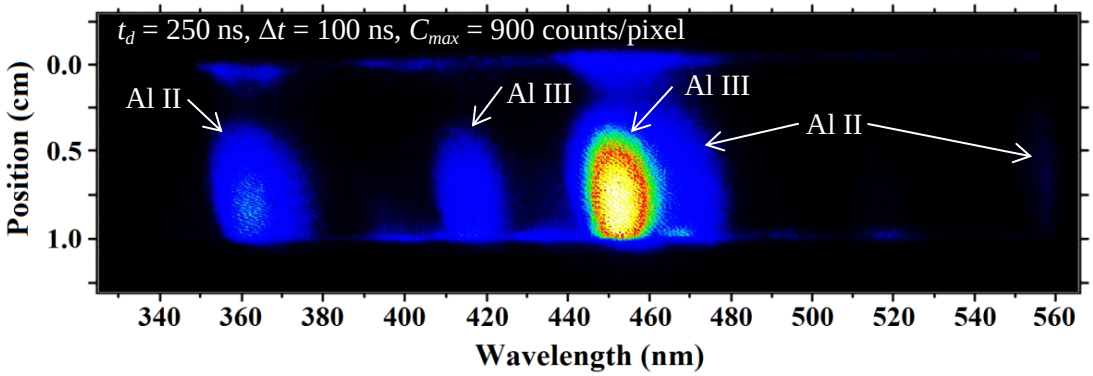

Fig. 3.26 – Spectral imaging of a 1 kV discharge triggered by a single laser plasma.

The emission in the single plasma triggered discharge quickly becomes very similar to those presented for the colliding laser plasma triggered case. The emission also follows the same trend of a strong pair of continua at the surface of each electrode. As they are largely the same, the full range is not presented.

On the following pages a series of the novel spectral images are presented. These show the dynamics of the colliding laser plasma triggered discharge charged to 1 kV. The series covers from the time of laser ablation at t_d = 0 ns up to t_d = 1.4 μs.

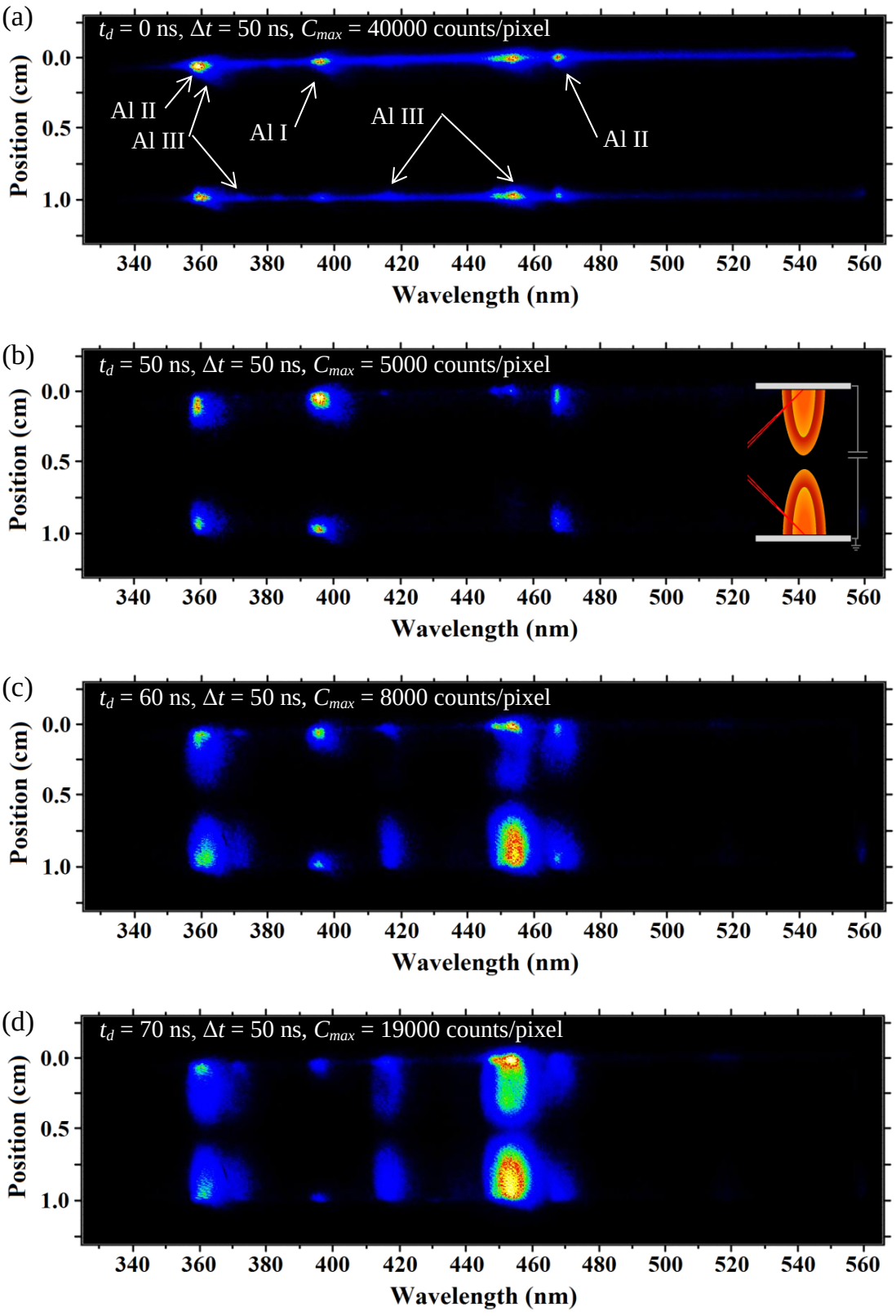

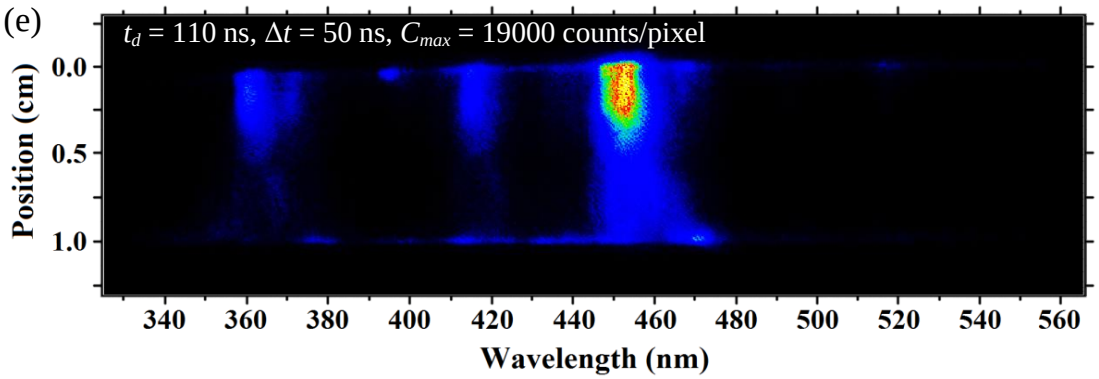
(e)
t_d = 110 ns, Δt = 50 ns, C_{max} = 19000 counts/pixel
Position (cm)
0.0
0.5
1.0
340 360 380 400 420 440 460 480 500 520 540 560
Wavelength (nm)

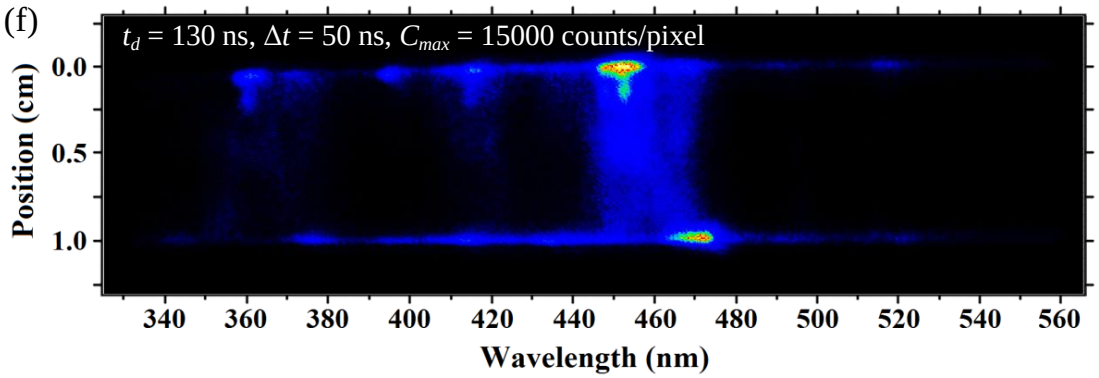
(f)
t_d = 130 ns, Δt = 50 ns, C_{max} = 15000 counts/pixel
Position (cm)
0.0
0.5
1.0
340 360 380 400 420 440 460 480 500 520 540 560
Wavelength (nm)

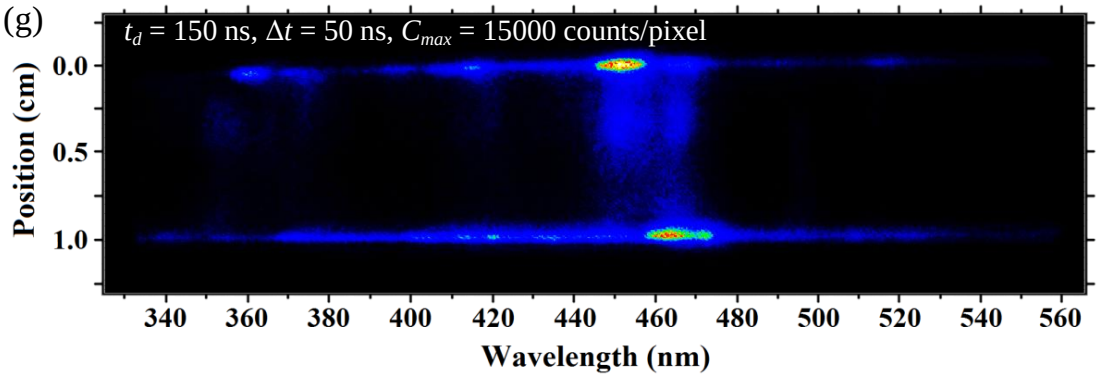
(g)
t_d = 150 ns, Δt = 50 ns, C_{max} = 15000 counts/pixel
Position (cm)
0.0
0.5
1.0
340 360 380 400 420 440 460 480 500 520 540 560
Wavelength (nm)

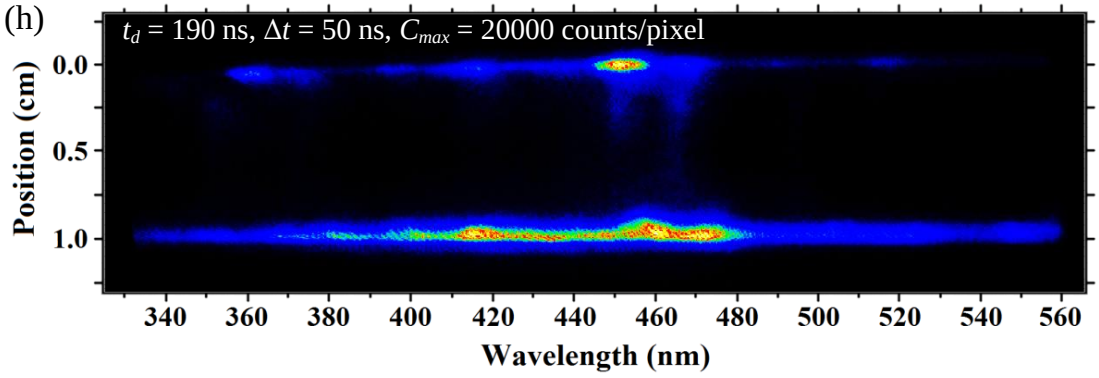
(h)
t_d = 190 ns, Δt = 50 ns, C_{max} = 20000 counts/pixel
Position (cm)
0.0
0.5
1.0
340 360 380 400 420 440 460 480 500 520 540 560
Wavelength (nm)

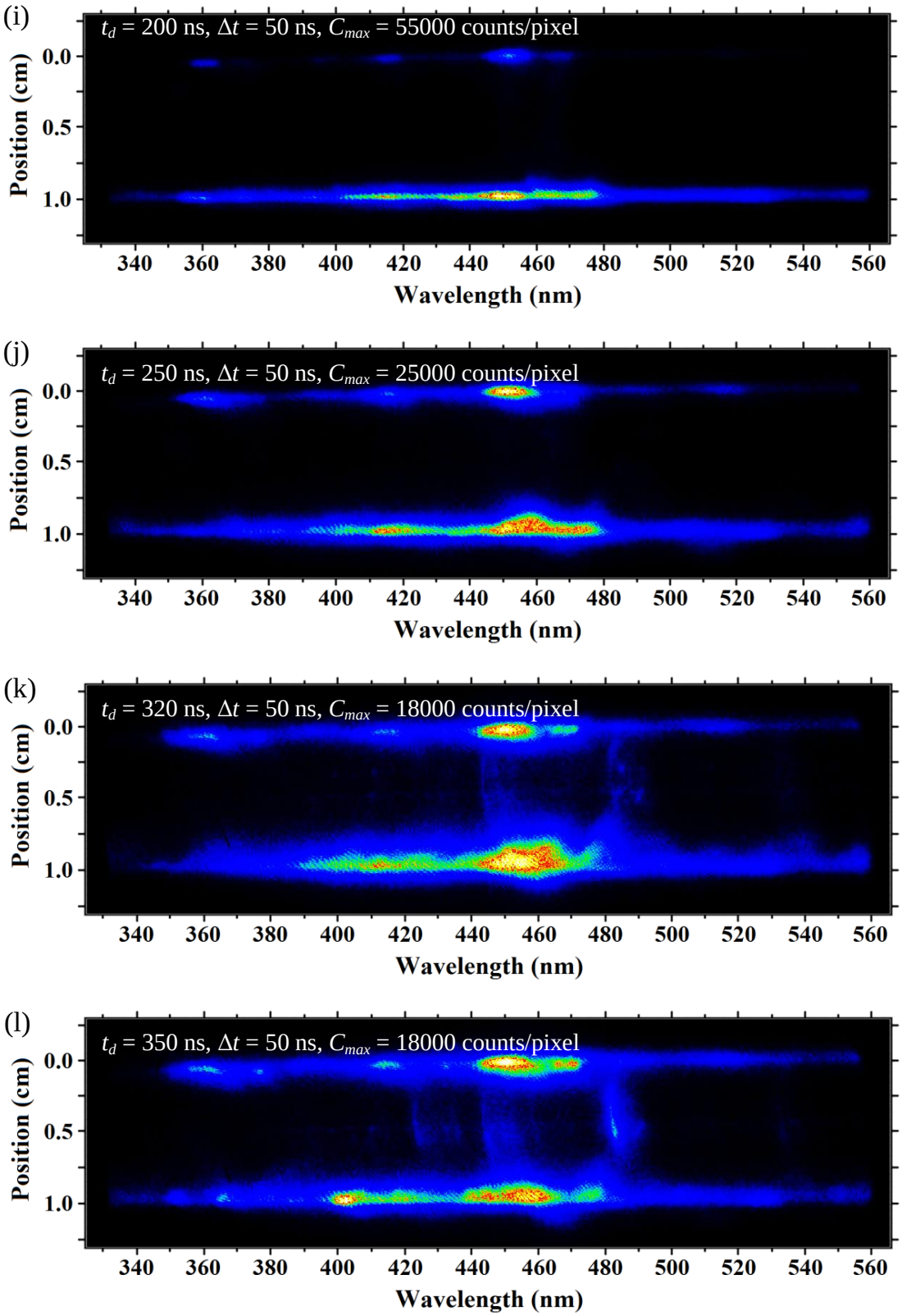
(i)
t_d = 200 ns, Δt = 50 ns, C_{max} = 55000 counts/pixel
(j)
t_d = 250 ns, Δt = 50 ns, C_{max} = 25000 counts/pixel
(k)
t_d = 320 ns, Δt = 50 ns, C_{max} = 18000 counts/pixel
(l)
t_d = 350 ns, Δt = 50 ns, C_{max} = 18000 counts/pixel
Position (cm)
0.0
0.5
1.0
340 360 380 400 420 440 460 480 500 520 540 560
Wavelength (nm)

(m)

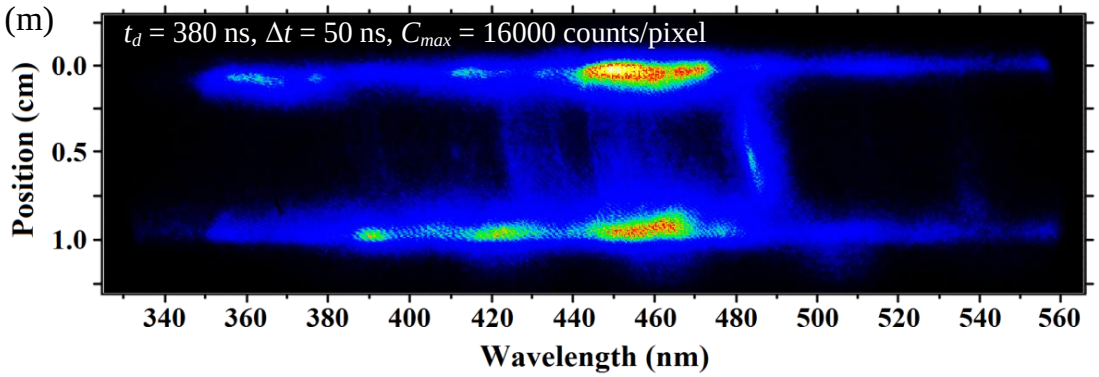
t_d = 380 ns, Δt = 50 ns, C_{max} = 16000 counts/pixel
Position (cm)
0.0
0.5
1.0
340 360 380 400 420 440 460 480 500 520 540 560
Wavelength (nm)

(n)

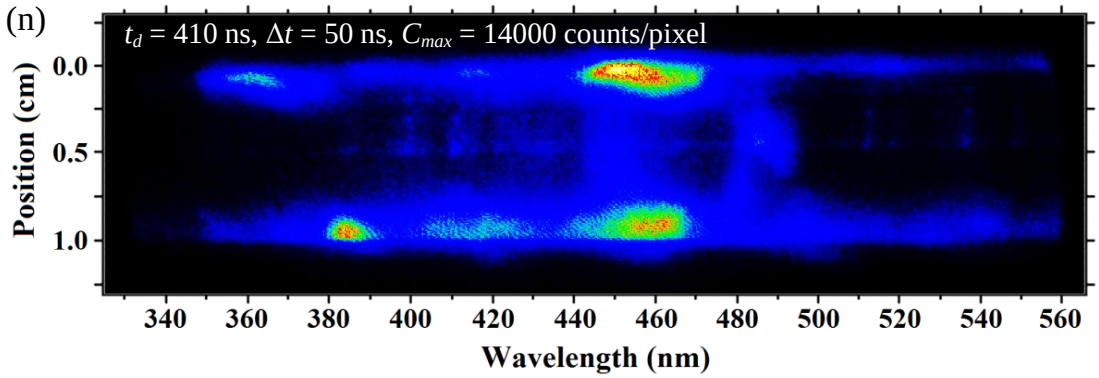
t_d = 410 ns, Δt = 50 ns, C_{max} = 14000 counts/pixel
Position (cm)
0.0
0.5
1.0
340 360 380 400 420 440 460 480 500 520 540 560
Wavelength (nm)

(o)

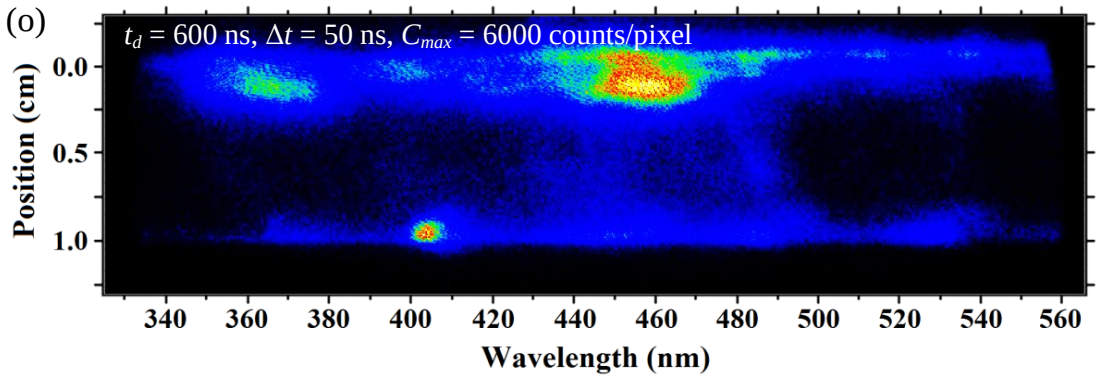
t_d = 600 ns, Δt = 50 ns, C_{max} = 6000 counts/pixel
Position (cm)
0.0
0.5
1.0
340 360 380 400 420 440 460 480 500 520 540 560
Wavelength (nm)

(p)

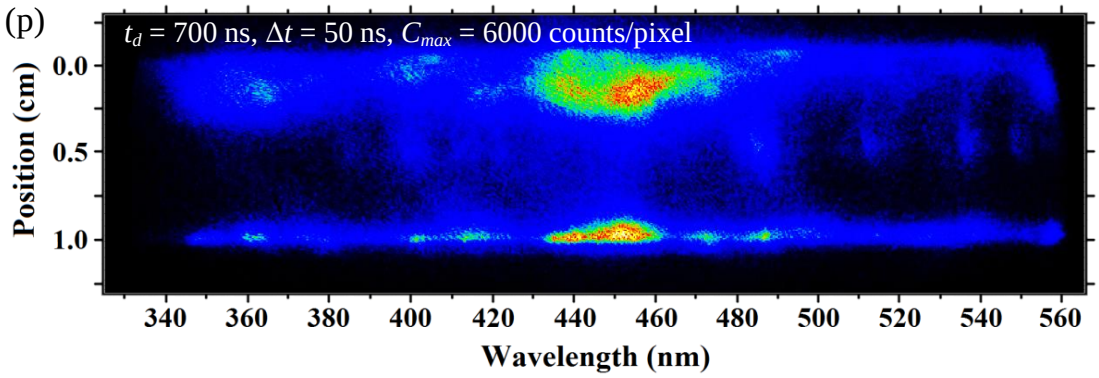
t_d = 700 ns, Δt = 50 ns, C_{max} = 6000 counts/pixel
Position (cm)
0.0
0.5
1.0
340 360 380 400 420 440 460 480 500 520 540 560
Wavelength (nm)

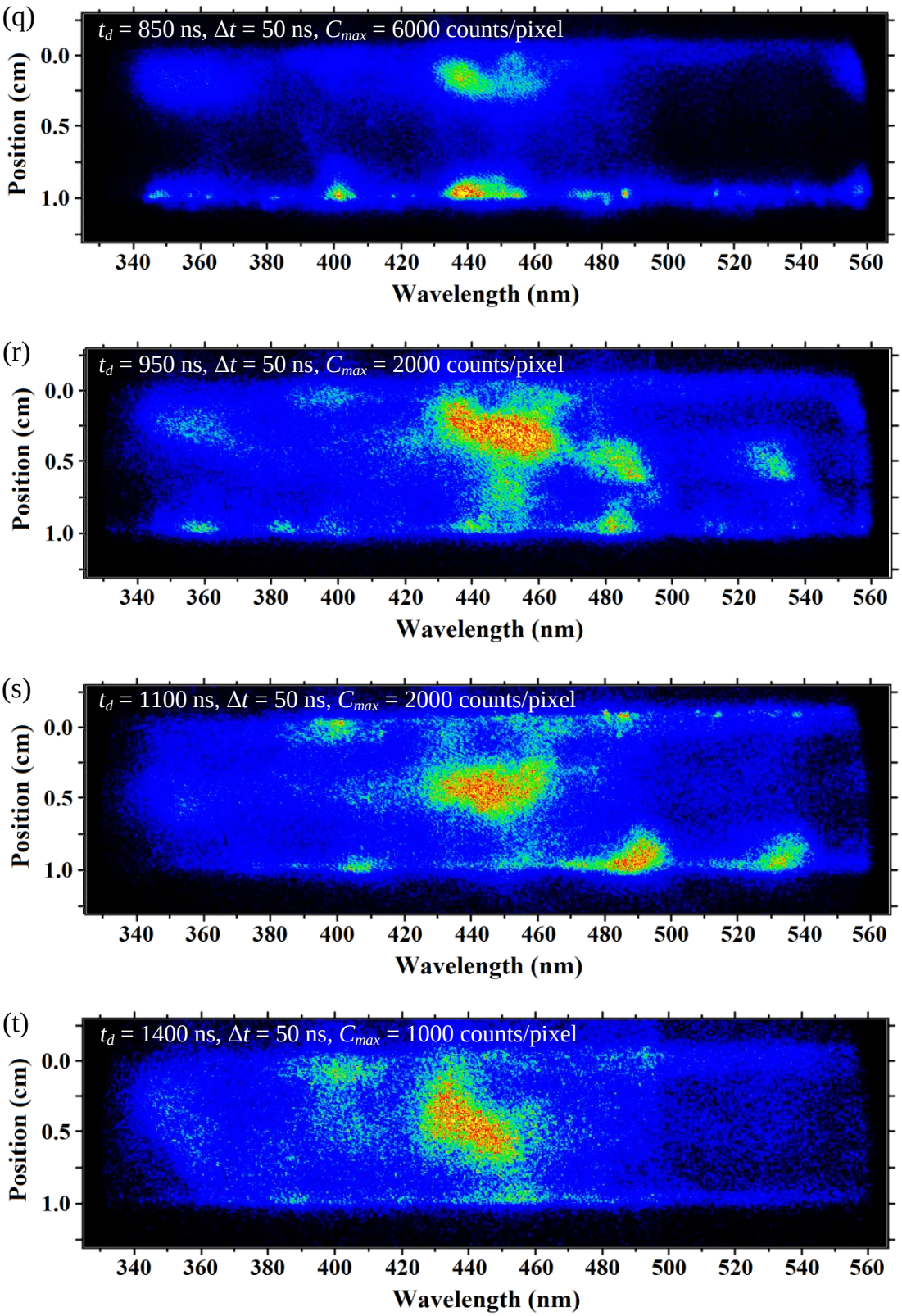

Fig. 3.27 – (a) – (t) Novel spectral imaging of the colliding laser plasma triggered discharge with a charging voltage of 1 kV (0.94 J).

This series of spectral images show similar features to the optical emission spectra of a colliding laser produced plasma triggered 1 kV discharge presented earlier. The advantage of these images is the additional width information of the features observed. For example the very narrow filament like feature observed in Fig. 3.27 (l) and (m). If compared to features at later times this appears very constricted suggesting a compression. The ion species for this wavelength has not been identified.

The plasma is observed to begin accumulating on the counter electrode at approximately 150 ns after the laser pulse. The emission rapidly decays from the Al III and Al II lines with only the Al I lines observed at late times (Fig. 3.28).

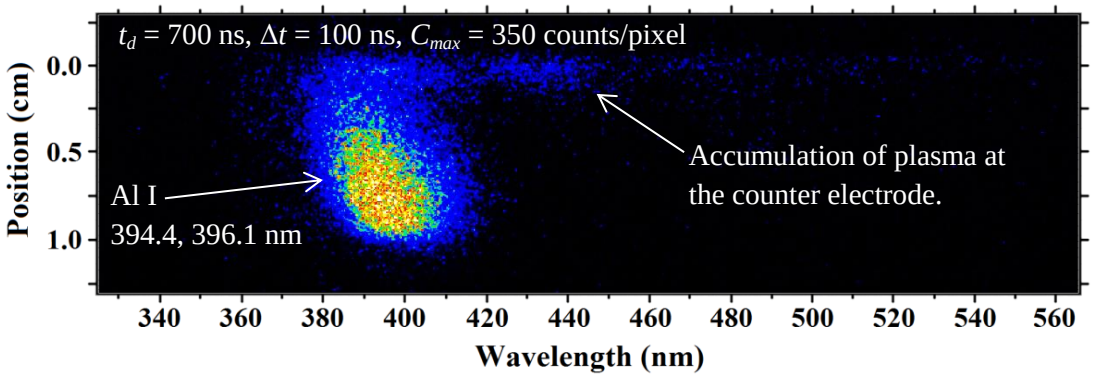

Fig. 3.28 – Spectral imaging of a single laser plasma in the inter-electrode gap at late time with no discharge. The plasma is observed to accumulate on the counter electrode.

This can be compared to the colliding plasma case at the same delay time, here the plasma has roughly equal counts/pixel but a different spatial distribution with a seemingly dark central region, suggesting the plasmas are separating at this time.

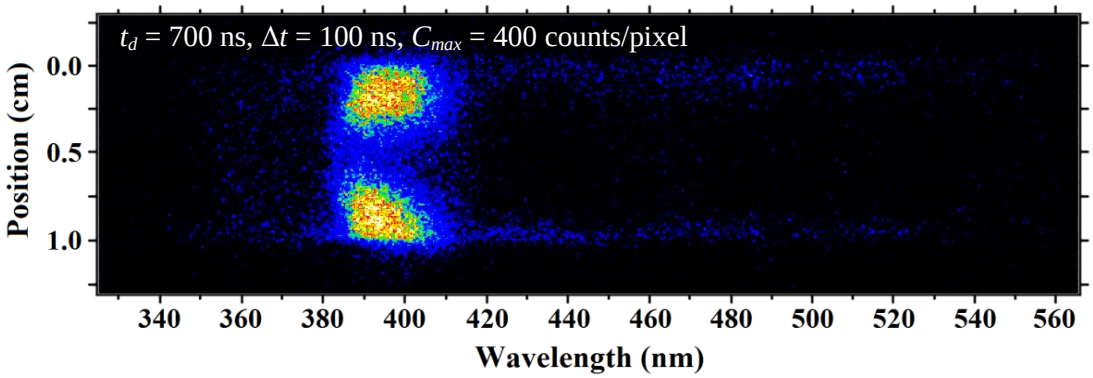

Fig. 3.29 – Spectral imaging of colliding laser plasmas with no discharge at the same delay as Fig. 3.28.

3.4 Chapter discussion

In this experiment the effect of igniting a fast Z-pinch discharge with colliding laser produced plasmas was investigated. The ion fluence was studied perpendicular to the discharge axis. The total ion fluence increased by a factor of 6 with a 1 kV discharge. The kinetic energy of the ion peak also increased from 800 eV with no discharge to 3.65 keV for 1 kV. The profile of the laser produced plasma was investigated using a translational ion probe, the angular distribution was fit with a k value of 2.0.

It is desirable to generate the pinch at the max of current, this allows the most efficient coupling of electrical energy to the pinched plasma. The two parameters controlling the time to pinch are the magnetic pressure and the plasma pressure. The simplest method therefore to adjust the pinch time to the peak of current is changing the plasma load, by varying the laser energy. It is apparent in Fig. 3.7 that in the case of both trigger cases the pinch occurs before the current maximum. This indicates that more material is necessary to yield an efficient pinch. The colliding plasma triggered case had a pinch event closer to the current maximum along with a greater rate of rise of current.

The visible emission from the plasma was studied in the range 340 – 560 nm with a spectral resolution of roughly 1 nm. The spectra were spatially and temporally resolved with a spatial resolution of approximately 0.7 mm, and a minimum temporal gate time of 20 ns. These spectra were used to estimate the plasma temperature and density, showing an initial laser plasma with Te ~3 eV, Ne ~1×10^{18} cm^{-3}. The discharge parameters were varied, both the triggering mechanism and the charging voltage. For the main study presented of the colliding laser produced plasma triggered discharge, with a charging voltage of 1 kV, plasma heating was noted with an estimated electron temperature of 4.50 ± 0.55 eV and density of $(8.0 \pm 1.5) \times 10^{18}$ cm^{-3} at the peak of discharge current. The presence of several strong Al III and Al V lines suggest a higher temperature plasma. Possible a study of the Al V EUV lines in the 10 – 14 nm range from $2p^5$-3s transitions, as a follow up experiment could also be utilised to verify this assertion.

Chapter 4.

Laser Assisted Vacuum Arc lamp

Presented in this chapter are the results of the Laser Assisted Vacuum Arc lamp (LAVA-lamp) experiments comparing the ion fluence, extreme ultraviolet (EUV), and visible emission characteristics of tin and galinstan as source materials. Galinstan is a eutectic metal alloy composed of gallium, indium and tin (atomic %: Ga: 78.35, In: 14.93, Sn: 6.72). Galinstan has not previously been studied as an EUV source material in a laser assisted discharge plasma (LDP) source. Current state-of-the-art LDP sources utilise liquid metal coatings to overcome the problem of electrode erosion, which is typically a large source of down time and increase in cost-of-ownership in discharge sources, which makes them less suitable for industrial applications. In current LDP sources tin is maintained above its melting temperature of 232 °C to coat the electrodes. Galinstan is liquid at room temperature, with a melting point of -19 °C, therefore there is no need to heat the source material, somewhat simplifying the source design. Discharge sources have the potential to provide higher “wall-plug” efficiency than laser produced plasma sources[29].

4.1 Chapter introduction

4.1.1 LAVA-lamp EUV source

The LAVA-lamp Z-pinch EUV source is based on a laser-triggered discharge struck between two rotating disc electrodes, which are coated in liquid metal by partial immersion in liquid metal baths. The source was developed at the Russian Institute of Spectroscopy (ISAN)[104] and is currently housed in SpecLab, University College Dublin. The disc electrodes are tilted so that the separation at closest approach is 4 mm. For galinstan, the metal baths are maintained at ambient temperature, while for tin they are heated to 300 °C. The anode is grounded to the chamber while the cathode is connected to the live electrode of a 0.39 µF capacitor bank. The charging voltage was varied from 2.5 to 5.5 kV (1.25 to 6.05 J). The discharge is triggered using a Nd:YAG laser pulse to form a LPP on the cathode electrode at the point of closest approach to the anode. The LPP expands into the vacuum away from the cathode and triggers the discharge when it reaches the anode. This geometry of LDP source had been studied previously with tin as source material[104], [105]. The major focus of the previous studies using LAVA-lamp was on debris characterisation, with the aim of debris mitigation in industrial LDP sources. Research has also been conducted on alternate geometries of discharge based extreme ultraviolet (EUV) light sources[11], [26], [31], [44].

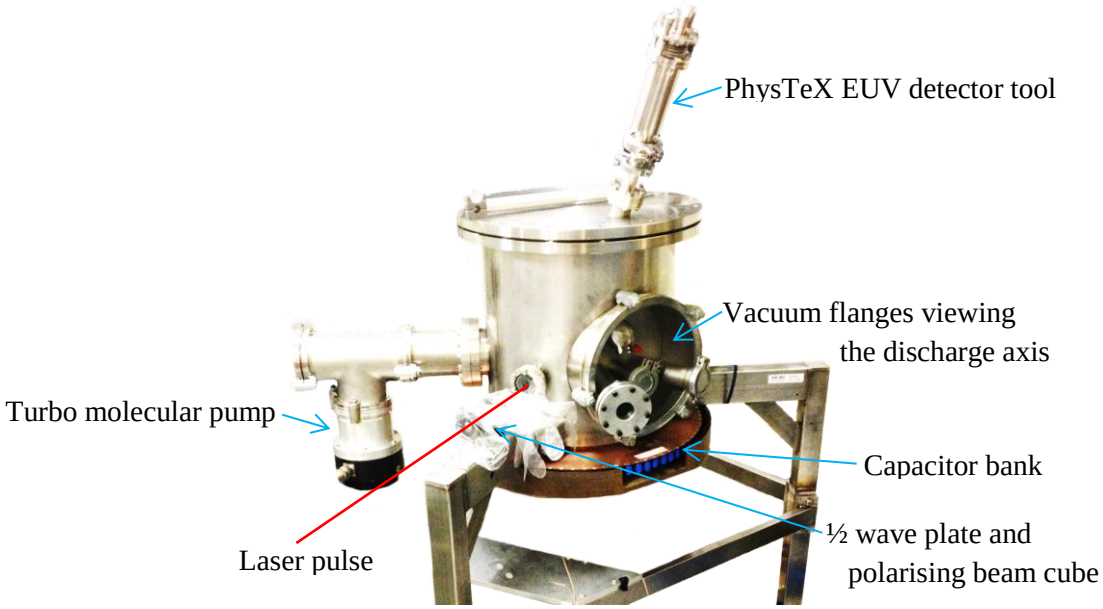

Fig. 4.1 – Laser Assisted Vacuum Arc lamp photographed with PhysTeX EUV detector deployed.

4.1.2 Diagnostic tools

In these experiments the discharge current profile was monitored using a Rogowski coil placed in the vicinity of the current path between the capacitor and the cathode. A planar Langmuir ion probe was used to characterise the laser produced plasma, which triggered the discharge. A Faraday cup ion detector was also deployed to monitor the plasma outflow from the discharge. The visible emission from the source was analysed by time- and space-resolved spectroscopic imaging of the inter-electrode gap before and throughout the discharge. The spatial, spectral, and temporal characteristics of the EUV emission were measured. A full description of the tools used is given in Section 2.5. All of these tools were used for experiments with various different discharge energies. In Fig. 4.2 the positioning of each of the diagnostic tools is shown.

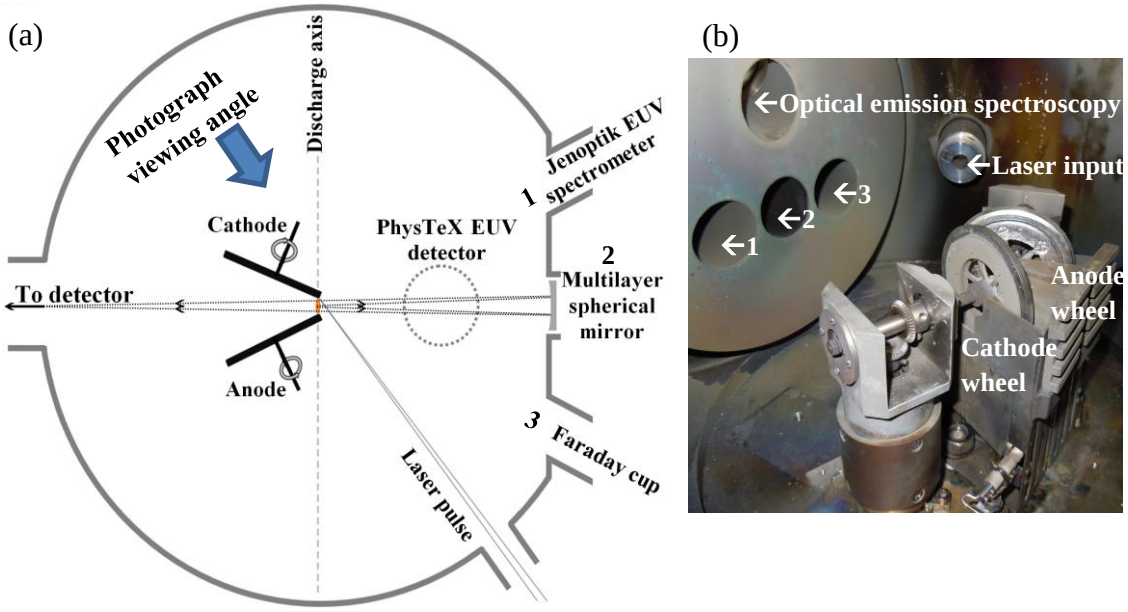

Fig. 4.2 – (a) Schematic diagram of LAVA-lamp and (b) photograph taken inside the chamber, displaying the positioning of each of the diagnostic tools in relation to the electrode wheels.

4.2 Laser ablation

4.2.1 Laser ablation of the liquid metal coating

The Nd:YAG laser system, used in the experiments on the LAVA-lamp, was operated at a wavelength of 1064 nm with a maximum repetition rate of 10 Hz. The laser pulse was measured at the exit of the laser using a laser power meter and a fast photodiode with 1 ns rise-time. An power of ~160 mW was recorded at 2 Hz (~80 mJ/shot) in a 30 ns full-width half-max pulse (Fig. 4.3).

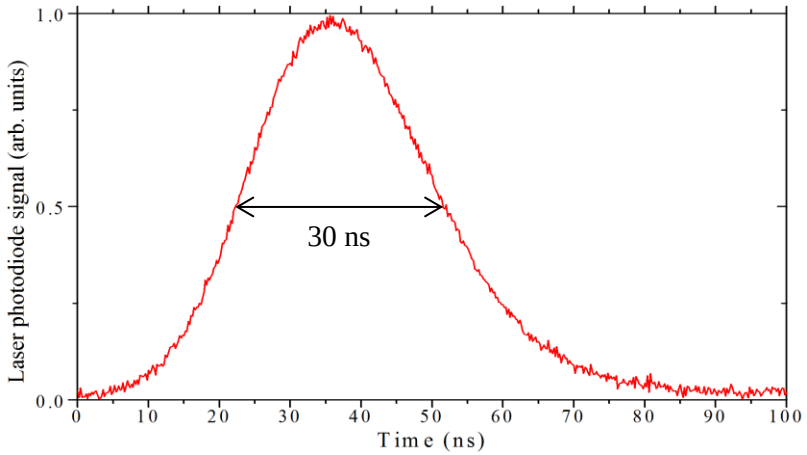

Fig. 4.3 – Laser pulse temporal profile measured by a fast photodiode with rise-time of 1 ns, showing a full-width at half-max of 30 ns.

The laser energy was attenuated using a combination of a rotatable half-wave plate and a polarising beam splitter cube, which enabled fine energy adjustment between ~5 – 55 mJ (Fig. 4.4). The portion of the laser beam transmitted through the beam-splitting cube was focused using a 30 cm focal length, plano-convex lens positioned at 30 cm from the cathode wheel target.

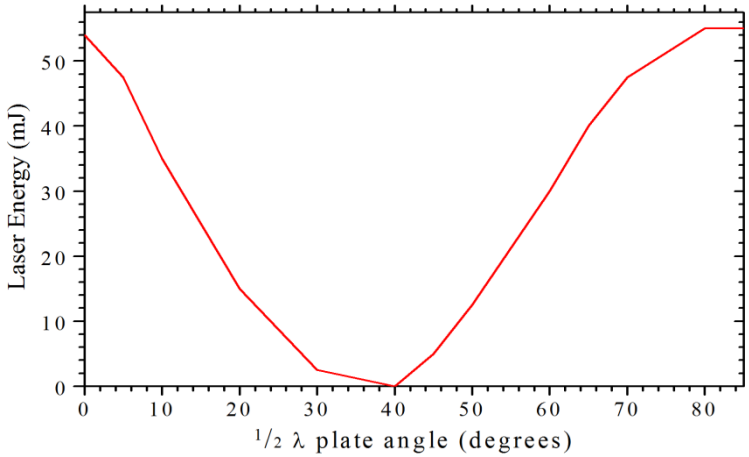

Fig. 4.4 – Laser energy measured inside vacuum chamber roughly 5 cm after the focusing lens. The laser energy was controlled by the half-wave plate angle and polarising beam splitter giving a range from 0 mJ to ~53 mJ.

The focused beam was incident on the cathode at the point of closest approach of the two electrode wheels, and thus minimise the path length for the discharge current. A time integrated photograph is shown in Fig. 4.5 of a laser ablation plasma on the cathode wheel along with an illustration of the elements in the photo.

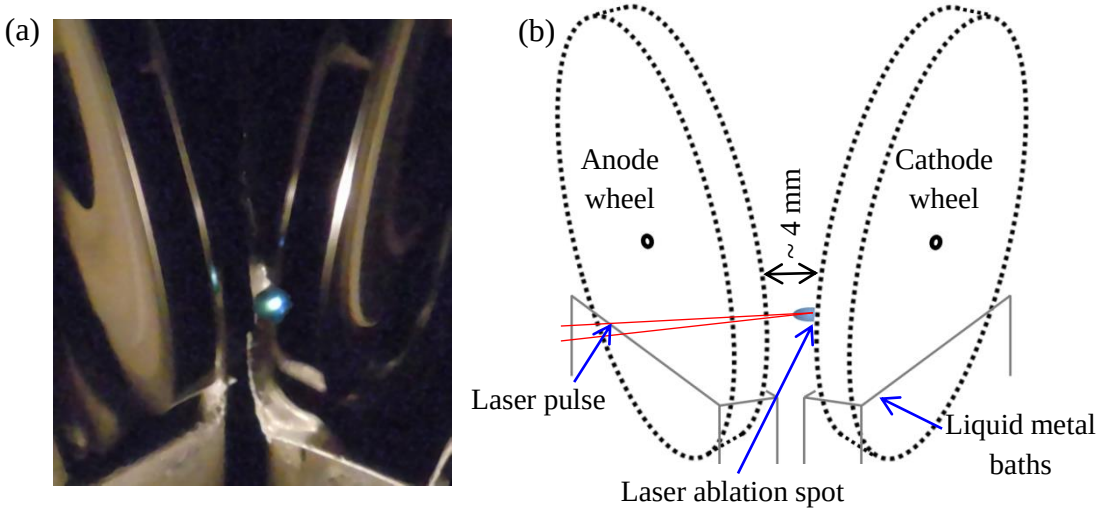

Fig. 4.5 – (a) Time integrated photograph of laser ablation plasma on cathode wheel, showing both electrode wheels in liquid metal baths and (b) schematic diagram illustrating the key elements of the photograph.

Initially the unfocused beam was found to be not quite circular. The rear mirror of the laser was adjusted to maximise the output energy using the fine adjustment tilt screws; this yielded the best beam quality also. Using a Coherent BeamView-USB LaserCam-HR, 1.3 megapixel, CMOS camera with a series of neutral density filters (to decrease the laser pulse fluence to well below the damage threshold of the sensor) the

unfocused laser beam profile was recorded (Fig. 4.6). The optimised beam spot was roughly Gaussian although slightly elliptical.

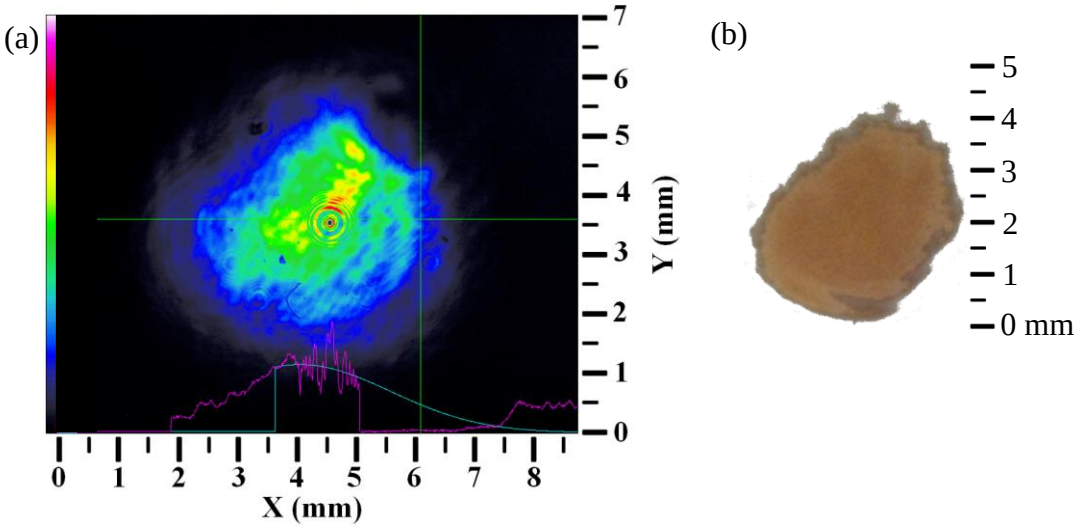

Fig. 4.6 – (a) BeamView USB camera image of unfocused laser beam, the ripple effects are artefacts caused by the series of neutral density filters used to attenuate some of the light reaching the detector to avoid saturating the camera sensor. (b) Burn pattern of the unfocused laser beam on photographic paper at the same position as the BeamView camera.

The fluence of the focused laser beam was too large to use the BeamView camera with the neutral density filters available. To measure the focused beam profile dimensions a set of ablation craters were made at the position of the cathode wheel. Burn paper spots were also taken on photographic paper at this position. The laser was incident at 30° from normal on the target surface, and the beam spot was elongated in the horizontal by approximately 1.15 times. The burn patterns from the focused laser beam (Fig. 4.7) were measured as ~650 µm × 450 µm for the 12 mJ laser pulse and ~1150 µm × 800 µm for the 55 mJ laser pulse. The area from these burn patterns are therefore ~2.3 $\times 10^{-3}$ cm^{-2} and ~7.2 $\times 10^{-3}$ cm^{-2} respectively. The size of the burn was due to the change in energy, this occurs because the threshold for burning is greater than the wings of the Gaussian laser beam.

If the spatial distribution of the laser beam is approximated as an elliptical Gaussian, the fluence can be written as:

$$F = F_p \, e^{-2\left(\frac{x}{W_{0,X}}\right)^2} \, e^{-2\left(\frac{y}{W_{0,Y}}\right)^2} \qquad \text{Eqn. 4.1}$$

where F_p is the peak fluence, and W_0 the $1/e^2$ beam waist of the elliptical beam spot in X or Y (i.e. 86.5% of the peak fluence at the centre of the beam).

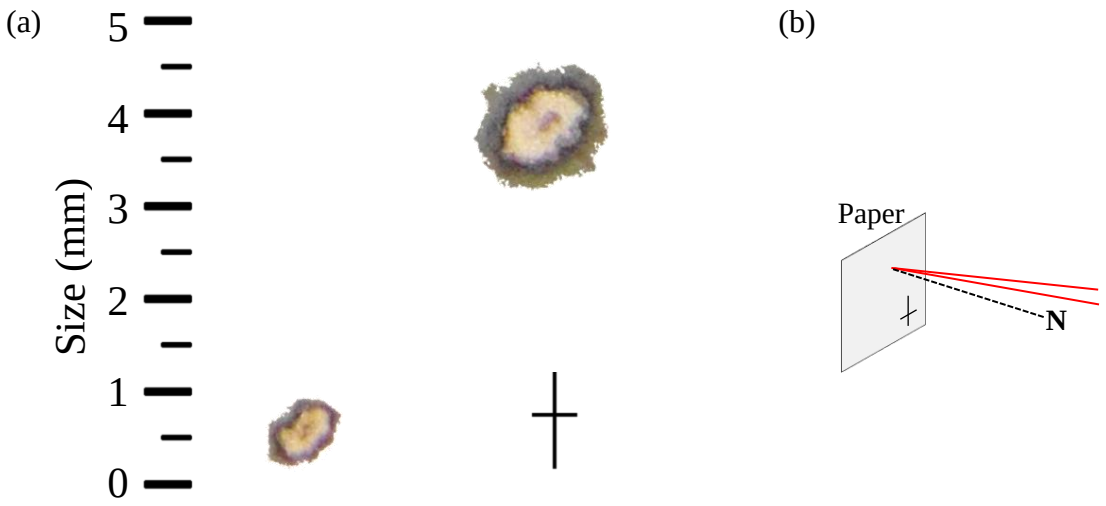

Fig. 4.7 – Burn pattern of the focused laser beam at the cathode position on photographic paper. The upper burn was made by a laser pulse with an energy of 55 mJ while the lower was 12 mJ. The cross-hairs is included to illustrate the orientation of the photographic paper with respect to the laser, incident at 30° to the normal **N**.

The peak fluence of a Gaussian beam is given by[106]:

$$F_p = \frac{2\,E_l}{\pi\, W_{0,X} W_{0,Y}} \qquad \text{Eqn. 4.2}$$

where E_l is the energy of the laser pulse.

To obtain the beam waist parameters $W_{0,X}$ and $W_{0,Y}$ the dimensions of the burn profile for the two laser energies are written as x_{th} and y_{th} following the method of J. M. Liu[106]. Solving Eqn. 4.1 for (x_{th},0) and for (0,y_{th}) we can write:

$$x_{th} = \sqrt{\tfrac{1}{2}\left(W_{0,X}\right)^2 ln\left(E/E_{th}\right)} \qquad \text{Eqn. 4.3}$$

Writing this in terms of the diameter X_{th} $(X_{th} = 2x_{th})$

$$(2x_{th})^2 = 2\left(W_{0,X}\right)^2 (ln(E) - ln(E_{th})) \qquad \text{Eqn. 4.4}$$

Therefore a plot of the threshold diameter squared $(2x_{th})^2$ versus the natural log of the laser energy $(ln(E))$ will yield a slope of $2\left(W_{0,X}\right)^2$ and an intercept of $ln(E_{th})$. The same process can be followed to obtain a value for $W_{0,Y}$.

Using the two burn spots, made for two laser energies at focus, we will characterise the laser beam. The information presented in Table 4.1 and a plot is made for both the X and Y dimensions of the laser beam spot.

Table 4.1 – Laser burn spot diameters and pulse energy taken from the burns in Fig. 4.7

E_l (mJ)	$\ln(E_l)$	X_{th} (µm)	X_{th}^2 (10^5 µm^2)	Y_{th} (µm)	Y_{th}^2 (10^5 µm^2)
12	2.4849	650	4.225	450	2.025
55	4.0073	1150	13.225	800	6.4

Plotting the threshold beam diameter squared versus the natural log of laser pulse energy:

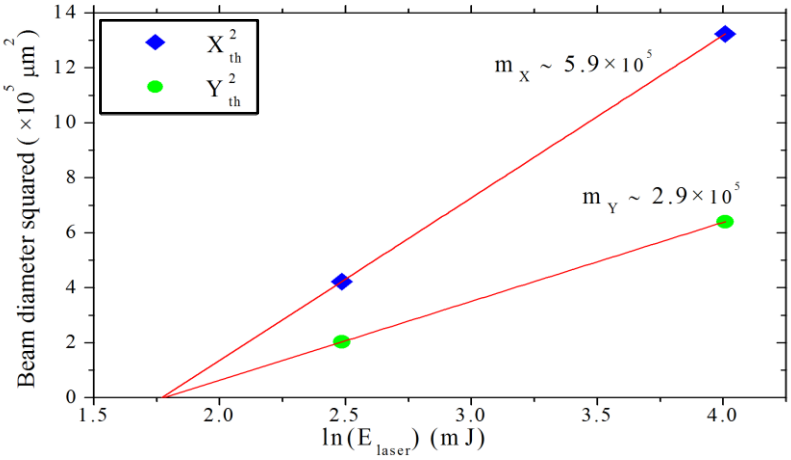

Fig. 4.8 – Plot of threshold beam diameter squared versus natural log of laser energy for X and Y. The slope of each line, m_X and m_Y, are equal $2(W_{0,X})^2$ and $2(W_{0,Y})^2$ respectively. Only two data points were collected, however some confidence is gained by the intersection on the x axis.

The slope of each line from Fig. 4.8 is then:

$m_X \sim 5.91 \times 10^5$ $\quad\therefore 2(W_{0,X}) \sim \sqrt{5.91 \times 10^5} \sim 770$ µm

$m_Y \sim 2.87 \times 10^5$ $\quad\therefore 2(W_{0,Y}) \sim \sqrt{2.87 \times 10^5} \sim 540$ µm

The beam waists of the Gaussian laser pulse are therefore 770 µm and 540 µm, and so from Eqn. 4.2 the peak fluence F_p can be calculated for a set energy. For example for the 12 mJ laser pulse energy used during the tin experiments the peak and average fluences are 7.4 J cm^{-2} and 3.7 J cm^{-2}. While for the 5 mJ laser pulse used in the galinstan experiments the peak and average fluences are 3.0 J cm^{-2} and 1.5 J cm^{-2}.

From the graph it is also possible to find the value of E_{th} from the intercept. The intercept of both lines was found to be the same. The threshold for damage E_{th} was therefore found to be 5.9 mJ.

Tin is a relatively low melting point metal which can cause issues in making an accurate measure of the beam spot via ablation crater, as large recast melt walls may be created. For ablation crater analysis the cathode wheel was replaced by a polished tin target and craters were made of 10, 20, and 50 shots. The ablation craters were then studied using a DEKTAK depth profilometer. The crater made with 10 shots was measured as approximately 580 µm × 380 µm in diameter (Fig. 4.9); with high recast walls on either side of the crater with an ablation depth of ~10 µm.

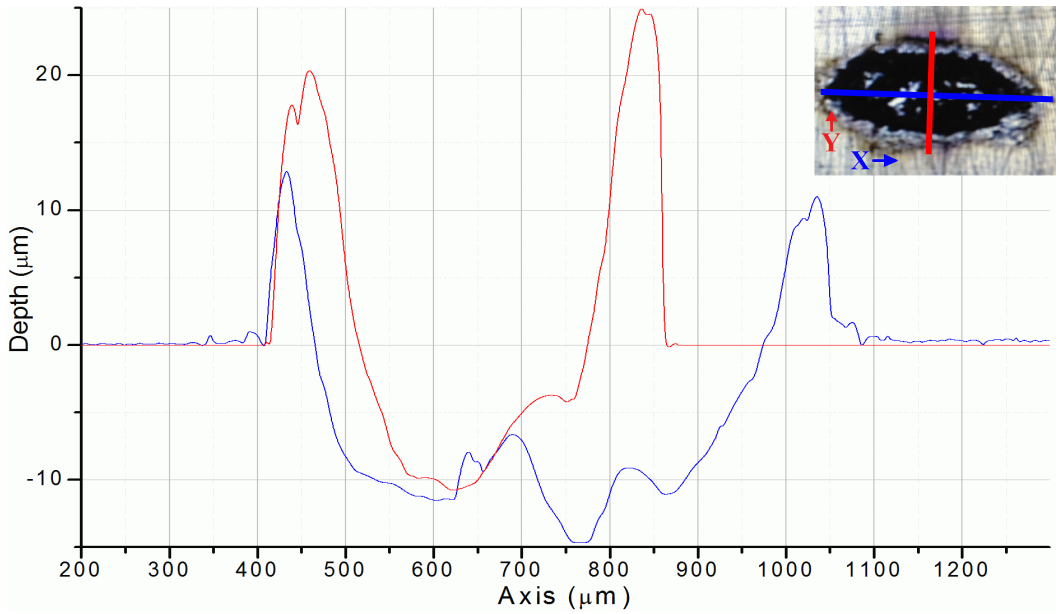

Fig. 4.9 – The resulting crater profile recorded by the DEKTAK along the X and Y direction. An inset photograph of the ablation crater recorded by the DEKTAK camera is shown.

The volume of the semi-ellipsoid ablated by the 10 laser pulses is:

$$V = \frac{4}{6}\pi\, r_X\, r_Y\, d = \frac{4}{6}\pi\,(0.013 \times 0.0255 \times 0.001) = 1.4 \times 10^{-6}\text{cm}^3;$$

where r_X and r_Y are the radius of the beam spot in X and Y. From this, therefore ~1.4 ×10^{-7} cm^3 is ablated per laser pulse, from this we can calculate the amount of material and number of atoms ablated per pulse from the Sn target.

The mass ablated from the crater is given by:

$$m = \rho \times V = (7.365\ ) \times (1.4 \times 10^{-6}) = 10.3 \times 10^{-6}\ \text{g} \qquad \text{Eqn. 4.5}$$

where the density (ρ) of solid tin is 7.365 g cm^{-3}. This value is for 10 laser shots, therefore the mass ablated per shot m_V~1 µg.

The number of atoms ablated per shot is given by:

$$N_{atom} = \rho \div m \qquad \text{Eqn. 4.6}$$

Therefore the number of atoms ablated per shot is ~5 ×10^{15}.

In Fig. 4.9 it is clear that substantial melt walls are present on the ablation crater, the amount of material in these walls is hard to quantify, but is clearly large. This casts considerable doubt on the measure of the ablated material.

In this section we have looked at the laser beam profile using various methods, the information gained is useful in characterising the laser plasma initial conditions which in turn allow us infer details about the plasma at the time of discharge ignition.

4.2.2 Ion probe measurement of the laser produced plasma

In this study, two ion probes were used to measure the ion fluence of the laser produced plasma. To measure the ion plume shape and distribution, a translational planar Langmuir ion probe was placed 8.6 cm from the target. The plane perpendicular to the target normal was scanned as shown in Fig. 4.10. For these measurements it was necessary to remove the anode wheel, which was directly in the path of the plume. In addition to using the Langmuir probe, a Faraday cup was positioned at three angles (giving slightly different distances) facing the electrode wheels and inter-electrode gap. These three angles are with respect to the chamber centre line denoted **C** in Fig. 4.10, and were 30°, 0°, and -30°. The plasma forward direction was along the normal line **N**, perpendicular to the centre line **C**. Both probes were used with the same bias (-25.0 V) and load resistor (100 Ω) with effective surface areas of 0.103 cm^2 and 0.0570 cm^2 for the Langmuir probe and Faraday cup respectively.

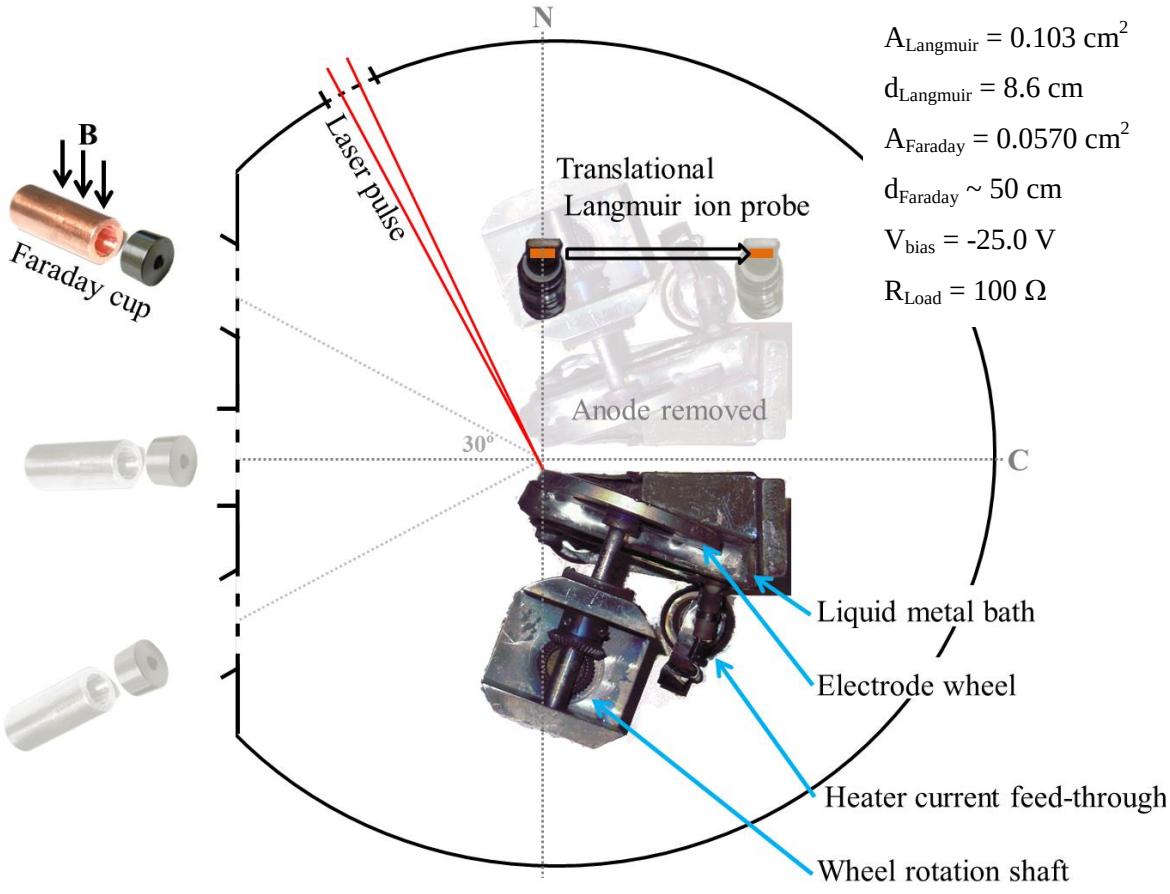

Fig. 4.10 – Configuration of ion probes used to measure the ablation plume expansion.

The Langmuir ion probe was translated from a position normal to the plasma forward direction up to 45° off normal (a maximum translated distance of 8.6 cm). Ion time-of-flight signals for a range of angles are shown in Fig. 4.11, with the laser photopeak at time zero, for a sample of the angles.

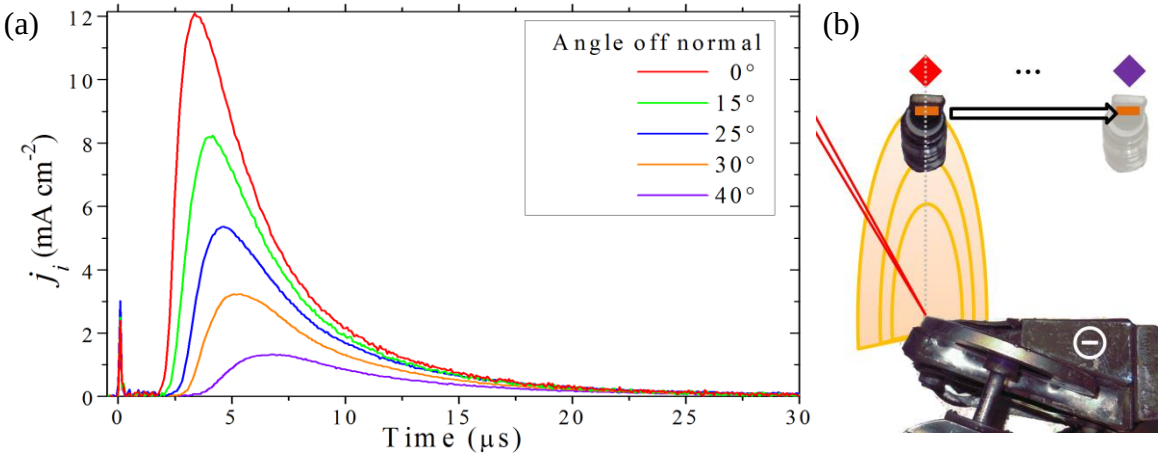

Fig. 4.11 – Ion current density signals measured at different angles with respect to the plasma forward expansion axis with a strong laser photopeak at t = 0 μs.

The probe was linearly translated across a plane perpendicular to the plasma forward expansion axis, illustrated by a grey dotted line in Fig. 4.11 (b). The distance travelled by the probe from the normal was ~ -0.8 – 7.2 cm, giving an angular measure of ~ -5.5° up to 40°.

The ion current density $j_i(t)$ drawn from the bias capacitor by the ion current onto the Langmuir ion probe with area A_p is given by:

$$j_i(t) = \frac{V_i(t)}{A_p\, R_L} \qquad \text{Eqn. 4.7}$$

where $V_i(t)$ is the voltage measured across the load resistor R_L.

The ion current density can also be written in terms of the ion number density n_i at probe position z_p with respect to time t:

$$j_i(t) = n_i(z_p, t) v_i\, e \qquad \text{Eqn. 4.8}$$

Eqn. 4.8 assuming the plasma consists of singly ionised species. This is reasonable as we expect the laser plasma to be dominated by singly ionised or neutral species for this laser energy.

Rearranging Eqn. 4.8:

$$n_i(z_p, t) = \frac{j_i(t)}{v_i\, e} \qquad \text{Eqn. 4.9}$$

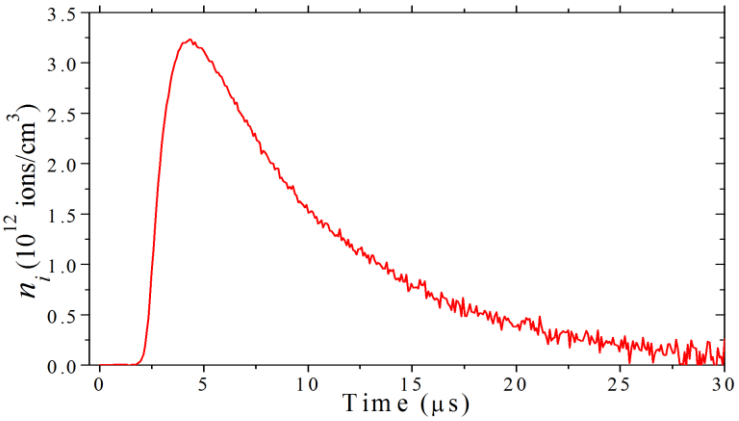

Fig. 4.12 – Ion number density from ion current calculated by probe normal to the plasma expansion.

The ion energy distribution of the plasma plume can be calculated from the measured ion current temporal profiles:

$$F_i = \frac{1}{e}\int j_i(t)\, dt = \int \frac{dN}{dE}\, dE \qquad \text{Eqn. 4.10}$$

$$\frac{dN}{dE}\, dE = \frac{dN}{dE}\,\frac{dE}{dt} dt \qquad \text{Eqn. 4.11}$$

By substituting $E = \frac{1}{2} m\, {v_i}^2$, where $v_i = \frac{z_p}{t}$, into Eqn. 4.11 we can write the ion energy distribution as:

$$\frac{dN}{dE} = \frac{j_i(t)\, t^3}{e\, m\, {z_p}^2} \qquad \text{Eqn. 4.12}$$

The ion velocity distribution of the plasma plume can similarly be calculated from:

$$F_i = \frac{1}{e}\int j_i(t)\, dt = \int \frac{dN}{dv}\, dv \qquad \text{Eqn. 4.13}$$

$$\frac{dN}{dv}\, dv = \frac{dN}{dv}\,\frac{dv}{dt} dt \qquad \text{Eqn. 4.14}$$

Substituting $v = z_p/t$ into Eqn. 4.14 gives:

$$\frac{dN}{dv} = \frac{j_i(t)\, t^2}{e\, z_p} \qquad \text{Eqn. 4.15}$$

Plotting the ion energy distribution, $\frac{dN}{dE}$ versus E, (Fig. 4.13 (a)) gives the probable ion energy as ~25 eV from the laser plasma plume measured normal to the target by the planer Langmuir ion probe. Similarly the ion velocity distribution (Fig. 4.13 (b)) shows a probable ion velocity of ~1.25 ×10^4 m/s.

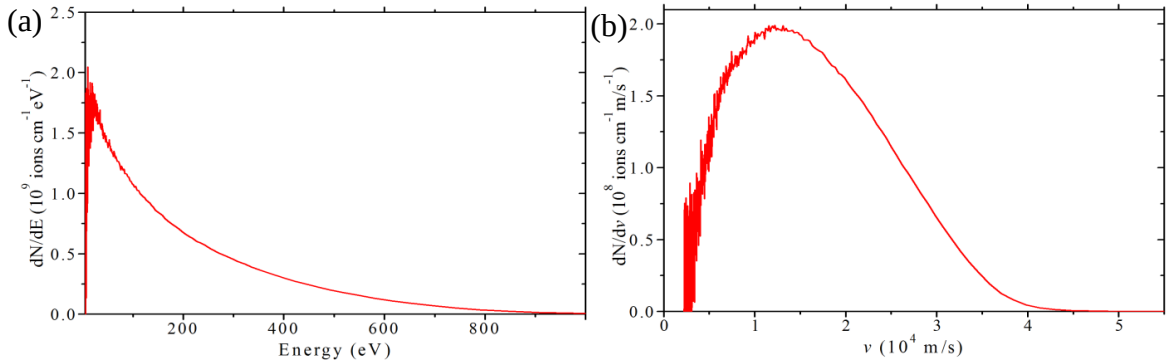

Fig. 4.13 – (a) Ion energy distribution and (b) ion velocity distribution calculated from the ion current fluence measured by the planar Langmuir ion probe normal to the plasma expansion.

A line fitting is made of the integrated ion fluence angular distribution, assuming symmetry about the normal, with the Anisimov gas dynamic model[53] discussed in Section 1.1.2. This model describes the three-dimensional adiabatic and isentropic expansion of a laser ablation plume, to find the plume expansion aspect ratio k. The model is based on three key assumptions; (1) the plume expansion is entirely adiabatic after the laser pulse, (2) the plasma expansion is isentropic, and finally (3) the expansion is self-similar, i.e. the plasma parameters such as density and pressure are constant across semi-ellipsoid surfaces.

The analytical expression for the ion fluence at an angle of θ degrees measured along a planar surface (as is the case for a translated ion probe) is given by:

$$F(\theta) = F_N \left(\frac{1}{1 + k^2 \tan^2(\theta)} \right)^{\frac{3}{2}} \qquad \text{Eqn. 4.16}$$

where F_N is the ion current along the normal.

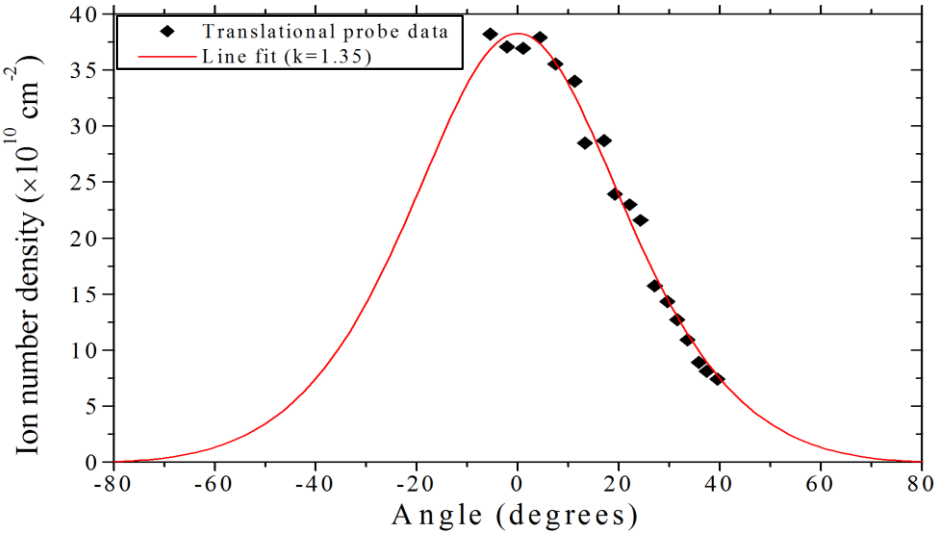

Fig. 4.14 – Line fitting from translational ion probe data; the k value was found to be 1.35 for best fit.

The total ion yield per pulse can be calculated from the Anisimov model[53]:

$$F_T = \frac{2\pi {z_p}^2 F_N}{k_{xz} k_{yz}} \qquad \text{Eqn. 4.17}$$

Assuming the plume expansion aspect ratio k, found by fitting the translational probe data (Fig. 4.14), to be the same in x and y the total ion yield is ~1 ×10^{14}. Comparing this to the total atomic yield per shot (~5 ×10^{15}) shows the laser ablation plume has majority of neutral atomic constituents rather than ionic. However this value is an overestimate, due to issues with the ablation crater as discussed previously in this section. The discharge is initiated once the LPP has traversed the inter-electrode gap, connecting both electrodes. By taking the front and probable ion velocities, ~4.3 ×10^4 m/s and ~1.25 ×10^4 m/s respectively, we can estimate the onset time of discharge as between ~90 ns and 320 ns. From the Rogowski coil measure of $\frac{dI}{dt}$ we know the onset of discharge is 170 ±10ns after the laser pulse strikes the cathode, giving a plasma velocity of approximately (2.3 ±0.1) ×10^4 m/s.

Based on the laser produced plasma expansion being inertial, after the temporal end of the laser pulse (at t = 30 ns), and by manipulating Eqn. 4.8, we can plot the ion fluence at a set position z_0 with respect to time t':

$$n_i(z_0, t') = n_i(z_p, t) \times \left(z_p / z_0\right)^3 \qquad \text{Eqn. 4.18}$$

$$t' = t \times \left(z_0 / z_p\right) \qquad \text{Eqn. 4.19}$$

The expansion can also be written in terms of a set time t_0 with respect to position z'

$$n_i(z', t_0) = n_i(z_p, t) \times (t/t_0)^3 \quad \text{Eqn. 4.20}$$

$$z' = z_p \times (t_0/t) \quad \text{Eqn. 4.21}$$

Using these expressions for the ion plume self-similar expansion we can plot the ion fluence around the onset time of discharge ~170 ns after the laser pulse (Fig. 4.15), and at the anode position ~4 mm from the cathode ablation spot (Fig. 4.16). These plots give an estimate of the ion number density throughout the inter-electrode gap at the time of onset of discharge.

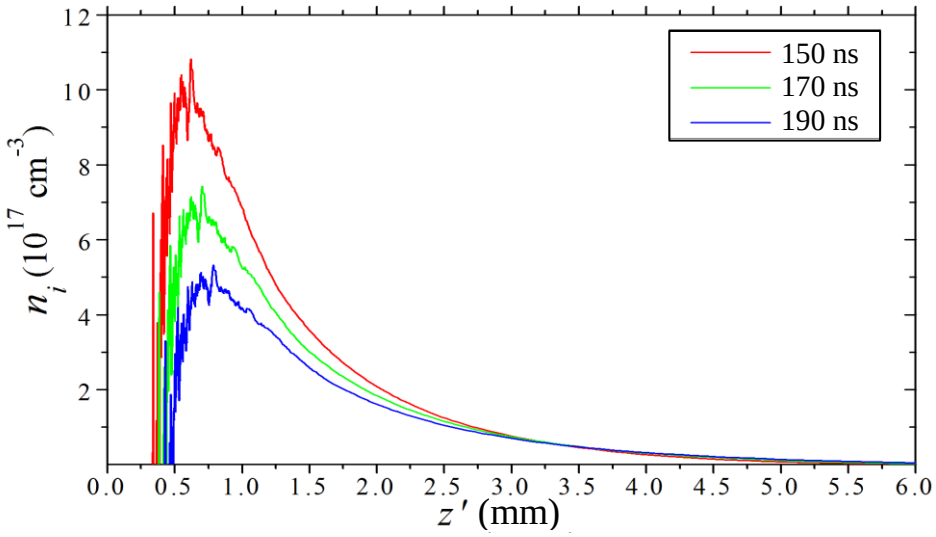

Fig. 4.15 – Ion number density as a function of distance *z'* in mm, where the cathode electrode is at 0 mm and the anode at ~4 mm, showing a density of ~3 ×10^{16} cm^{-3} at the anode surface at 170 ns.

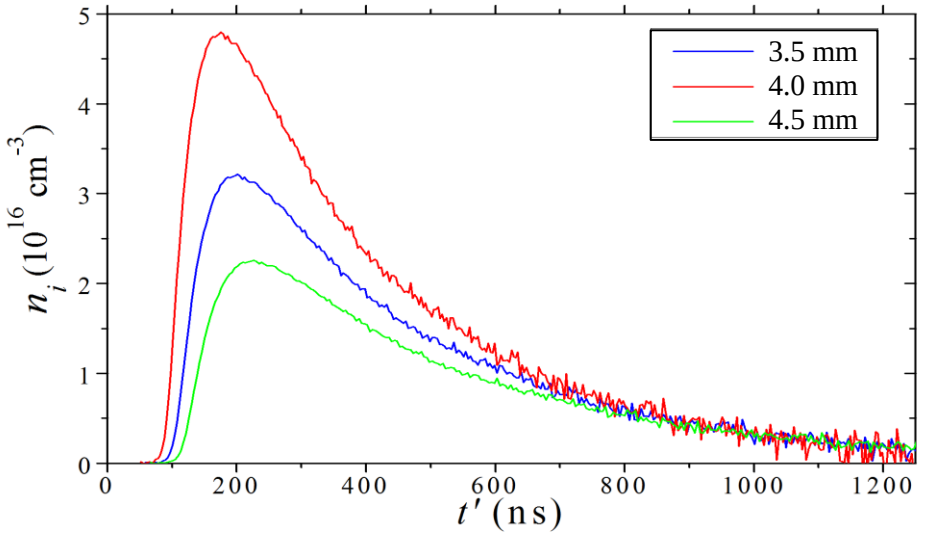

Fig. 4.16 – Ion number density as a function of time *t'* in ns at the anode position. This gives a density of ~3 ×10^{16} cm^{-3} at the anode surface at 170 ns.

4.3 Extreme ultraviolet emission measurements

4.3.1 EUV source characteristics

This section describes the measurement of the EUV emission, both in terms of in-band energy output with the PhysTeX detector tool and in a broader EUV band of 8 – 18 nm recorded by the absolutely calibrated Jenoptik EUV spectrometer. The spatial profile and position of the EUV emitting region are also characterised using a 13.5 nm 2% bandwidth spherical MLM. Some of the EUV diagnostic tools were used together, while some were deployed in separate experiments. The EUV emission from the plasma was recorded from three angles shown in Fig. 4.17. The PhysTeX EUV detector was positioned 60º above the horizontal plane, facing normal to the discharge axis. Both the Jenoptik EUV spectrometer and the EUV imaging system were placed in the horizontal plane, with the Jenoptik at 60º to the discharge axis facing the anode and the multilayer spherical mirror perpendicular to the discharge axis.

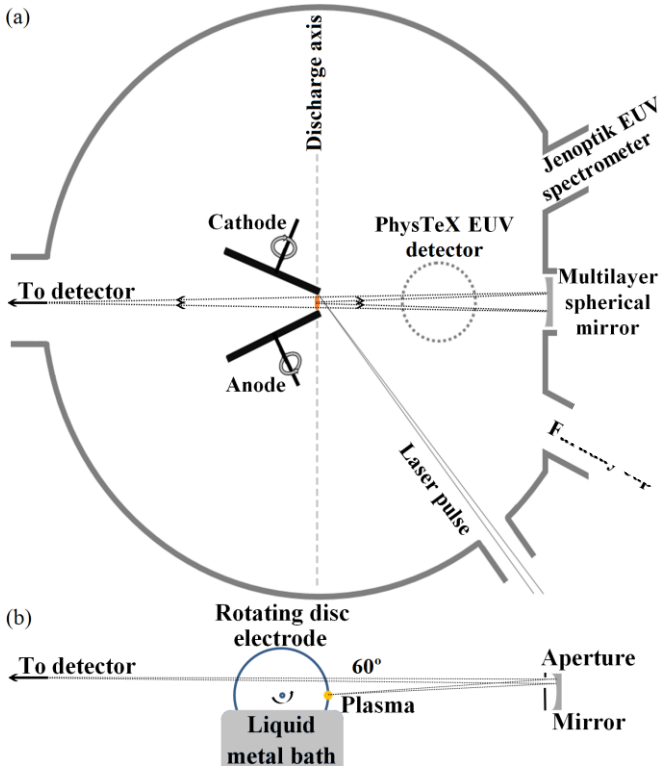

Fig. 4.17 – (a) Schematic diagram of LAVA-lamp illustrating the apparatus and diagnostic tools utilised, and (b) side-on view of the EUV imaging system highlighting the off axis view taken.

4.3.2 PhysTeX EUV detector

The PhysTeX EUV detector [89] is a well characterised[90], absolutely calibrated (in-house in 2006 with cross-calibration carried out since), in-band EUV tool. To measure the EUV radiation in a 2% band at 13.5 nm the energy monitor is equipped with a Mo/Si multilayer mirror (MLM) assembly which was designed to mimic the 2% band-pass of an 11 mirror Mo/Si multilayer system (11 mirrors being the industry expectation for a working source-to-wafer optical delivery system) as discussed in Section 2.5.1. A 250 nm thick zirconium filter was positioned after the MLM assembly, to remove out-of-band radiation as the mirrors are highly reflective in the visible.

The temporal full-width-half-max (FWHM) duration of a typical EUV pulse measured by the PhysTeX was ~140 ns (Fig. 4.18). This is substantially longer than the expected life-time of the EUV emitting portion of the plasma ~10 – 50 ns, based on modelling of an LPD source[107]. We judge the PhysTeX detector to be not time resolving for the EUV events measured here. A second EUV sensitive photodiode, with a much faster rise-time, was also employed to verify this (see Fig. 4.23). The onset of EUV emission is observed to coincide with the notch in the *dI/dt* consistently.

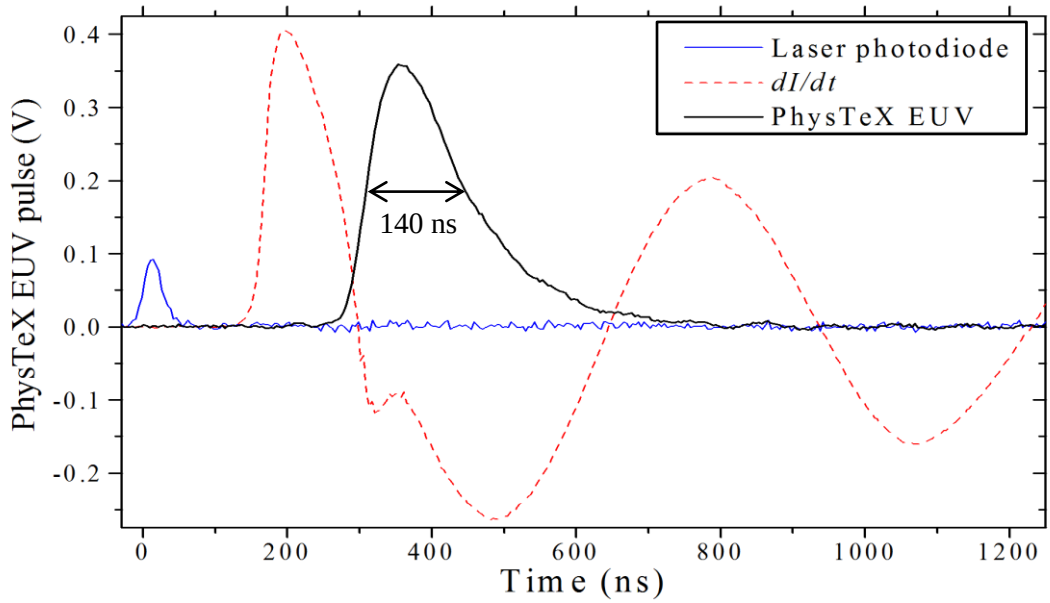

Fig. 4.18 – Typical PhysTeX EUV pulse with laser photodiode and Rogowski coil signals.

The energy per pulse E_a measured through the entrance aperture is given by[90]:

$$E_a = \frac{Q\, d^2}{A\, S_D T_M T_F} \qquad \text{Eqn. 4.22}$$

where $Q = \frac{1}{50\,\Omega}\int V_{\mathrm{EUV}}(t)dt$, d is the distance to the entrance aperture (49 cm), A is the aperture area (1.5×6.0 mm^2), S_D is the photodiode sensitivity given by manufacturer (0.19 C/J), while T_M (0.30) and T_F (0.42) are the measured transmission of the multilayer mirror assembly and the Zr filter respectively.

For the EUV pulse shown in Fig. 4.18, the integrated voltage signal recorded by the oscilloscope is found to be 6.05×10^{-8} Vs therefore the total charge $Q = 1.21$ nC. This gives an energy $E_a = 1.35$ mJ/sr. As has been mentioned previously, it is common when discussing EUV in literature to refer to the EUV emission into 2π sr, therefore $E_{2\pi}$ ~8.5 mJ/2π sr

Some shot-to-shot variation is obvious in the EUV pulse. An example of this variation is shown in Fig. 4.19 for 4.5 kV charging voltage triggered by 12 mJ laser pulse with tin as source material. The average EUV pulse profile is composed of 32 consecutive events with the laser set to 2 Hz, while the others are a representative selection of profiles recorded with the laser on single pulse mode.

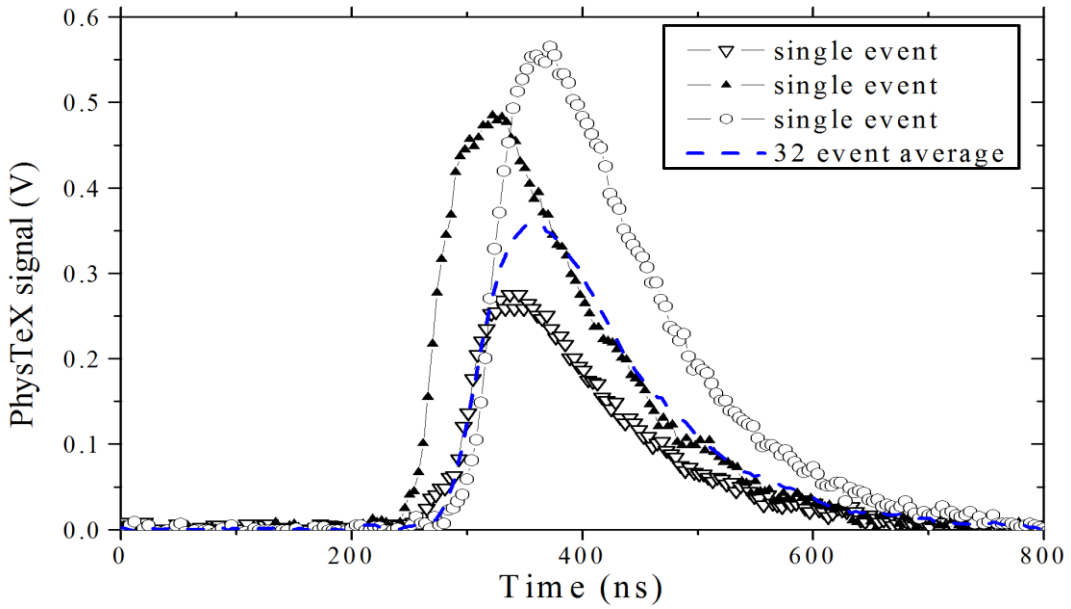

Fig. 4.19 –Non-consecutive PhysTeX EUV pulses showing shot-to-shot variation in profile (symbol plots) with an average of 32 consecutive pulses (blue dashed line).

The variation in the measured in-band EUV energy versus discharge energy is presented in Fig. 4.20 for both tin and galinstan. The maximum and minimum in-band energy recorded at a set discharge energy with the laser in single shot mode are plotted, with an average energy, recorded from 32 consecutive shots with the laser at 2 Hz. For both tin and galinstan the EUV emission is seen to increase with increasing discharge energy. In the case of tin as source material we see the maximum EUV output with a 4 J, however the shot-to-shot variation means there is a more consistently strong EUV output with a 6 J discharge. In the case of galinstan the average energy from 32 consecutive shots is considerably lower than the mean position of the max-min for all discharge energies. This indicates perhaps that the pinching is not optimised for galinstan, with a performance improvement the source could operate with comparable in-band EUV output as with tin as source material.

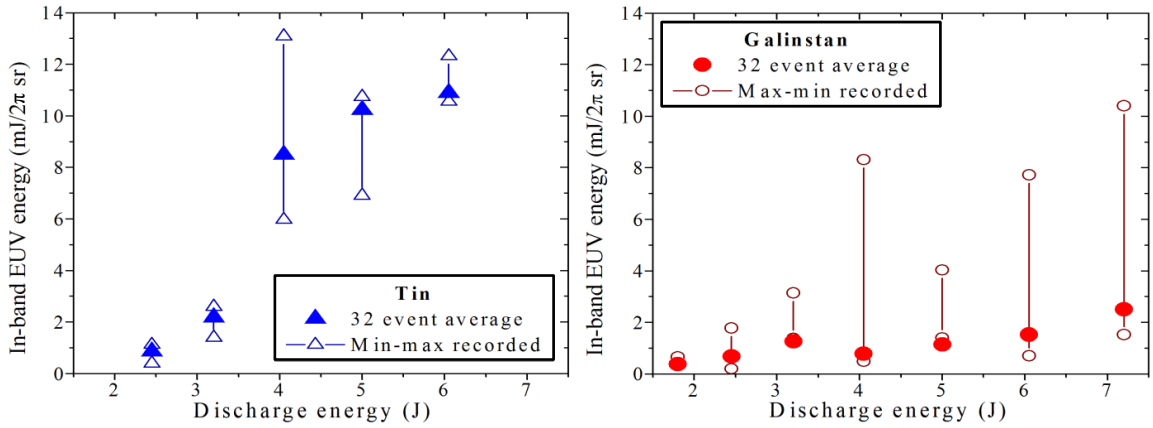

Fig. 4.20 – In-band EUV energy versus discharge energy for both tin (▲) and galinstan (●) showing the maximum and minimum recorded with single shot mode and an average of 32 consecutive shots.

The data plotted here shows the 32 shot average, which can be considered the EUV source power output for the parameters at each data point. However we have also plotted the single shot maximum and minimum recorded EUV output, these show a considerable asymmetry, especially in the case of galinstan. This give an indication of the shot-to-shot likelihood of the EUV output being close to max or min.

Fig. 4.21 shows the average in-band EUV energy, with standard deviation error bars, for a range of discharge energies for both tin and galinstan as source materials. These measures were made with the laser in single shot mode and were recorded only for pinching events, i.e. those that showed a clear notch in the Rogowski coil. This data is from the same set as the max-min plotted in Fig. 4.20.

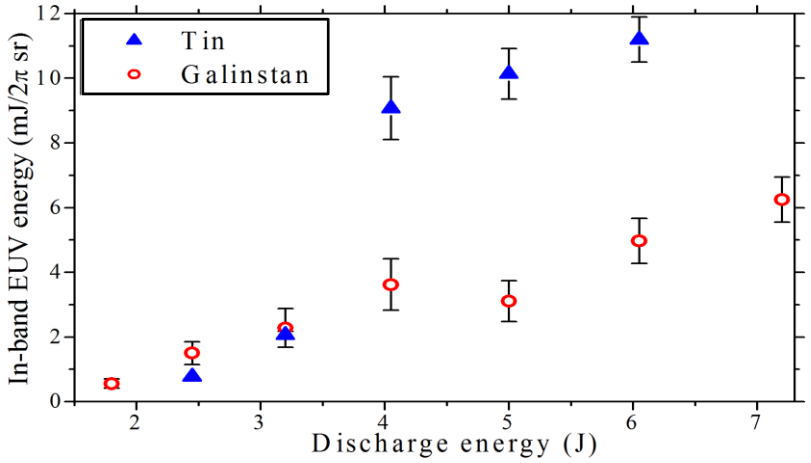

Fig. 4.21 – Discharge energy dependence of the average in-band (2% bandwidth centred at 13.5 nm) EUV emission into 2π sr for tin (▲) and galinstan (○) triggered in single shot mode. This data was selected depending on the pinching, as judged by the Rogowski coil signals.

Another convenient unit for discussion of EUV sources is conversion efficiency (CE), the percentage EUV energy output over energy input to the source. Fig. 4.22 is a re-plot of the data in Fig. 4.21 in terms of CE for both tin and galinstan. A peak CE of ~0.4% was found for tin with a 4 J (4.5 kV) discharge, with ~0.1% for the corresponding discharge energy for galinstan.

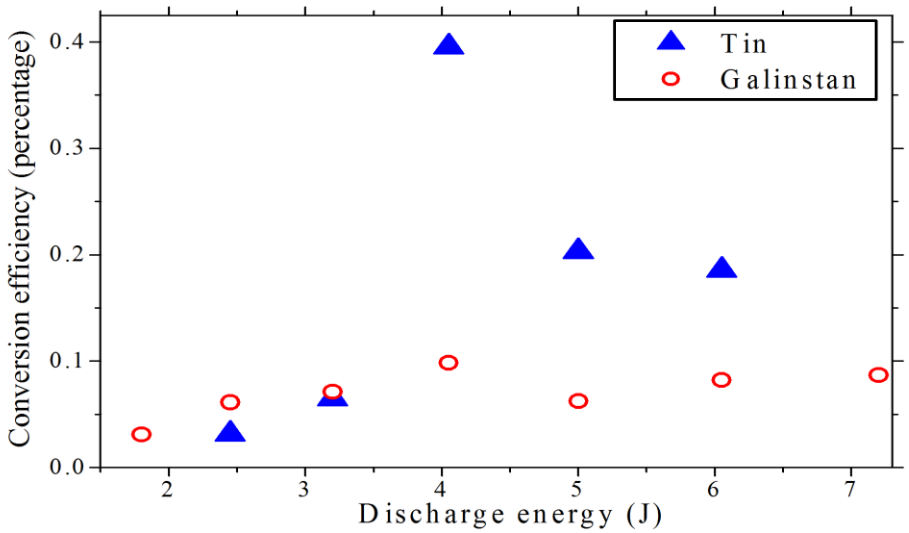

Fig. 4.22 – Conversion efficiency of LAVA-lamp for tin (▲) and galinstan (○) for the range of available discharge energies with 12 mJ and 5 mJ trigger laser energies respectively.

Along with the PhysTeX detector tool a separate EUV filtered fast photodiode (PD) was deployed, an IRD AXUV-HS-5 with a 0.5 µm thick Zr filter mounted in front. This fast photodiode has a rise-time of 750 ps. Without a MLM assembly the photodiode measured the EUV with a band-pass of ~6 – 18 nm. The fast PD was not as well-shielded from the discharge noise as the PhysTeX tool had been. Despite these issues, a FWHM of ~35 ns was measured for a 4.5 kV discharge triggered by a 12 mJ laser pulse with tin as source material (Fig. 4.23). The shot-to-shot variation in the EUV signal measured here was also very high, and as is apparent the signal to noise ratio made it more difficult to analyse the data.

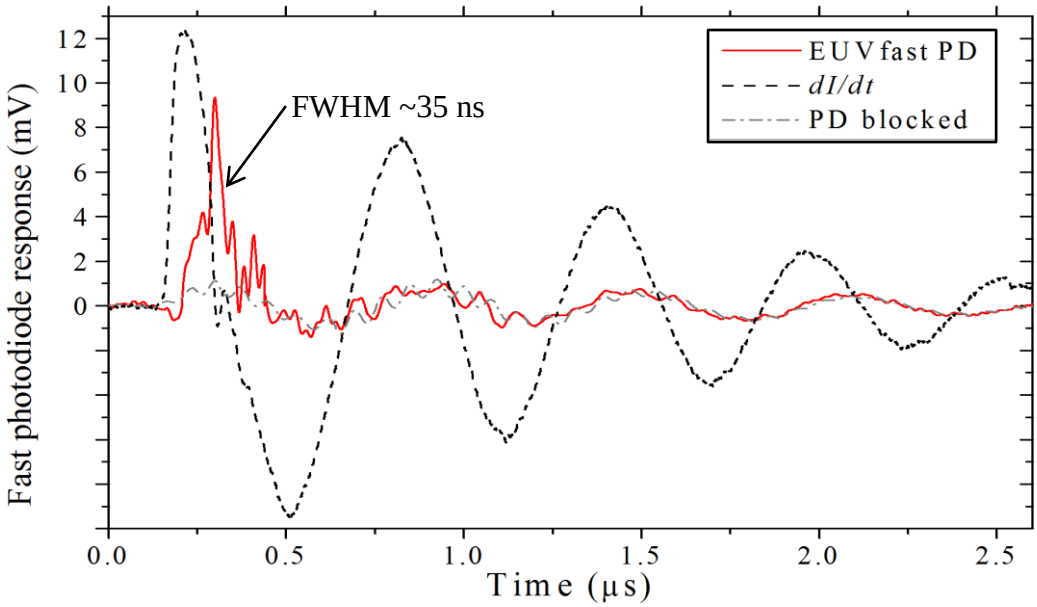

Fig. 4.23 – Fast photodiode response for a 4.5 kV discharge triggered by a 12 mJ laser pulse with tin as source material, the Rogowski coil *dI/dt* is plotted on the same scale to illustrate the timing and source of the noise.

4.3.2 Jenoptik EUV spectrometer

In this section the results from an absolutely calibrated time-integrated EUV spectrometer are presented. The spectrometer recorded a spectral range from 10 – 18 nm with a resolution of ~0.03 nm. It viewed the plasma in the horizontal plane at 60º from the discharge axis, facing the anode (see Fig. 4.2 at the beginning of this chapter). The time integrated spectra were recorded using the laser in both single shot mode and at 2 Hz, with an integration time of between 1 and 4 s, for a variety of discharge energies studying both tin and galinstan as source material. Fig. 4.24 shows an uncalibrated EUV spectrum recorded for a single EUV pulse from a 4.5 kV discharge triggered by 12 mJ laser pulse with tin as source material.

The raw recorded spectra are processed with the Matlab program which calibrates the horizontal pixel scale into wavelength and takes an average pixel counts along the vertical in a set range and calibrates into spectral radiant energy. The integrated EUV energy in the 2% band will be compared with the values obtained from the PhysTeX EUV detector tool, which viewed the discharge axis from a different angle.

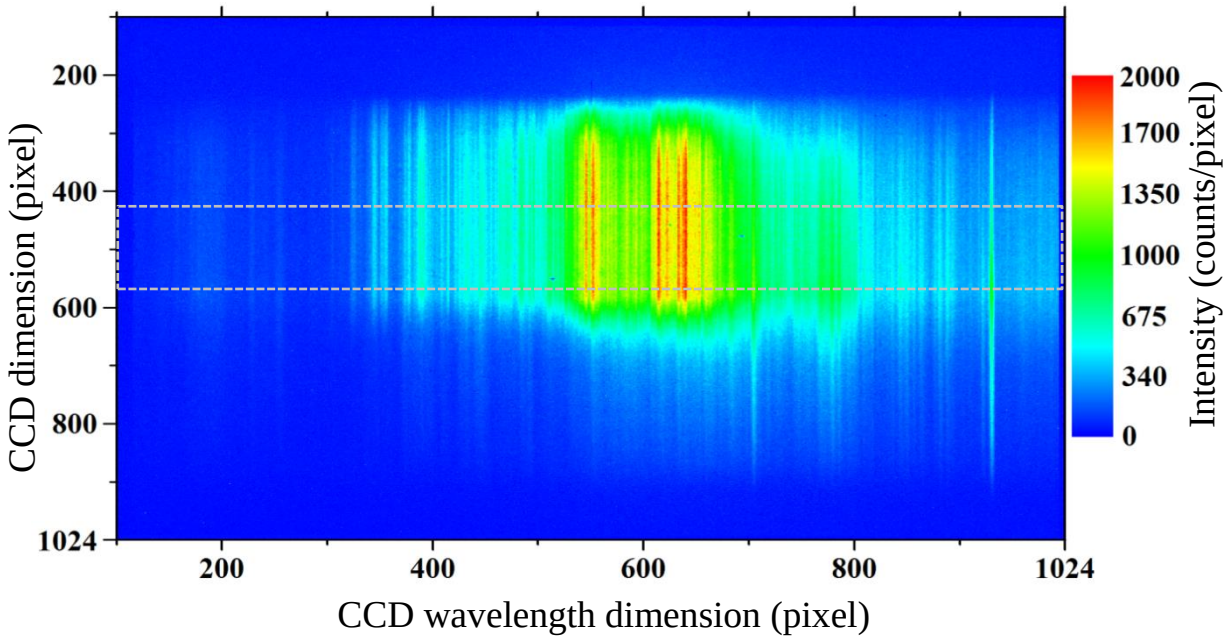

Fig. 4.24 – Raw spectral image for 4.5 kV discharge triggered by 5 mJ laser pulse with galinstan. The calibrated spectra are averaged in the vertical across the pixel region marked by the grey dash box.

As mentioned in the previous section, the shot-to-shot variation in the source leads to considerable spread in the in-band EUV energy output. Fig. 4.25 illustrates the variation with a sample set of EUV spectra for tin and galinstan with a 4 J discharge. By identifying the ion species[108], [109] emitting in each region of the recorded spectral range we will qualitatively discuss the differences observed in the EUV spectra due to shot-to-shot variability. Although the 4 J discharge with tin is a much stronger emitter in this range it also appears to have a substantially larger variation in comparison to galinstan.

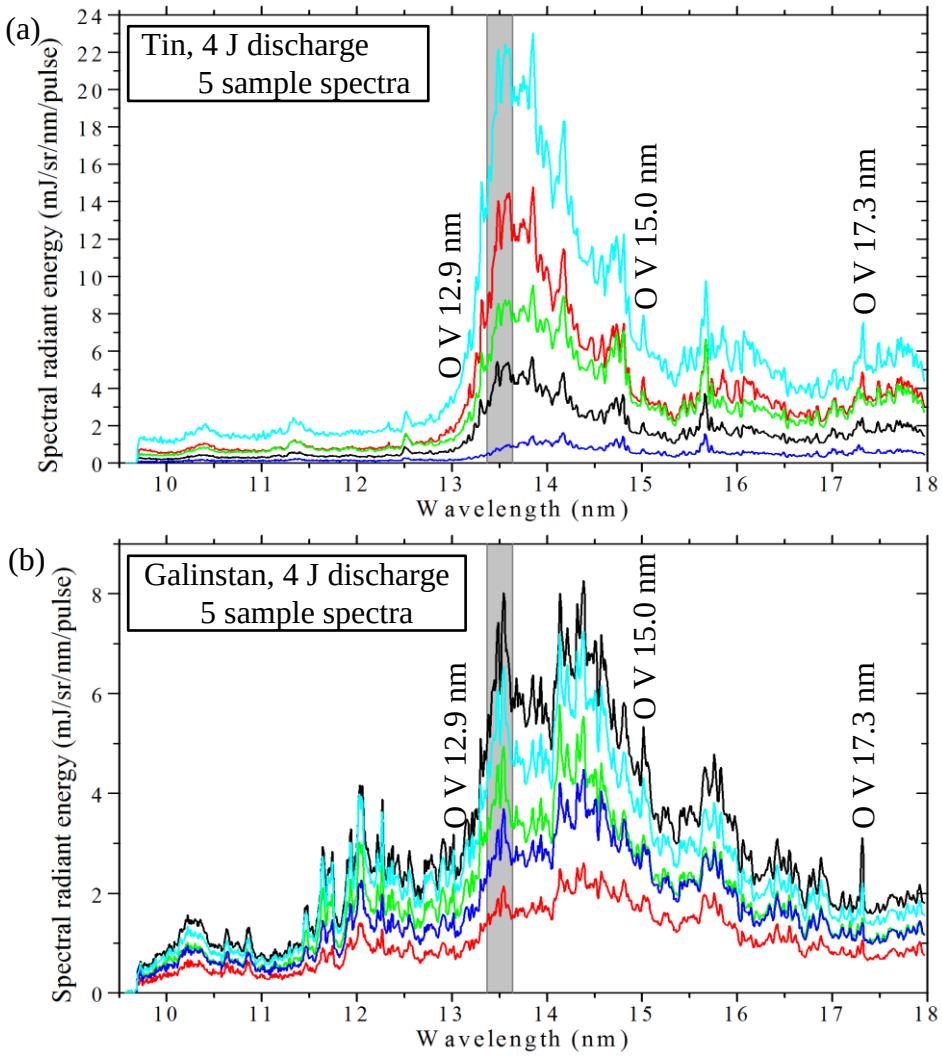

Fig. 4.25 – Sample set of 5 spectra chosen to illustrate the shot-to-shot variation in EUV spectral emission for 4 J (4.5 kV) discharge triggered by (a) 12 mJ laser with tin and (b) 5 mJ laser with galinstan as source materials. The 2% band measured by the PhysTeX is marked by the grey shading.

The presence of oxygen emission lines is noted in Fig. 4.25. These lines were identified from NIST[101] as O V lines at 12.9 nm (2p–4d), 15.0 nm (2s–3p), and 17.3 nm (2p–3d). The transition probabilities for these lines are presented in Table 4.2.

Table 4.2. Transition probabilities[110] and emission line information[101] for O VI spectral lines in the EUV spectral range recorded by the Jenoptik.

Transition	Wavelength / nm	E_i / eV	E_k / eV	g_i	g_k	A_{ki} / $\times 10^{10}$ s^{-1}
$1s^2 4d\ ^2D_{3/2} \rightarrow 1s^2 2p\ ^2P_{1/2}$	12.9785	11.94898	107.47943	2	4	2.43 ± 3%
$1s^2 4d\ ^2D_{5/2} \rightarrow 1s^2 2p\ ^2P_{3/2}$	12.9871	12.01500	107.48208	4	6	2.91 ± 3%
$1s^2 4d\ ^2D_{3/2} \rightarrow 1s^2 2p\ ^2P_{3/2}$	12.9875	12.01500	107.47943	4	4	0.485 ± 3%
$1s^2 3p\ ^2P_{3/2} \rightarrow 1s^2 2s\ ^2S_{1/2}$	15.0089	0	82.60692	2	4	2.62 ± 5%
$1s^2 3p\ ^2P_{1/2} \rightarrow 1s^2 2s\ ^2S_{1/2}$	15.0125	0	82.58751	2	2	2.62 ± 5%
$1s^2 3d\ ^2D_{3/2} \rightarrow 1s^2 2p\ ^2P_{1/2}$	17.2935	11.94898	83.64292	2	4	7.33 ± 3%
$1s^2 3d\ ^2D_{5/2} \rightarrow 1s^2 2p\ ^2P_{3/2}$	17.3079	12.01500	83.64926	4	6	8.78 ± 3%
$1s^2 3d\ ^2D_{3/2} \rightarrow 1s^2 2p\ ^2P_{3/2}$	17.3095	12.01500	83.64292	4	4	1.46 ± 3%

These oxygen lines are only observed during the first few discharge events, after the chamber has been vented to air. This is caused by the oxidation of surface layers of tin, this issue is especially apparent if the tin has been molten while exposed to air leading to a substantial quantity of tin oxide forming on the surface. Tin oxide is easily observed as sub-millimetre sized lumps on the electrode wheels. It will remain solid as it has a much higher melting point than pure tin, 1080 °C rather than ~230 °C. If the source is operated under vacuum for a few hundred shots the presence of the oxygen emission lines was noted to cease. These emission lines are however useful for both verification of the spectral calibration and for estimation of the temperature of the emission plasma through intensity line ratio.

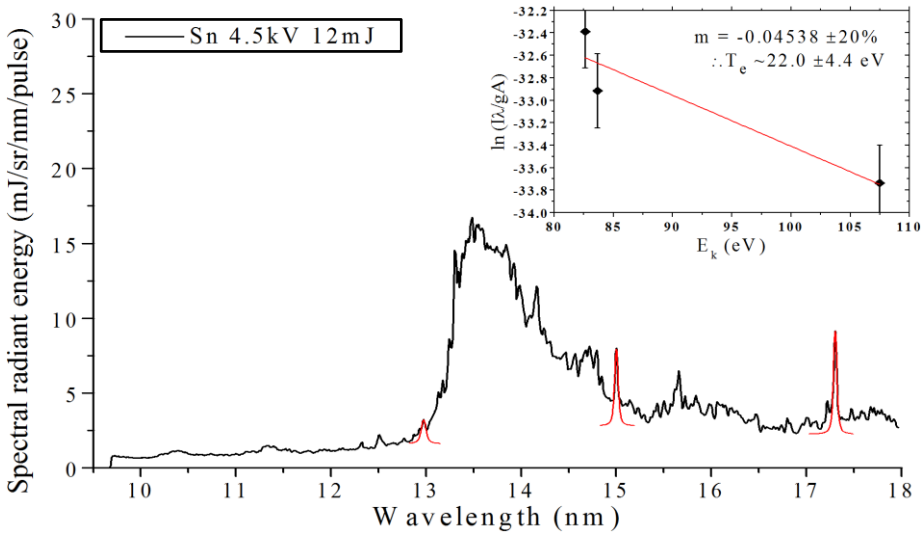

Fig. 4.26 – Boltzmann plot made of the O V EUV emission lines observed; the fitting is quite uncertain as the contribution of the Sn UTA overlaps strongly. The estimated electron temperature is in the expected range.

The EUV output for tin and galinstan with a 4 J discharge has been noted to have a substantial shot-to-shot variation. The total integrated energy per pulse in the spectral range is found to be 18 ±11 mJ for tin and 14 ±5 mJ for galinstan (Fig. 4.27), with the uncertainty indicating the standard deviation observed. The total EUV output is comparable for both sources, however the in-band EUV is nearly a factor of 2 less with galinstan as source material where for tin $E_{in\text{-}band}$ = 11 ±9 mJ/2π sr compared to 6.0 ±2.5 mJ/2π sr for galinstan (Fig. 4.28).

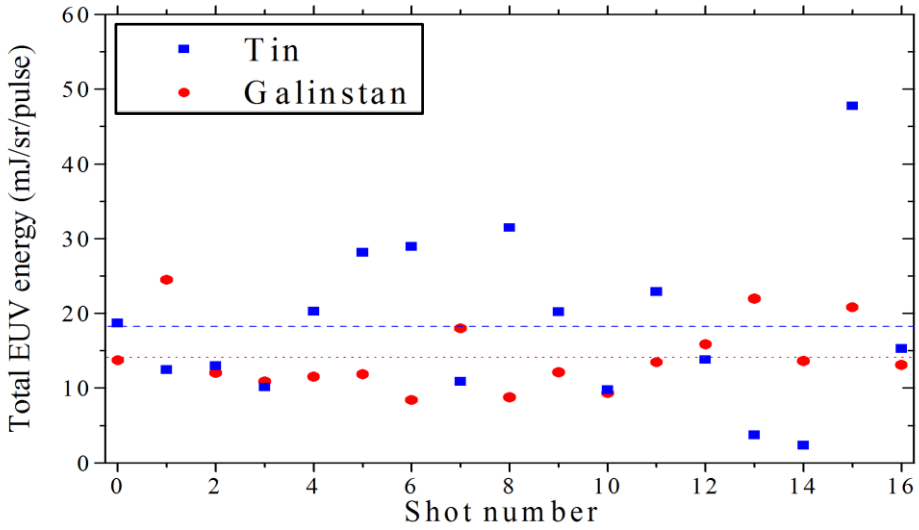

Fig. 4.27 – Total EUV energy output in the 10 – 18 nm range measured by the Jenoptik spectrometer, with the average value marked by a blue dashed or red dotted line for tin and galinstan respectively. Each shot was consecutive and operating the laser in single shot mode.

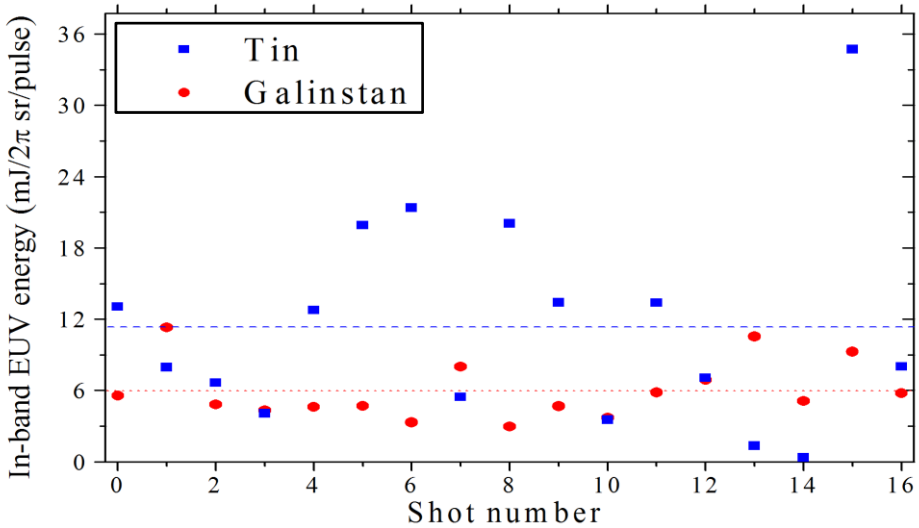

Fig. 4.28 – In-band energy output into 2π sr obtained from the same spectra as in Fig. 4.27, with the average value marked by a blue dashed or red dotted line for tin and galinstan respectively.

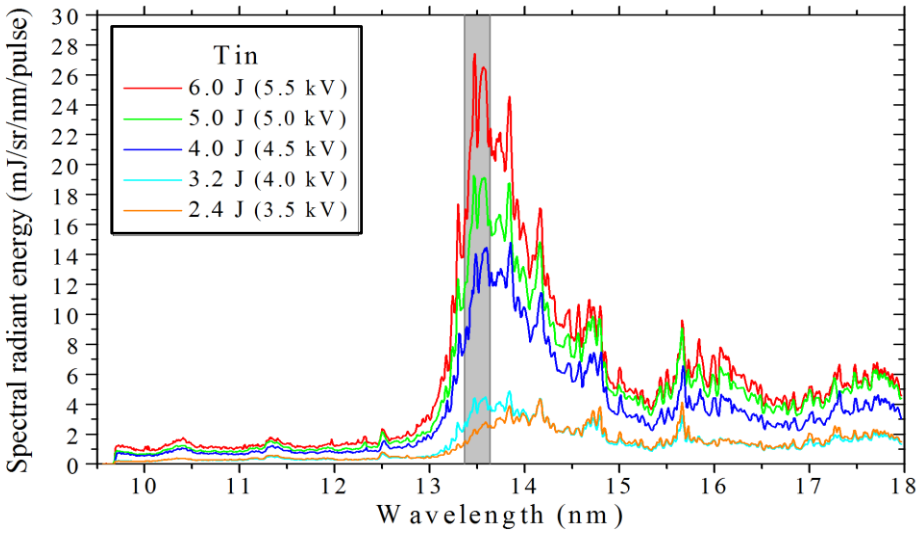

Fig. 4.29 – EUV spectral radiant energy averaged over two pulses for a range of discharge energies with tin.

The out-of-band EUV emission also varies strongly with discharge energy as shown in Fig. 4.29. The shape of the spectrum can indicate the opacity of the emitting plasma[108].

In this section it is clear that there is considerable shot-to-shot variation in the EUV output from the source, both using tin and galinstan as emitter materials. This is partly owing to the inherent instabilities in a Z-pinch and also to some mechanical variation in the source. However, it is possible to further optimise this set up and this may yield a more stable, higher average power, EUV source.

4.3.2 EUV imaging system

In this subsection, unlike the previous EUV results sections, we will present the results for galinstan alone as source material in the LAVA-lamp. No images were recorded of the tin EUV emitting region. This was due to time constraints of equipment availability. The galinstan EUV emitting region was imaged for a range of trigger laser energies and discharge charging voltages:

- 4.5 kV charging voltage with 5 mJ, 8 mJ and 35 mJ trigger laser energies,
- 3 kV – 6 kV charging voltages, in 0.5 kV steps, with 5 mJ laser energy.

The majority of the EUV images have the corresponding data recorded by the Jenoptik EUV spectrometer, Rogowski coil, and visible spectrometer captured simultaneously. A cross comparison of selected shots will be presented in the EUV summary subsection to follow. The optimum pinching parameters for a 4.5 kV discharge was observed to be with a 5 mJ laser pulse for Galinstan. EUV imaging was undertaken in tandem with other measurements, having first aligned to a fixed spot deemed to be the most accurate position to view the EUV emitting region. Each EUV image was post-processed to remove the contribution of direct illumination, i.e. light not collected via the multilayer mirror (MLM). This direct illumination contribution is stray light from the EUV emitting plasma region, observed through the EUV filter, which was not collected and imaged by the MLM. The direct illumination was subtracted from the recorded images in post-processing using a sample image recorded with the MLM blocked. It was also necessary to use a Fast Fourier Transform (FFT) code to remove the shadow cast by the mesh structure supporting the EUV filter.

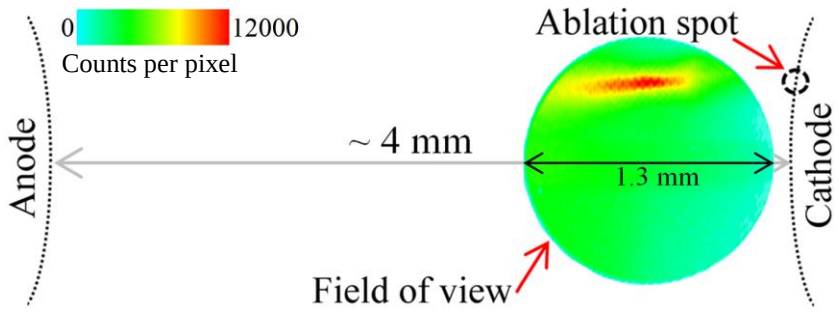

Fig. 4.30 – Time-integrated EUV emission of a typical 4 J discharge in galinstan triggered by a 5 mJ laser pulse. The schematic shows that the 1.3 mm diameter field of view is located in the 4 mm inter-electrode gap, but closer to cathode.

The spherical Mo/Si multilayer mirror (MLM) viewed the plasma perpendicular to the discharge axis at ~13.5 mm, with a radius of curvature of 125 mm. Fig. 4.31 shows (a) top down and (b) side on views of the EUV imaging system, not pictured are the ICCD and 1.6 mm Zr filter, positioned ~1.6 m to the left of the discharge axis. A series of apertures were also included to minimise stray light in the long vacuum arm used to mount the ICCD. The imaging system had a magnification of 13. The MLM was shuttered to avoid contamination when it was not in use.

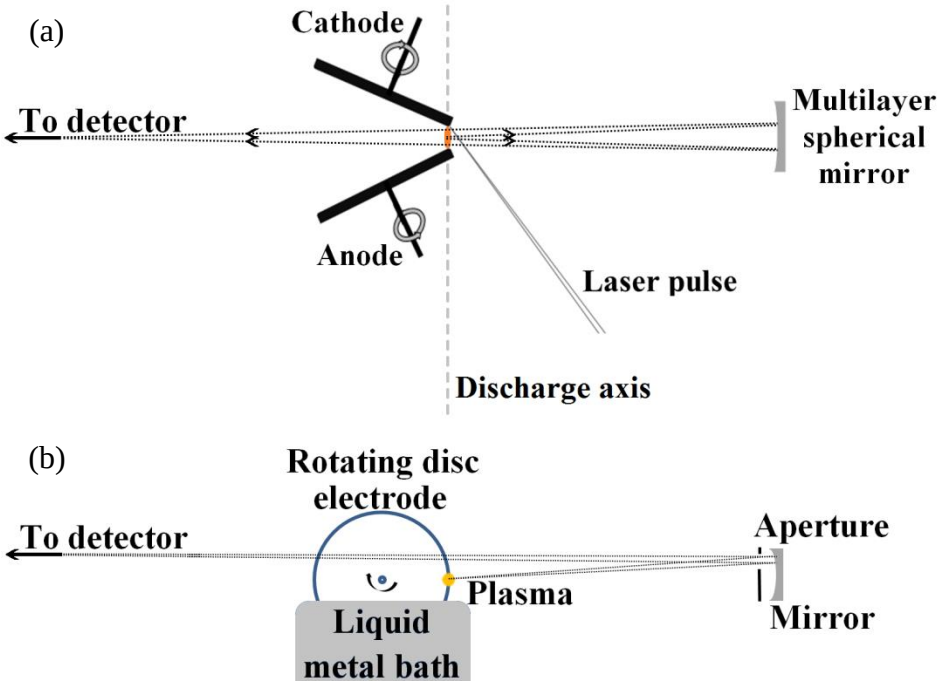

Fig. 4.31 – (a) Top and (b) side view of the EUV imaging setup. The EUV imaging system of the inter-electrode gap region. The multilayer mirror is highly reflective in the visible so a Zr filter was included in front of the ICCD leading to the circular aperture seen in Fig. 4.30.

Through the EUV imaging we found that the EUV emitting region of the plasma was consistently close to the cathode (Fig. 4.30) and that there is substantial change in the shape of the time integrated EUV emitting portion of plasma but this portion does not vary strongly spatially. A sample set of time integrated EUV images are shown in Fig. 4.32, the three separate events are recorded for 4 J (4.5 kV) discharge triggered by 8 mJ laser. The peak intensity of (a) is twice that of (b) and (c), which are roughly equivalent.

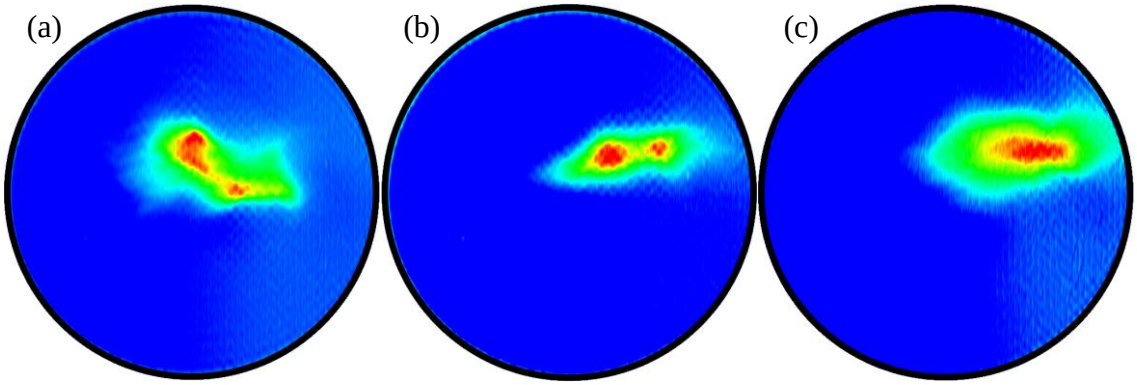

Fig. 4.32 – Separate, non-secuential, time integrated EUV images for three shots of 4.5 kV discharge with 8 mJ trigger. The peak intensity of (a) is found to be twice that of (b) and (c), which are roughly equivalent.

As with the observations made from the other EUV diagnostic tools, there is significant shot-to-shot variation in intensity of the EUV source; this is also seen for the shape of the EUV emitting region.

The discharge voltage has an effect on the intensity, size and shape of the EUV emitting region; presented on the following page in Fig. 4.33 are a representative set of images for 1.8 – 7.2 J discharges with galinstan, each triggered by a 5 mJ laser pulse. These images show the change in peak intensity (maximum counts-per-pixel), size and shape of the EUV emitting region, inside the fixed 3 mm aperture, viewing close to the cathode as shown in Fig. 4.30. The trend in these images shows the peak counts going up with increasing discharge energy. There is also an apparent narrowing of the EUV emitting region as the discharge energy increases to 4 J.

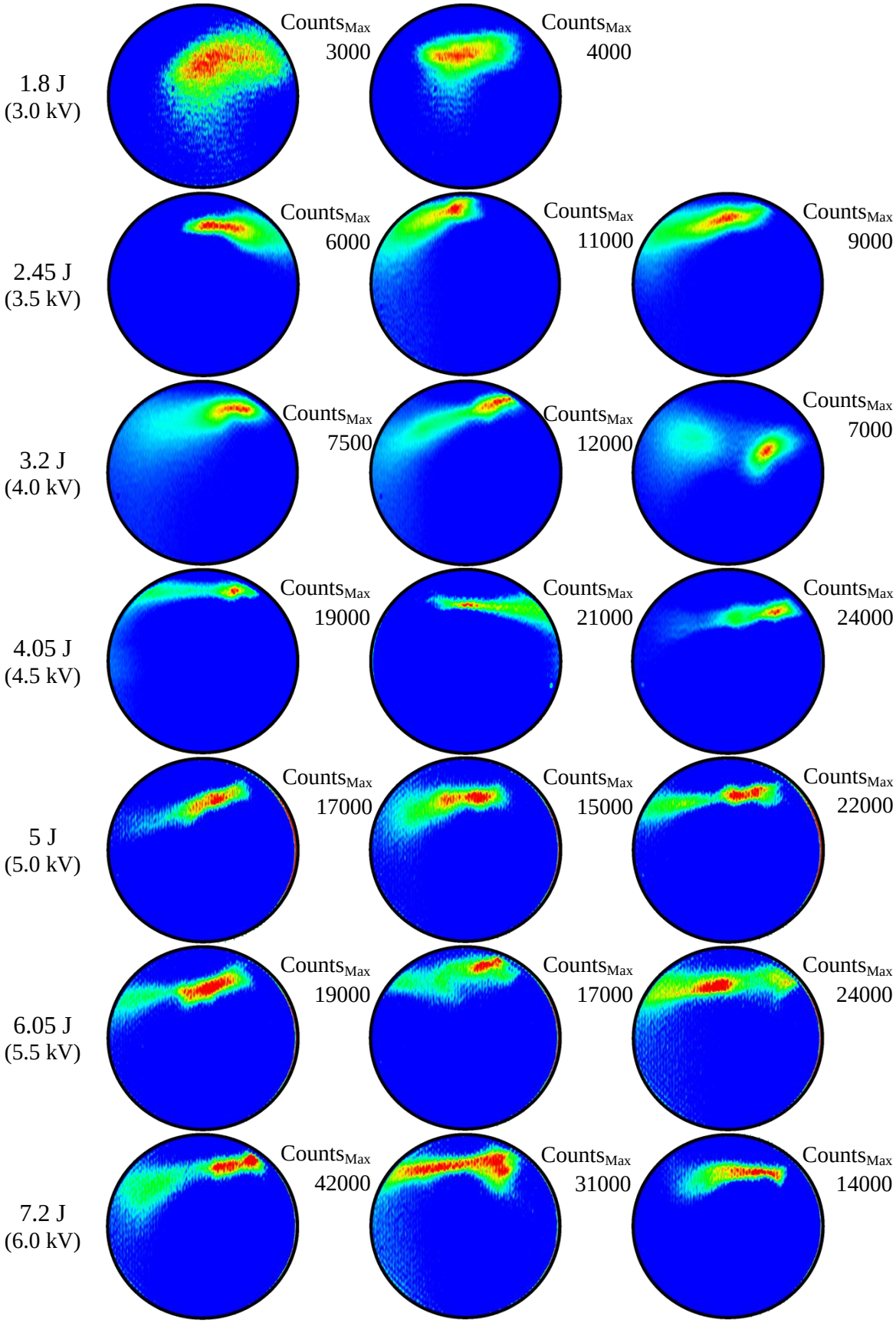

Fig. 4.33 – Time integrated images of the EUV emitting region of galinstan discharges with varied voltage, triggered by 5 mJ laser in each case. The maximum counts-per-pixel (C_{Max}) is noted for each image, indicating the EUV emission intensity for each event.

By measuring the full widths at half maximum of the emission, the cylindrically shaped galinstan EUV source was found to have an average diameter of 110 ± 25 µm and length of 500 ± 125 µm in the case of a 4 J discharge, triggered with a 5 mJ laser pulse. The centre of mass of the EUV emitting region was calculated, based on a threshold emission value taken as approximately half the peak emission; this allowed us to plot the shot-to-shot deviation in the position (Fig. 4.34). This resulted in a standard deviation of 125 µm in the *x* and 90 µm in the *y* for the centre of mass of the EUV emitting region.

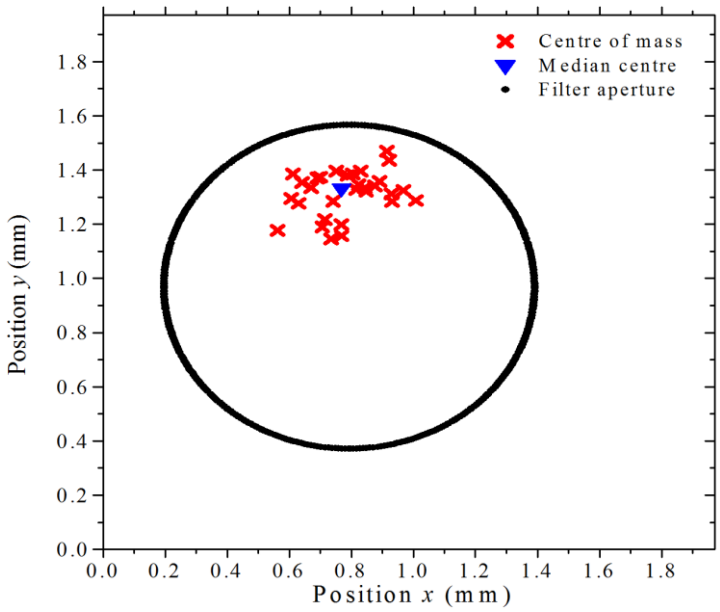

Fig. 4.34 – ICCD area with an outline of the filter aperture showing the calculated centre of mass in the case of 4 J discharge triggered by 5 mJ laser pulse with galinstan as source material.

4.3.5 Summary of EUV emission studies

The laser energy used to trigger the discharge is a key parameter, adjusted to yield Z-pinch and efficient EUV emission. The aim for EUV sources has been to maximise the in-band emission, maintain relatively stable output power, and maximise spectral efficiency (ratio of in-band to out-of-band emission). A range of laser energies were used to trigger a 4 J discharge with galinstan as source material; the EUV emission was studied to find the optimum laser energy. Throughout the work with galinstan the trigger laser energies used were 5 mJ, 8 mJ, and 40 mJ, all with the 1064 nm 30 ns Nd:YAG laser. The average peak discharge current was found to be 24 kA, 22 kA, and 28 kA, with the average time of pinch event at ~275 ns, ~340 ns, and ~390 ns respectively.

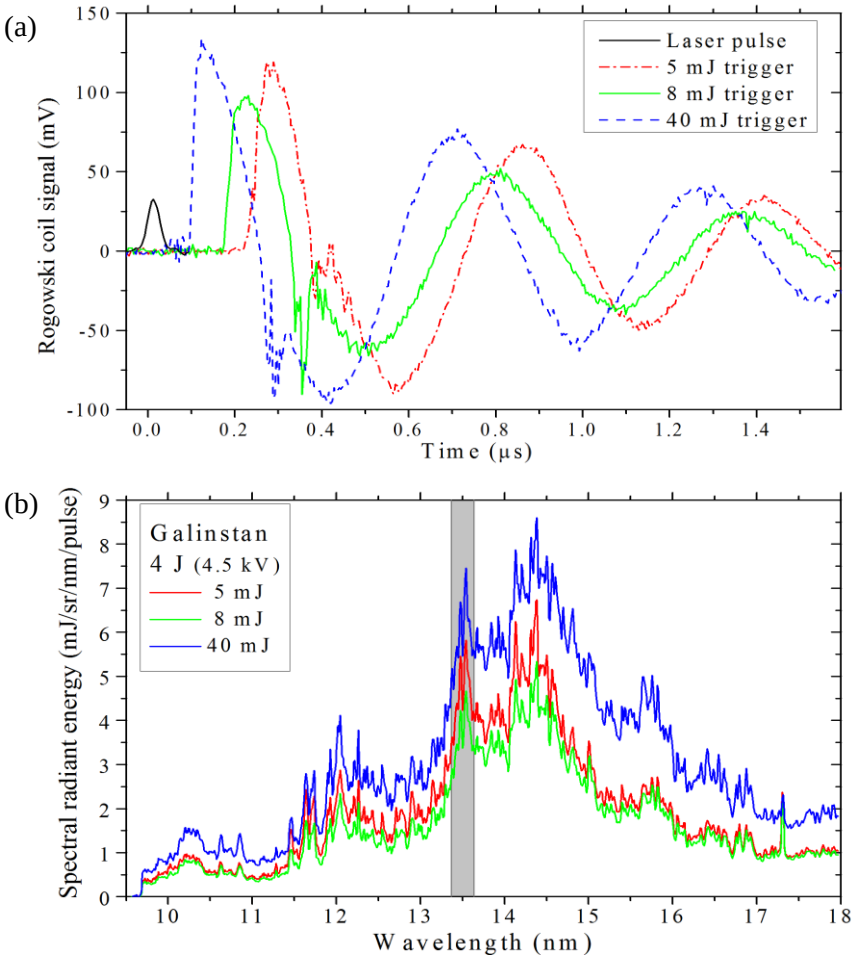

Fig. 4.35 – (a) Rogowski coil (*dI/dt*) signals recorded for three different trigger laser energies with a 4 J discharge using galinstan as source material. The onset of discharge is observed decreasing as the plasma is more energetic with the higher laser energies. (b) The corresponding EUV spectra for the varied trigger pulse.

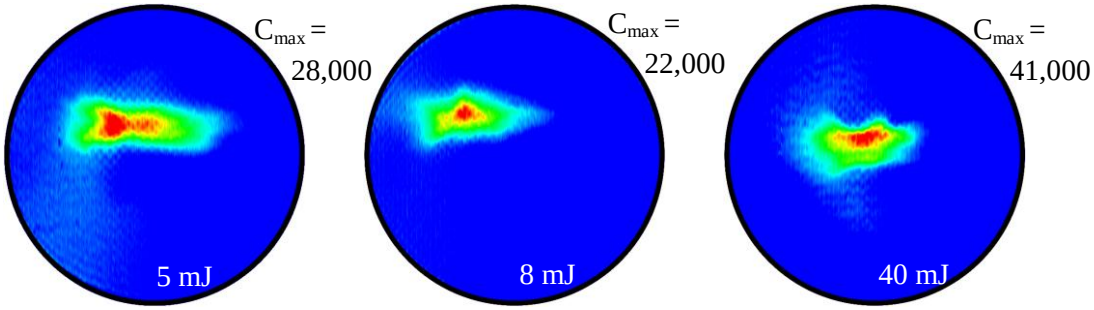

Fig. 4.36 – Images of the EUV emitting region for the corresponding events are shown in Fig. 4.35. The images are recorded as outlined by Fig. 4.30.

The percentage in-band EUV energy with respect to the total out-of-band in the 10-18 nm range for these trigger laser parameters was also noted. The percentage in-band was found to be: 7.8%, 6.9%, and 6.25% respectively. The total in-band energy into 2π sr per pulse for these was measured from the Jenoptik spectra as: 10.7 ±4.4 mJ/2π sr/pulse, 9.4 ±0.3 mJ/2π sr/pulse, and 13.8 ±4.4 mJ/2π sr/pulse respectively. The EUV spectral emission (Fig. 4.35 (b)) was recorded in synchronisation with EUV imaging (Fig. 4.36). The Rogowski coil measurements of *dI/dt* for the range of trigger laser energies are shown in Fig. 4.35 (a). For the higher laser energies the onset of discharge occurred faster, with discharge times of ~240 ns, ~180 ns, and ~100 ns after laser pulse respectively. This is caused by the laser plasma being more energetic with the higher laser energies. The notch indicating pinching is noted to shift to later times with respect to the onset of discharge. The pinching is optimum when it occurs at peak current, i.e. when $dI/dt = 0$.

4.4 Ion flux & debris analysis

In the design of an EUV source it is necessary to characterise the ionic, neutral, and particulate material emitted by the plasma. These emitted particles must be mitigated for any EUV source to be cost effective, with the high costs associated with EUV optical elements, any impinging material can damage the sensitive surface layers and decrease the reflectivity.

4.4.1 Faraday cup ion probe

The Faraday cup was used to record the ion flux associated with the plasma outflow; typical ion signals for 4 J discharges in tin and galinstan are shown in Fig. 4.37. These are obtained by averaging over 32 consecutive discharges. While a Faraday cup does not give any information about the ion charge distribution, if an average value of ion charge is assumed, then the ion TOF signal can be used to determine the energy distribution and fluence of ions at the position of the Faraday cup.

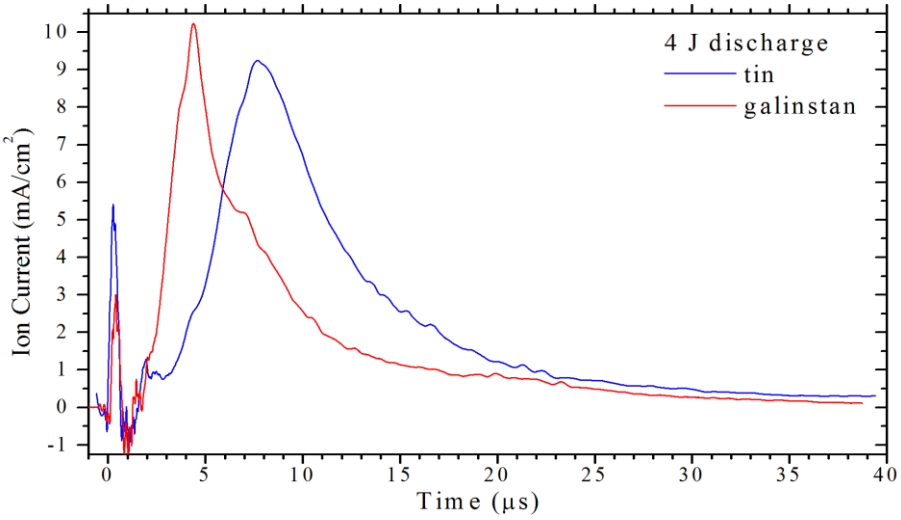

Fig. 4.37 – Faraday cup ion ToF profiles measured for tin and galinstan averaged over 32 consecutive 4 J discharges. Peak ion energies of tin and galinstan were 2.1 keV and 3.8 keV respectively.

Estimates for the average ion charge of tin and galinstan were calculated using a simple atomic code named FLYCHK[111]. Values of 12 and 10 were taken respectively where the calculation for galinstan was carried out using gallium as it is the primary constituent. The peak of the ToF signal corresponds to 2.1 keV and 3.8 keV for tin and galinstan with a 4 J discharge (Fig. 4.37).

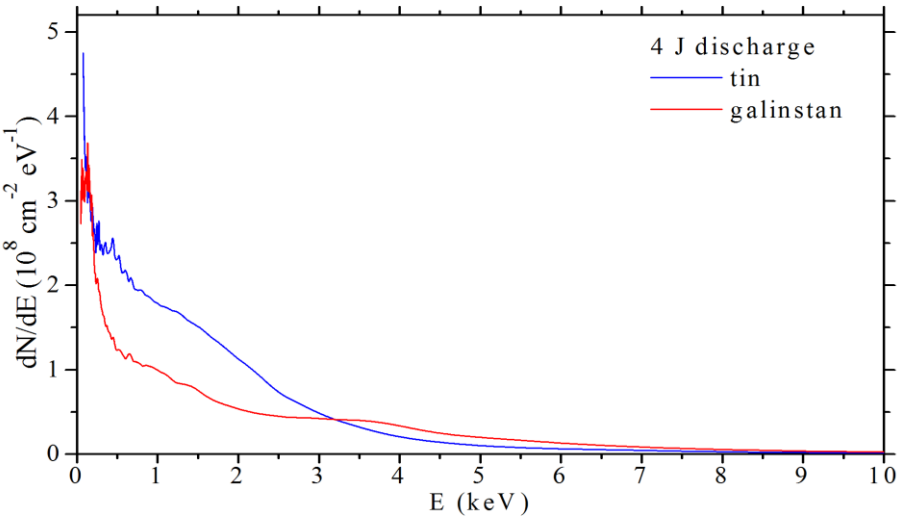

Fig. 4.38 – Faraday cup ion ToF profiles measured for tin and galinstan with no discharge.

The average ion energy, taking the values of average ion charge, was found to be 2.10 keV and 2.41 keV for tin and galinstan respectively (Fig. 4.38). The total ion fluence per discharge at the position of Faraday cup 50 cm from the discharge axis was calculated as 4.3×10^{10} ions/cm^2 for tin and 3.8×10^{10} ions/cm^2 for galinstan, In both cases roughly 2% of the ion fluence are found to be above 10 keV.

4.4.2 Thin film deposition

The angular distribution of material from the plasma was deposited on a curved transparent plastic substrate. This thin film was analysed using a calibrated flatbed scanner operating in transmission mode. The scanned image was recorded with a resolution of 150 dots per inch meaning each pixel is approximately 170 μm. The thin film thickness profile was obtained by measuring the optical transmission of the film. The image data was processed to separate the data into red, green and blue counts matrices. Only the green part of the image matrix was required, assuming a wavelength of 515 nm. The scanner data was calibrated at this wavelength using a fitting function to yield a percentage transmission distribution for the film. Using the bulk refractive index values for the thin film material, in this case tin, the transmission can be converted to thickness.

A curved plastic substrate was placed in the path of the plasma expansion with a radius of 4 cm centred on the ablation spot as shown in Fig. 4.39. The anode wheel and bath were removed to accomplish this. A thin film was deposited on the substrate with 6000 shots at a laser energy of 12 mJ. The bath was heated and cathode wheel rotated as in the discharge experiments. A hole was cut in the substrate to act as a window for the laser pulse. The angular distribution of the material is analysed by scanning the substrate flat and calibrating the image matrix to give transmission versus angle.

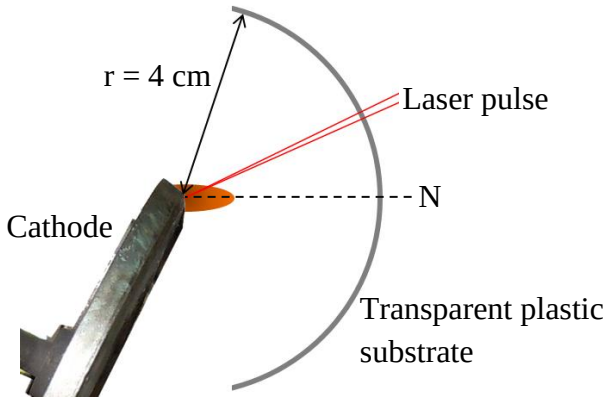

Fig. 4.39 – Top down schematic of the cathode wheel and laser plasma with a curved transparent plastic substrate placed 4 cm from the ablation spot.

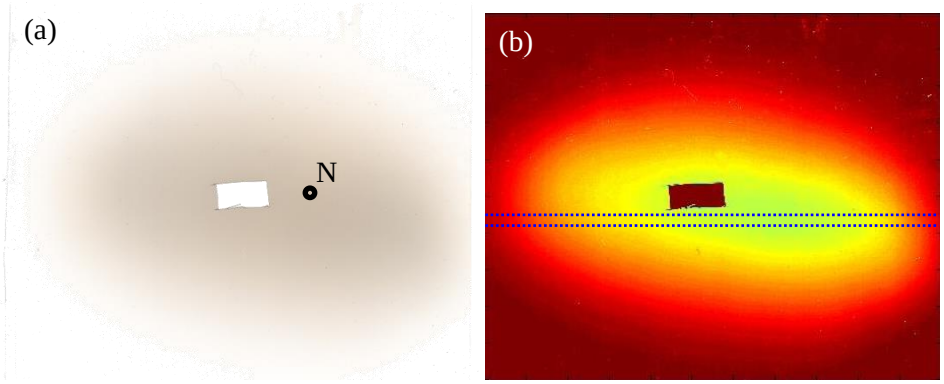

Fig. 4.40 – (a) Flatbed scanner image of thin film deposition from 6000 laser shots with the plasma expansion normal N indicated and (b) green transmission at 515 nm with the region averaged across marked by a blue dotted lines.

The transmission of the thin film was converted to a thickness per shot by taking the bulk absorption of tin at 515 nm. Based on this assumption a thickness of approximately 27 pm per shot was deposited at 4 cm from the ablation spot along the plasma expansion normal. The thickness distribution is plotted per shot in Fig. 4.41.

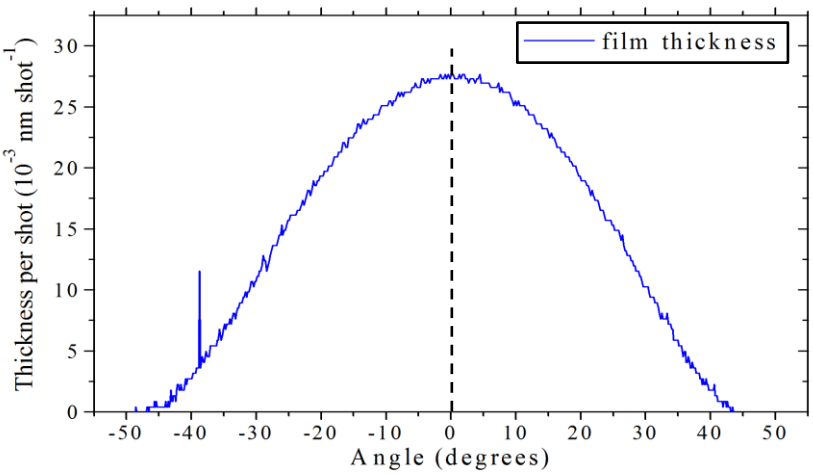

Fig. 4.41 – Ablated material distribution in thickness per shot, the film was deposited onto a curved transparent plastic substrate positioned 4 cm from the ablation spot with 6000 shots.

The profile of the deposited material in Fig. 4.41 is similar to the ion angular distribution measured with the translational ion probe. It can be noted that no material is deposited above roughly 45° here although the Anisimov fit of the ion angular distribution predicted that material would be deposited on the semi-circular substrate up to approximately 60° from target normal. No material is expected perpendicular to the plasma flow, and this is in agreement with thin film deposition made as shown in Fig. 4.50.

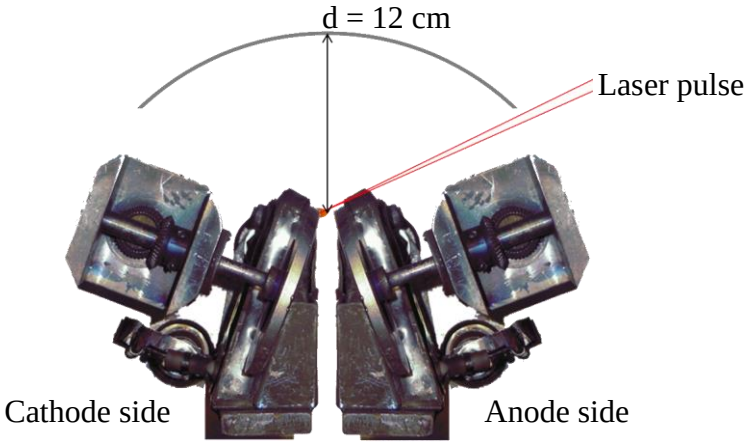

Fig. 4.42 – Top down schematic of both electrode wheels with a curved transparent plastic substrate placed 12 cm from the discharge axis with a radius of curvature of roughly 18 cm. In this setup thin films were made with and without discharge.

The thin film depositions made around the perpendicular with no discharge (Fig 4.43) showed a very small amount of material flow at angles above the edge of the substrate at 30° to the plasma expansion normal or discharge axis. At the centre of this film, perpendicular to the discharge axis, more than 95% transmission is measured.

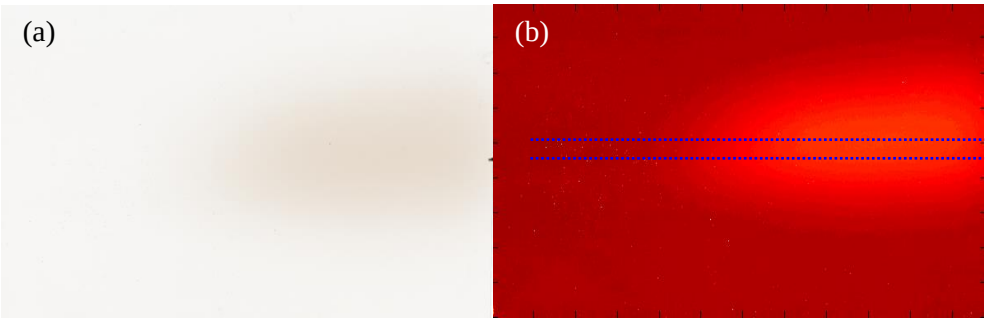

Fig. 4.43 – (a) Flatbed scanner image of thin film deposition from 15000 laser shots and (b) green transmission at 515 nm with the region averaged across marked by a blue dotted lines.

A thin film was also deposited in the same position as in Fig. 4.51, with a 4 J (4.5 kV) discharge. The film was deposited with 1500 shots, in this case the plastic deposition has much lower transmission (Fig. 4.45), with a mirror like reflection at the thickest point. There is also a strong green-blue hue. The film was analysed as with the other films above, resulting in a relatively flat topped thickness distribution. The estimation of thickness at the lower transmission is not well characterised. In Fig. 2.44 presented in the experimental procedure for this analysis it can be seen that no data points were collected below roughly 30% transmission. However, based on the remainder of the film some points of interest are apparent.

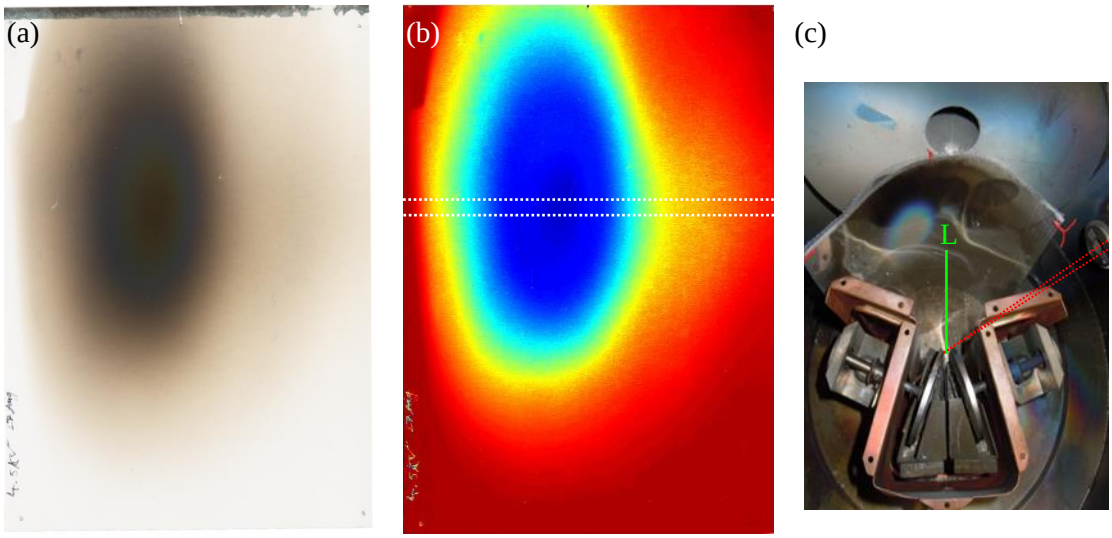

Fig. 4.45 – Thin film deposition made on a transparent curved plastic sheet with tin as source material. The film was produced with a 4 J discharge ignited by a 12 mJ laser plasma over 1500 shots. The inlay photograph was not taken as a top view to clearly show the orientation of the plastic sheet. The plastic sheet had a 18 cm radius of curvature centred on the middle of the chamber. The sheet is approximately 12 cm from the discharge axis measured along a perpendicular line L.

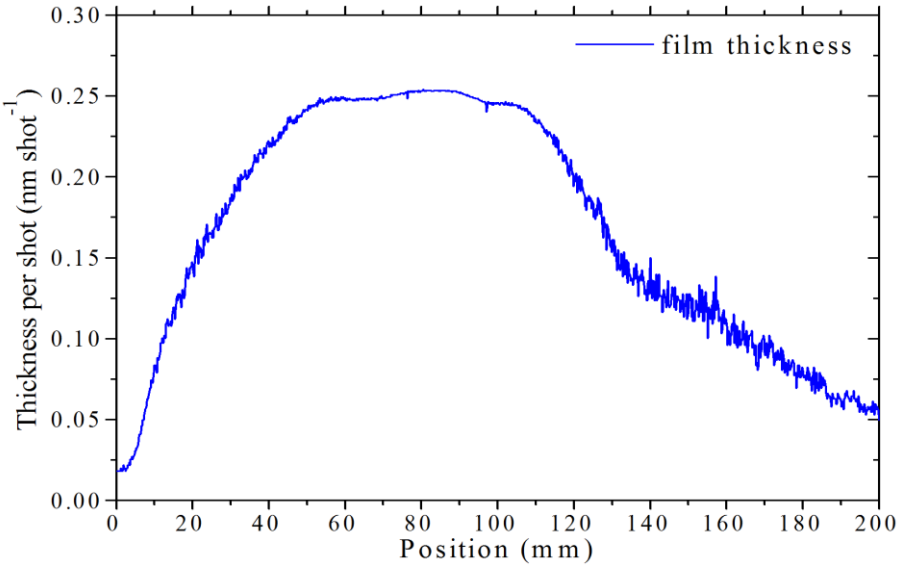

Fig. 4.46 – Distribution of material along a region selected on the film shown in Fig. 4.45 marked by white lines in (b). The flat topped shape is possibly erroneous due to the lack of calibration data at low transmission values.

The thin film deposited with 1500 shots of a 4 J discharge shown in Fig. 4.45 and Fig. 4.46 has a much larger thickness per shot than without discharge as expected. The interesting result from this is the apparent bias in distribution to one side of the chamber.

4.5 Optical emission spectroscopy

4.5.1 Temporally- and spatially resolving spectroscopy

The visible emission from the Laser Assisted Vacuum Arc lamp was studied using the 0.25 m Oriel MS260i spectrometer and Andor DH-520 ICCD camera described in Section 2.4. The time- and space-resolved optical emission spectroscopy (OES) recorded the emission from near the surfaces of both electrode wheels and inter-electrode gap, using a minimum ICCD gate time of 10 ns.

A schematic of the optical imaging system is shown in Fig. 4.47 (a). Reading from right to left; the light from the plasma was transmitted through a vacuum flange mounted glass window placed orthogonal to the discharge axis and 30º above the horizontal plane. The first mirror M1 was used to direct the light along the horizontal plane to the periscope (consisting of mirrors M2 and M3). The periscope is used to rotate the light 90º such that the horizontal discharge axis is imaged onto the vertical spectrometer slit. It was necessary to include a Dove prism to rotate the imaging plane further, due to the effect of viewing plasma at 30º above the horizontal plane. The lens position was selected to image of a ~5.3 mm long region at the discharge axis (with the inner-electrode gap being ~4 mm long), onto the 3 mm spectrometer slit with a magnification of 0.56. The spatial resolution of the system was checked by imaging the inter-electrode gap onto the slit with a uniform light source behind the object plane. The rising edges of the image were shown to be 10 pixels with each pixel being 26 µm, meaning a spatial resolution $\Delta x \approx 260$ µm at the object plane. The spectral range throughout this experiment was selected as 390 – 600 nm.

Fig. 4.47 (b) shows a time integrated photograph of the discharge axis, viewed from the same vacuum flange mounted window used for the OES. This photograph has a red box overlaid to indicate the imaged region of the discharge axis, with both electrode wheels marked. To capture this photograph a pair of polaroid sheets were rotated to lower the transmitted light and avoid saturating the digital camera (Nikon Coolpix S3500). This allowed for the intense emission regions of the plume to be recorded.

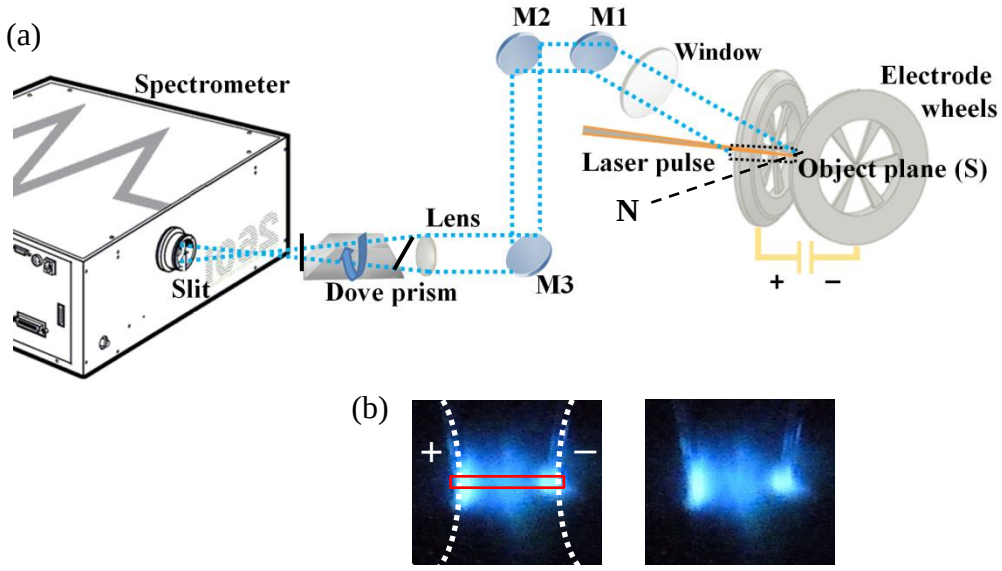

Fig. 4.47 – (a) Schematic of the optical emission spectroscopy imaging system and (b) time integrated photograph of the plasma with a 4.5 kV discharge illustrating the electrode wheel positions (white dash) and the region imaged onto the spectrometer slit (red rectangle).

Fig. 4.48 shows top and side view schematics of the two electrode wheels to display OES field of view throughout this work. The discharge axis, shown by a grey dashed line in (a), was viewed at 30° to the horizontal.

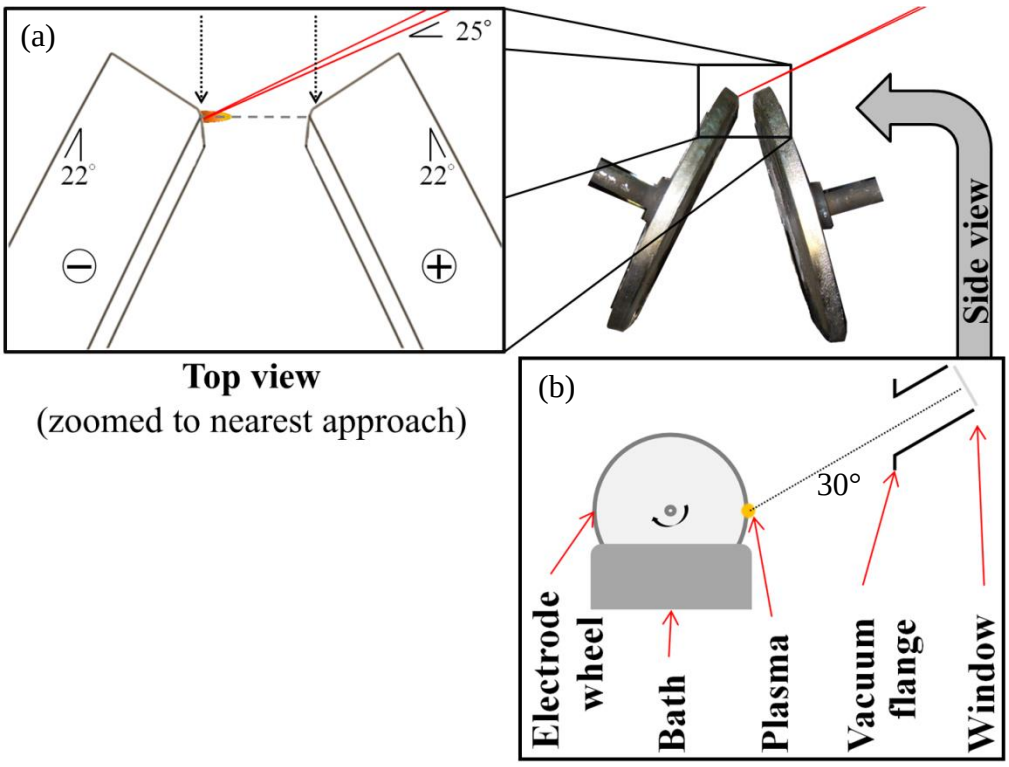

Fig. 4.48 – (a) Top view and (b) side view schematics of the OES field of view, oriented to view the discharge axis at 30° to the horizontal.

A scale representation of the limiting apertures and light collection of the free space optics used in the OES system is presented in Fig. 4.49. The optical system has a total length of 1.3 m from the object plane S to the spectrometer slit, with the lens positioned 82 cm from S, 48 cm from the slit. The collected cone of light is elliptical due to the 2.54 cm diameter periscope mirrors M2 and M3 being at 45°, presenting an elliptical aperture to the light path with the minor radii of the ellipse being due to M3 (red line). This ellipse determines the solid angle of the optical system.

$$\Omega_{sys} = \frac{(\pi(r_1 \times r_2))}{x^2} \qquad \text{Eqn. 4.23}$$

From Eqn. 4.23 the solid angle of the cone viewed by the spectrometer is 6.29×10^{-4} sr, where x is the distance from S to the lens (82 cm). Estimating Ω_{sys} for the LAVA lamp OES imaging system allows us to calculate the spectra in spectral radiance $L(\lambda)$ [$Wm^{-2}nm^{-1}sr^{-1}$]. The ellipse at the lens position maps out acceptance half angles at the spectrometer slit of $\theta_1 = 1.26°$ and $\theta_2 = 1.52°$ from the lens. Both of these angles are smaller than the spectrometer acceptance half angle θ_{spect} =7.4°, we are therefore under-filling the spectrometer slit. These acceptance half angles, as with those shown in Fig. 4.49 were calculated using Eqn. 4.24.

$$\theta = \tan^{-1}\left(\frac{r}{x}\right) \qquad \text{Eqn. 4.24}$$

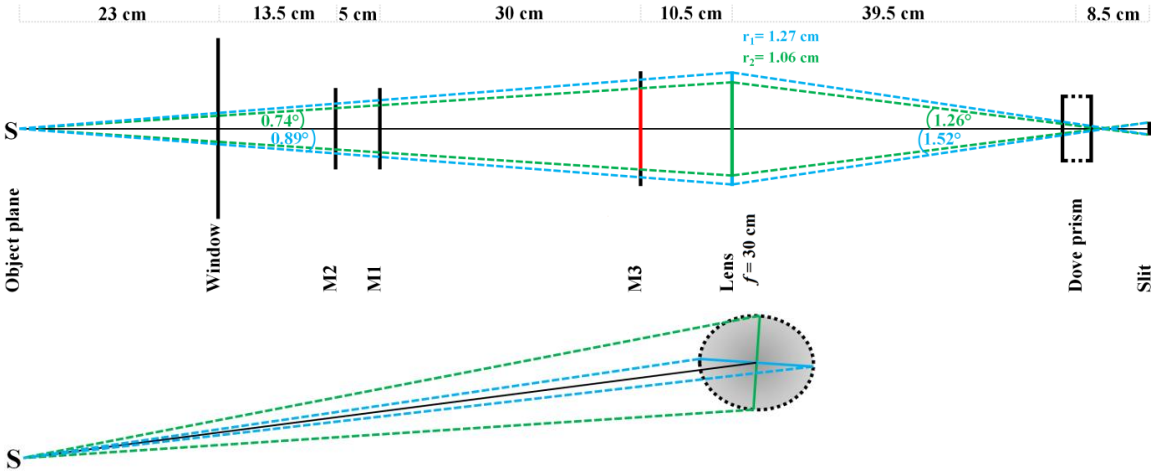

Fig. 4.49 – Scale representations of the optical system showing the limiting apertures dictating the light collection solid angle. The light collection resulting from the system is elliptical with major and minor radii mapped onto the lens position (r_1 and r_2 above), the minor radii caused by M3 mapped onto the lens.

In the rest of this section the experimental results from the OES of tin as emitter materials in the LAVA lamp, will be presented. The time- and space-resolved spectra will be broken into five time phases and 3 main spatial regions. The five plasma phases are named according to the characteristics of the visible emission spectra;

1) ablation plasma expansion phase,

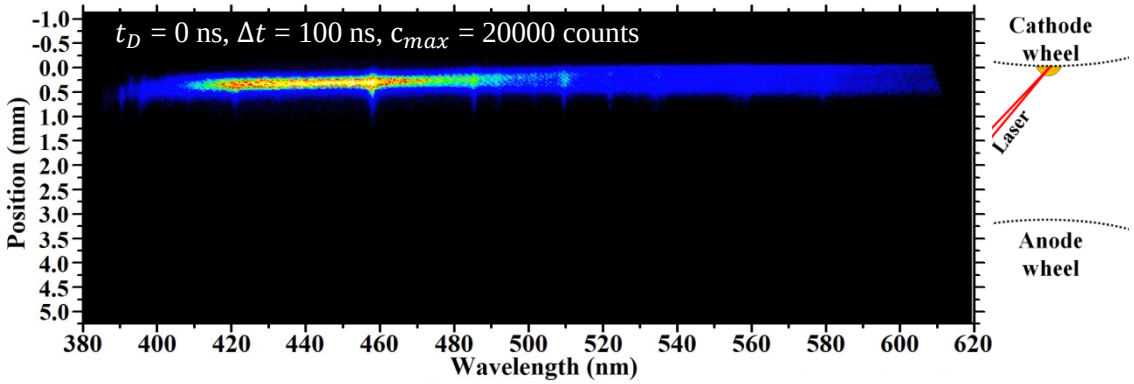

Fig. 4.50 – Early continuum and line emission of Sn ~1×10^8 W cm^{-2} laser triggered 4.5 kV discharge plasma.

2) anode emission,

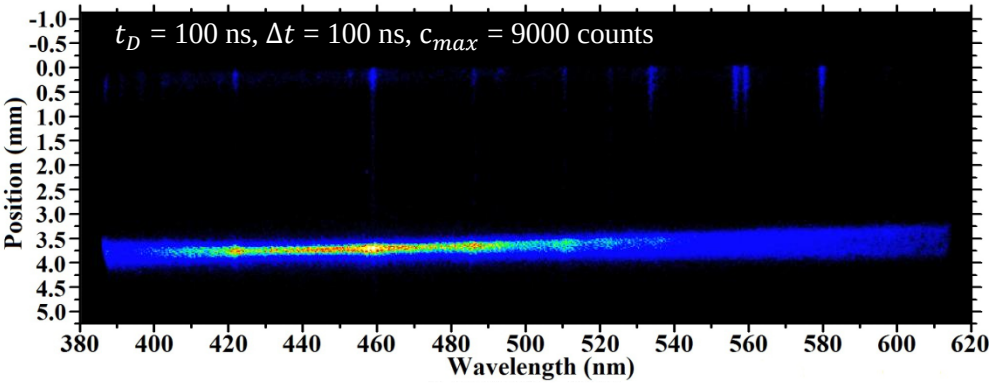

Fig. 4.51 – Hot anode emission originating around the onset of 4.5 kV Sn, the laser produced plasma reaches the anode at ~170 ns after the laser pulse begins, without voltage this intense anode continuum is not observed.

3) emission on both electrodes,

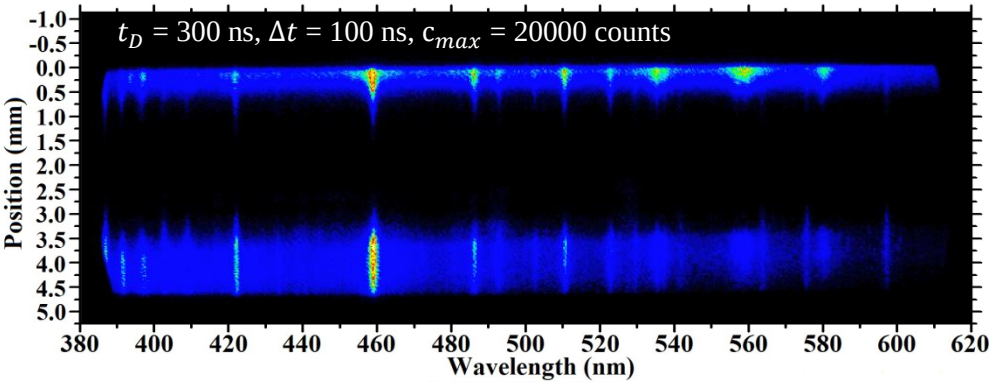

Fig. 4.52 – Strongly broadened Sn line emission and quasi-continua on both electrodes at 300 ns delay.

4) localised inter-electrode emission,

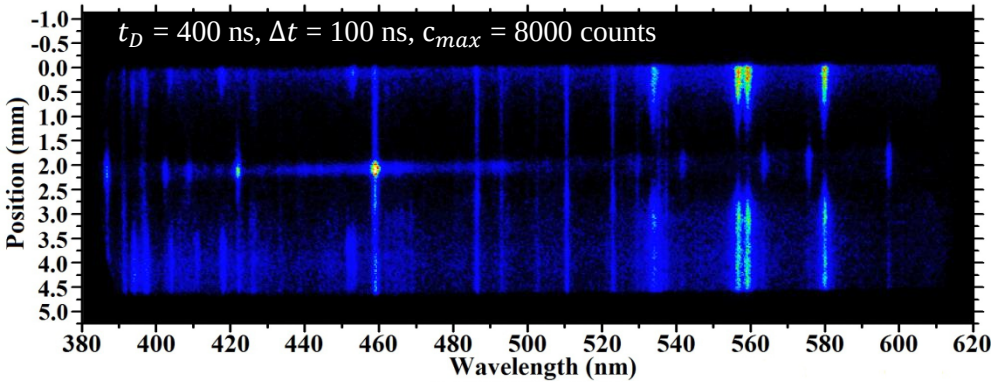

Fig. 4.53 – Quasi-continuum emission in the centre region recorded at 400 ns delay for Sn discharge plasma.

5) extended inter-electrode emission.

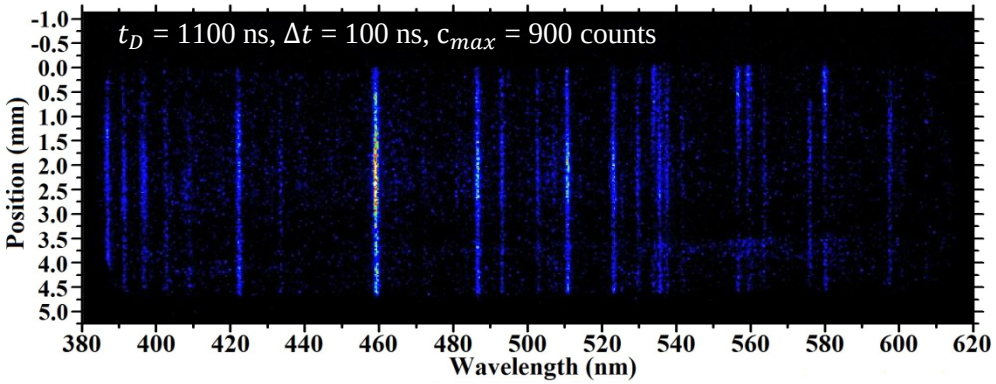

Fig. 4.54 – Sn line emission throughout the spatial scale at 1.1 μs delay from Sn II – Sn IV.

As can be seen from Fig. 4.50 to Fig. 4.53 the visible emission shows substantial spectral broadening and intense quasi-continua. The last of these plasma phases (Fig. 4.54) shows narrow line emission with decaying intensity into late times as the amplitude damped discharge oscillation decreases. In the analysis of these spectra the spatial domains are broken into three main sections, the cathode region, the inter-electrode gap, and the anode region (behind, on and in-front of the cathode/anode along with a variety of positions in the gap have been studied). Each of the selected spatial domains is spatially averaged over 6 ICCD pixels which corresponds to ~170 μm length of the discharge axis (each pixel being 26 μm with a total optical system magnification of 0.93 from discharge axis to ICCD).

Fig. 4.55 shows an illustration of the electrode wheels and inter-electrode gap highlighting sample regions and giving their pixel position and corresponding distances from cathode. The temporal and spatial regions will analyse in terms of electron temperature and density by their spectra line emission. The five plasma phases will be discussed with respect to the ICCD delay time $\mathbf{t}_D$ with a noted gate time. Fig. 4.56 shows an example TTL pulse used to trigger and gate the ICCD (indicating the delay time).

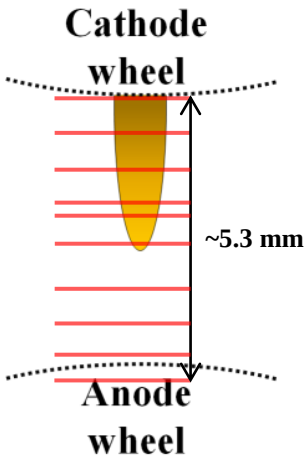

Pixel position	Distance from cathode
202	0.09 mm
183	0.66 mm
161	1.33 mm
141	1.93 mm
133	2.17 mm
116	2.68 mm
88	3.50 mm
68	4.13 mm
49	4.70 mm
30	5.28 mm

Fig. 4.55 – Illustration of the electrode wheels showing an example of the spatial regions studied by OES with the pixel position and distance from cathode of these sample regions given. The inner-electrode gap was approximately 4 mm and the region imaged onto the spectrometer slit was ~5.3 mm.

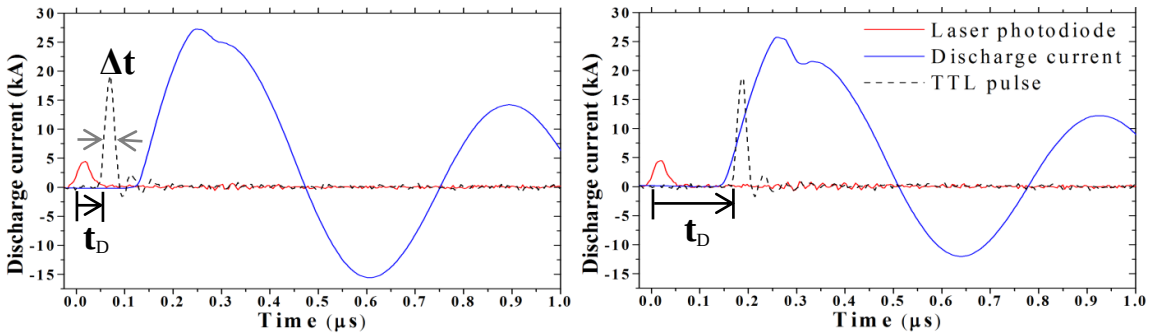

Fig. 4.56 – Two sample temporal current profiles for 12 mJ laser triggered Sn 5.5 kV discharges plasmas, showing the trigger laser pulse profile recorded by fast photodiode, along with the digital delay generator transistor–transistor logic (TTL) pulse used to trigger the ICCD with delay $\mathbf{t}_D$ and gate $\mathbf{\Delta t}$.

4.5.2 Tin as a source material

Here the OES results presented are for the 6 J discharge with tin as source material. The dynamics of the laser assisted discharge plasma (LDP) are somewhat different for tin and galinstan experiments, so it is useful to consider the temporal profile of the discharge current when examining the spectra, to understand the transient events more completely. In Fig. 4.57 a typical current profile for a 5.5 kV (6 J) discharge triggered by a 12 mJ, 30 ns, 1064 nm laser pulse shows the temporal profiles of the laser pulse, Rogowski coil $\left(\frac{dI}{dt}\right)$, and PhysTeX EUV detector, normalised to the current axis. Line indicators are added to mark the start of each of the five plasma phases described above ($\mathbf{t_1}$ to $\mathbf{t_5}$ in Fig. 4.57). The plasma compression, or Z-pinch, event is marked by a red box at ~300 ns after the laser pulse (during the third phase) where the notch in $\frac{dI}{dt}$ and onset of EUV pulse are observed. The temporal shot-to-shot variation for each given set of parameters was noted and will be stated for each case reported.

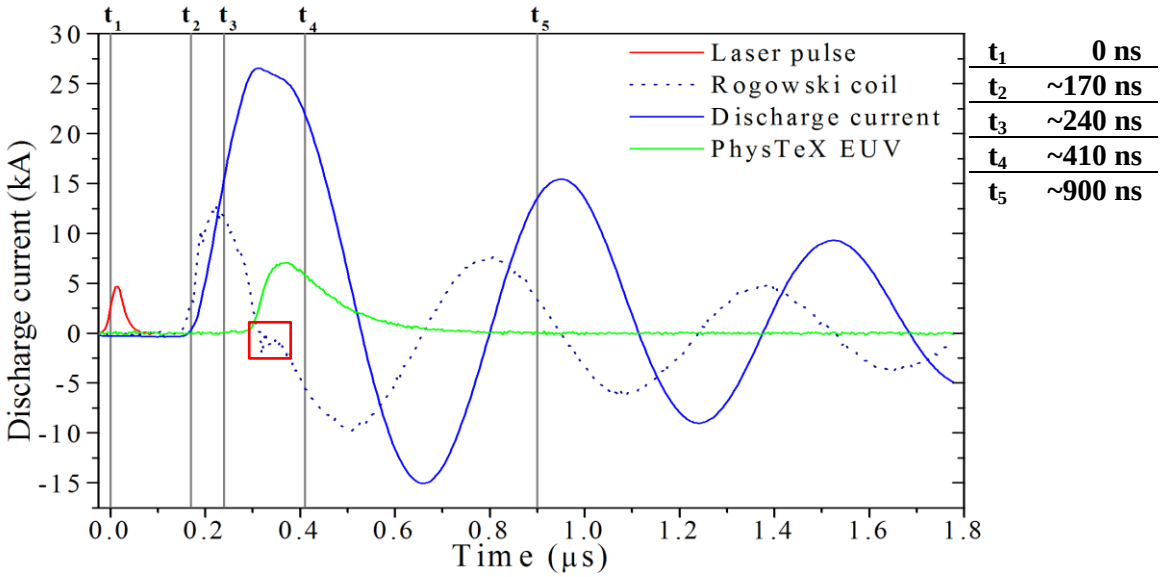

Fig. 4.57 – Sample current profile for a 5.5 kV (6 J) showing normalised laser pulse, Rogowski coil, and PhysTeX EUV detector signals along with line markings indicating the start of each plasma phase.

A literature review was undertaken to gather information on Sn line emission for the wavelength range of interest (~390 – 600 nm) to enable us to diagnose both the laser produced and the discharge heated plasmas. The information obtained from the literature is presented on the following pages for Sn I – Sn IV. Grotrian energy level diagrams are shown of the important transitions, followed by data tables with the transition probabilities and Stark width parameters for the observed atomic and ionic emission lines.

The large set of data given here is to help support any future optical emission spectroscopy of tin, as this author found it very difficult to gather resources to complete this work.

The information obtained from the literature for Sn I line emission in the spectral range of interest, the Stark broadening parameters and transition probabilities, are presented in Table 4.3 and Table 4.4 respectively with the accompanying Grotrian diagram Fig. 4.58.

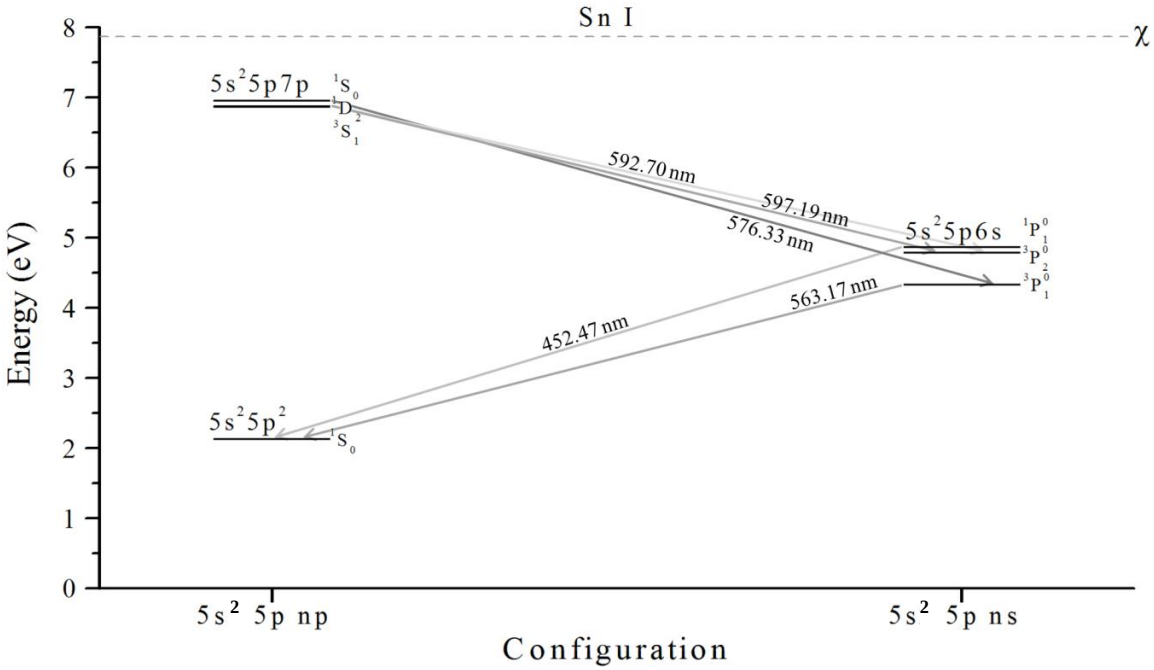

Fig. 4.58 – Grotrian diagram for transition lines of interest in Sn I from literature.

Table 4.3. Transition probabilities and emission line information for Sn I spectral lines from a variety of references presented for comparison of consistency between publications.

Transition	λ (nm)	E_i (eV)	E_k (eV)	g_i	g_k	A_{ki} (10^8 s^{-1})	Ref.
5p6s $^1P^0_1$ → 5p^2 $^1S_0$	452.474	2.12788	4.86725	1	3	0.26 ± 0.07	[101], [112]
						0.35 ± 0.12	[113]
						0.21 ± 0.02	[114]
5p6s $^3P^0_1$ → 5p^2 $^1S_0$	563.171	2.12788	4.32882	1	3	0.024 ± 0.012	[101], [115]
						0.18 ± 0.09	[113]
						0.021 ± 0.003	[114]
5p7p $^1S_0$ → 5p6s $^3P^0_1$	576.33	4.3288191	6.9560596	3	1	0.0048 ± 0.0024	[115]
						0.0038 ± 0.0004	[114]
5p7p $^1D_2$ → 5p6s $^3P^0_2$	592.70	4.7893700	6.8812433	5	5	0.022 ± 0.011	[115]
						0.017 ± 0.003	[114]
5p7p $^3S_1$ → 5p6s $^3P^0_2$	597.19	4.7893700	6.8654802	5	3	0.096	[101]
						0.095 ± 0.0475	[115]
						0.060 ± 0.006	[114]

*T indicates that the transition probability is a theoretical calculation

Table 4.4. Stark broadening full-width at half-max (FWHM) of Sn I spectral lines for various electron temperatures (T_e) and electron densities (N_e) from cited literature.

Transition	λ (nm)	T_e (eV)	N_e (10^{16} cm^{-3})	$\Delta\lambda$ (nm)	Ref.
5p6s $^1P^0_1$ → 5p^2 $^1S_0$	452.474	1.00	10.0	0.130 ± 0.04	[113]
		0.86	1.0	0.012 ± 0.004	[116]
		1.12	5.1	0.0134 ± 0.0021	[117]
		0.95	1.0	0.0086 ± 0.0013	[118]
5p6s $^3P^0_1$ → 5p^2 $^1S_0$	563.171	1.12	5.1	0.0424 ± 0.0068	[117]
		0.95	1.0	0.0054 ± 0.0008	[118]

The line emission from Sn II in the spectral range of interest is important for the Stark width electron density estimation. The most frequently observed Sn II lines are those from 6d and 4f which have a very similar upper energy level meaning the respective intensity of these lines will not be very sensitive to temperature. The Stark broadening parameters and transition probabilities are presented in Table 4.5 and Table 4.6 respectively with the accompanying Grotrian diagram Fig. 4.58.

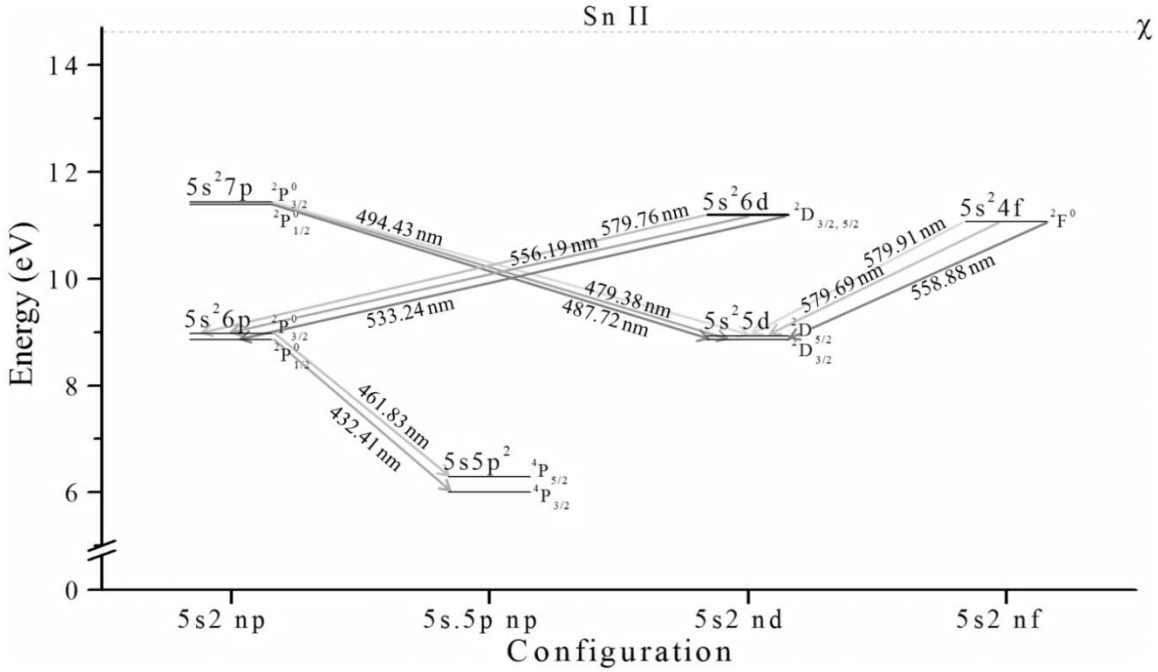

Fig. 4.59 – Grotrian diagram for lines of interest in Sn II from literature.

Table 4.5. Transition probabilities and emission line information for Sn II spectral lines from a variety of references presented for comparison of consistency between publications.

Transition	λ (nm)	E_i (eV)	E_k (eV)	g_i	g_k	A_{ki} (10^8 s^{-1})	Ref.
$6p\ ^2P^0_{1/2} \rightarrow 5s5p^2\ ^4P_{3/2}$	432.41	5.99687	8.86416	4	2	0.0011 *T	[119]
$6p\ ^2P^0_{3/2} \rightarrow 5s5p^2\ ^4P_{5/2}$	461.83	6.28972	8.97360	6	4	0.0054 ± 0.0019	[113]
						0.0059 ± 0.0010	[120]
						0.0096 *T	[119]
$7p\ ^2P_{3/2} \rightarrow 5d\ ^2D_{3/2}$	479.38	8.85317	11.43952	4	4	0.0052 *T	[119]
$7p\ ^2P_{1/2} \rightarrow 5d\ ^2D_{3/2}$	487.72	8.85317	11.39452	4	2	0.013 ± 0.005	[120]
						0.049 *T	[119]
$7p\ ^2P_{3/2} \rightarrow 5d\ ^2D_{5/2}$	494.43	8.93276	11.43952	6	4	0.011 ± 0.003	[120]
						0.048 *T	[119]
$6d\ ^2D_{3/2} \rightarrow 6p\ ^2P^0_{1/2}$	533.24	8.864	11.18846	2	4	0.86 ± 0.31	[101], [115]
						1.20 ± 0.3	[113]
						0.58 ± 0.1	[120]
						1.09 *T	[119]
$6d\ ^2D_{5/2} \rightarrow 6p\ ^2P^0_{3/2}$	556.19	8.9736	11.2021	4	6	1.2	[101]
						1.18 ± 0.40	[115]
						1.30 ± 0.32	[113]
						0.91 ± 0.19	[120]
						1.15 *T	[119]

*T indicates that the transition probability is a theoretical calculation

Table 4.5. *continued…*

Transition	λ (nm)	E_i (eV)	E_k (eV)	g_i	g_k	A_{ki} (10^8 s^{-1})	Ref.
4f $^2F^0_{5/2}$ → 5d $^2D_{3/2}$	558.88	8.85321	11.07104	4	6	0.85	[101]
						0.87 ± 0.35	[115]
						1.10 ± 0.28	[113]
						0.68 ± 0.06	[120]
						0.58 *T	[119]
6d $^2D_{3/2}$ → 6p $^2P^0_{3/2}$	559.76	8.9736	11.18846	4	4	0.15	[101]
						0.147 ± 0.05	[115]
						0.13 ± 0.055	[113]
						0.13 ± 0.02	[120]
						0.19 *T	[119]
4f $^2F^0_{5/2}$ → 5d $^2D_{5/2}$	579.69	8.93281	11.06303	6	6	0.28 ± 0.10	[101], [115]
						0.1 ± 0.05	[113]
						0.088 ± 0.1	[120]
						0.038 *T	[119]
4f $^2F^0_{7/2}$ → 5d $^2D_{5/2}$	579.91	8.93281	11.0703	6	8	0.81 ± 0.29	[101], [115]
						0.74 ± 0.23	[113]
						0.81 ± 0.16	[120]
						0.57 *T	[119]

*T indicates that the transition probability is a theoretical calculation

Table 4.6. Stark broadening full-widths-at-half-max (FWHM) of Sn II spectral lines for various electron temperatures (T_e) and electron densities (N_e) from cited literature.

Transition	λ (nm)	T_e (eV)	N_e (10^{16} cm^{-3})	Δλ (nm)	Ref.
7p $^2P^0_{1/2}$ → 5d $_2D_{3/2}$	487.722	0.86	1.0	0.044 ± 0.006	[116]
		1.12	5.1	0.0445 ± 0.0062	[117]
7p $^2P^0_{3/2}$ → 5d $_2D_{5/2}$	494.60	0.86	1.0	0.040 ± 0.008	[116]
6d $^2D_{3/2}$ → 6p $^2P^0_{1/2}$	533.236	1.0	10.0	0.530 ± 0.07	[113]
		0.86	1.0	0.060 ± 0.008	[116]
		1.12	5.1	0.0298 ± 0.0042	[117]
		0.95	1.0	0.055 ± 0.007	[118]
6d $^2D_{5/2}$ → 6p $^2P^0_{3/2}$	556.195	1.0	10.0	0.530 ± 0.07	[113]
		0.86	1.0	0.052 ± 0.008	[116]
		1.12	5.1	0.0298 ± 0.0042	[117]
		0.95	1.0	0.055 ± 0.007	[118]
4f $^2F^0_{5/2}$ → 5d $^2D_{3/2}$	558.892	1.0	10.0	0.380 ± 0.1	[113]
		2.85	9.6	0.077	[121]
		0.86	1.0	0.0380 ± 0.006	[116]
		1.12	5.1	0.0310 ± 0.0043	[117]
		0.95	1.0	0.036 ± 0.004	[118]
6d $^2D_{3/2}$ → 6p $^2P^0_{3/2}$	559.62	0.86	1.0	0.046 ± 0.006	[116]
		0.95	1.0	0.063 ± 0.008	[118]
4f $^2F^0_{5/2}$ → 5d $^2D_{5/2}$	579.720	0.86	1.0	0.036 ± 0.006	[116]
		1.14	7.2	0.0548 ± 0.0077	[117]
4f $^2F^0_{7/2}$ → 5d $^2D_{5/2}$	579.918	1.0	10.0	0.420 ± 0.12	[113]
		0.86	1.0	0.0340 ± 0.008	[116]
		1.12	5.1	0.0366 ± 0.0051	[117]

The Sn III line emission observed has not been studied by many authors, with the substantial information on these being from theoretical calculations based mainly on the need to characterise astrophysical Sn plasmas. The Stark broadening parameters and transition probabilities are presented in Table 4.7 and Table 4.8 respectively with the accompanying Grotrian diagram Fig. 4.60.

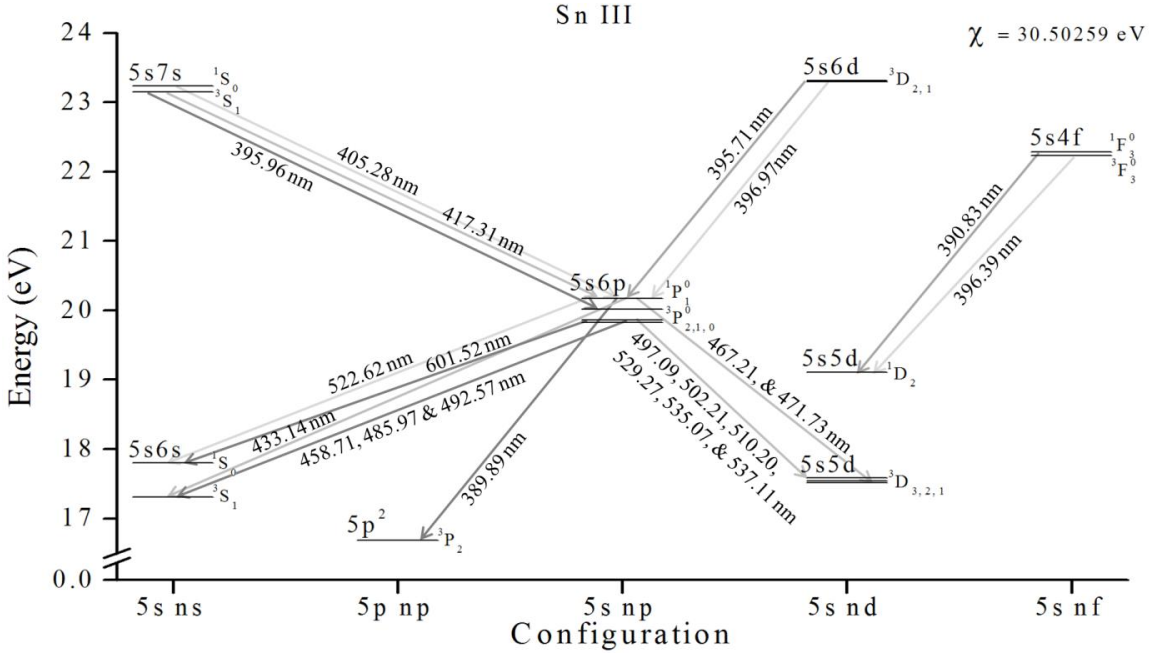

Fig. 4.60 – Grotrian diagram for lines of interest in Sn III from literature.

Table 4.7. Theoretical transition probabilities for Sn III spectral lines calculated by Colón, Alonso-Medina and Rivero[122] with configuration information taken from NIST[101].

Transition	λ (nm)	E_i (eV)	E_k (eV)	g_i	g_k	A_{ki} (10^8 s^{-1})	Ref.
6p $^3P_1$ → 5p^2 $^3P_2$	389.89	16.68420	19.86418	5	3	0.0073 *T	[122]
4f $^1F_3$ → 5d $^1D_2$	390.83	19.10788	22.28023	5	7	0.95 *T	[122]
6d $^3D_2$ → 6p $^1P_1$	395.71	20.17534	23.30857	3	5	0.12 *T	[122]
7s $^3S_1$ → 6p $^3P_2$	395.96	20.01581	23.1464	3	5	2.1 *T	[122]
4f $^3F_3$ → 5d $^1D_2$	396.39	19.10788	22.2357	5	7	0.055 *T	[122]
6d $^3D_1$ → 6p $^1P_1$	396.97	20.17534	23.29858	3	3	0.094 *T	[122]
7s $^1S_0$ → 6p $^1P_1$	405.28	20.17534	23.23457	3	1	2.6 *T	[122]
7s $^3S_1$ → 6p $^1P_1$	417.31	20.17534	23.1464	3	3	0.79 *T	[122]
6p $^1P_1$ → 6s $^3S_1$	433.14	17.31289	20.17534	3	3	0.14 *T	[122]
6p $^3P_2$ → 6s $^3S_1$	458.71	17.31289	20.01581	3	5	1.53 *T	[122]
6p $^1P_1$ → 5d $^3D_1$	467.21	17.52163	20.17534	3	3	0.023 *T	[122]
6p $^1P_1$ → 5d $^3D_2$	471.73	17.54704	20.17534	5	3	0.064 *T	[122]
6p $^3P_1$ → 6s $^3S_1$	485.97	17.31289	19.86418	3	3	1.22 *T	[122]
6p $^3P_0$ → 6s $^3S_1$	492.57	17.31289	19.83001	3	1	1.26 *T	[122]
6p $^3P_2$ → 5d $^3D_1$	497.09	17.52163	20.01581	3	5	0.010 *T	[122]
6p $^3P_2$ → 5d $^3D_2$	502.21	17.54704	20.01581	5	5	0.15 *T	[122]
6p $^3P_2$ → 5d $^3D_3$	510.20	17.58568	20.1581	7	5	0.81 *T	[122]
6p $^1P_1$ → 6s $^1S_0$	522.62	17.80299	20.17534	1	3	0.89 *T	[122]
6p $^3P_1$ → 5d $^3D_1$	529.27	17.52163	19.86418	3	3	0.20 *T	[122]
6p $^3P_1$ → 5d $^3D_2$	535.07	17.54704	19.86418	5	3	0.59 *T	[122]
6p $^3P_0$ → 5d $^3D_1$	537.11	17.52163	19.83001	3	1	0.83 *T	[122]
6p $^3P_1$ → 6s $^1S_0$	601.52	17.80299	19.86418	1	3	0.046 *T	[122]

*T indicates that the transition probability is a theoretical calculation

Table 4.8. Stark broadening full-width at half-max (FWHM) of Sn III spectral lines for various electron temperatures (T_e) and electron densities (N_e) calculated by Alonso-Medina and Colón[123].

Transition	λ (nm)	T_e (eV)	N_e (10^{16} cm^{-3})	$\Delta\lambda$ (nm)	Ref.
6p $^3P_1$ → 5p^2 $^3P_2$	389.89	1.0	10.0	0.0852	[123]
		2.15	10.0	0.0524	[123]
		4.31	10.0	0.0350	[123]
		6.46	10.0	0.0280	[123]
4f $^1F_3$ → 5d $^1D_2$	390.83	1.0	10.0	0.08762	[123]
		2.15	10.0	0.05970	[123]
		4.31	10.0	0.04221	[123]
		6.46	10.0	0.03447	[123]
6d $^3D_2$ → 6p $^1P_1$	395.71	1.0	10.0	0.13991	[123]
		2.15	10.0	0.08772	[123]
		4.31	10.0	0.05949	[123]
		6.46	10.0	0.04804	[123]
7s $^3S_1$ → 6p $^3P_2$	395.96	1.0	10.0	0.1543	[123]
		2.15	10.0	0.0953	[123]
		4.31	10.0	0.0639	[123]
		6.46	10.0	0.0513	[123]
4f $^3F_3$ → 5d $^1D_2$	396.39	1.0	10.0	0.10711	[123]
		2.15	10.0	0.06677	[123]
		4.31	10.0	0.04495	[123]
		6.46	10.0	0.03614	[123]
6d $^3D_1$ → 6p $^1P_1$	396.97	1.0	10.0	0.11429	[123]
		2.15	10.0	0.07152	[123]
		4.31	10.0	0.04843	[123]
		6.46	10.0	0.03908	[123]
7s $^1S_0$ → 6p $^1P_1$	405.28	1.0	10.0	0.0849	[123]
		2.15	10.0	0.0528	[123]
		4.31	10.0	0.0356	[123]
		6.46	10.0	0.0287	[123]
7s $^3S_1$ → 6p $^1P_1$	417.31	1.0	10.0	0.1118	[123]
		2.15	10.0	0.0694	[123]
		4.31	10.0	0.0467	[123]
		6.46	10.0	0.0376	[123]
6p $^1P_1$ → 6s $^3S_1$	433.14	1.0	10.0	0.1535	[123]
		2.15	10.0	0.0953	[123]
		4.31	10.0	0.0642	[123]
		6.46	10.0	0.0516	[123]
6p $^3P_1$ → 6s $^3S_1$	458.71	1.0	10.0	0.2440	[123]
		2.15	10.0	0.1510	[123]
		4.31	10.0	0.1012	[123]
		6.46	10.0	0.0813	[123]
6p $^1P_1$ → 5d $^3D_1$	467.21	1.0	10.0	0.1480	[123]
		2.15	10.0	0.0915	[123]
		4.31	10.0	0.0613	[123]
		6.46	10.0	0.0492	[123]
6p $^1P_1$ → 5d $^3D_2$	471.73	1.0	10.0	0.1816	[123]
		2.15	10.0	0.1120	[123]
		4.31	10.0	0.0748	[123]
		6.46	10.0	0.0599	[123]
6p $^3P_1$ → 6s $^3S_1$	485.97	1.0	10.0	0.1968	[123]
		2.15	10.0	0.1218	[123]
		4.31	10.0	0.0817	[123]
		6.46	10.0	0.0657	[123]
6p $^3P_0$ → 6s $^3S_1$	492.57	1.0	10.0	0.1234	[123]
		2.15	10.0	0.0764	[123]
		4.31	10.0	0.0512	[123]
		6.46	10.0	0.0411	[123]
6p $^3P_2$ → 5d $^3D_1$	497.09	1.0	10.0	0.2520	[123]
		2.15	10.0	0.1553	[123]
		4.31	10.0	0.1037	[123]
		6.46	10.0	0.0832	[123]

Table 4.8. *continued ...*

Transition	λ (nm)	T_e (eV)	N_e (10^{16} cm^{-3})	$\Delta\lambda$ (nm)	Ref.
$6p\ ^3P_2 \rightarrow 5d\ ^3D_2$	502.21	1.0	10.0	0.3830	[123]
		2.15	10.0	0.1797	[123]
		4.31	10.0	0.1198	[123]
		6.46	10.0	0.0960	[123]
$6p\ ^3P_2 \rightarrow 5d\ ^3D_3$	510.28	1.0	10.0	0.3378	[123]
		2.15	10.0	0.2076	[123]
		4.31	10.0	0.1382	[123]
		6.46	10.0	0.1106	[123]
$6p\ ^1P_1 \rightarrow 6s\ ^1S_0$	522.62	1.0	10.0	0.1416	[123]
		1.0	10.0	0.122 ± 50%	[124]
		1.72	10.0	0.1077	[123]
		2.58	10.0	0.0881	[123]
		4.31	10.0	0.0682	[123]
		6.46	10.0	0.0557	[123]
$6p\ ^3P_1 \rightarrow 5d\ ^3D_1$	529.27	1.0	10.0	0.1649	[123]
		1.0	10.0	0.0860 ± 30%	[124]
		2.15	10.0	0.1125	[123]
		4.31	10.0	0.0795	[123]
		6.46	10.0	0.0649	[123]
$6p\ ^3P_1 \rightarrow 5d\ ^3D_2$	535.07	1.0	10.0	0.1992	[123]
		1.0	10.0	0.0680 ± 30%	[124]
		2.15	10.0	0.1362	[123]
		4.31	10.0	0.0963	[123]
		6.46	10.0	0.0791	[123]
$6p\ ^3P_0 \rightarrow 5d\ ^3D_1$	537.11	1.0	10.0	0.0887	[123]
		1.0	10.0	0.0640 ± 30%	[124]
		2.15	10.0	0.0604	[123]
		4.31	10.0	0.0427	[123]
		6.46	10.0	0.0349	[123]

The information in the literature for Sn IV visible spectroscopy is limited, with no relevant lines being found in published material. PrismSPECT the spectral synthesis suite[68], used by our group to model experimental spectra, was found to output several Sn IV lines in the visible emission range. Although these lines did not seem to match the experimentally observed Sn lines, by using the energy level information available from NIST[101] it was found that there was some correlation in the lines once wavelength shifted based on the NIST values. Consideration must be taken with the information presented in Table 4.9 which is based on the data tables in PrismSPECT, as some transitions are known to be missing from the software's data tables.

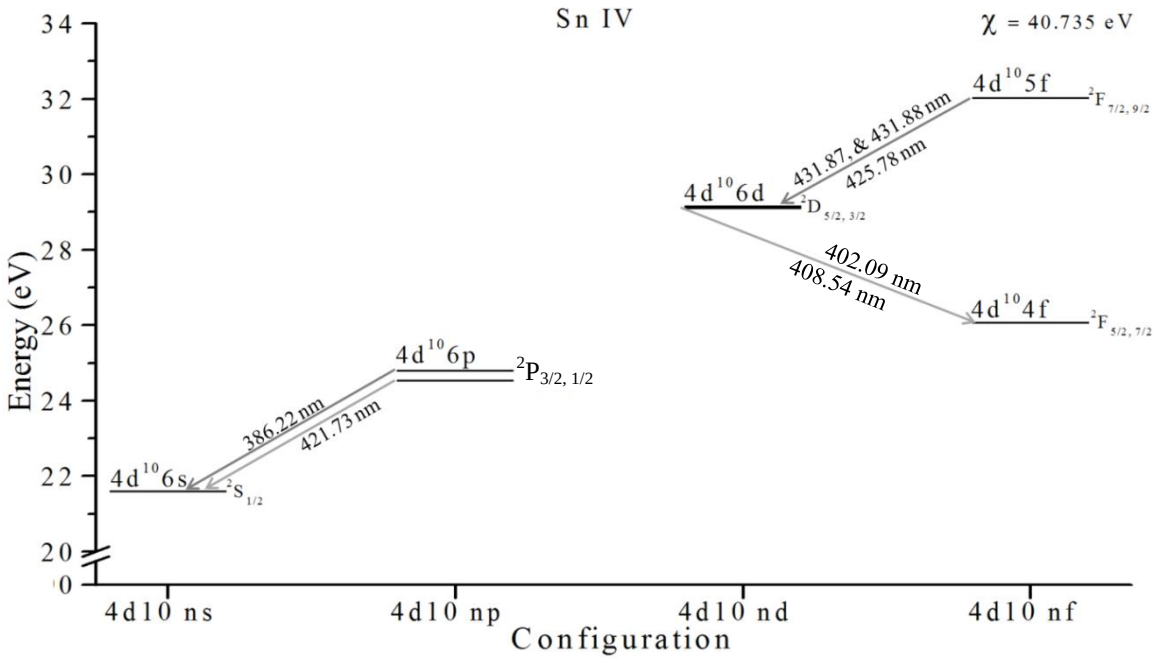

Fig. 4.61 – Grotrian diagram for lines of interest in Sn IV, line information taken from PrismSPECT[68], using NIST[101] to verify the configuration information where available.

Table 4.9. Line information for Sn IV spectral lines from PrismSPECT[68]

Transition	λ (nm)	E_i (eV)	E_k (eV)	g_i	g_k
6p $^2P_{3/2}$ → 6s $^2S_{1/2}$	386.22	21.59046	24.80066	2	6
6d $^2D_{5/2}$ → 4f $^2F_{7/2}$	402.09	26.06863	29.15212	6	8
6d $^2D_{3/2}$ → 4f $^2F_{5/2}$	408.54	26.07613	29.11096	4	6
6p $^2P_{1/2}$ → 6s $^2S_{1/2}$	421.73	21.59046	24.53038	2	2
5f $^2F_{9/2}$ → 6d $^2D_{3/2}$	425.78	29.11096	32.02292	4	9
5f $^2F_{7/2}$ → 6d $^2D_{5/2}$	431.87	29.15212	32.02297	6	8
5f $^2F_{9/2}$ → 6d $^2D_{5/2}$	431.88	29.15212	32.02292	6	9

Due to the large number of parameter variations studied (laser energies and discharge voltages) and the volume of data recorded for each experiment, the presented data will be limited to illustrative sets and interesting observations. The focus of the OES experimental study was on the plasma dynamics in terms of plasma temperatures and densities extracted from the spectra. To give a representative view of the data one set of time- and spatially-resolved OES images will be presented for each of the Sn and the galinstan experiments.

A sample set of optical emission spectra of a Sn laser plasma triggered discharge are presented, with a 12 mJ (~1×10^8 W cm^{-2}) laser pulse and a 6 J (5.5 kV) discharge. Each image has the max counts per pixel c_{max}, gate times Δt, and delay times t_D noted in the top left corner. The gate time was set at 10 ns for t_D < 220 ns, 20 ns thereafter, and 100 ns for t_D > 700 ns. The sample set is broken into the five plasma phases described previously (Section 4.6.1). The temperature and densities discussed for each phase with an overall comparison is presented towards the end of this section.

1) Laser produced plasma expansion phase

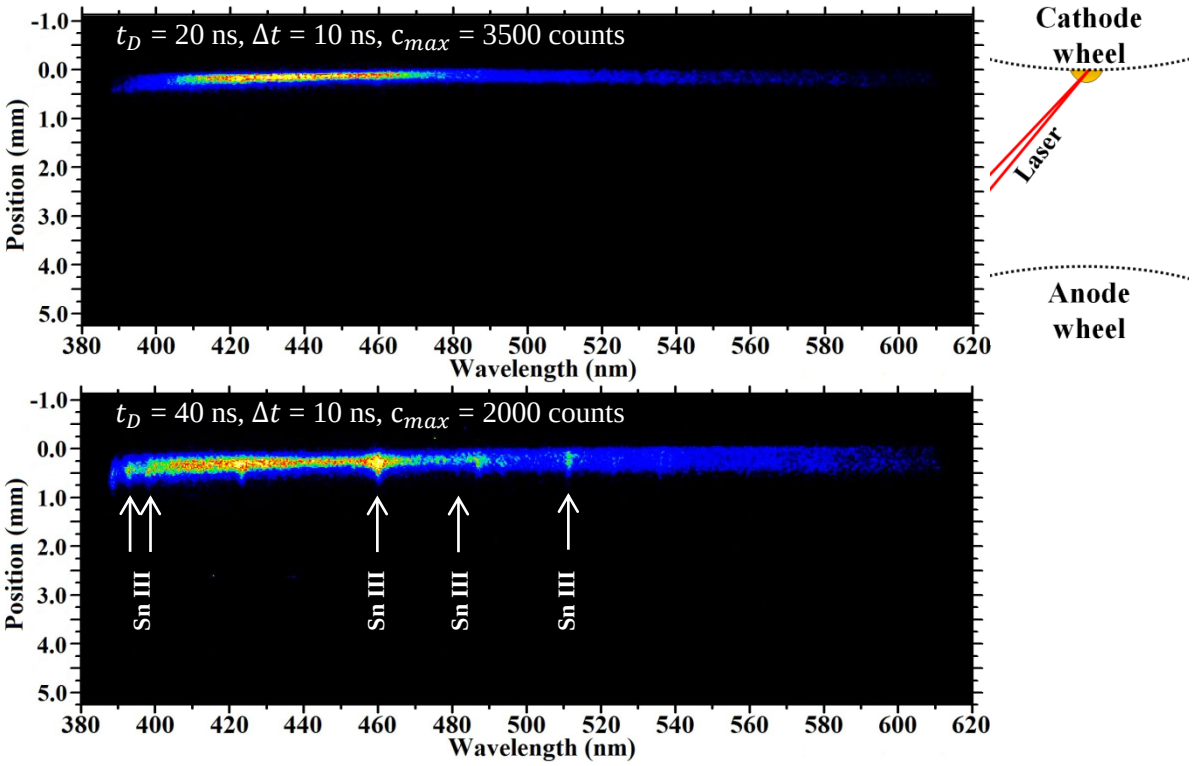

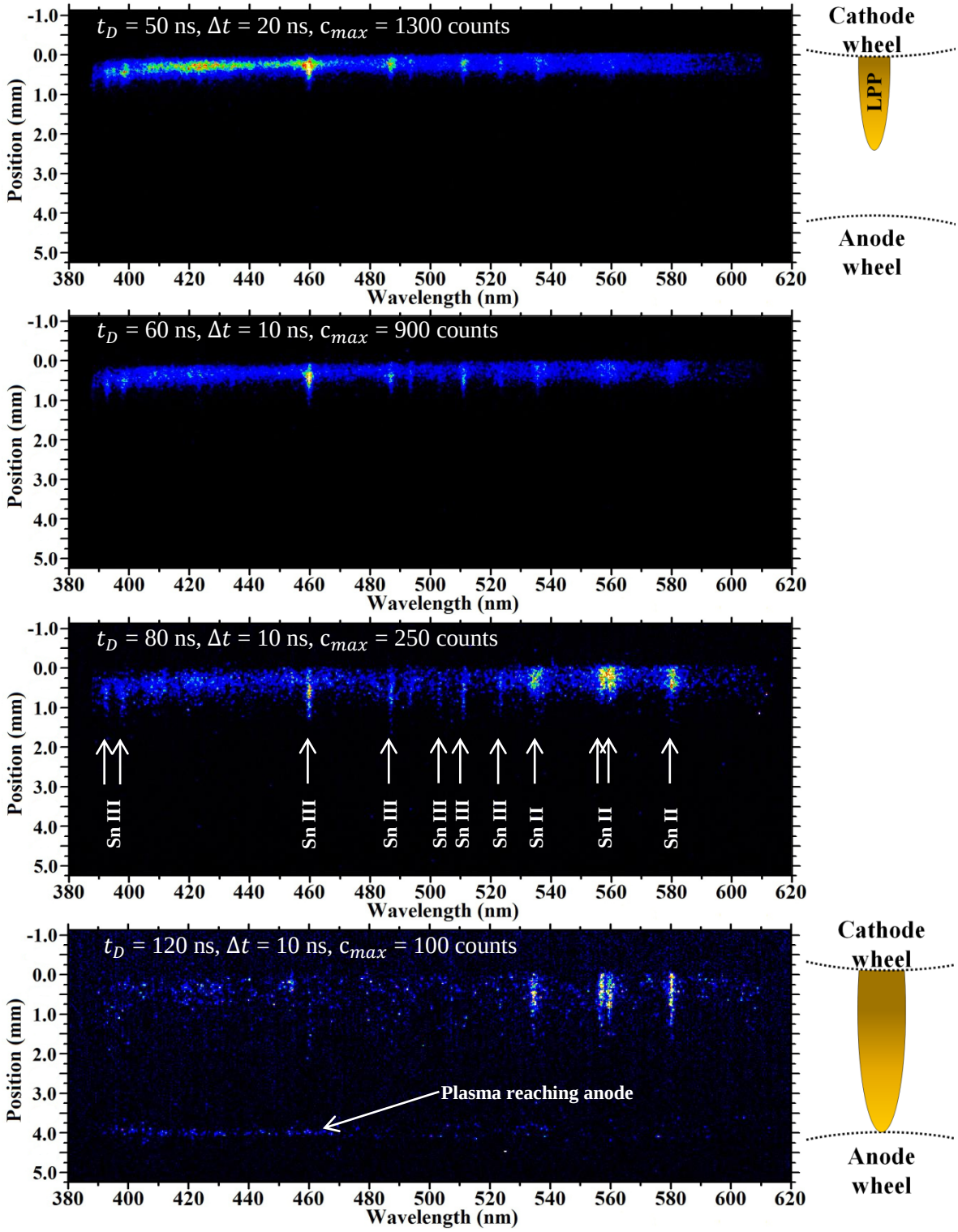

Fig. 4.62 – Spatially resolved OES of Sn 6 J discharge, during laser produced plasma expansion phase.

During this temporal phase a typical laser produced plasma expansion can be expected, the laser pulse ablates the cathode (seen at the top of the image at position 0 mm) and the laser pulse ends at $t_D \approx 30$ ns. The continuum emission observed is due mainly to bound-bound transitions between strongly Stark broadened energy levels[70],

with a peak emission found at ~420 nm (Fig. 4.63). At later times broad spectral lines emerge from the continuum, these lines narrow over time and the continuum emission decreases as the plasma expands into the inter-electrode gap and the plasma density decreases. The first lines to emerge from the continuum emission at these early times are broad Sn IV (6s-6p: 421.73 nm and 5f-6d: 431.87 nm) and Sn III lines (6s-6p: 458.71 nm and 485.97 nm along with 5d-6p: 510.2 nm) near the cathode surface followed by a period of mostly Sn II lines (6p-6d: 533.24 nm, 556.19 nm, along with 5d-4f: 558.88 nm and 579.91 nm), as the plume further expands and cools.

The recorded spectra at and near the cathode surface are presented in Fig. 4.63 with respect to time during the first plasma phase. The positions further from the cathode surface are similar to those presented at the later times, but with lower intensity. During these times there is a clear shift from continuum into Sn IV and Sn III emission followed by Sn II and some weak Sn I line emission toward the end of this first phase.

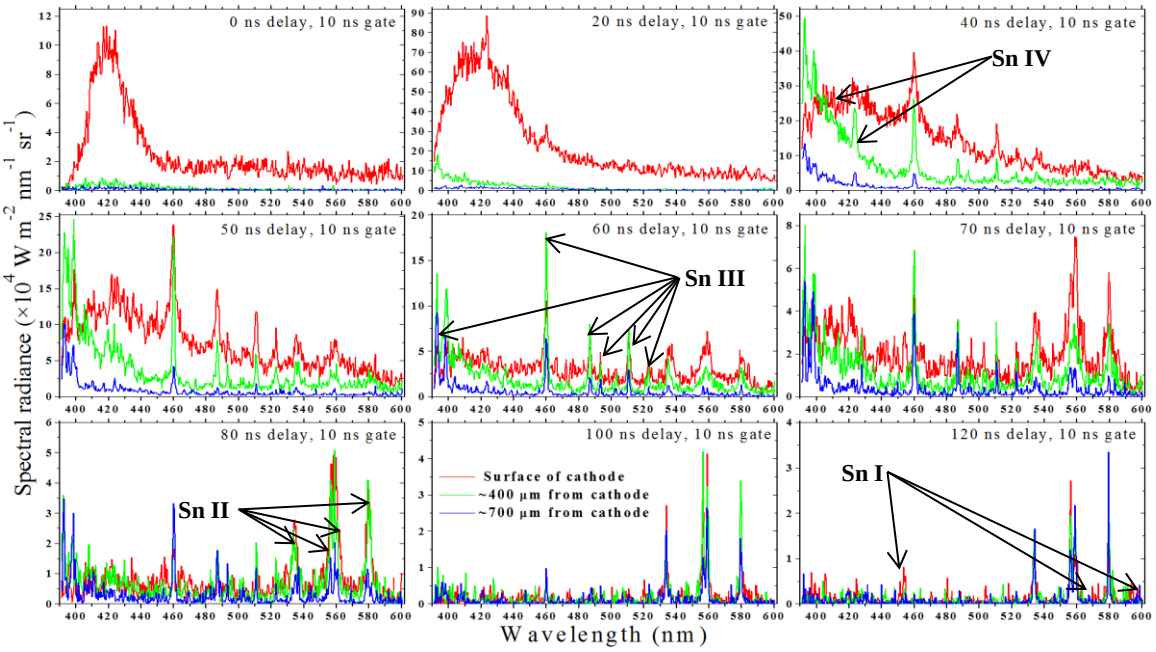

Fig. 4.63 – Full set of spectra for the first plasma phase, showing the shift from continuum to narrow line emission over time. The first lines that emerge are Sn IV and Sn III followed by Sn II at 70 ns. Three positions close to the cathode are shown.

Making an accurate estimate of the plasma temperature can be challenging during the early plasma phase due to the strong continuum with many overlapping broadened lines. The physical origin of such continua observed in the early stages of ns-LPP are discussed by this author with O'Connell et al.[70]. In that work the estimated temperature and density for the early laser produced plasma plume were estimated to be approximately 2 eV and 3×10^{19} cm^{-3}. Although the spectra presented in this work are not using zinc as the plasma material, we will assume these values as a rough guide for the tin and galinstan spectra in this work.

The spectral image is during the 30 ns laser pulse, mapping from the delay 20 ns to the end of the pulse (10 ns gate). Following this at 40 ns delay the line emission begins to become apparent. The broadened line widths at this time delay give an estimated electron density (N_e) of $(3.8 \pm 2.0) \times10^{17}$ cm^{-3} at the cathode surface with a fall off to $(2.2 \pm 0.4) \times10^{17}$ cm^{-3} at ~700 µm from the cathode (Fig. 4.64).

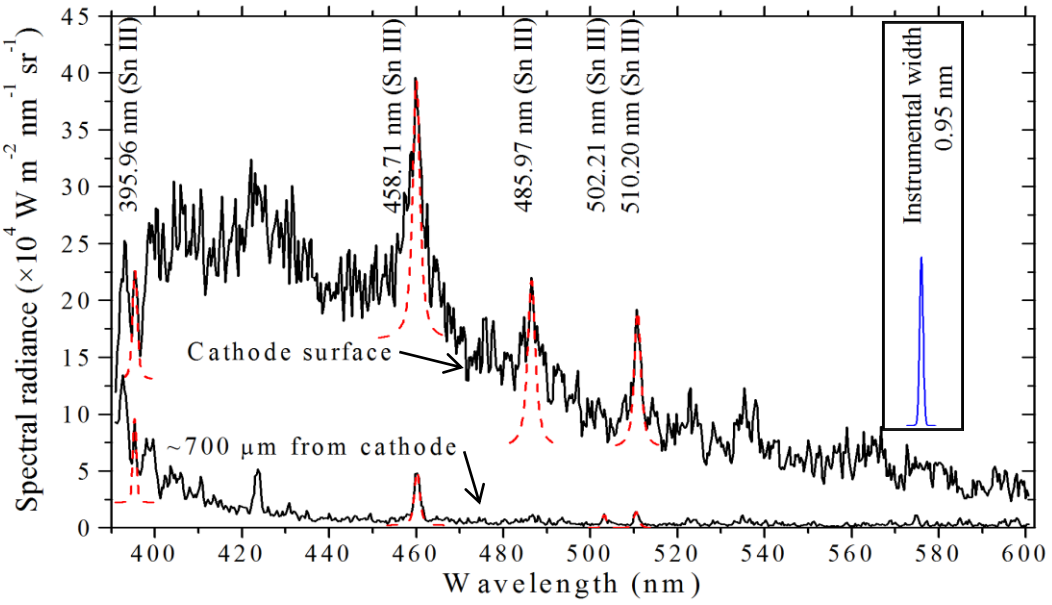

Fig. 4.64 – Early emission spectra showing the onset of line emission (40 ns delay with 10 ns gate) with three Sn III lines fit with Voigt profiles to estimate the electron density as $3.86 \pm 1.60 \times10^{17}$ cm^{-3} via Stark broadening.

Boltzmann plots made for the Sn III lines labelled in Fig. 4.64 ($7s\ ^3S_1 \rightarrow 6p\ ^3P_2$ 395.96 nm, $6p\ ^3P_1 \rightarrow 6s\ ^3S_1$ 485.97 nm, $6p\ ^3P_2 \rightarrow 5d\ ^3D_2$ 502.21 nm, and $6p\ ^3P_2 \rightarrow 5d\ ^3D_3$ 510.20 nm), for a spectra recorded with a 40 ns delay and 10 ns gate, gives an estimate for the electron temperature (T_e) of ~2.0 ±0.4 eV (Fig. 4.65) at the cathode surface and ~2.10 ±0.5 eV at ~700 µm from the cathode.

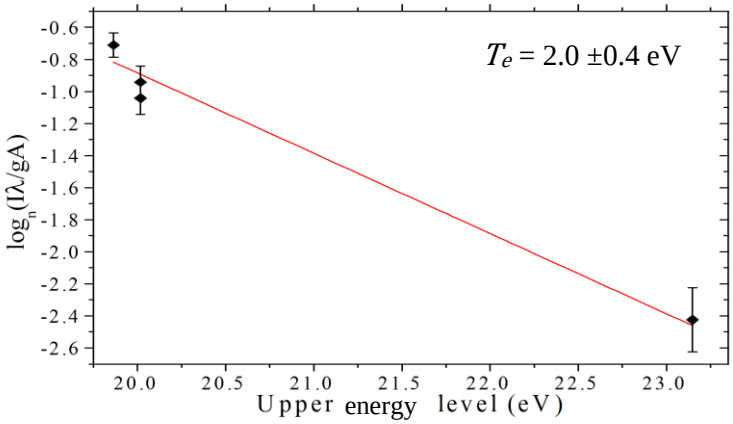

Fig. 4.65 – Boltzmann plot for the lines fit in Fig. 4.64, as this spectrum is dominated by continuum emission the error on the line fit for 395.9 nm is quite large leading to uncertainty in the estimated temperature.

As time progresses and the plume expands into the inter-electrode gap the emission shifts from Sn III line emission to Sn II, due to the decreasing plasma temperature and density. The Sn II lines observed do not have a wide spread in upper energy levels and so are not very sensitive to temperature. A Boltzmann plot is therefore not possible for these times. However using the density calculated from the Stark width of these lines, the theoretical ionisation fraction was calculated in PrismSPECT[68], shown in Fig. 4.66. From this we assume the electron temperature to be on the order of 1 eV during the Sn II dominated spectra.

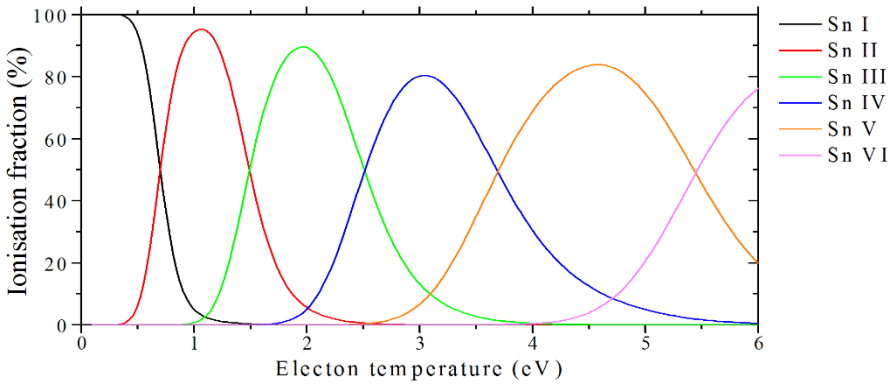

Fig. 4.66 – Theoretical Sn ion fraction percentage versus plasma temperature for an electron density of 10^{17} cm^{-3} calculated in PrismSPECT[68].

During the first plasma phase the fall off in temperature and density is easily observed, and based on this information we can gauge the plasma temperature and density (Fig. 4.67) immediately before the onset of discharge. This information is very useful for any calculations or modelling of the discharge.

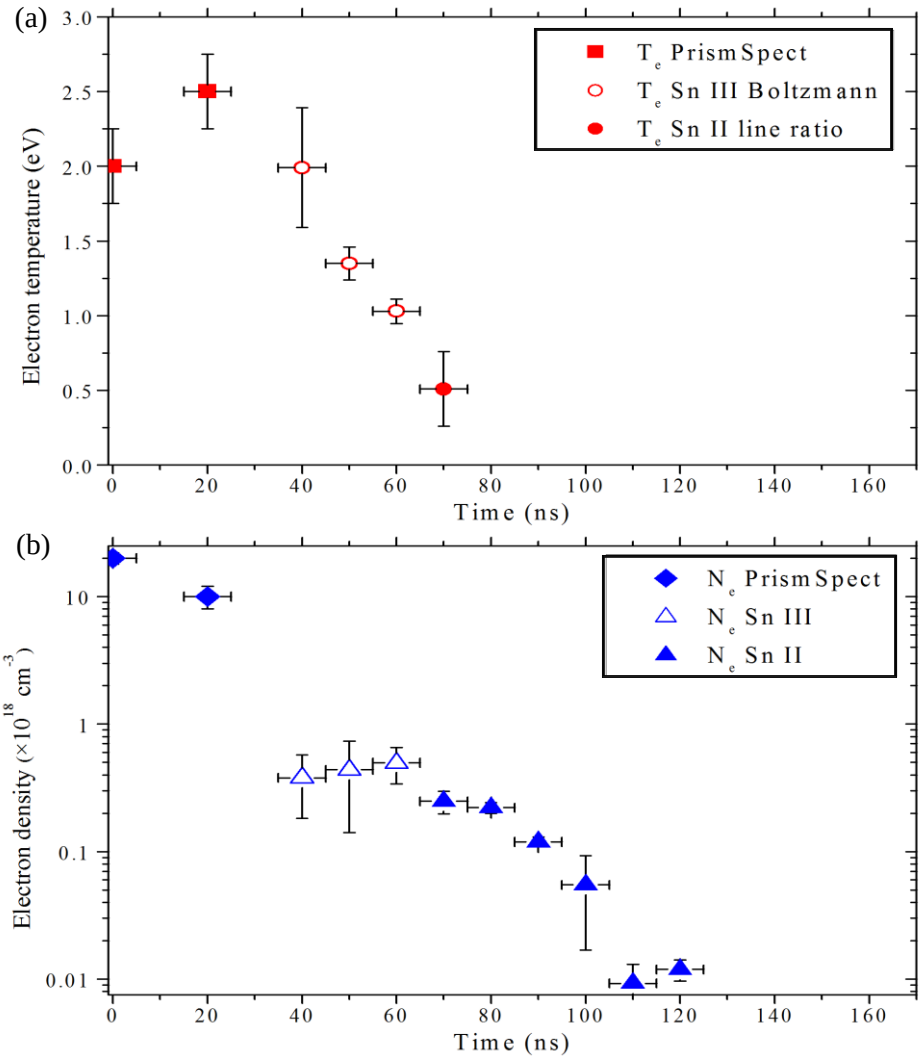

Fig. 4.67 – (a) temperature and (b) densities estimated at the cathode surface during the initial laser produced plasma phase, obtained from PrismSPECT, Boltzmann plot and Stark broadening.

2) anode emission

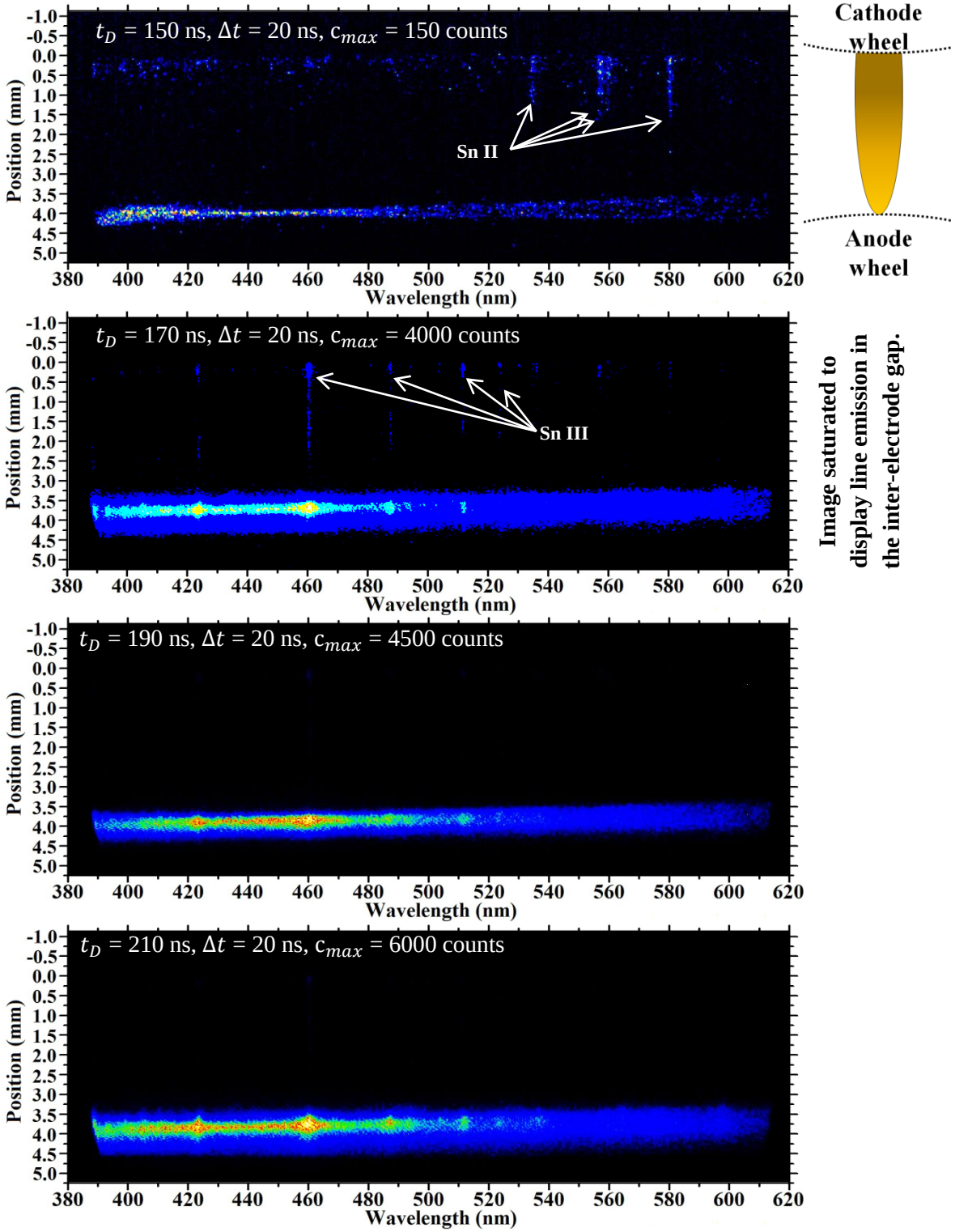

Fig. 4.68 – Spatially resolved OES of Sn 6 J discharge, during anode emission phase.

By the time the laser produced plasma has reached the anode the emission is composed of relatively weak, narrow Sn II lines indicating a low density and relatively cool plasma. The lowest measured density from Sn II lines gives a density

$N_e \sim 1 \times 10^{16}$ cm^{-3} at $\mathbf{t}_D > 120$ ns (with the onset of discharge at roughly $\mathbf{t}_D = 170$ ns). Once the electrical discharge is triggered it induces magnetic compression and ohmic heating of the plasma leading to strongly broadened line emission from higher ion stages than in the initial plasma.

Once the discharge is initiated, at ~170 ns after laser pulse, the relatively weak Sn II line emission observed in the inter-electrode gap directly before the onset of discharge are replaced by Sn IV and Sn III line emission along with an intense quasi-continuum and strong broadened line emission at the anode surface (Fig. 4.68). The lack of confidence in the line information for Sn IV leads to a focus on the times and spaces in which Sn II and Sn III lines can be used to characterise the plasma. Due to the shot-to-shot variation observed in the visible emission of the LAVA-lamp several spectra were recorded for each time step, this phase is perhaps the most obvious for this variation as the onset time of discharge varies from ~150 ns to ~180 ns. There is also the issue of shot-to-shot variation in compression event, both in terms of time and efficiency of compression (judged by the amount of EUV emission observed). For these reasons the presented spectra in the time scan were chosen based on their having similar discharge characteristics and EUV emission.

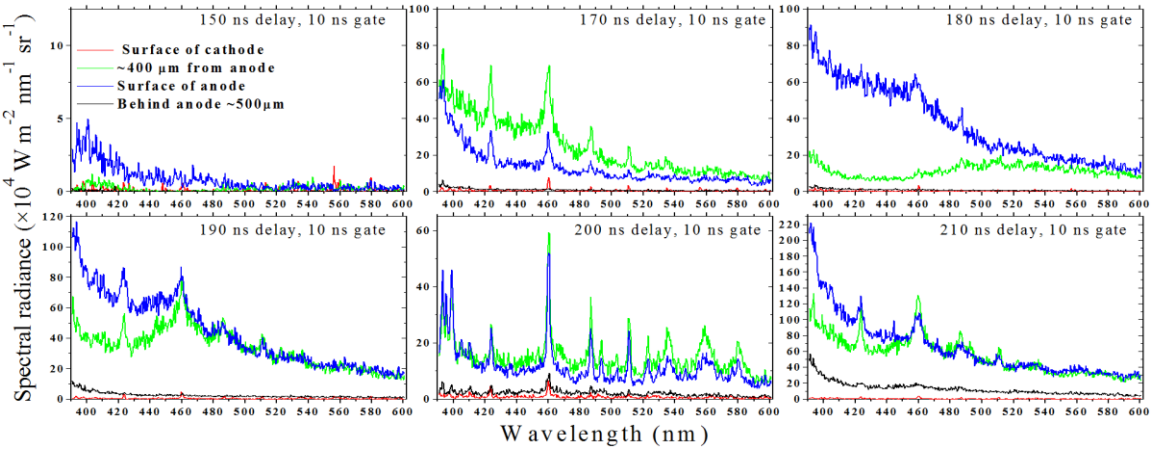

Fig. 4.69 – Quasi-continuum and broad Sn IV and Sn III line emission around anode during onset of discharge, cathode surface is included for reference. Delay times and gates are indicated for each.

As the emission at the anode increases in intensity strong broadened Sn IV and Sn III lines with a quasi-continuum become apparent. It can be seen at 170 ns delay that the emission at the cathode has also shifted to Sn IV and Sn III lines but without the continuum observed at the anode. The density at the cathode at 150 ns is estimated,

from Sn III line broadening, to be ~1 ±0.5 $\times 10^{15}$ cm^{-3}. This measure is reaching the limit of the spectral resolution. The shot-to-shot variation can help explain the discrepancies between the consecutive spectra shown in Fig. 4.69 between 190 ns and 200 ns delays.

The strong broadening observed at these delay times makes temperature and density estimates difficult as many of the useful lines are strongly overlapping or dominated by the quasi-continuum. The quasi-continuum suggests a strong free-free and bound-free constituent in the emission, and is noted to increase towards lower wavelengths in the visible emission range studied.

The temperature and density estimates at the onset of discharge were 5.8 ±0.5 eV and (1.1 ±0.4) $\times 10^{18}$ cm^{-3} at the cathode surface. These estimates come from strong broad Sn III emission lines, as mentioned above there are also strong Sn IV lines observed which could not be used for temperature/density analysis.

In the spectra presented for a time delay of 200 ns after the laser pulse the spectra appears to have a substantially weaker continuum. The temperature and density estimated from the Sn III emission here shows 3.5 ±0.2 eV and (8.1 ±1.2) $\times 10^{17}$ cm^{-3}.

At 210 ns delay roughly 400 µm from the anode surface the temperature and density are estimated as 4.2 ±0. 5 eV and (2.3 ±0.6) $\times 10^{18}$ cm^{-3}. The lines at the anode surface at this time delay were not possible to accurately fit. This issue was consistent during this phase of the laser assisted discharge plasma evolution. For this reason no temperature/density plots were made here.

3) emission on both electrodes

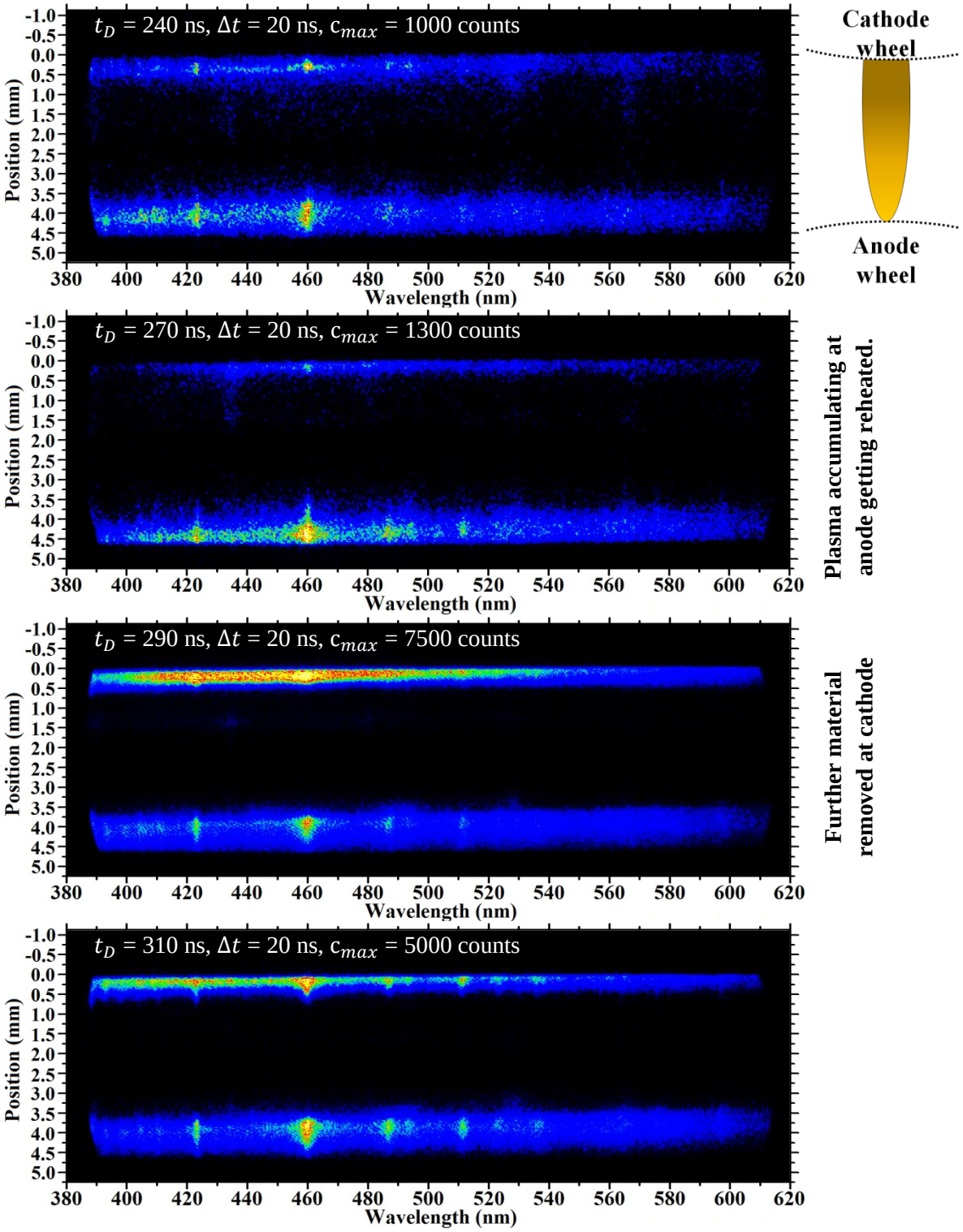

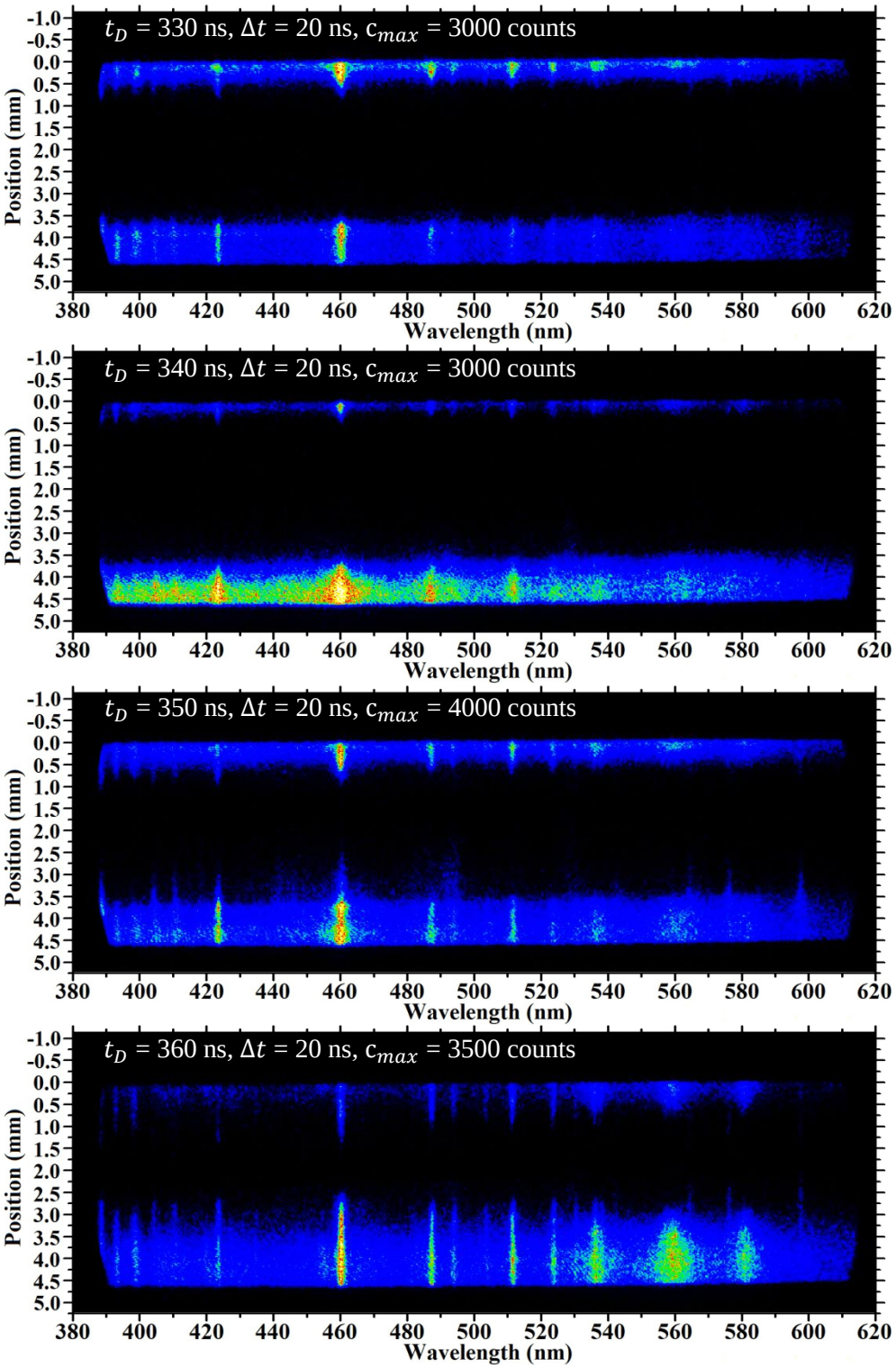
t_D = 330 ns, Δt = 20 ns, c_{max} = 3000 counts
t_D = 340 ns, Δt = 20 ns, c_{max} = 3000 counts
t_D = 350 ns, Δt = 20 ns, c_{max} = 4000 counts
t_D = 360 ns, Δt = 20 ns, c_{max} = 3500 counts
Position (mm)
Wavelength (nm)

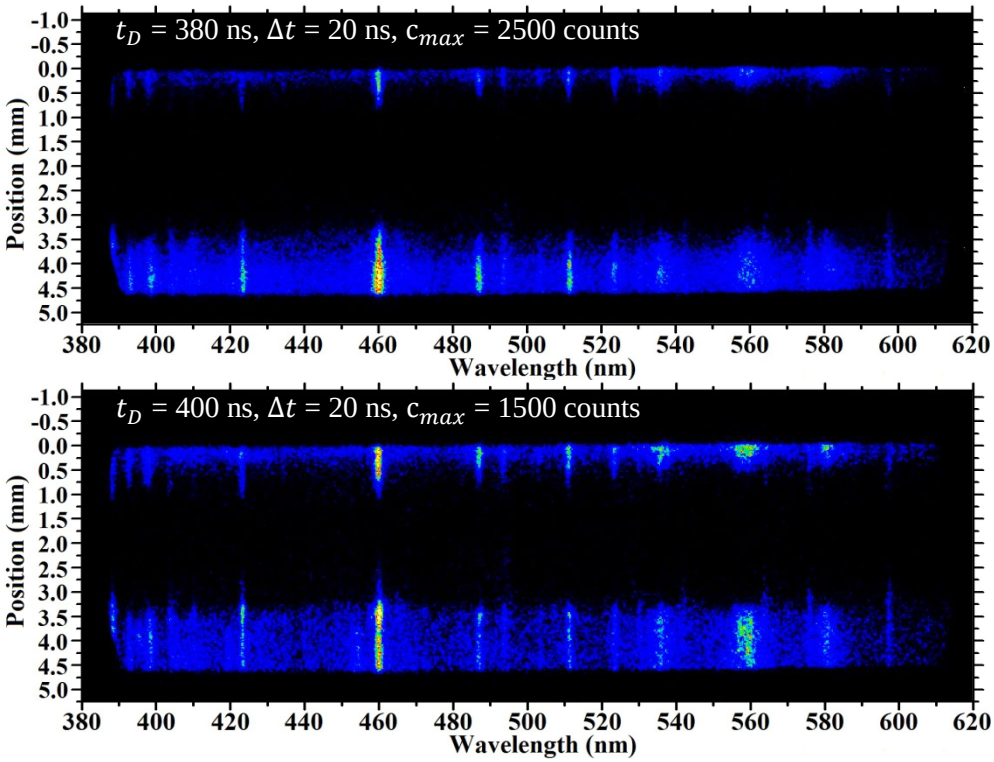

Fig. 4.70 – Spatially resolved OES images of Sn 6 J discharge, during the quasi-continuum on each electrode phase.

Through this long set (240 ns – 400 ns) of OES images the visible emission is observed to increase at the cathode as a continuum and broadened Sn III and Sn IV lines. As the discharge current reaches the first maxima (~300 ns after laser pulse, ~130 ns after onset of discharge) the anode continuum emission is mirrored by a similar emission at the cathode, this pair of quasi-continuum emission with broadened lines is the dominant emission in the visible range during the current peak. Following this the Sn ionic line emission extends into the inter-electrode gap with narrowing of the Sn III lines observed before the Sn II. It has been noted[125] that EUV emission from the plasma itself can lead to further ablation of material from the target, forming a dense plasma with temperatures of 1 – 4 eV in the region close to the target surface.

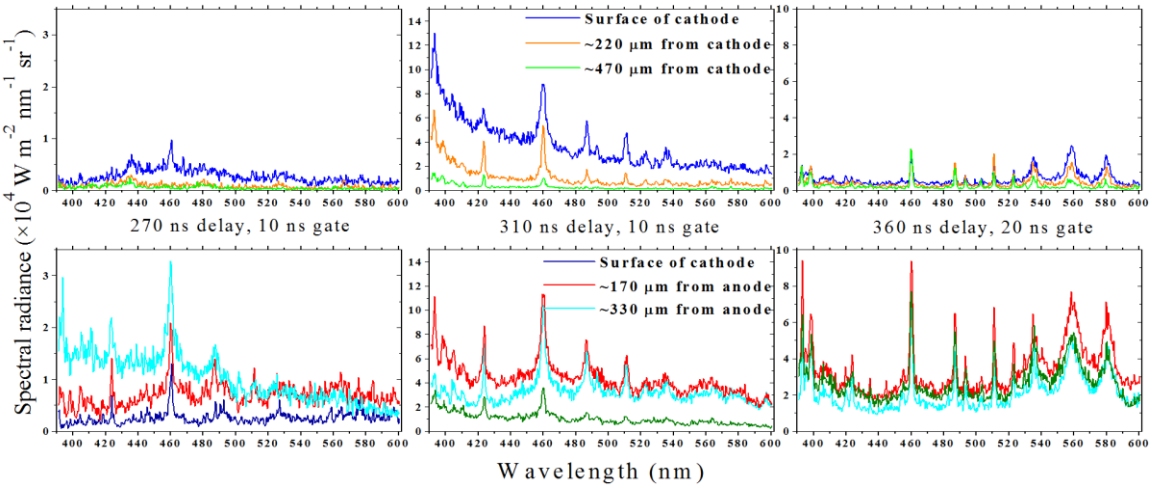

Fig. 4.70 – Sample spectral line outs for three different delays at six spatial positions. The cathode positions are shown in the top set of spectra with the anode positions shown in the bottom. The time of pinch is roughly 280 ns – 320 ns.

In Fig. 4.70 three time delays are taken at six spatial positions around the time of the current maximum and pinch event. Similarly to the previous phase of the plasma evolution the visible emission from the electrode positions has a strong continuum feature.

During the early times in this phase the Sn II and Sn III lines used to estimate temperature and density are dominated by other overlapping lines. By 360 ns after the laser pulse the plasma visible emission at the electrodes has decayed to strongly broadened Sn II and Sn III emission lines. Fitting the Sn III lines gives a temperature estimate of 6.1 ±0.8 eV and a density estimate of (8.3 ±0.9) $\times 10^{18}$ cm^{-3} at a delay time directly following the discharge current maximum.

4) localised inter-electrode emission

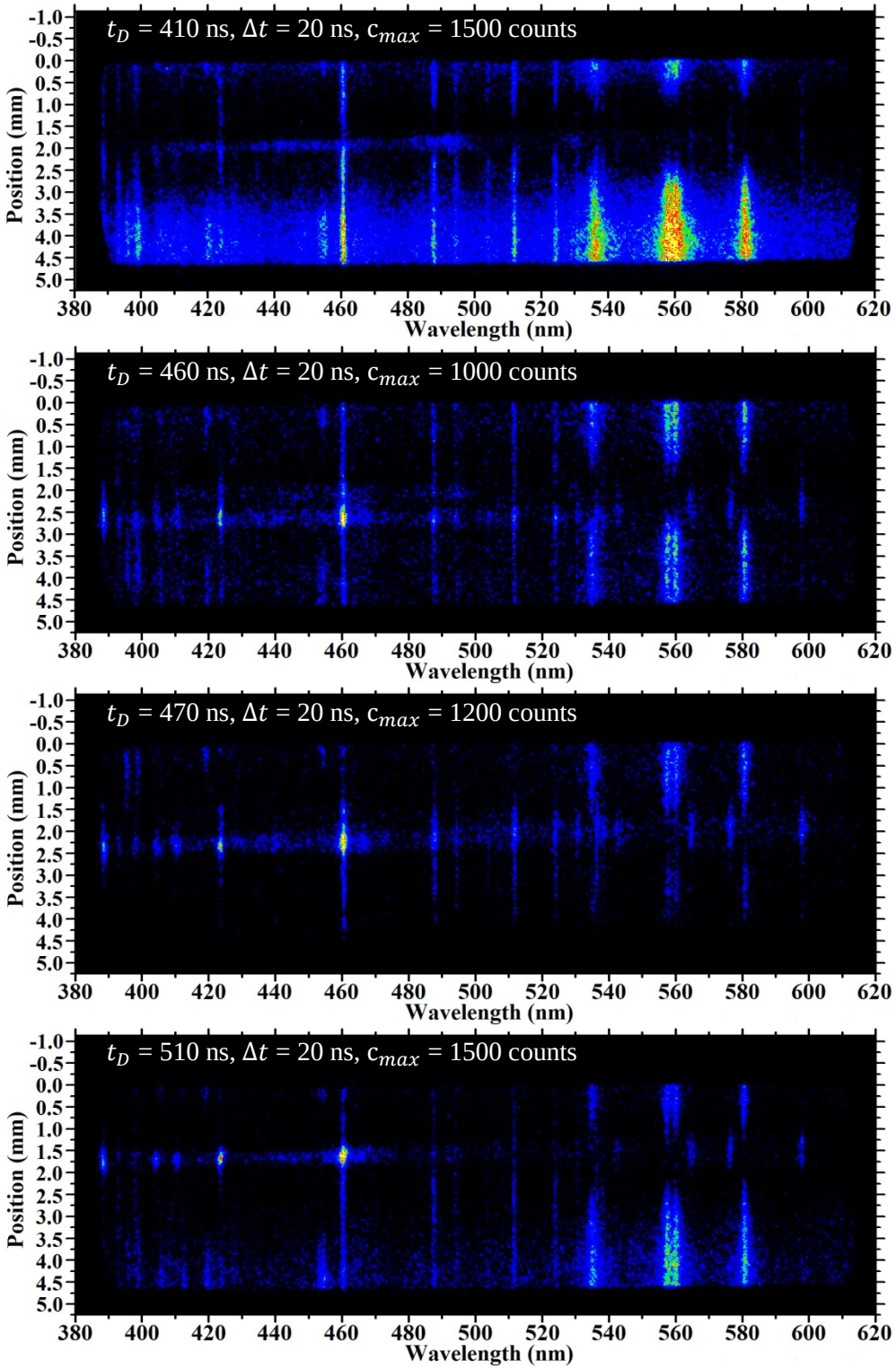

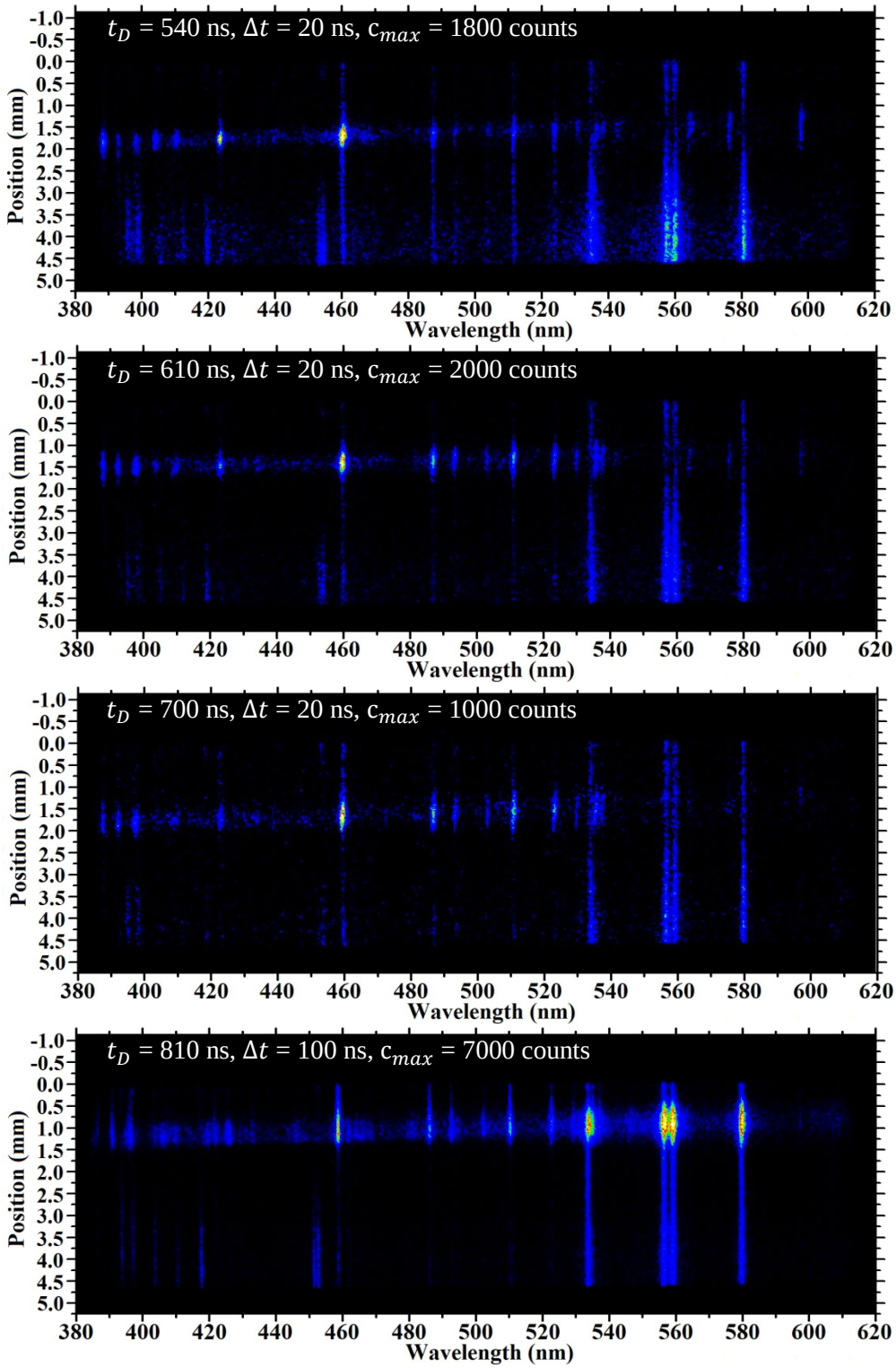

Fig. 4.71 – Spatially resolved OES images of Sn 6 J discharge, showing the highest intensity to be localised in the inter-electrode gap.

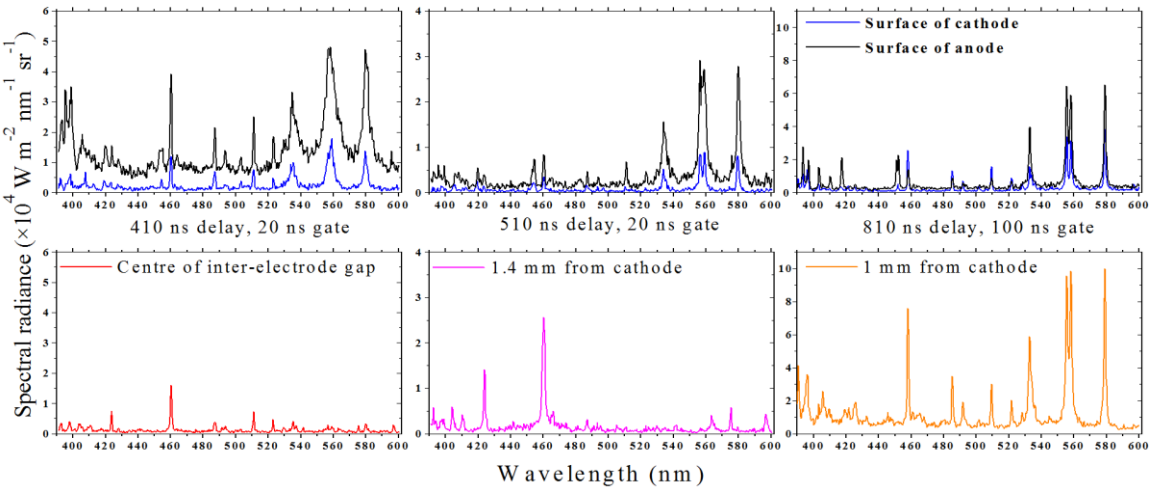

Fig. 4.72 – Sample spectral line outs for three different delays at three spatial positions. The electrode emission line-outs are shown in the top spectra with the localised inter-electrode emission in the bottom.

In Fig. 4.72 three time delays are taken as a representative scan of the fourth plasma evolution phase. In this phase the notable feature is the localised inter-electrode emission. In the figure the top three spectral line-outs are taken at the cathode and anode to give a comparison between the electrode emission and the emission in the gap presented in the bottom three. The Sn II lines at ~560 nm can be seen to narrow as the delay time increases with two lines being clearly distinguishable at 810 ns after the laser pulse. The Sn III emission lines also decay during this time leaving Sn II lines as the dominant emission in this range. This trend is similar in the localised inter-electrode gap emission. As time delay increases this emission is observed to increase in intensity with the dominant lines shifting to Sn II at around 810 ns.

1) 5) extended inter-electrode emission

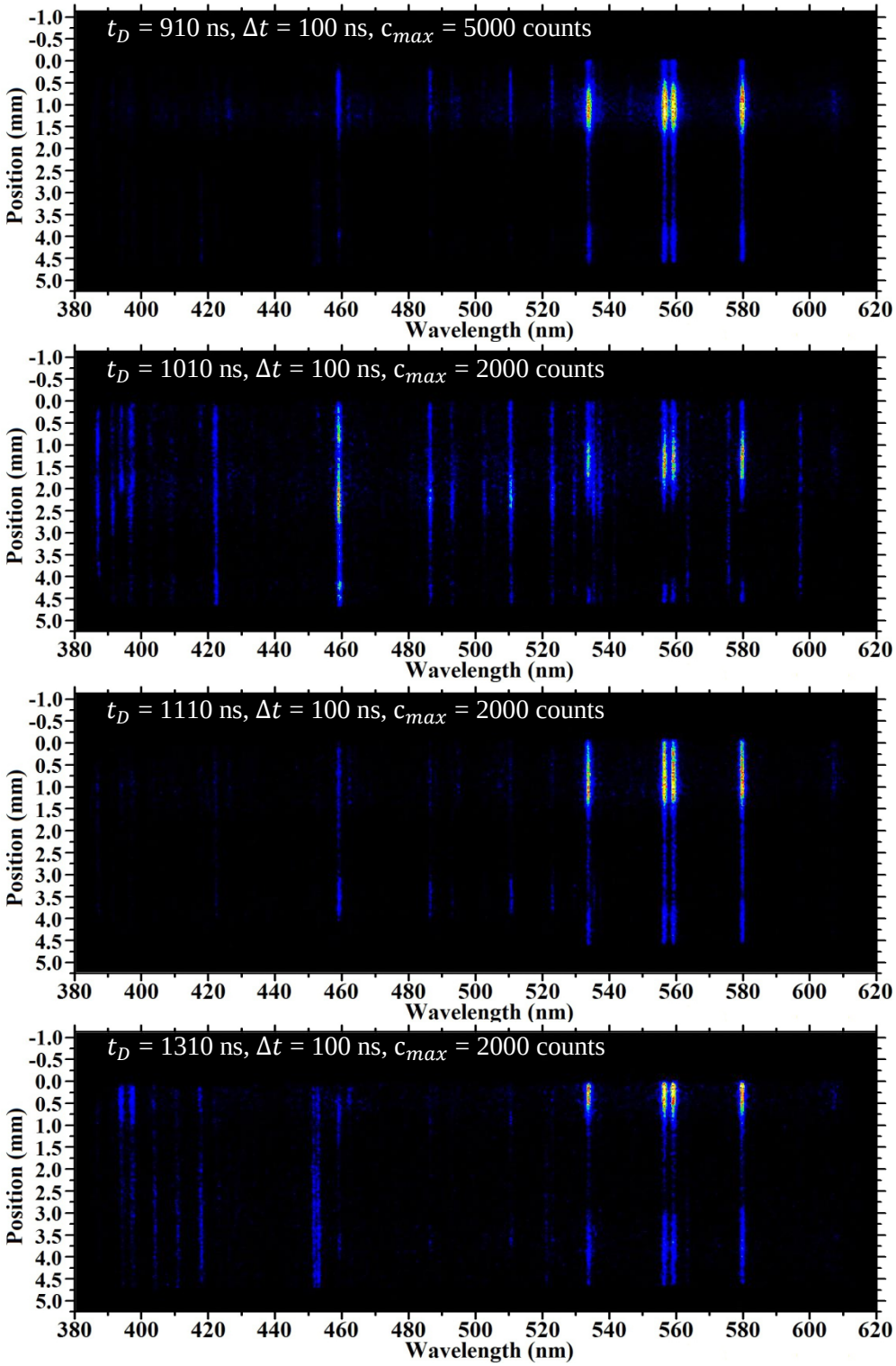

Fig. 4.72 – Spatially resolved OES images of Sn 6 J discharge, during the late 'long' line emission phase.

Chapter 5.

Conclusions and future work

In this chapter the summary and final conclusions from this work are presented. This is accompanied by a short discussion on the possible areas of research leading on from this work and the future areas of interest for laser assisted discharge plasma research in TCD.

5.1 Conclusions

The laser triggered fast Z-pinch sources used in this work were characterised using aluminium, tin and galinstan (Ga, In, Sn alloy) as source materials. The laser produced plasmas used to ignite the discharge were generated using ns Nd:YAG 1064 nm lasers, with variable fluence to control the plasma load delivered. The sources investigated prior to and at the beginning of this work were miniature fast Z-pinch discharges[43], [83]. The main aims for these sources was the investigation of discharge circuit and plasma load parameters and the optimisation of these sources for the high temperatures and densities required in short wavelength sources. The geometry investigated in UCD is a more robust larger scale device centred around rotating electrode wheels and a high voltage pulsed power supply.

5.1.1 Colliding Laser Plasma Triggered Discharge

The colliding laser plasma triggered discharge (CLP-TD) geometry is a small device with an interchangeable capacitor bank and replaceable target electrodes. The design of this source was focused on the study of varied discharge parameters with a selection of materials in a laser assisted discharge plasma source. The discharge energy could be varied up to a maximum of 3.75 J (C = 1.88 µF, V = 2 kV). The discharge was triggered by ablation of one or both parallel electrodes. The inter-electrode gap could be

varied from 0.8 cm to 1.2 cm wide. The interaction of the colliding laser plasmas was studied with and without discharge. This collisional interaction was evident from ion flows perpendicular to the collision axis which is not observed in the single laser plasma case and from an increase in spectral line emission from higher ion stages than observed from a single laser plasma. The main aim of this experiment was to investigate the effect of triggering a high current discharge with a colliding pair of laser plasmas.

A plasma pinch or compression event was noted on the Rogowski coil dI/dt profile at approximately 200 ns after the laser pulse. A peak discharge current of 8 kA with a half-period of roughly 450 ns was achieved with a 1 kV discharge. The ion time-of-flight was measured perpendicular to the discharge axis with a Langmuir ion probe positioned 31.5 cm from the axis. The ion kinetic energy increased from 800 eV to 3.65 keV with an increased ion fluence of a factor from 4.8×10^{11} ions/cm^2 to 2.9×10^{12} ions/cm^2 from the 0 V colliding plasmas to the 1 kV.

The visible emission spectroscopy showed a large increase in spectral radiance with the discharge, along with strong emission from Al III lines until much later times. Several lines were identified from higher ionisation stages with strong Al IV and Al V emission during the first half-period of the discharge. The information available for Al IV emission lines is limited and no transition probabilities were obtained. There are also several unidentified lines in the discharge plasma. Using Boltzmann plots of Al III line emission the discharge was seen to heat the laser plasma from approximately 1.5 eV at the time of collision to 4.8 ± 0.3 eV during the first half-period of the discharge. Based on the plasma densities estimated directly before and after the pinch event and the strong Al IV and Al V emission the temperature is expected to increase further. The ionisation fractions calculated at 1×10^{18} cm^{-3} gives an expected temperature range of 8 – 12 eV during the discharge current peak.

The results from the novel spectral imaging gave a clear perspective on the collisional interaction and spectral separation of ion species in the plume. The higher ionisation stages were noted to begin accumulating in the centre of the inter-electrode gap at roughly 100 ns after the laser pulse. The most intense emission was recorded at each electrode, although interesting features were recorded in the inter-electrode gap with filament-like structures apparent during the discharge.

Further study of the CLP-TD as a possible short wavelength or high energy ion source should be undertaken. It also has potential in generating a target plasma for laser reheating[126], [127]. In this role it would be necessary to adjust the pinching parameters to give a slower compression, as instead of generating a very hot dense plasma using the discharge energy the aim would be to reheat a compressed plasma with a second, intense, laser pulse.

The main areas to be improved with the CLP-TD geometry would be further control of plasma load, decrease down-time by improving target lifetime, and improve collection solid angle. Although the targets were rastered to avoid laser drilling, it was noted that both targets developed arcing spots[128] at various locations across their surface. The targets had to be sanded frequently to give an even surface for ablation. This is a common problem in discharge plasma sources, electrode erosion and re-deposition limits the life-time of such devices. This source should also be characterised with tin as a target material and be optimised for higher discharge current for EUV generation (~20kA).

The CLP-TD experiment was very successful in terms of developing a fast high current discharge device, heating of the plasma was observed along with compression or constriction (based on the increased density near both anode and cathode at the time of pinch). The simplicity of the device is possibly the most useful aspect, as it could lend itself to a wide range of applications or studies, with the small volume and easy target replacement.

5.1.2 Laser Assisted Vacuum Arc - lamp

The Laser Assisted Vacuum Arc (LAVA) - lamp source is a robust fast Z-pinch device with rotating liquid metal coated electrode wheels. The use of liquid metal coatings on the target electrode wheels avoids the issue of arcing spots of laser drilling. The capacitor bank is mounted on the chamber with one bath/electrode wheel connected to the live cathode while the chamber and counter electrode are grounded. The discharge energy can be varied from roughly 1 J up to a maximum of 7 J.

In the LAVA-lamp chapter the main aims were to characterise the tin EUV and visible emission and compare these results with galinstan as a source material. The source was investigated with the same laser pulse and discharge parameters with a suite of diagnostic tools. The EUV emission was analysed using an in-band, calibrated photodiode, time-integrated imaging, and absolutely calibrated EUV spectroscopy. The ion fluence was also studied using a Faraday cup. Along with these diagnostics spatially and temporally resolved visible emission spectra were recorded for a range of discharge voltages.

The EUV output was observed to increase with increasing discharge voltage, the convenient measure for EUV output is conversion efficiency (CE). CE is the ratio of EUV energy output in the 2% band around 13.5 nm into 2π sr over the laser/discharge energy input. The LAVA-lamp CE was found to peak at 4.5 kV (4 J) discharge with a value of 0.4% for tin and 0.1% for galinstan i.e. 16 mJ/2π sr and 4 mJ/2π sr respectively. The in-band EUV emission from tin with a 4 J discharge was found to be approximately 7% of the EUV emission in the range 10 – 18 nm. The average EUV energy output with galinstan as source material was much lower than for tin across all discharge energies, although it did yield a much more spectrally flat emission over the EUV range observed. This makes it a useful material for use in metrology where narrow-band emission is not desirable. The shot-to-shot variation in this EUV output must also be taken into account when considering the total EUV output. The difference in EUV energy output between tin and galinstan is due in part to the shot-to-shot variation in galinstan. It was noted that the EUV energy output varies by ±80% with a

4 J discharge. In the case of tin this variation is approximately ±20% for the same discharge parameters. Oxygen line emission was observed in the EUV spectra during the initial operation of the source after each time the chamber was opened. This line emission was used to make an estimate of the plasma temperature. Boltzmann plot temperature estimates for both tin and galinstan gave an average value of 24.5 ±6.3 eV. It must be noted that these spectra are time and line integrated.

The EUV emission from galinstan is more spectrally flat over the range 10 – 18 nm than from tin, this could be useful as a tool for analysis of out-of-band mirror reflectivity or as a broadband EUV metrology source. Using a filtered EUV sensitive fast photodiode the EUV emission was noted to last approximately 35 ns. This emission coincides with the pinch event as expected. The dimensions of the EUV emitting region of the galinstan plasma were imaged using a concave multilayer mirror, the EUV source was found to have an average diameter of 110 ± 25 µm and length of 500 ± 125 µm in the case of a 4 J discharge, triggered with a 5 mJ laser pulse.

Temporally- and spatially-resolved optical emission spectroscopy was used to investigate the plasma dynamics in a laser triggered Z-pinch EUV source. Discharge heating and magnetic compression of the plasma was observed in the spectra. Though Z-pinching of the plasma is clearly observed by monitoring the discharge current and the EUV emission, no clear signature of the pinch has been identified in the optical measurements, although unexplained features were observed in the inter-electrode gap which could have been caused by pinching. It was also observed that the optical emission was concentrated in the regions near the electrodes, suggesting ablation plume pileup and discharge erosion of the electrodes. The temperature and density of the plasma load were diagnosed from line emission and line widths during the laser plasma expansion and the discharge phase. The plasma density during the first half-period of the discharge was observed to increase from approximately 0.8 eV without discharge to 4.5 eV with a 4 J discharge. The broadened spectral lines overlap strongly at the peak of current making estimate difficult during the pinch. This issue also makes temperature estimation impossible. Several lines observed during the discharge are also unidentified. The visible emission from ions stages above Sn IV has not been well documented in the literature.

5.2 Future work

As discussed previously the key factors in designing a Z-pinch plasma source are the rate of rise of current and the plasma load. In this work the discharge circuit was designed with the aim of minimising the inductance, and the laser energy was varied to control the plasma load. There are different methods to achieve these goals, and different types of pinch which could be used to yield a more stable pinch. The biggest issue noted in the operation of the LAVA-lamp is the reproducibility. To function as a light source the device must have a more stable EUV output. Experiments have continued with the LAVA-lamp in UCD, with the focus on changing the plasma load through varied laser parameters. Recently the EUV emission from LAVA-lamp was compared when triggered using a 7 ns laser pulse and a 160 ps laser pulse[129]. The results showed an increased in-band EUV output, possibly owing to a lower opacity in the plasma. This work is ongoing and final results are pending. There is also interest in using multiple laser pulses to shape the plasma load delivered to the pinch and also to reheat the pinched plasma to yield a higher temperature plasma.

Laser assisted discharge sources have been proposed as short wavelength sources in the 6 nm and 2-4 nm "water-window" ranges[130]. For these wavelengths a significantly larger energy is required to reach the necessary temperatures. In the case of 13.5 nm sources a plasma temperature of 30 eV and density of the order of 10^{19} cm^{-3} is required, for the shorter wavelength sources, e.g. a 6 nm source the plasma temperature required is over 100 eV[131].

One such alternate geometry under investigation is a θ-pinch based source for plasma spraying and high energy ion generation. In a θ-pinch the current flow is in the azimuthal θ direction, generated by a strong magnetic field directed along the z axis[132], [133]. Another alternate geometry is a combination of both Z-pinch and θ-pinch designs, with a high current pulse along the z axis followed by a θ-pinch to sustain the compression for longer times. This geometry could be of possible use in extending the lifetime of the EUV emission from a single event.

A geometry similar to that used by E. Sterling et al.[45] has also been proposed, utilising several apertures to select a novel plasma load. This would either take the form of several thin parallel columns of laser plasma or a narrow annular plasma load. This ring would surround a central plasma load and would be ignited separately to make a staged Z-pinch. In this geometry the outer plasma will compress towards the axis of the central plasma which will yield a longer pinching event.

References

[1] G. E. Moore, “Cramming more components onto integrated circuits,” *Electronics*, vol. 38, no. 8, pp. 114–117, 1965.

[2] S. Miller, “ASML’s NXE platform for volume production,” in *Semicon West*, 2013.

[3] C.-M. Lim, S.-M. Kim, Y.-S. Hwang, J.-S. Choi, K.-D. Ban, S.-Y. Cho, J.-K. Jung, E.-K. Kang, H.-Y. Lim, H.-S. Kim, and S.-C. Moon, “Positive and negative tone double patterning lithography for 50nm flash memory,” in *Proc. SPIE 6154, Optical Microlithography XIX*, 2006, vol. 6154, pp. 615410–615418.

[4] M. Switkes, R. R. Kunz, M. Rothschild, R. F. Sinta, M. Yeung, and S.-Y. Baek, “Extending optics to 50 nm and beyond with immersion lithography,” *J. Vac. Sci. Technol. B Microelectron. Nanom. Struct.*, vol. 21, no. 6, p. 2794, 2003.

[5] B. L. Henke, E. M. Gullikson, and J. C. Davis, “X-ray interactions: photoabsorption, scattering, transmission and reflection at E=50-30,000 eV, Z=1-92,” *At. Data Nucl. Data Tables*, vol. 54, pp. 181–342, 1993.

[6] P. Marczuk and W. Egle, “Grazing-incidence EUV collectors,” in *EUV sources for lithography*, V. Bakshi, Ed. Bellingham, Washington: SPIE Press, 2005, pp. 873–891.

[7] S. Yulin, N. Benoit, T. Feigl, and N. Kaiser, “Interface-engineered EUV multilayer mirrors,” *Microelectron. Eng.*, vol. 83, no. 4–9, pp. 692–694, Apr. 2006.

[8] L. Juschkin, L. Loetgering, D. Rudolf, R. Xu, S. Brose, S. Danylyuk, and J. Miao, “Tabletop coherent diffraction imaging with a discharge plasma EUV source,” in *X-Ray Lasers and Coherent X-Ray Sources: Development and Applications*, 2013, vol. 8849, p. 9.

[9] V. A. Slemzin, S. V Kuzin, I. A. Zhitnik, J.-P. Delaboudiniere, F. Auchere, A. N. Zhukov, R. Van der Linden, O. I. Bugaenko, A. P. Ignat’ev, A. V Mitrofanov, A. A. Pertsov, S. N. Oparin, A. I. Stepanov, and A. N. Afanas’ev, “Observations of Solar EUV Radiation with the CORONAS-F/SPIRIT and SOHO/EIT Instruments,” *Sol. Syst. Res.*, vol. 39, no. 6, pp. 489–500, 2005.

[10] J.-P. Halain, D. Berghmans, D. B. Seaton, B. Nicula, A. De Groof, M. Mierla, A. Mazzoli, J.-M. Defise, and P. Rochus, “The SWAP EUV Imaging Telescope. Part II: In-flight Performance and Calibration,” *Sol. Phys.*, vol. 286, no. 1, pp. 67–91, 2013.

[11] S. F. Horne, M. M. Besen, D. K. Smith, P. A. Blackborow, and R. D’Agostino, “Application of a high-brightness electrodeless Z-pinch EUV source for metrology, inspection, and resist development,” in *Proc SPIE 31st International Symposium on Microlithography*, 2006, vol. 6151.

[12] J. Pomplun, S. Burger, F. Schmidt, F. Scholze, C. Laubis, and U. Dersch, “Metrology of EUV Masks by EUV-Scatterometry and Finite Element Analysis,” in *Photomask and Next-Generation Lithography Mask Technology XV*, 2008, vol. 7028, p. 12.

[13] G. De Stasio, B. Gilbert, T. Nelson, R. Hansen, J. Wallace, D. Mercanti, M. Capozi, P. a. Baudat, P. Perfetti, G. Margaritondo, and B. P. Tonner, "Feasibility tests of transmission x-ray photoelectron emission microscopy of wet samples," *Rev. Sci. Instrum.*, vol. 71, no. 1, p. 11, 2000.

[14] I. a Artyukov, R. M. Feschenko, a V Vinogradov, Y. a Bugayev, O. Y. Devizenko, V. V Kondratenko, Y. S. Kasyanov, T. Hatano, M. Yamamoto, and S. V Saveliev, "Soft X-ray imaging of thick carbon-based materials using the normal incidence multilayer optics," *Micron*, vol. 41, no. 7, pp. 722–8, Oct. 2010.

[15] M. Phillips, "Enabling EUVL for HVM Insertion," in *International workshop on EUV and soft x-ray sources*, 2013.

[16] S. Harilal, M. Tillack, B. O'Shay, C. Bindhu, and F. Najmabadi, "Confinement and dynamics of laser-produced plasma expanding across a transverse magnetic field," *Phys. Rev. E*, vol. 69, no. 2, p. 026413, Feb. 2004.

[17] S. S. Harilal, B. O'Shay, Y. Tao, and M. S. Tillack, "Ambient gas effects on the dynamics of laser-produced tin plume expansion," *J. Appl. Phys.*, vol. 99, no. 8, 2006.

[18] T. Higashiguchi, M. Kaku, M. Katto, and S. Kubodera, "Suppression of suprathermal ions from a colloidal microjet target containing SnO2 nanoparticles by using double laser pulses," *Appl. Phys. Lett.*, vol. 91, no. 151503, 2007.

[19] Y. Ueno, G. Soumagne, A. Sumitani, A. Endo, T. Higashiguchi, and N. Yugami, "Reduction of debris of a CO2 laser-produced Sn plasma extreme ultraviolet source using a magnetic field," *Appl. Phys. Lett.*, vol. 92, no. 211503, 2008.

[20] G. O'Sullivan and R. Faulkner, "Tunable narrowband soft x-ray source for projection lithography," *Opt. Eng.*, vol. 33, no. 12, pp. 2–7, 1994.

[21] Y. Ueno, G. Soumagne, A. Sumitani, and A. Endo, "Enhancement of extreme ultraviolet emission from a CO2 laser-produced," *Appl. Phys. Lett.*, vol. 91, no. 231501, 2007.

[22] Y. Ueno, T. Ariga, G. Soumagne, I. Pogorelsky, I. Pavlishin, D. Stolyarov, M. Babzien, K. Kusche, and V. Yakimenko, "Efficient extreme ultraviolet plasma source generated by a CO2 laser and a liquid xenon microjet target," *Appl. Phys. Lett.*, vol. 90, no. 191503, 2007.

[23] E. Kieft, J. van der Mullen, G. Kroesen, and V. Banine, "Time-resolved pinhole camera imaging and extreme ultraviolet spectrometry on a hollow cathode discharge in xenon," *Phys. Rev. E*, vol. 68, no. 5, p. 056403, Nov. 2003.

[24] K. Gielissen, Y. Sidelnikov, D. Glushkov, W. a. Soer, V. Banine, and J. J. a. M. v. d. Mullen, "Gated pinhole camera imaging of the high-energy ions emitted by a discharge produced Sn plasma for extreme ultraviolet generation," *J. Appl. Phys.*, vol. 106, no. 8, p. 083301, 2009.

[25] V. G. Novikov, V. V Ivanov, K. N. Koshelev, A. S. Grushin, V. M. Krivtsun, and A. D. Solomyannaya, "Modelling of laser produced plasma source of radiation at the wavelength for 6.7 nm for future lithography," *Phys. Extrem. States Matter*, 2011.

[26] K. Bergmann, G. Schriever, O. Rosier, M. Mu, and W. Neff, "Highly repetitive, extreme-ultraviolet radiation source based on a gas-discharge plasma," *Appl. Opt.*, vol. 38, no. 25, 1999.

[27] E. Louis, E. D. van Hattum, S. Alonso van der Westen, P. Sallé, K. T. Grootkarzijn, E. Zoethout, F. Bijkerk, G. von Blanckenhagen, and S. Müllender, "High reflectance multilayers for EUVL HVM-projection optics," in *Extreme Ultraviolet (EUV) Lithography*, 2010, vol. 7636, p. 76362T–76362T–5.

[28] L. Juschkin, G. Derra, and K. Bergmann, “EUV Light Sources,” in *Extreme ultraviolet lithography*, V. Bakshi, Ed. New York, NY: SPIE Press, 2008.

[29] G. Schrieve, O. Semprez, J. Jonkers, M. Yoshioka, and R. Apetz, “Laser-produced plasma versus laser-assisted discharge plasma: physics and technology of extreme ultraviolet lithography light sources,” *J. Micro/Nanolithography, MEMS, MOEMS*, vol. 11, no. 2, May 2012.

[30] A. Endo, “CO2 Laser Produced Tin Plasma Light Source as the Solution for EUV Lithography,” in *Lithography*, M. Wang, Ed. InTech, 2010, pp. 161–176.

[31] K. Koshelev, V. Krivtsun, V. Ivanov, O. Yakushev, A. Chekmarev, V. Koloshnikov, E. Snegirev, and V. Medvedev, “New type of discharge-produced plasma source for extreme ultraviolet based on liquid tin jet electrodes,” *J. Micro/Nanolithography, MEMS, MOEMS*, vol. 11, no. 2, pp. 21103–21106, 2012.

[32] J. Jonkers, “EUVL - A Reality in the Making,” in *International workshop on EUV and soft x-ray sources*, 2012.

[33] M. a. Liberman, J. S. De Groot, A. Toor, and R. B. Spielman, *Physics of High-Density Z-Pinch Plasmas*. New York, NY: Springer New York, 1999.

[34] S. A. Slutz, A. C. Owen, K. Tomlinson, M. R. Gomez, S. B. Hansen, M. C. Herrmann, M. C. Jones, G. K. Robertson, G. A. Rochau, M. E. Savage, D. G. Schroen, and W. A. Stygar, “Modified helix-like instability structure on imploding z-pinch liners that are pre-imposed with a uniform axial magnetic field,” vol. 056307, no. May, p. 8, 2014.

[35] D. D. Ryutov, M. S. Derzon, and M. K. Matzen, “The physics of fast Z-Pinches,” *Rev. Mod. Phys.*, vol. 72, no. 1, pp. 167 – 223, 2000.

[36] W. H. Bennett, “Magnetically Self-Focussing Stream,” *Phys. Rev.*, vol. 45, pp. 890–897, 1934.

[37] J. L. Ellsworth, S. Falabella, V. Tang, a Schmidt, G. Guethlein, S. Hawkins, and B. Rusnak, “Design and initial results from a kilojoule level Dense Plasma Focus with hollow anode and cylindrically symmetric gas puff.,” *Rev. Sci. Instrum.*, vol. 85, no. 1, p. 013504, Jan. 2014.

[38] V. Fortov, K. Dyabilin, M. Lebedev, E. Grabovskij, V. Smirnov, B. Sharkov, A. Golubev, D. H. H. Hoffmann, and K. Eidmann, “The application of high intensive Z-pinch radiation and heavy ion beams for research on high energy density physics,” in *12th International Conference on High-Power Particle Beams*, 1998, vol. 6, no. 5.

[39] O. A. Nassef and H. E. Elsayed-Ali, “Spark discharge assisted laser induced breakdown spectroscopy,” *Spectrochim. Acta Part B At. Spectrosc.*, vol. 60, no. 12, pp. 1564–1572, Dec. 2005.

[40] M. E. Foord, Y. Maron, G. Davara, L. Gregorian, and A. Fisher, “Particle Velocity Distributions and Ionization Processes in a Gas-Puff Z Pinch,” *Phys. Rev. Lett.*, vol. 72, no. 24, 1994.

[41] S. V. Lebedev, R. Aliaga-Rossel, S. N. Bland, J. P. Chittenden, a. E. Dangor, M. G. Haines, and I. H. Mitchell, “The dynamics of wire array Z-pinch implosions,” *Phys. Plasmas*, vol. 6, no. 5, p. 2016, 1999.

[42] M. D. Johnston, Y. Y. Lau, R. M. Gilgenbach, T. S. Strickler, M. C. Jones, M. E. Cuneo, and T. a. Mehlhorn, “Caterpillar structures in single-wire Z-pinch experiments,” *Appl. Phys. Lett.*, vol. 83, no. 24, p. 4915, 2003.

[43] E. Sterling and C. Pagano, “Influence of fast electrical discharge on expansion of laser produced plasma,” *Appl. Phys. A Mater. Sci.*, vol. 92, no. 4, pp. 1031–1035, 2008.

[44] E. Kieft, J. van der Mullen, G. Kroesen, V. Banine, and K. Koshelev, "Characterization of a vacuum-arc discharge in tin vapor using time-resolved plasma imaging and extreme ultraviolet spectrometry," *Phys. Rev. E*, vol. 71, no. 2, p. 026409, Feb. 2005.

[45] E. Sterling and J. G. Lunney, "Z-Pinch Discharge in Laser Produced Plasma," in *International symposium on high power laser ablation*, 2010.

[46] B. N. Chichkov, C. Momma, S. Nolte, F. von Alvensleben, and A. Tunnermann, "Femtosecond , picosecond and nanosecond laser ablation of solids," *Appl. Phys. A*, vol. 63, 1996.

[47] J. G. Lunney and R. Jordan, "Pulsed laser ablation of metals," *Appl. Surf. Sci.*, vol. 127–129, pp. 941–946, 1998.

[48] S. Amoruso, R. Bruzzese, N. Spinelli, and R. Velotta, "Characterization of laser-ablation plasmas," *J. Phys. B At. Mol. Opt. Phys.*, vol. 32, no. 14, pp. R131–R172, Jul. 1999.

[49] V. N. Tokarev and A. F. H. Kaplan, "An analytical modeling of time dependent pulsed laser melting," *J. Appl. Phys.*, vol. 86, no. 5, p. 2836, 1999.

[50] S. Dushman, *Scientific foundations of vacuum technique*, 2nd Ed. New York, NY: Wiley, 1962.

[51] B. Wu and Y. C. Shin, "Modeling of nanosecond laser ablation with vapor plasma formation," *J. Appl. Phys.*, vol. 99, no. 8, p. 9, 2006.

[52] Y. B. Zel'dovich and Y. P. Raizer, *Physics of Shock Waves and High-Temperature Hydrodynamic Phenomena*. Elsevier, 1967.

[53] S. I. Anisimov, B. S. Luk'yanchuk, and A. Luches, "An analytical model for three-dimensional laser plume expansion into vacuum in hydrodynamic regime," *Appl. Surf. Sci.*, vol. 96–98, pp. 24–32, Apr. 1996.

[54] J. G. Lunney and B. Doggett, "Langmuir probe diagnosis of laser ablation plasmas," in *Eight international conference on laser ablation*, 2007, vol. 59.

[55] T. N. Hansen, "Ion outflow and soft X-ray radiation from a micro capillary discharge," Trinity College Dublin, 2001.

[56] M. Aschwanden, *Physics of the Solar Corona*, 1st ed. Berlin Heidelberg: Springer-Verlag, 2005.

[57] E. W. Weisstein, *CRC concise encyclopedia of mathematics*, 2nd Ed. Boca Raton, Florida: Chapman & Hall/CRC, 2003.

[58] D. Potter, "The formation of high-density z-pinches," *Nucl. Fusion*, vol. 18, no. 6, p. 813, 1978.

[59] S. Lee, "An energy-consistent snow-plough model for pinch design," *J. Phys. D. Appl. Phys.*, vol. 16, pp. 2463–2469, 1983.

[60] V. . Vikhrev, V. . Ivanov, and G. . Rozanova, "Development of sausage-type instability in a Z-pinch plasma column," *Nuclear Fusion*, vol. 33, no. 2. pp. 311–321, 1993.

[61] J. P. Chittenden, R. Aliaga Rossel, S. V Lebedev, I. H. Mitchell, M. Tatarakis, A. R. Bell, and M. G. Haines, "Two-dimensional magneto-hydrodynamic modeling of carbon fiber Z-pinch experiments," *Phys. Plasmas*, vol. 4, no. 12, p. 9, 1997.

[62] Q. Zhu, J. Yamada, N. Kishi, M. Watanabe, A. Okino, K. Horioka, and E. Hotta, “Investigation of the dynamics of the Z-pinch imploding plasma for a laser-assisted discharge-produced Sn plasma EUV source,” *J. Phys. D. Appl. Phys.*, vol. 44, no. 145203, p. 12, 2011.

[63] B. Huang, T. Tomizuka, B. Xie, Y. Sakai, Q. Zhu, I. Song, A. Okino, F. Xiao, M. Watanabe, and E. Hotta, “Simulation and mitigation of the magneto-Rayleigh-Taylor instabilities in Z-pinch gas discharge extreme ultraviolet plasma radiation sources,” *Phys. Plasmas*, vol. 20, no. 11, p. 9, 2013.

[64] A. G. Rousskikh, A. S. Zhigalin, V. I. Oreshkin, N. A. Labetskaya, S. A. Chaikovsky, A. V Batrakov, and G. Yu, “Study of the stability of Z-pinch implosions with different initial density profiles,” *Phys. Plasmas*, vol. 21, no. 052701, p. 7, 2014.

[65] A. P. Thorne, *Spectrophysics*. Netherlands: Springer, 1988.

[66] R. W. P. McWhirter, *Plasma Diagnostic Techniques*. New York: Academic Press, 1965.

[67] E. N. Dulov and D. M. Khripunov, “Instrumental broadening of spectral line profiles due to discrete representation of a continuous physical quantity,” *J. Quant. Spectrosc. Radiat. Transf.*, vol. 109, no. 10, pp. 1922–1930, Jul. 2008.

[68] PrismSPECT, “http://www.prism-cs.com/Software/PrismSpect/PrismSPECT.htm.” .

[69] C. Pagano, S. Hafeez, and J. G. Lunney, “Influence of transverse magnetic field on expansion and spectral emission of laser produced plasma,” *J. Phys. D Appl. Phys.*, vol. 42, no. 15, p. 11, 2009.

[70] G. O’Connell, I. Tobin, and J. G. Lunney, “Early stage optical emission in nanosecond laser ablation,” *Appl. Phys. A*, vol. 110, no. 3, pp. 731–734, Sep. 2012.

[71] T. Donnelly and J. G. Lunney, “Confined laser ablation for single-shot nanoparticle deposition of silver,” *Appl. Surf. Sci.*, vol. 282, pp. 133–137, Oct. 2013.

[72] G. G. Il’in, A. S. Ramanazov, I. S. Fishman, and I. S. Shaimanov, “Calculation of the apparatus function for the case of a generalized Voigt contour,” *J. Appl. Spectrosc.*, vol. 3, no. 4, pp. 237–240, 1965.

[73] H. R. Griem, “Semiempirical formulas for the electron-impact widths and shifts of isolated ion lines in plasmas,” *Phys. Rev.*, vol. 165, no. 1, p. 9, 1968.

[74] S. Sahal-Bréchot, “Impact theory of the broadening and shift of spectral lines due to electrons and ions in a plasma,” *Astron. Astrophys.*, vol. 1, pp. 91–123, 1969.

[75] S. Sahal-Bréchot, “Impact theory of the broadening and shift of spectral lines due to electrons and ions in a plasma (continued),” *Astron. Astrophys.*, vol. 2, pp. 322–354, 1969.

[76] M. S. Dimitrijević and N. Konjević, “Stark widths of doubly- and triply-ionized atom lines,” *J. Quant. Spectrosc. Radiat. Transf.*, vol. 24, no. 6, pp. 451–459, Dec. 1980.

[77] M. A. Gigosos, “Stark broadening models for plasma diagnostics,” *J. Phys. D. Appl. Phys.*, vol. 47, no. 34, p. 343001, 2014.

[78] H. R. Griem, “Stark broadening by electron and ion impacts of nα hydrogen lines of large principal quantum number,” *Astrophys. J.*, vol. 148, pp. 547–558, 1967.

[79] J. Purić and N. Konjević, “Stark shifts of some isolated spectral lines of singly ionized earth alkaline metals,” *Zeitschrift für Phys.*, vol. 249, pp. 440–444, 1972.

[80] N. Konjević and W. L. Wiese, “Experimental Stark Widths and Shifts for Spectral Lines of Neutral and Ionized Atoms,” *J. Phys. Chem. Ref. Data*, vol. 19, no. 6, pp. 1307–1385, 1990.

[81] N. Konjević, “Experimental Stark Widths and Shifts for Spectral Lines of Neutral and Ionized Atoms (A Critical Review of Selected Data for the Period 1989 Through 2000),” *J. Phys. Chem. Ref. Data*, vol. 31, no. 3, p. 819, Sep. 2002.

[82] R. Dengler, “Self inductance of a wire loop as a curve integral,” *arXiv:1204.1486*, 2012.

[83] E. Sterling, I. Tobin, and J. G. Lunney, “Z-Pinch Discharge in Laser Produced Plasma,” in *37th EPS Conference on Plasma Physics*, 2010.

[84] D. A. Ward and J. L. T. Exon, “Using Rogowski coils for transient current measurements,” *Eng. Sci. Educ. J.*, pp. 105–113, 1993.

[85] B. Doggett and J. G. Lunney, “Langmuir probe characterization of laser ablation plasmas,” *J. Appl. Phys.*, vol. 105, 2009.

[86] D. W. Koopman, “Langmuir probe and microwave measurements of the properties of streaming plasmas generated by focused laser pulses,” *Phys. Fluids*, vol. 14, no. 8, pp. 1707–1716, 1971.

[87] Y. Franghiadakis and C. Fotakis, “Energy distribution of ions produced by excimer-laser ablation of solid and molten targets,” *Appl. Phys. A Mater.*, vol. 397, pp. 391–397, 1999.

[88] M. S. del Río, “XOP 2.1 — A New Version of the X-ray Optics Software Toolkit,” in *AIP Conference Proceedings*, 2004, vol. 705.

[89] L. A. Shmaenok, N. N. Salashchenko, N. I. Chkhalo, E. B. Kluenkov, K. A. Prokhorov, and N. Novgorod, “A tool for direct EUV source metrology in the ‘ at-wafer ’ spectral band,” in *International Sematech EUV Source Workshop*, 2004.

[90] P. Dunne, O. Morris, E. Sokell, G. O’Sullivan, F. O’Reilly, N. Murphy, P. Hayden, and V. Bakshi, “Cross-calibration of absolute spectral measurements and PhysTeX energy monitor for the in-band and out-of-band region on a tin (Sn) LPP source,” in *Sematech Technology Transfer*, 2006.

[91] O. Morris, P. Hayden, F. O’Reilly, N. Murphy, P. Dunne, and V. Bakshi, “Angle-resolved absolute out-of-band radiation studies of a tin-based laser-produced plasma source,” *Appl. Phys. Lett.*, vol. 91, no. 8, p. 081506, 2007.

[92] M. C. Schuermann, T. Missalla, K. R. Mann, S. Kranzusch, R. M. Klein, F. Scholze, G. Ulm, R. Lebert, and L. Juschkin, “Metrology tools for EUVL-source characterization and optimization,” *Proc. SPIE Emerg. Lithogr. Technol. VII*, vol. 5037, 2003.

[93] T. Missalla, M. C. Schuermann, R. Lebert, C. Wies, L. Juschkin, Roman M. Klein, F. Scholze, G. Ulm, A. Egbert, B. Tkachenko, and B. N. Chichkov, “Metrology tools for EUV-source characterization and optimization,” in *Proc. SPIE Emerging Lithographic Technologies VIII*, 2004, vol. 5374, no. Emerging Lithographic Technologies VIII.

[94] T. Harada and T. Kita, “Mechanically ruled aberration-corrected concave gratings.,” *Appl. Opt.*, vol. 19, no. 23, pp. 3987–93, Dec. 1980.

[95] J. D. Ramboz, “Machinable rogowski coil, design, and calibration,” *IEEE Trans. Instrum. Meas.*, vol. 45, no. 2, pp. 511–515, 1996.

[96] J. Douglass, J. Greenly, D. Hammer, B. Kusse, R. McBride, and S. Pikuz, "Design and use of Small Rogowski Coils for use with Large, Fast Current Pulses," *2005 IEEE Pulsed Power Conf.*, pp. 717–720, Jun. 2005.

[97] E. Woryna, P. Parys, J. Wołowski, and W. Mróz†, "Corpuscular diagnostics and processing methods applied in investigations of laser-produced plasma as a source of highly ionized ions," *Laser Part. Beams*, vol. 14, no. 3, pp. 293–321, Mar. 1996.

[98] E. C. Benck, "Plasma diagnostic techniques," in *EUV sources for lithography*, V. Bakshi, Ed. Bellingham, WA: SPIE, 2009, pp. 735–758.

[99] "CXRO." [Online]. Available: www.cxro.lbl.gov.

[100] R. M. Klein, F. Scholze, G. U. P. Bundesanstalt, and D.- Berlin, "JENOPTIK Mikrotechnik GmbH Tools for EUVL-source characterization and optimization Abstract :," p. 2004, 2004.

[101] NIST, "http://www.nist.gov/pml/data/asd.cfm," *National Institute of Standards and Technology*. .

[102] A. W. Allen, M. Blaha, W. W. Jones, A. Sanchez, and H. R. Griem, "Stark-broadening measurement and calculations for a singly ionized aluminium line," *Phys. Rev. A*, vol. 11, no. 2, pp. 477–479, 1975.

[103] O. Djilianova, M. J. Sadowski, E. Skladnik-Sadowska, K. Malinowski, M. Scholz, a Blagoev, and K. Paskalev, "The Cu spectra as a tool for late plasma focus diagnostics," *J. Phys. Conf. Ser.*, vol. 44, pp. 175–178, Jul. 2006.

[104] V. Y. Banine, K. N. Koshelev, and G. H. P. M. Swinkels, "Physical processes in EUV sources for microlithography," *J. Phys. D. Appl. Phys.*, vol. 44, no. 25, p. 253001, Jun. 2011.

[105] K. Gielissen, Y. Sidelnikov, D. Glushkov, W. a. Soer, V. Banine, and J. J. a. M. V. D. Mullen, "Characterization of ion emission of an extreme ultraviolet generating discharge produced Sn plasma," *J. Appl. Phys.*, vol. 107, no. 1, p. 013301, 2010.

[106] J. M. Liu, "Simple technique for measurements of pulsed Gaussian-beam spot sizes," *Opt. Lett.*, vol. 7, no. 5, p. 196, May 1982.

[107] V. S. Zakharov, L. Juschkin, S. V Zakharov, G. O. Sullivan, E. Sokel, and I. Tobin, "Laser-initiated discharge produced plasma ablated from liquid metal electrodes," in *International workshop on EUV and soft x-ray sources*, 2012.

[108] J. White, P. Hayden, P. Dunne, A. Cummings, N. Murphy, P. Sheridan, and G. O'Sullivan, "Simplified modeling of 13.5 nm unresolved transition array emission of a Sn plasma and comparison with experiment," *J. Appl. Phys.*, vol. 98, no. 11, p. 113301, 2005.

[109] T. Krücken, K. Bergmann, L. Juschkin, and R. Lebert, "Fundamentals and limits for the EUV emission of pinch plasma sources for EUV lithography," *J. Phys. D. Appl. Phys.*, vol. 37, no. 23, pp. 3213–3224, 2004.

[110] W. L. Wiese, J. R. Fuhr, and T. M. Deters, "Atomic transition probabilities of carbon, nitrogen and oxygen," *J. Phys. Chem. Ref. Data*, vol. 7, p. 532, 1996.

[111] H.-K. Chung, M. H. Chen, W. L. Morgan, Y. Ralchenko, and R. W. Lee, "FLYCHK: Generalized population kinetics and spectral model for rapid spectroscopic analysis for all elements," *High Energy Density Phys.*, vol. 1, no. 1, pp. 3–12, Dec. 2005.

[112] T. Wujec and J. Musielok, "Measurements of absolute transition probabilities of Sn I and Sn II lines by method of emission spectroscopy," *Astron Astrophys*, vol. 50, pp. 405–411, 1976.

[113] M. Miller, R. Roig, and R. Bengtson, “Experimental transition probabilities and Stark-broadening parameters of neutral and singly ionized tin,” *Phys. Rev. A*, vol. 20, no. 2, pp. 499–506, 1979.

[114] A. Alonso-Medina, “A spectroscopic study of laser-induced tin–lead plasma: Transition probabilities for spectral lines of Sn I,” *Spectrochim. Acta Part B At. Spectrosc.*, vol. 65, no. 2, pp. 158–166, Feb. 2010.

[115] T. Wujec and S. Weniger, “Atomic transition probabilities for Sn(I), Sn(II) and Cl(I) lines in the 5300–6850 Å wavelength range,” *J. Quant. Spectrosc. Radiat. Transf.*, vol. 18, no. 5, pp. 509–514, 1977.

[116] B. Martínez and F. Blanco, “Experimental and theoretical Stark width and shift parameters of neutral and singly ionized tin lines,” *J. Phys. B At. Mol. Opt. Phys.*, vol. 32, pp. 241–247, 1999.

[117] S. Djeniže, a Srećković, and Z. Nikolić, “On the Sn I and Sn II Stark broadening,” *J. Phys. B At. Mol. Opt. Phys.*, vol. 39, no. 14, pp. 3037–3045, Jul. 2006.

[118] A. Alonso-Medina and C. Colón, “Measured Stark Widths of Several Sn i and Sn ii Spectral Lines in a Laser-induced Plasma,” *Astrophys. J.*, no. 672, pp. 1286–1291, 2008.

[119] A. Alonso-Medina, C. Colón, and C. Rivero, “Theoretical Transition Probabilities of some Lines of 5s2(1S)nl and 5s 5p2 Levels of Sn II,” *Phys. Scr.*, vol. 154, no. 71, pp. 6–11, 2005.

[120] A. Alonso-Medina and C. Colón, “Interpretation of the spectrum of Sn II: Experimental and theoretical transition probabilities,” *Phys. Scr.*, vol. 61, pp. 646–651, 2000.

[121] S. Djeniže, A. Srećković, and J. Labat, “Stark width and shift of singly-ionized tin spectral lines,” *Zeitschrift für Phys. D Atoms, Mol. Clust.*, vol. 86, pp. 85–86, 1990.

[122] C. Colón and a Alonso-Medina, “Calculation of oscillator strengths, transition probabilities and radiative lifetimes of levels in Sn III,” *J. Phys. B At. Mol. Opt. Phys.*, vol. 43, no. 16, p. 165001, Aug. 2010.

[123] A. Alonso-Medina and C. Colón, “Stark broadening of Sn iii spectral lines of astrophysical interest: predictions and regularities,” *Mon. Not. R. Astron. Soc.*, vol. 414, no. 1, pp. 713–726, 2011.

[124] E. Kieft, J. Van Der Mullen, G. Kroesen, and V. Banine, “Stark broadening experiments on a vacuum arc discharge in tin vapor,” *Phys. Rev. E*, vol. 066402, pp. 1–8, 2004.

[125] J. Filevich, J. J. Rocca, E. Jankowska, E. C. Hammarsten, K. Kanizay, and M. C. Marconi, “Two-dimensional effects in laser-created plasmas measured with soft-x-ray laser interferometry,” *Phys. Rev. E*, vol. 67, no. 056409, pp. 1–6, 2003.

[126] T. Wu, X. Wang, S. Wang, J. Tang, P. Lu, and H. Lu, “Time and space resolved visible spectroscopic imaging CO2 laser produced extreme ultraviolet emitting tin plasmas Time and space resolved visible spectroscopic imaging CO 2 laser produced extreme ultraviolet emitting tin plasmas,” vol. 063304, 2012.

[127] J. Freeman and S. Harilal, “Enhancements of extreme ultraviolet emission using prepulsed Sn laser-produced plasmas for advanced lithography applications,” *J. Appl. Phys.*, vol. 083303, no. 2011, 2011.

[128] I. Brown, *Handbook of Vacuum Arc Science and Technology*. Elsevier, 1996.

[129] G. A. Beyene, E. Scally, P. Hayden, L. Juschkin, V. S. Zakharo, S. V Zakharov, P. Dunne, O. Sullivan, and O. Reilly, “Comparison of ns vs ps Laser Assisted Vacuum Arc EUV Source,” in *International workshop on EUV and soft x-ray sources*, 2013.

[130] C. Laubis, F. Scholze, and G. Ulm, “Metrology in the Soft X-Ray Range – from EUV to the Water Window,” in *Advances in Optical Thin Films III*, 2008, vol. 7101, p. 71011U–71011U–12.

[131] T. Otsuka, D. Kilbane, J. White, T. Higashiguchi, N. Yugami, T. Yatagai, W. Jiang, A. Endo, P. Dunne, and G. O’Sullivan, “Rare-earth plasma extreme ultraviolet sources at 6.5 – 6.7 nm,” *Appl. Phys. Lett.*, vol. 97, pp. 8–10, 2010.

[132] A. Hassanein, I. Konkashbaev, and B. Rice, “Method for Plasma Formation for EUVL Theta Pinch,” 2007.

[133] I. Doi and G. N. Wakamatu, “A Theta-Pinch Laser,” vol. 13, no. 1, 1998.